MAX PLANCK INSTITUTE
FOR POLYMER RESEARCH

JOHANNES GUTENBERG
UNIVERSITÄT MAINZ

Structural variations of amyloid-like peptides and their interaction with neural cells

Dissertation

zur Erlangung des Grades

DOCTOR RERUM NATURALIUM (Dr. rer. nat.)

der Fachbereiche:

FB09 Chemie, Pharmazie, Geographie und Geowissenschaften

der Johannes Gutenberg-Universität Mainz

Yu-Liang Tsai

Geboren in Taipei, Taiwan

Mainz, Juli 2025

First Reviewer: Prof. Dr. Tanja Weil

Second Reviewer: Prof. Dr. Shikha Dhiman

Date of Defense: 16.07.2025

Die vorliegende Arbeit wurde in der Zeit von April 2021 bis Juli 2025 am Max-Planck-Institut für Polymerforschung in der Arbeitsgruppe von Prof. Dr. Tanja Weil angefertigt.

Hiermit versichere ich gemäß § 11 (4) der Promotionsordnung vom May 26, 2009
Ich habe die jetzt als Dissertation vorgelegte Arbeit selbst angefertigt und alle benutzten Hilfsmittel (Literatur, Apparaturen, Material) in der Arbeit angegeben. Ich habe oder hatte die jetzt als Dissertation vorgelegte Arbeit nicht als Prüfungsarbeit für eine staatliche oder andere wissenschaftliche Prüfung eingereicht. Ich hatte weder die jetzt als Dissertation vorgelegte Arbeit noch Teile davon bei einer anderen Fakultät bzw. einem anderen Fachbereich als Dissertation eingereicht.

This work was carried out at the Max Planck Institute for Polymer Research in the research group of Prof. Dr. Tanja Weil from April 2021 to July 2025.

In accordance with § 11 (4) of the doctoral regulations dated May 26, 2009:
I hereby declare that I wrote the dissertation submitted without any unauthorized external assistance and used only sources acknowledged in the work. All textual passages which are appropriated verbatim or paraphrased from published and unpublished texts as well as all information obtained from oral sources are duly indicated and listed in accordance with bibliographical rules. In carrying out this research, I complied with the rules of standard scientific practice as formulated in the statutes of Johannes Gutenberg University Mainz to ensure standard scientific practice.

Mainz, June 2025

Yu-Liang Tsai

Acknowledgement

“Everything will be okay in the end. If it's not okay, it's not the end”. This is the sentence that best summarizes my Ph.D. journey. Starting during the pandemic period and handling unfortune incidents in my life, I feel so relieved at the moment as I am finally reaching the end of this journey.

First of all, I deeply appreciated my family for supporting and trusting me so that I can be the first one in the family to have the chance and honor to receive this academic laurel. I know it is a bit late, but I want to say, “Dad and Mom, I made it as I promised you and thank you for giving me the support and freedom to explore different possibilities and be myself.”

I really appreciated Prof. Dr. Tanja Weil for leading a positive and supporting working environment and for understanding my struggle in 2023. I would like to show my gratitude to my group leader, Dr. Christopher Synatschke, for helping to me settle in Mainz, supporting me to attend conferences and training programs, and supporting me to overcome my hardship.

It would not be possible for me to complete this journey without the help of my colleagues and alumni for scientific discussions and leisure activities. I would like to give special thanks to Marius for being my bike doctor and helping me through German bureaucracy. I sincerely appreciate Julian’s support in pulling me out of my depressing moment and inviting me to many activities that felt heartwarming. Sotiria and Primiana, thank you both for working alongside me with positive feedback, and I hope that you picked up some skills from me. Additionally, I also want to say thank you to Prof. Dr. Amann-Winkel, Dr. Berger, Dr. Kuan, Dr. Ng, Dr. Räder, Dr. Wagner, and Dr. Wu for the scientific suggestion, and the Biocore for technical support. I had wonderful memory in Rüdesheim, Ringberg, Cuxhaven, and all institutional events. My gratitude goes towards all my peers and members in the entire Max Planck Institute for Polymer Research. I feel spoiled embarking on my Ph.D. journey in this well-equipped, diverse, and international research institute.

I would also show my gratitude to my important collaborators outside of the institute. Prof. Dr. Torsten John at Constructor University, the former postdoc in AK Weil, provided his expertise in computational modeling which enriched my research project. Prof. Dr. Kristina Endres at Universitätsmedizin Mainz and Hochschule Kaiserlautern offered her expertise to help me establish a new neuronal cell line.

Another appreciation note goes to my neighbors who invited me to many celebrations, barbecues, and movie nights, and to my friends with whom I play basketball, “Fußball”, and bouldering. Your accompany means a lot to me and spices up my life in Germany.

Abstract

The nervous system, including the peripheral nervous system (PNS) and the central nervous system (CNS), is composed of multiple neurons that are classified based on diverse molecular, morphological, connectional, and functional properties. Although there are a wide variety of neurons, they have one thing in common, that is, neurons are sensitive to subtle physical changes and biochemical cues arising from the environment. Therefore, this thesis focuses on structural variations of amyloid-like self-assembling peptides – a promising material for artificial neural scaffolds – and their interaction with neural cells.

Amyloid-like peptides, associated with neurodegenerative diseases, such as Parkinson's, Alzheimer's, and Huntington's, are misfolded peptide molecules that are highly resistant to degradation. The misfolding or self-assembly occurs under physiological conditions and is affected by various factors, such as the peptide sequence, concentration, and solvent effect. Taking advantage of their non-degradable characteristic and diverse assembly morphologies, amyloid-like peptides have been used as hierarchical nano-templates for neuroscience, neural drug development, and neural tissue engineering.

The goal of this thesis is to investigate the correlation between the structure of self-assembling peptides and the bioactivity of neural cells. The most straightforward strategy is employed first: a library of nine amyloid-like peptides is designed by systematically varying the hydrophobic core of the peptide backbone. The physicochemical properties of the peptides are extensively analyzed from the atomistic, molecular, and microscopic level. Furthermore, molecular dynamics simulations are used to provide theoretical insights to explain the differences in peptide assembly. With deeper structural insights, these peptides are examined for their neural activity using a human neuroblastoma cell line to understand the relationship between peptide structure and neural activity. The results of this project demonstrated that the computational simulations could help the rational design of peptide sequences for neural repair.

The following chapter, an important but often overlooked factor, the solvent effect, is investigated to understand how the solvation effect influences the assembly behavior of amyloid-like peptide and their neural activity. The same peptide sequence that is produced by different manufacturers, dissolved in different solvents, or tested at various time points, demonstrates different self-assembly behavior. The difference derived from the self-

assembly behavior is reflected in the activation of the formyl peptide receptor 1 in both mouse and human neural cells, highlighting that the processing history and solvent effect influenced the structure-property relationship of amyloid-like peptide and neural activity.

Neural differentiation requires a long period of incubation, so it is of importance to build a stable amyloid-like SAP substrate that can resist frequent washing. Amyloid-like peptides functionalized with vinyl groups are synthesized and immobilized on thiolated substrates prepared by chemical vapor deposition via a photo-triggered thiol-ene reaction. This peptide immobilization strategy offers a facile route to fabricate a large and customized two-dimensional amyloid-like peptide layer to manipulate neural cell adhesion.

In summary, this thesis aims to investigate different factors that influence the self-assembled structure of amyloid-like peptides and correlate the structural differences with neural behavior to provide insights into the structure-property relationship between amyloid-like peptides and neural cells.

Zusammenfassung

Das Nervensystem, einschließlich des peripheren Nervensystems (PNS) und des zentralen Nervensystems (ZNS), besteht aus einer Vielzahl von Neuronen, die auf der Grundlage verschiedener molekularer, morphologischer, konnektiver und funktioneller Eigenschaften klassifiziert werden. Obwohl es eine große Vielfalt an Neuronen gibt, haben sie eines gemeinsam: sie reagieren auf subtile physikalische Veränderungen und biochemische Hinweise aus der Umwelt. Daher konzentriert sich diese Arbeit auf strukturelle Variationen amyloidähnlicher Peptide und deren Interaktion mit Nervenzellen.

Amyloid-ähnliche Peptide, die mit neurodegenerativen Krankheiten wie Parkinson, Alzheimer und Huntington in Verbindung gebracht werden, sind fehlgefaltete Peptidmoleküle, die sehr widerstandsfähig gegen den Abbau sind. Die Fehlfaltung oder Selbstassemblierung erfolgt unter physiologischen Bedingungen und wird durch verschiedene Faktoren wie Sequenzdesign, Konzentration und Solvatationseffekte beeinflusst. Amyloid-ähnliche Peptide wurden aufgrund ihrer schlechten Abbaubarkeit und ihrer vielfältigen Assemblierungsmorphologien als hierarchische Nano-Templates für die Neurowissenschaften, die Entwicklung neuronaler Arzneimittel und das neuronale Tissue Engineering verwendet.

Ausgehend von der einfachsten Strategie wird eine Bibliothek von neun amyloidähnlichen Peptiden durch systematische Variation des hydrophoben Kerns des Peptidrückgrats entwickelt. Die physikochemischen Eigenschaften der Peptide werden auf atomarer, molekularer und mikroskopischer Ebene eingehend analysiert. Darüber hinaus werden Molekulardynamiksimulationen eingesetzt, um theoretische Erkenntnisse zur Erklärung der Unterschiede im Peptidaufbau zu gewinnen. Mit einem tieferen Einblick in die strukturellen Informationen werden diese Peptide anhand einer menschlichen Neuroblastom-Zelllinie auf ihre neuronale Aktivität untersucht, um die Beziehung zwischen Peptidstruktur und neuronaler Aktivität zu verstehen.

Im folgenden Kapitel wird ein wichtiger, aber oft übersehener Faktor, der Solvatationseffekt, untersucht, um zu verstehen, wie dieser das Assemblierungsverhalten von amyloidähnlichen Peptiden und ihre neuronale Aktivität beeinflusst. Dieselbe Peptidsequenz, die von verschiedenen Herstellern produziert, in verschiedenen Lösungsmitteln gelöst oder zu verschiedenen Zeitpunkten getestet wird, zeigt ein

unterschiedliches Selbstassemblierungsverhalten. Der Unterschied, der sich aus dem Selbstassemblierungsverhalten ergibt, spiegelt sich in der Aktivierung des Formylpeptidrezeptors 1 sowohl in neuronalen Zellen der Maus als auch des Menschen wider, was die Verarbeitungsplastizität und die Struktur-Eigenschafts-Beziehung von amyloidartigen Peptiden und neuronaler Aktivität verdeutlicht.

In den beiden vorangegangenen Kapiteln wurden amyloidähnliche Peptide in Kulturmedium suspendiert, um mit Nervenzellen in einer Dimension zu interagieren. Nervenzellen verhalten sich unterschiedlich als Reaktion auf Umweltreize. Amyloid-ähnliche Peptide, die mit Vinylgruppen funktionalisiert sind, werden synthetisiert und auf thiolierten Substraten immobilisiert, die durch chemische Abscheidung aus der Dampfphase mittels einer durch Licht ausgelösten Thiol-En-Reaktion hergestellt wurden. Diese Peptid-Immobilisierungsstrategie stellt einen einfachen Weg zur Herstellung einer großen und maßgeschneiderten zweidimensionalen amyloidartigen Peptidschicht dar, um die Adhäsion von Nervenzellen zu beeinflussen.

Zusammengefasst zielt diese Arbeit darauf ab, verschiedene Faktoren zu untersuchen, die die Selbstassemblierungsstruktur von amyloidähnlichen Peptiden beeinflussen, und die strukturellen Unterschiede mit dem neuronalen Verhalten zu korrelieren, um Einblicke in die Struktur-Eigenschafts-Beziehung zwischen amyloidähnlichen Peptiden und neuronalen Zellen zu gewinnen.

Die deutsche Zusammenfassung wurde auf der Grundlage der englischen Zusammenfassung mit DeepL Translator.

Contents

1. Introduction

Section 1.4. to 1.6. have been adapted with permission with changes from

Yu-Liang Tsai, Jialei Song, Rachel Shi, Bernd Knöll, Christopher V. Synatschke, A Roadmap of Peptide-Based Materials in Neural Regeneration, Adv. Healthcare Mater. 2024, 2402939, Copyright 2024, WILEY-VCH Verlag GmbH & Co.

1.1.General Introduction to Amyloid-Like Self-Assembly Peptide

Self-assembling and folding of peptide molecules are commonly seen in nature and play vital roles in humans' physiological functions when they fold or assemble correctly; for example, actin fibrils in eukaryotic cells for cell motility and synthesis and deposition of melanin in vertebrate melanosomes.[1,2] However, the misfolding of these specific peptide molecules along with additional proteins and carbohydrates, as known as amyloidosis, in different organs is associated with multiple diseases, including type II diabetes and neural degenerative diseases, such as Parkinson's, Alzheimer's, and Huntington's.[1–3] These amyloid SAPs are highly resistant to degradation; therefore, early research has been conducted to explain the formation mechanisms and to inhibit amyloid formation.[2] In recent years, scientists gained more in-depth knowledge of amyloid structures, which possess a variety of morphologies with multiple dimensions.[1,2,4,5] Once been considered as a disadvantage, the undegradable nature and diverse morphologies of amyloid-like SAPs provide robust templates for hierarchical nanostructures for biomedical applications, for instance, biofilms, cell scaffolds and biosensors.[1,2,4]

1.2.Characteristics and Morphology of Self-Assembling Peptide

The self-assembly and folding of peptide molecules into higher ordered structures are driven by non-covalent interactions, such as hydrogen bonding (H-bonding), electrostatic interactions, hydrophobic interactions, metal-ion coordination, etc.[1,3,5,6] These ordered structures involve multiple length scales ranging from nm to μm, as illustrated in **Figure 1**.

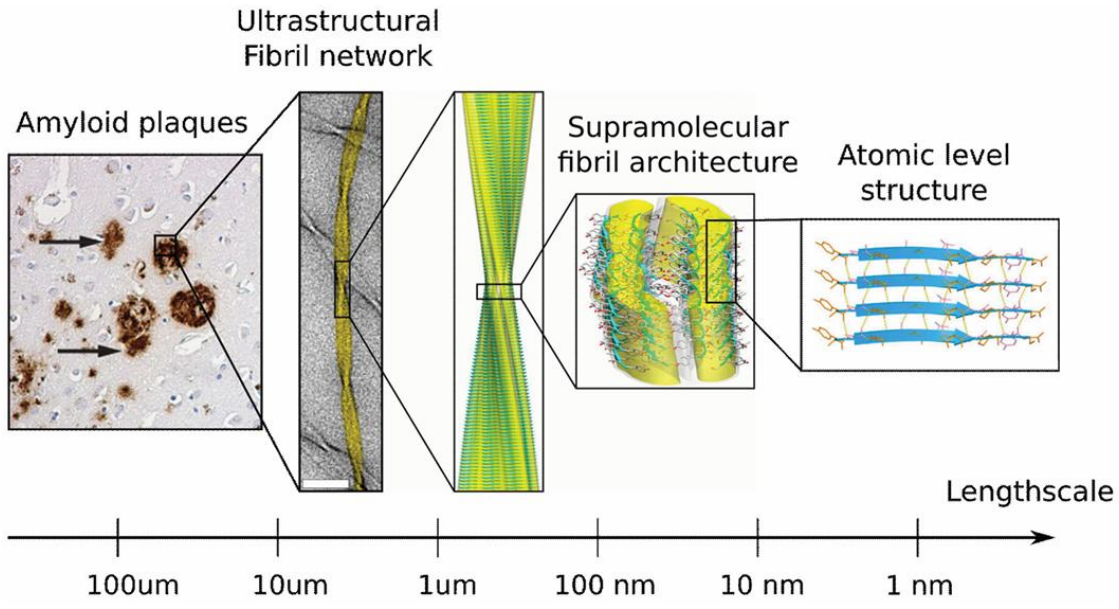

Figure 1. Overview of the different length scales at which the characteristic amyloid-like structures appear. Reprinted with permission.[4] Copyright 2016, WILEY-VCH Verlag GmbH & Co.

At the atomistic length-scale, peptide molecules assemble into β-strands (~ 4 Å apart) perpendicular to the fibril axis and tightly packed into β-sheets. Each β-sheet is parallel to each other and the intersheet distance is roughly ~10–12 Å.[1–3,7] The intramolecular secondary structures, such as α-helical and β-strand, further evolve into tertiary structure and intermolecular quaternary structure, which is also referred to as hierarchical nanostructures.[7–10] These hierarchical nanostructures range from zero-dimensional (nanoparticles and nanospheres), one-dimensional (nanofibrils, nanoribbons, and nanotubes), two-dimensional (nanosheets and nanofilms) to three-dimensional scaffolds.[1,2] Typical techniques for structural characterization include molecular, microscopic, and spectroscopic analysis. At molecular level, Congo red[11] and Thioflavin T (ThT)[12] molecules bind with β-sheets in the amyloid-like self-assembly peptide. Spectroscopic techniques, such as Fourier transform infrared spectroscopy (FT-IR)[13], circular dichroism (CD)[14], and nuclear magnetic resonance (NMR)[15] provide information on secondary structures. Crystallography, such as X-ray diffraction[3,16] and electron diffraction[3], gives insight into molecular packing distance of the amyloid-like SAP. At the microscopic length

scale, dynamic light scattering (DLS) provides information on microscopic aggregates in solution.[17] Atomic force microscopy (AFM) and electron spectroscopy, including scanning electron microscopy (SEM), transmission electron microscopy (TEM), and cryogenic electron microscopy (Cryo-EM), generate images and characterize the surface topography and morphology of the amyloid-like SAP.[17–20] In particular, Cryo-EM generate images at the atomic level, allowing the reconstruction of 3D molecular models[18–20] of amyloid-like SAP for further investigation in dynamics and computation modeling.

1.3. Factors Affecting Self-Assembly Peptides

The first step in designing SAP is design of amino acid sequence, which directly influences its propensity to form aggregates or defined structures.[21] Multiple sequential intrinsic factors can affect the peptide self-assembly behavior. Peptide concentrations play important roles in modulating the kinetics and stability of the SAP.[21] Given the same amino acids in the peptide sequence, altering the position of amino acids, i.e. constitutional isomers and stereoisomers, changes the charge distribution and steric profile of the hydrophobic side chains, influencing the morphology and kinetic of self-assembly.[22,23] Similar peptide sequences varying only the side groups of hydrophobic group can change the morphologies of the SAP. For example, Wang et al. modified the terminal residues of the Islet amyloid-polypeptide and suggested that sequences with more hydrophobicity and β-sheet strength led to planar nanoribbons, while other more hydrophilic sequences formed twisted structures.[24] Hussain Sangji and coworkers altered hydrophobic groups in the β-sheet-forming region of the peptide amphiphile, and they found that varying the hydrophobic groups changed not only the self-assembly structure but also the chirality of the structure.[25]

External factors, such as salt ions, ionic strength, pH, temperature, additional molecules, and sample processing, also have significant effects on the peptide self-assembly behavior.[1,2,17,21] Solvation effect, including salt ions, ionic strength, and pH, is ions interplaying with the hydrophobic groups of peptide molecules, which can either improve or interfere self-assembly.[1,2,17,21] For example, Roy et al. demonstrated that incubating the same aromatic short peptide amphiphiles in solvents with different the anions, such as phosphates, sulfates, chlorine ions, thiocyanate, etc., led to different assembly

morphologies and mechanical properties of the resulting hydrogel.[26] Shanbhag and colleagues reported a pH and magnesium ion (Mg^{2+}) sensitive protein-peptide conjugate, which could assemble into nanoparticles. The size of the nanoparticles was mediated by pH of the solution, and the self-assembly is reversible based on the presence and absence of Mg^{2+}.[27] Temperature is critical for tuning hydrophobic interaction and H-bonding, and thereby it can manipulate the self-assembly morphologies.[1,2,17] For instance, Miravet et al. prepared a peptide amphiphile that underwent structure transition from nanofibers to micelle upon heat treatment.[28] A comprehensive example reported by Yuan et al. highlighted that peptide amphiphiles with heat treatment and addition of electrolytes at different time points altered supramolecular polymerization pathways; therefore, these differences changed the properties and bioactivity of peptide amphiphiles towards a chondrogenic cell line.[29]

Taken together, SAPs are a class of material that can be designed with distinct molecular characteristics and different self-assembly morphologies. Additionally, SAPs have high processing plasticity to further change their structures. Furthermore, Schilling et al. identified a small library of amyloid-like SAP nanofibrils that are intrinsically neurotrophic.[30] The above-mentioned advantages make amyloid-like SAPs attractive candidates to investigate their structure and neural activity.

1.4. Self-Assembling Peptide Material for Neural Regeneration

Natural biomaterials, such as collagen, gelatin, hyaluronic acid, alginate, and chitosan, have been utilized for neural regeneration.[31] They hold the advantages of inherent bioactivity and biodegradability because they stem from acellularized tissue and extracellular matrix-derived macromolecules. Large-scale synthesis is another benefit of using natural biomaterials for neuronal regeneration. However, batch-to-batch variability in production and an uncontrollable degradation profile are drawbacks that need to be considered.[32,33] In contrast to natural biopolymers, synthetic polymers, like polycaprolactone, poly-L-lactic acid, and polyethylene glycol (PEG), are another category of biomaterials implemented for neural regeneration.[34] They are known for their high reproducibility, processability, and tunability, which compensate for the shortcomings of natural biomaterials. However, they lack biological cues due to their chemical nature; thus,

more synthetic approaches to decorating bioactive motifs on synthetic polymers are necessary to increase their biocompatibility. It is also worth noting that the degradation product of lactic acid-based materials acidifies the local physiological environment, which may be disadvantageous.[32,33]

Synthetic peptides, consisting of amino acids, offer an alternative class of biomaterials for neural repair, with non-cytotoxic degradation products. Based on sequential designs, they can incorporate bioactive groups and synchronously serve as a matrix for cell adhesion. Moreover, synthetic peptides can be synthesized with high purity using commercially available automated synthesizers.[35,36] Combining the advantages of both natural biomaterials and synthetic polymers, synthetic peptides provide new possibilities for neural tissue engineering.

The ECM is an essential component of all tissues, providing mechanical support and barrier function for the structural integrity of multicellular organisms. Furthermore, the ECM functions as a reservoir for signaling cues thereby regulating cell fate. In the design of functional biomaterials for neural regeneration, scientists are aiming to emulate those cues provided by the ECM.[37] In neural tissue, the ECM is a fibrous network, primarily consisting of proteins, proteoglycans, and glycosaminoglycans. The ECM environment surrounding neurons is complex because of its multiscale architecture, various cell types, multiple biomolecules, fibrous network, and interpenetrating vascular systems.[38] Therefore, mimicking the neural ECM necessitates incorporating as many aspects of the neural environment as possible.

SAPs are a class of materials consisting of short peptide sequences and show potential for mimicking the neural ECM. They form nanofibers thereby reflecting essential properties of the neural ECM under physiological conditions.[39] SAPs form their structure via non-covalent interactions, for instance, hydrogen bonding, π–π stacking, electrostatic interactions, and van der Waals interactions. Although non-covalent interactions are generally weaker than covalent bonds, these weaker but directional interactions give rise to the reversibility, stimulus responsiveness (e.g. redox, pH, etc.), and nanostructures of SAPs, which resemble tubulin proteins inside of cells.[40] SAPs are solid or gel matrix that can potentially assemble and attach at the site of interest (e.g. injection at the injury site), which not only allows minimally invasive surgery but also bypasses the blood brain barrier

or the blood spinal cord barrier.[35] Additionally, SAPs are easily modified with aromatic groups, lipid chains, and biomolecules to tune the physical (i.e. topography) and biochemical (i.e. growth factor mimic) properties of the neural ECM.[39,40] Furthermore, with appropriate sequence design and control over the assembly pathway, hierarchically ordered, and aligned structures can be produced which in turn influence cell behavior.[29,41]

With these attractive features of SAPs, this class of materials is a promising ECM mimic for neural regeneration. In the following sections, we expand on how the physical and biochemical properties of the ECM influence neural behavior and update and highlight some examples of SAPs for neural regeneration. Mimicking the ECM requires more than merely providing a biocompatible niche for neural cells to attach to. The conceptual schematic shown in Figure 2 illustrates how the physical and biochemical properties of the ECM strongly influence neural behaviors, such as cell adhesion, cell migration, cell morphology, cell signaling pathways, cell differentiation, and neurite outgrowth.[42]

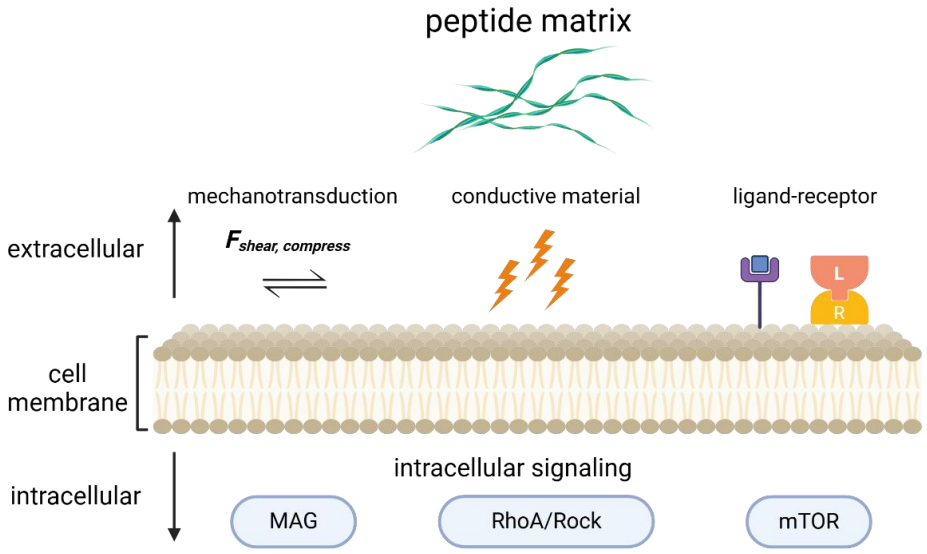

Figure 2. A schematic of extracellular stimuli provided by self-assembling peptide for neural regeneration (generated using Biorender). This graph illustrates how SAPs as ECM mimics can trigger intracellular cascades, such myelin-associated glycoprotein (MAG),[43] Rho-associated protein kinase (RhoA/Rock),[43,44] mammalian target of rapamycin (mTOR),[34,43] etc., for neural regeneration, through ligand-receptor pairing, mechanotransduction, and electrical stimuli. Copyright 2024, WILEY-VCH Verlag GmbH & Co.

1.5. Physical Properties of Self-Assembly Peptide on Neural Cells

1.5.1. Matrix stiffness

Mechanotransduction refers to the process of cells sensing and modifying their behavior in response to the ECM stiffness and mechanical forces, such as osmotic pressure, shear force, and compressive load from the surroundings. This process regulates tissue-specific differentiation and maintains tissue homeostasis.[45] For example, the interruption of interstitial fluid in the brain disrupts the balance between Ca^{2+} and Na^{+} ions, thus, mechanically stimulating axons and triggering Ca^{2+}-mediated neurotoxicity.[46] In terms of designing a matrix for neural repair, the stiffness of neural tissue depends on the cell type and location. Tissues in the PNS are generally stiffer than those in the CNS because of more aligned nerve fibers and protective connective tissue in the PNS.[32] In contrast, the brain ECM consists mostly of interstitial fluid, which gives rise to viscoelastic properties and a low stiffness of brain tissue.[32,47] More comprehensive mechanisms of how mechanotransduction influences axon outgrowth are systematically reviewed elsewhere.[48]

At the cellular level, Koser et al. reported that axons of retinal ganglion cells grow towards softer tissue, mediated by mechanosensitive ion channels.[49] Neural stem cells (NSCs) form synapses and are more prone to differentiate into neurons with neurite extension and branching on a soft matrix (0.1-0.5 kPa). In contrast, a stiffer matrix (0.5-10 kPa) stimulates NSC migration and differentiation into glia cells.[32] MSCs and pluripotent embryonic stem cells tend to express higher levels of neural markers when cultured on a soft matrix (0.1-1 kPa).[45] It was reported that a stiffer matrix (above 200 KPa or scar tissue) reduced the viability of neural cells in both an in vitro study and in the clinic.[32] Typically, SAPs form a rather soft matrix, which is beneficial for mimicking the mechanical properties of natural brain tissue and it may be possible to create materials, possibly in combination with covalent polymers, with anisotropic mechanical properties that better reflect the complexity needed for improving neural regeneration in the future.

1.5.2. Topography

Neurons have a polarized morphology with soma and dendrites for receiving biological signals from other neurons, and axons for sending biological signals outwards. Random neurite growth results in an inefficient neural network.[42] Udvary et al. published

that neuronal morphology also has an impact on cellular behavior and the architecture of neural networks.[50] This phenomenon indicates that the architecture of the neural environment and neuronal morphology complement each other. The environment of neural cells is multiscale and influences cell behavior, such as adhesion, alignment, and morphology.[32,47] Vedaraman and colleagues implemented a two-photon lithography technique to fabricate precise substrates, suggesting that substrates with anisotropic (having different physical properties in different directions), discontinuous geometry at the micrometer scale can support the alignment of dorsal root ganglia.[51] From a microscopic scope, Yang and coauthors published a review on the correlation between neural regeneration and different topographies. For continuous topography, embryonic hippocampal neurons tend to grow in parallel in deeper grooves and grow into multipolar cells when the grooves are wider. For discontinuous topography, PC12 cells grew fewer and shorter neurites on smooth surfaces, as illustrated in **Figure 3**. For random topography, hippocampal neurons showed higher survival rates on surfaces with nanoroughness.[42] These findings suggested that different topographic features on the same type of substrate influence the behaviors of neural cells.

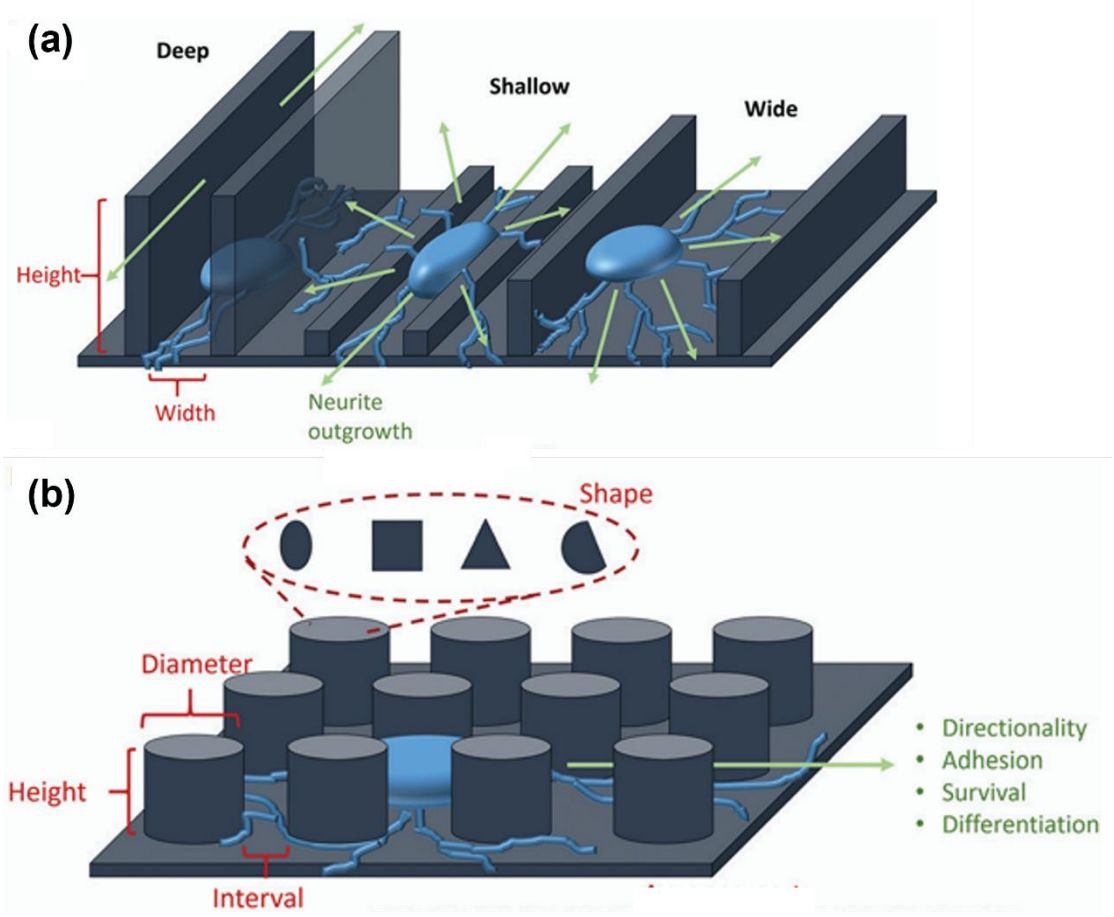

Figure 3. A schematic of topographical effects on neural cells. (a) Neural cells in blue experience continuous topographies, provided by defined grooves. The depth and width of the grooves can affect the direction of neurite outgrowth. Adapted with permission.[42] Copyright 2021, Royal Society of Chemistry. (b) Neural cells in blue encounter discontinuous topographies established by randomly positioned pillars. These pillars with different diameters, heights, intervals, and shapes can influence the adhesion, survival, and differentiation of PC12 neural cells as well as the alignment of neurite outgrowth. Adapted with permission.[42] Copyright 2021, Royal Society of Chemistry.

In addition to fabricating anisotropic substrates, a peptide nanofiber hydrogel composed of aligned fibrin and functionalized SAPs was prepared for functional recovery after PNI.[52] The aligned fibrin structure was first electrospun into a construct and soaked in the solution of SAP and growth factor mimic-functionalized SAP to obtain an interpenetrating peptide nanofiber hydrogel. Under scanning electron microscopy, the pure

aligned fibrin showed uniform and smooth microfibers. In contrast, the hybrid exhibited aligned microfibers surrounded by dense nanofibers. Hybridization of this construct with functional SAP increased surface roughness for improved cell adhesion, enabled the adjustment of substrate stiffness, and provided an aligned structure for directional SC outgrowth.[52] These findings exemplified that SAPs introduced structural heterogeneity, which is an important aspect for the neural ECM.[47] Tran et al. encapsulated carbonyl iron microparticles in a SAP monomer solution, enabling magnetically-induced alignment of peptide nanofiber hydrogel. Compared with the non-aligned nanofibers, the aligned structure stimulated MSCs to express higher levels of brain-derived neurotrophic factor (BDNF) and exhibit anti-inflammatory effects, while neuron progenitor cells increased the number of infiltrating axons. This work provided a new strategy to tailor the mechanical properties and topography of the matrix for SCI repair.[53] These examples show that controlling topographical cues is very challenging with pure peptide systems. However, when combined with (bio-)polymers, peptide can lead to significantly improved outcomes in nerve growth.

1.5.3. Epitope presentation on SAPs

The spatial arrangement of epitopes or growth factor mimicking peptides is critically important for efficient cell adhesion and correct molecular recognition. Compared with the meso-scale topographical effect, this section highlights how molecular design at nano-scale can influence cellular behavior. Epitopes that are presented on SAPs enable easy adjustment of various factors that determine cell receptor binding, such as overall epitope concentration, epitope spacing, etc.

Controlling sub-nanometer epitope spacing by a SAP hydrogel is one strategy to statically tune the spatial arrangement between matrix and cells, as illustrated in **Figure 4 (a)**. In this work, Pashuck et al. designed two fibronectin epitopes and site-specifically conjugated the epitopes on a linear SAP with three different sub-nanometer distances ranging from 0.7 nm to over 6 nm. Human umbilical vein endothelial cells (hUVECs) showed the most promising bioactivity for SAPs presenting two epitopes with 3.2 nm apart. This study demonstrated that the proper design of SAPs allowed for the tuning of the location and density of epitopes presented to cells at the nano-scale level, thereby precisely

modulating the cellular response.[54] This research pioneered investigations on how sub-nanometer epitope spacing could influence cellular responses. We believe that this concept also applies to neural regeneration as epitope spacing can be designed to match surface protein localization on neural cells.

The molecular design of SAPs is not only limited to the distance or density of the epitope, but also influences molecular chain dynamics to optimize the epitope presenting efficiency for neural cells, depicted in **Figure 4 (b)**. Peptide amphiphiles (PAs) are a class of materials containing a functional group and a structural forming peptide sequence linked to a hydrophobic alkyl tail. Álvarez and coauthors found that the mobility of the molecular chains could be adjusted by mutating the position of tetrapeptide sequence (i.e. Ala, Glu, Gly, and Val) connecting the three domains of the PA. The design and hypothesis were confirmed by molecular dynamics simulations. After tuning, the epitope and growth factor mimetic peptide functionalized PA became more mobile, leading to higher expression of neural markers and therapeutic effect in an *in vivo* SCI model.[40,55] In the future, greater efforts should be directed at understanding the role of dynamics and mobility in regards to epitope presentation on ECM mimics.

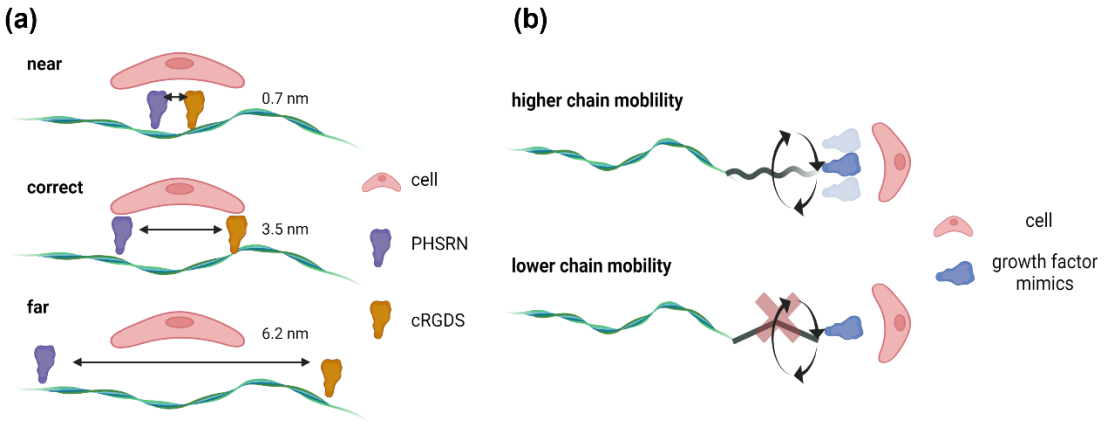

Figure 4. A cartoon illustration of spatial arrangement of epitopes presented statically and dynamically in SAP systems (generated using BioRender). (a) Sub-nanometer epitope spacing was achieved by site-specifically conjugation of epitopes on a linear SAP. The correct or suitable distance of epitopes on the SAP backbone increases the specificity in targeting cell surface proteins.[54] (b) Molecular chain dynamics of epitopes presenting PA were adjusted based on chain motion such as vibration and rotation. Higher molecular chain dynamic activity increases the efficiency of epitopes being presented to the receptor on the

cell membrane, leading to improved neural regeneration.[55] Copyright 2024, WILEY-VCH Verlag GmbH & Co.

1.5.4. Co-assembling

Co-assembling is the combination of two or more distinct monomers in supramolecular assemblies via complementary intermolecular interactions, for instance, charge-charge interaction, π-π interactions, and dipolar moment.[56] Controlling the properties of various peptide monomers is challenging as they can undergo disruptive, cooperative, or orthogonal assembly, i.e. depending on the types of peptides that are mixed together their assembly can be prevented, enhanced, or remain unaffected, respectively.[57] Nonetheless, this approach is still appealing for biomedical applications as the co-assembly of peptides can tune the mechanical properties and integrate multiple biological motifs into one homogenous architecture for a synergistic effect on cellular response via the spatial and chemical arrangement of multiple bioactive signals.[56,57] Understanding the molecular arrangement and mechanism of co-assembling or self-sorting peptides from empirical data, computer simulation, and real-time imaging could improve the design of new co-assembling peptides for different applications.[58–60]

Gelain's group co-assembled two complementary charged SAPs to form a composite SAP hydrogel. The authors applied computer simulations to study the co-assembled hydrogel and propose the co-assembly mechanism and potential structural arrangements. Imaging revealed that the co-assembled hydrogel contained a longer and more abundant fiber structure compared to individual peptide assemblies. The rheological data suggested that the co-assembled hydrogel had higher stiffness than the two counterparts did, which was consistent with the matrix stiffness for neuron culture. Additionally, both human and murine NSCs survived and differentiated well on the co-assembled hydrogel. Employing a SCI model also displayed the neuroregenerative potential of the co-assembled hydrogel.[58] On top of adjusting the molecular packing and tuning the stiffness of the SAP matrix, introducing multiple epitopes or growth factor mimics with synergistic effects is another advantage of implementing a co-assembly strategy. There are several groups using co-assembling methods with different SAP backbones, namely, the fibronectin and laminin-derived sequence modified with fluorenylmethoxycarbonyl (Fmoc), a protecting group for

site-specific chemical reaction. Those nanofibers have been used for modulating muscle progenitor cells,[61] nerve growth factor (NGF) mimic and BDNF mimic functionalized SAP for facilitating peripheral nerve regeneration,[62] and heparan sulfate mimic and laminin-derived sequence decorated PAs for SCI repair,[63] to name a few.

1.5.5. Conductive biomaterials

Electrical signals influence cell behavior through the membrane potential, ion channel activation, and electrophysiological state, resulting in proliferation, migration, and differentiation.[32] These electrical cues are crucial for neural cells as they are responsible for signal propagation.[32] Therapeutic approaches use implantable conductive materials that enable propagation of electrical signals, e.g. between neuronal cells, but also external electrical stimulation has been shown to be effective, illustrated in Figure 5.[64,65] Hybrid conductive materials are used for neural regeneration, in which conductivity is derived from conductive polymers, carbon-based materials, or metals. Most studies of conductive biomaterials for neural regeneration are limited to *in vivo* studies. Common drawbacks of applying conductive materials in further *in vivo* studies or clinical trials for neural repair are limited because of their solubility, biocompatibility, long-term stability, and consistent conductivity.[64,65]

In one example, a SAP-carbon nanotube hybrid hydrogel was designed to contain amino acids with aromatic groups and with imidazolium functionalization at the N-terminus of the SAP to increase the intermolecular cation−π interaction and π–π stacking. The introduction of an imidazolium group in the SAP system helped solubilize and stabilize the carbon nanotubes in the hybrid hydrogel. The *in vitro* study suggested that treating DRG neurons with the hybrid material and an external electrical stimulus promoted axon extension and myelination.[66] In another study, Arioz et al. identified a tetra(aniline)-conjugated peptide nanofiber and tested its potential for PNI repair. Unlike other PAs, this PA was designed with hydrophilic, β-sheet forming moieties, and a conductive oligomer as the hydrophobic tail. The conductivity of the hybrid peptide hydrogel was not measurable due to the insulating peptide backbone but was sufficient to facilitate the differentiation of PC12 cells.[67]

However, it is worth noting that even without using conductive materials implanted into a patient, electrical stimulation has demonstrated significant advantages in promoting nerve regeneration. For example, Courtine's lab successfully conducted one of the few clinical cases using non-invasive spinal cord electrical stimulation (ARC^{EX} Therapy) for treating SCI.[68] Therefore, we envision that the combination of implantable conductive biomaterials and non-invasive electrical stimulation for synergistic therapeutic effects can improve the well-being of patients suffering from PNI and SCI.

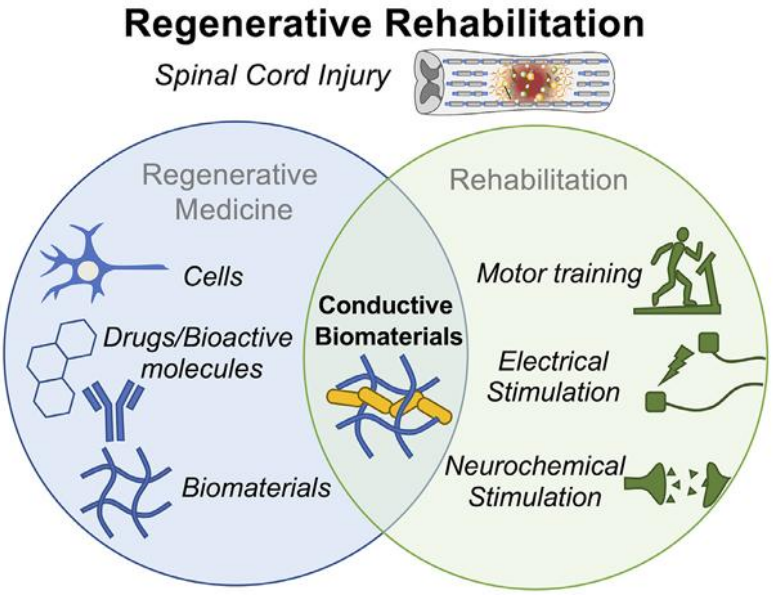

Figure 5. A Venn diagram of conductive biomaterials for regeneration and rehabilitation of spinal cord injury (SCI). At the cellular level, conductive biomaterials can stimulate cells and facilitate the release of drugs and bioactive molecules. For rehabilitation, conductive biomaterials provide neurochemical stimulation electrical stimulation, and motor training. Adapted with permission.[64] Copyright 2022, Elsevier.

1.6. Biochemical Properties of Self-Assembly Peptide on Neural Cells

Cells communicate not only via physical cues but also through the structural and signaling proteins present in the ECM. Interestingly, it was found that full proteins are not always required to achieve a desired biological response (attachment, survival, differentiation, etc.) from the cell. Small molecules or peptides that mimic the essential regions of the full protein can be sufficient to achieve comparable outcomes. When coupled to a matrix, such mimics tend to be more stable and less sensitive to the environment than

their full protein counterparts. Peptide epitopes on SAP nanofibers can actively interact with cells and initiate specific cell signaling pathways, in some cases with greater efficiency than endogenous proteins.[69] In the following section, functional peptide sequences known to affect neural functions such as neural regeneration are categorized into cell adhesion epitopes and growth factor mimics. Examples of sequences functionalized on SAPs are covered in the following sections and summarized in **Table 1**.

Table 1. Summary of different SAP backbones functionalized with growth factor mimics or epitopes and their respective *in vitro* and *in vivo* experiments.

Function	Protein source	Epitope	Backbone	Cell	*In vivo* models	Ref.
Cell adhesion	Cadherin	HAVDI	Fmoc, Nap	C6	X	[70]
	Fibronectin	RGD	α-Helical-peptide	m-NSC	X	[71]
	Laminin	IKVAV, YIGSR	Fmoc	C6 SH-SY5Y	X	[72]
	Tenascin-C	VFDNFVLK	Lauric acid	PC12	X	[73]
Neurotrophic factor	BDNF	RGIDKRHWNSQ	RADA	r-SC r-DRG PC12	r-PNI sciatic nerve	[62]
				r-SC h-UVEC	r-PNI sciatic nerve	[74]
	CMX-9236	KKDGDGDFAIDAPE	MDP	r-primary cortical neuron	r-TBI fluid percussion	[75]
	NGF	CTDIKGKCTGACDGKQC	RADA	r-SC r-DRG PC12	r-PNI sciatic nerve	[62]
	Netrin-1	CIDPC	Palmitic acid	m-primary cortical neuron	X	[76]
	FGF	YRSRKYSSWYVALKR	Palmitic acid	h-UVEC	X	[77]
	Osteopontin	SVVYGLR	RADA	r-NSC h-UVEC	z-TBI embryo toxicity test	[78]
Angiogenesis	PDGF	RPKPQQFFGLM	RADA	r-primary cortical neuron	r-SCI	[79]
		VRKKP	Nap+FF	m-NSC	r-SCI	[80]
	VEGF	KLTWQELYQLKYKGI	RADA	r-SC h-UVEC	r-PNI sciatic nerve	[74]
			MDP	r-primary cortical neuron	r-TBI fluid percussion	[81]

h is human, m is mouse, r is rat, and z is zebra fish. X stands for no *in vivo* experiment conducted.

1.6.1. Cell adhesion epitopes

Cell adhesion plays a critical role in facilitating cell-cell and cell-matrix interactions, enabling the transmission of environmental information to activate intracellular signaling.[69] Adhesion proteins, such as vitronectin, fibrinogen, laminin, and fibronectin,

contain multiple integrin ligands that interact with cell receptors such as integrin receptors responsible for cell adhesion.[69,82]

There are many peptide epitopes derived from fibronectin, such as RGD, PHSRN, and GRGDSP. Among them, the RGD peptide is the shortest and most investigated sequence, along with its analogues for cell adhesion.[83] Laminin-derived peptide epitopes, including IKVAV, YIGSR, and other derivates, have been used in SAP and PA systems to explore their potential for neural repair.[69,72] An octapeptide derived from tenascin-C, a class of glycoproteins, is involved in the regenerative progress of many tissues.[69] Sever et al. published tenascin-C decorated PA nanofibers, which enhanced the neurite outgrowth of PC12 cells.[73] The collagen superfamily consists of 46 different polypeptide groups, 28 of which can self-assemble into supramolecular structures. Collagen type I sequences, DGEA and GFOGER (O = hydroxyproline) have been conjugated to SAPs for bone tissue engineering.[69] Jain and colleagues developed nanofiber hydrogels based on a collagen-inspired peptide with the sequence FFGSO and co-assembled it with a laminin-derived peptide. These hydrogels showed high biocompatibility with both fibroblasts and glioma cells.[84] Cadherins, unlike the aforementioned cell adhesion peptides, are transmembrane cell receptors that facilitate cell-cell communication for cell migration and maintenance of tissue structure.[69] Roy's lab reported a SAP nanofiber system based on cadherin-derived peptides with aromatic moieties to modify the N-terminus. The SAP hydrogels promoted the proliferation of fibroblasts and neurite extension.[70]

Cell adhesion, involving integrins and cadherins, is an essential mechanism for cell-ECM communication that is ubiquitous across different cell types. Growth factor activation, on the other hand, is relatively cell-type selective.

1.6.2. Growth factor mimics

Growth factors regulate essential cellular processes, including cell proliferation, migration, and differentiation. The mechanisms rely on cellular receptors sensing and binding to growth factor ligands to activate intracellular cascades that reach the nucleus and influence transcription. Unlike full-length proteins which are prone to rapid denaturation, coupling growth factor mimics to artificial matrices provides a stable alternative while preserving the reactivity and specificity of the original.[69]

The growth factor mimics of BDNF and NGF can promote neurite outgrowth and neuroprotection, like their full-length protein counterparts.[69] Lu et al. investigated the therapeutic effects of SAPs modified with BDNF-derived peptides in an *in vivo* SCI model. Their results, such as electrophysiological recovery and motor functional analysis, showed promising potential in the treatment of SCI.[85] Other growth factor mimics or neurotrophic peptides, which promote neurogenesis, are summarized elsewhere.[69,83,86]

The angiogenesis pathway garners significant interest from many research groups because vascularization of tissue improves oxygen supply and metabolism, which is essential for tissue repair. A vascular endothelial growth factor (VEGF)-derived peptide coupled to SAPs not only increased blood vessel density in a rodent model but also improved cell survival.[81] Substance P, derived from osteopontin, is an angiogenic motif that improved adhesion, migration, and tube formation of endothelial cells. This motif was attached to SAPs and shown to be angiogenic and neurogenic in a rat SCI model.[79]

Fibroblast growth factor (FGF-2) regulates cell survival, differentiation, and homeostasis during tissue development. PAs modified with FGF-2-derived peptides facilitated the proliferation and migration of hUVECs *in vitro* and boosted cell survival and angiogenesis in a rat SCI model.[55,77]

Platelet-derived growth factor (PDGF) can promote angiogenesis and synaptogenesis, prevent neuronal death, and direct the differentiation of NSCs into oligodendrocytes and neurons.[80,87] PDGF mimetic peptides were coupled on two self-assembling motifs, naphthylacetic acid and diphenylalanine (FF), to trigger hydrogel formation for NSC encapsulation. This cell-laden SAP hydrogel attenuated the inflammatory response at the injury site, enhanced angiogenesis, promoted remyelination, and remarkably improved functional recovery in a rat SCI model.[80]

Co-assembly of different functional SAPs for synergistic biochemical effects is also one strategy to maximize the therapeutic potential of SAPs. Lu et al. investigated the synergistic effect arising from the co-assembly of SAPs decorated with NGF and BDNF mimetics on PC12, SCs, and DRG cells *in vitro*. Furthermore, the co-assembled SAPs were found to bolster axonal regeneration and functional recovery in a murine PNI model.[62] Another study on PNI repair investigated the co-assembly of VEGF and BDNF coupled to SAPs. The co-assembled SAP stimulated myelination of SCs and adhesion of hUVECs and

promoted angiogenesis and neurogenesis *in vivo*.[74] Co-assembly of laminin-derived peptides (i.e. IKVAV) and FGF-2 modified on PAs can synergistically activate two biological pathways. Alvarez et al. found that these co-assembled PAs induced remyelination and increased vascular area fraction, length, and branching. In a SCI model, these PAs also induced significant angiogenesis and functional recovery.[55]

Besides these established peptides, new functional peptide sequences can be revealed by applying phage display, computational screening, and artificial intelligence.[69] The coupling of various peptide epitopes or growth factor mimics onto SAPs is straightforward. However, it is challenging to increase the accessibility of functional domains on SAPs for several reasons: Poorly soluble peptide epitopes have limited exposure to the aqueous solvent and may be buried in the self-assembled structure. A spacer of the correct length may be necessary to facilitate efficient receptor binding. Furthermore, high concentrations of epitopes may interfere with the self-assembly behavior of SAPs and result in altered structures.[69,83]

We anticipate that significant advances will be made in the near future in creating ECM mimics with tailored bioactivity through the optimized presentation of bioactive epitopes. This is due to a better understanding of the complex interplay between different biological signals necessary for nerve regeneration supported by more powerful computational methods.

1.7. Generation of Self-assembly Peptide for Neural Cells

There are various supramolecular self-assembling structures based on different designs of the amino acid sequence, including α-helix, β-sheet, collagen-like, elastin-like, multidomain, PA, aromatic peptide amphiphile, etc. The amino acids building blocks of SAPs are illustrated in **Figure 6**. In the following sections, we elaborate on different peptide backbones and provide examples of SAPs for neural regeneration, summarized in **Table 1**.

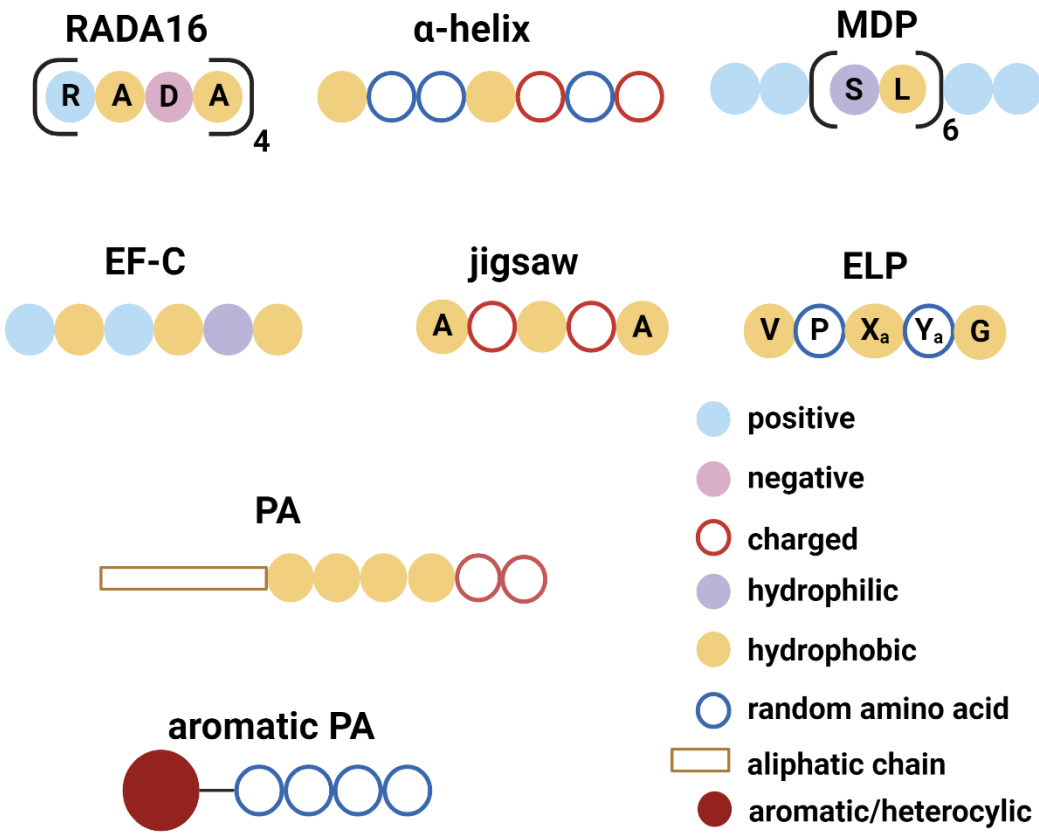

Figure 6. A schematic of different amino acid building blocks of SAPs. Different icons represent different amino acids, where Xa stands for either glycine or alanine and Ya can be any amino acid other than proline (generated using Biorender). Copyright 2024, WILEY-VCH Verlag GmbH & Co.

1.7.1. RADA

Derived from the yeast protein, RADA16 (RADARADARADARADA), EAK16 (AEAEAKAKAEAEAKAK), and their SAP variants are ionic self-complementary peptides, shown in **Figure 6**. The design principles of this class of peptides are (1) alternating hydrophilicity of amino acids, (2) alternating positively and negatively charged amino acids, (3) alternating chirality of natural L- or unnatural D-amino acids and (4) alternating polarity of amino acids.[88,89] The chirality, charge arrangement, and length of the amino acid sequence play important roles in defining the nanostructure and mechanical properties of these SAPs.[88,89] For example, LDLK12 (LKLKLKLKLKLK) and LDLD12 (LDLDLDLDLDLD) are SAP sequences designed and modified based on RADA16 and

EAK16 as neural scaffolds with very similar properties, due to the strictly alternating hydrophobic and charged pattern of amino acids.[35,90,91]

RADA16 was functionalized with BDNF and applied to astrocytes and human umbilical cord MSCs. The functionalized RADA16 SAP hydrogel provided mechanical support in the lesion site to ensure cell survival and BDNF to stimulate cell adhesion.[92]

In a different strategy, an angiogenic motif SVVYGLR derived from osteopontin, was modified on the RADA16 SAP hydrogel to promote the adhesion, migration, and tube formation of hUVECs. An *in vivo* optic tectum wound model in the brain of adult zebrafish was conducted to prove the neurogenesis of this SAP hydrogel.[78]

Lu et al. conducted research in the co-assembly of multiple growth factor mimetics modified with RADA SAPs. In one case, the co-assembly of BDNF-SAP and VEGF-SAP for PNI repair was investigated, illustrated in **Figure 7 (a)-(d)**. This co-assembled SAP hydrogel synchronously induced neural regeneration and angiogenesis in an *in vitro* study. When the functionalized SAP was filled into a chitosan nerve conduit, the therapeutic effect was comparable to the autograft for sciatic nerve repair.[74]

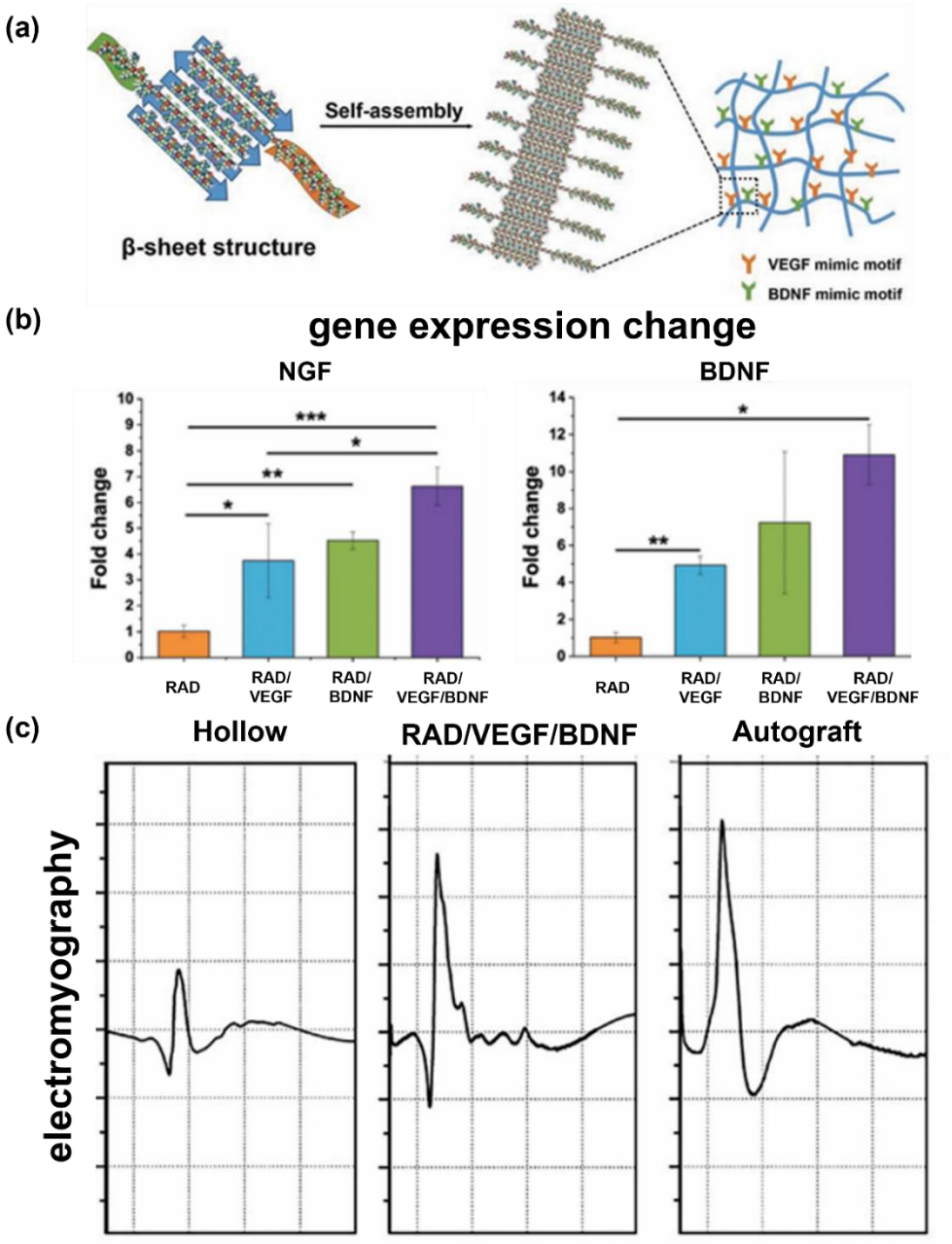

Figure 7. An example of RADA SAP for PNI repair. (a) The molecular model of RADA SAP decorated with VEGF and BDNF mimetic peptides. (b) Analysis of quantitative real-time polymerase chain reaction of NGF and BDNF mRNA abundance after 7 days of cultivating rat SCs on different SAPs. The increase in NGF and BDNF gene expression indicate the maturation and myelination of the SCs. (c) Motor functional recovery analysis (electromyography) of an *in vivo* PNI model showed that the therapeutic effect of different SAPs after 12 weeks of implantation. Adapted with permission.[74] Copyright 2019, Royal Society of Chemistry.

1.7.2. α-Helical peptides

α-helical peptides are mainly composed of a repeating unit of seven amino acids, abcdefg, with hydrophobic groups (a and d position) and charged groups (e and g position) to mediate assembly, as illustrated in **Figure 6**. The other residues (b, c, and f) are exposed on the surface of the assemblies and differ in design. The self-assembled configuration can be tuned by controlling conditions, such as temperature, pH, and ionic strength.[35,89] Woolfson's lab designed self-assembling fiber hydrogels based on α-helical peptides to facilitate the attachment and migration of murine embryonic NSCs. The SAP was first modified with an azido group and allowed for post modification with alkyne-decorated RGDS peptide to enhance cell adhesion. NSCs expressed more neural lineage markers (microtubule associated protein-2, MAP2) and less glial lineage marker (GFAP) when cultured on the RGDS modified SAP. This indicated that α-helical peptide SAPs modified with peptide epitopes mimic the biochemical and morphological properties of the neural ECM, indicating a potential platform for neural tissue engineering.[71]

1.7.3. Multidomain peptide

Multidomain peptides (MDPs), depicted in **Figure 6**, are composed of alternating hydrophilic and hydrophobic amino acids in the center (usually serine and leucine, SL) and charged amino acids on the two wings. MDPs assemble into short fibers in deionized water due to terminal charge repulsion. However, in the presence of multivalent ions, such as phosphate buffer, this class of peptides can self-assemble into longer fibers, allowing for molecular entanglement and hydrogel formation.[93]

Ma et al. functionalized VEGF mimetic peptides on MDPs and allowed them to assemble into hydrogels. The modified MDP hydrogels displayed high cytocompatibility for primary rat neurons and increased the density of new blood vessels in the injured brain. It also reduced neuronal loss at the injury site, indicating that this angiogenic MDP hydrogel is a promising treatment for neural and ischemic injury.[81]

Another example of a modified MDP hydrogel was conducted by Sarkar et al., demonstrated in **Figure 8 (a)-(c)**. The MDP hydrogel was decorated with a neuroprotective peptide derived from ependymin, also known as CMX-9236 (KKDGDGDFAIDAPE).

Ependymin, a glycoprotein component of the extracellular fluid, is a neuroprotective protein.[94] The *in vitro* data suggested that the functional MDP hydrogel reduced extracellular glutamate toxicity and that neurons harvested from cortices were able to survive, extend axons, and produce branches. The *in vivo* study further proved that this MDP hydrogel reduced acute injury such as cortical atrophy and ameliorated chronic injury such as neurotoxic hyperphosphorylation of tau protein. With long-term investigation and functional assessment, the authors plan to put this MDP hydrogel into the clinic.[75]

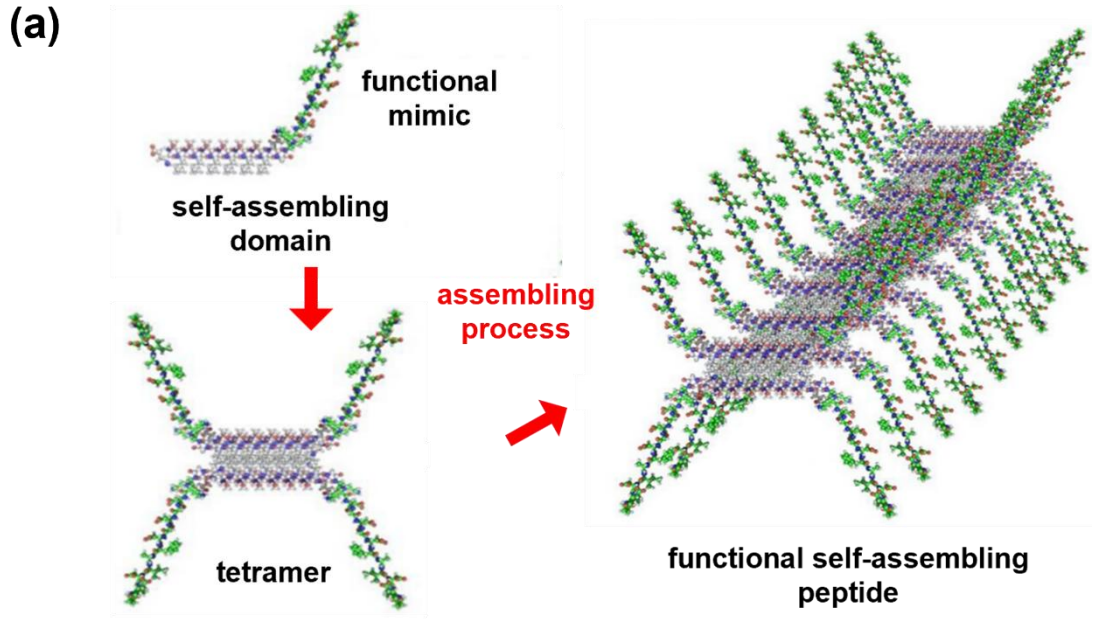

Figure 8. An example of MDP SAP for TBI repair. (a) The molecular model of MDP SAP and its assembly. (b) Immunostaining of brain sections of rats with antibodies directed against myelin basic protein, NeuN, and merged images in sham (the upper three images), injured model (the middle three images), and MDP SAP treated model (the lower three images). All images are with scale bar of 200 μm. Adapted with permission.[75] Copyright 2021, Elsevier.

1.7.4. Enhancing Factor C (EF-C)

EF-C is an amphiphilic peptide sequence consisting of 12 amino acids derived from the HIV envelope protein gp 120. When dissolved in polar solvents, such as water or cell culture media, EF-C self-assembles into nanofibers with an average length of hundred nanometers and a diameter of around 3 nm. EF-C nanofibers are polycationic and exhibit a positive zeta potential under physiological conditions, resulting in electrostatic interactions with the negatively charged cell membrane.[95] Additionally, these SAPs can easily be conjugated with fluorophores and co-assembled with unmodified SAP as a fluorescent probe without sacrificing their function.[96]

Our group developed an EF-C derived SAP library with most of the peptide sequences consisting of amphiphilic six amino acid sequences such as KIKIQI or KFKFQF, demonstrated in **Figure 6**. We screened and analyzed the physicochemical properties of 27 different peptides and correlated them with their bioactivity on DRG neurons: neuron number, neurite length, and neurite branching. Our data suggested that EF-C derived SAPs possessing the highest bioactivity regarding neuronal growth stimulation have (1) a strong tendency to form a fiber structure, (2) a positive net charge with a pattern of alternating hydrophobic and positively charged amino acids, (3) higher intermolecular β-sheet content, and (4) larger cross-sectional diameter in single-fiber atomic force microscopy analysis, as depicted in **Figure 9 (a, b)**. For visualization, SAPs were fluorescently labeled, and images of the material and cell localization were captured using microscopy, shown in **Figure 9 (c)**. The selected SAPs were further investigated in a facial nerve injury model. The SAPs adhered at the lesion site for up to three weeks after injury which is an important prerequisite for providing long-term bioactivity, depicted in **Figure 9 (e)-(i)**. After analyzing the functional recovery of mice treated with EF-C derived SAPs, we concluded

that the EF-C derived SAPs alone facilitated neural regrowth in a PNI model. Further, we anticipate that EF-C derived SAPs can play a role as a multifaceted platform for presenting multiple growth factors after fine tuning and chemical modification.[30]

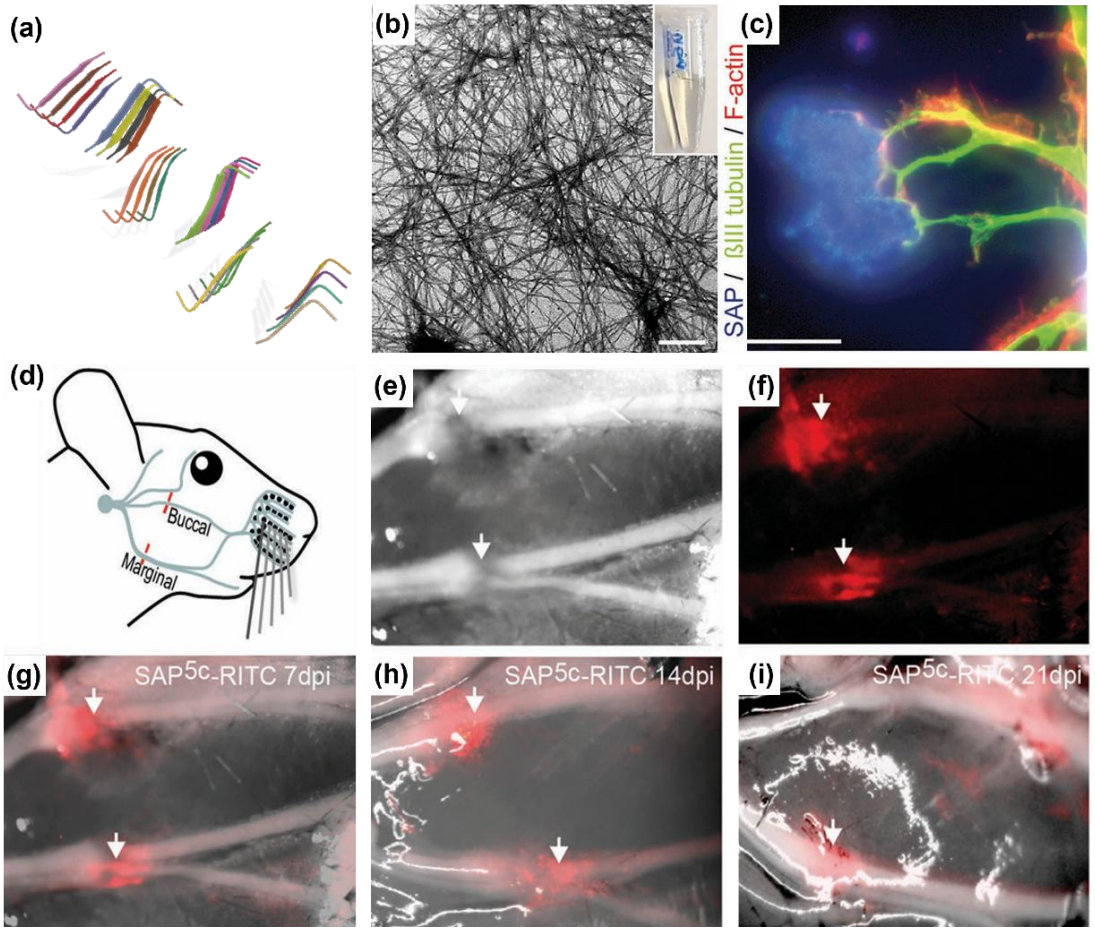

Figure 9. An example of EF-C-derived SAPs for PNI repair. (a) A 3D molecular model of EF-C derived SAP, CKFKFQF is visualized by Protein Data Bank (PDB: 8OKR).[97] (b) A TEM image of nanofibers assembled from EF-C monomer (scale bar = 600 nm). (c) A fluorescent image of fluorophore labeled EF-C derived SAP and cell adhesion points, stained with βIII-tubulin and F-actin (scale bar = 20 μm). (d) A schematic depicting the mouse facial nerve (blue) and lesion sites (red lines) at the buccal and marginal branch (e-i) Microscopic images of the lesion sites and EF-C SAP injection, indicated by arrows. Images of panel (e) and (f) were captured upon the injection, and images of panel (g) to panel (i) were recorded at 7, 14, and 21 post days post injury (dpi). Adapted with permission.[30] Copyright 2019, WILEY-VCH GmbH.

1.7.5. Other SAP backbones

Yaguchi and colleagues developed a cell-adhesive fiber-forming SAP hydrogel for the treatment of brain injury. The full sequence is RIDARMRADIR. The sequence has an amphiphilic core, $AX^1X^2X^3A$, with polar amino acids at X^1 and X^3 and a non-polar amino acid at X^2, shown in **Figure 6**. The jigsaw-shaped hydrophobic surface was achieved with the sequence I–A–M–A–I, which mimics the dovetail-packing domain of glycophorin A. The jigsaw-shaped hydrophobic surface allowed efficient encapsulation and sustained release of full-length VEGF. An *in vitro* study showed that hUVECs treated with a VEGF-loaded SAP hydrogel were prone to form a lumen-like network. The authors performed an *in vivo* ischemic stroke model to verify the therapeutic effect of the hydrogel, and the results demonstrated that this VEGF-loaded hydrogel promoted angiogenesis and neuroprotection.[98]

ECM protein mimetic peptides, e.g. collagen like peptide (CLP), elastin mimetic peptides (ELP), etc., aim to resemble the properties and functions of natural and large ECM proteins.[99] CLPs are composed of triple helix bundles with each strand consisting of "G-X-Y" tripeptide repeats, where X and Y are often proline and hydroxyproline.[100] CLP SAPs can assemble into higher-order structures and typically serve as bioactive domains and physical crosslinking agents in hydrogels for tissue engineering.[100] ELPs consist of a pentapeptide repeating unit, Val-Pro-Xa-Ya-Gly, where Xa is either glycine or alanine and Ya can be any amino acid other than proline, shown in **Figure 6**. ELP SAPs can undergo reversible and temperature-dependent self-assembly in aqueous solutions.[101] Nelson and coauthors summarized and highlighted some recent research using ELP SAPs for neural repair.[102] Generally, ECM mimetic peptides promote cell adhesion for various cell types. However, the structural complexity of ECM mimetic peptides affects the accessibility for cell-peptide recognition.[99] More comprehensive and detailed investigations on the structure-biofunction relationship on ECM mimetic peptides are encouraged in order to advance the class of materials in the field of neural regeneration.

Other than the peptide backbones that can be synthesized using automated synthesizers, which consist of only amino acids. This allows material scientists to rapidly modify the peptide sequence in a precise manner creating peptide libraries and enabling studying sequence-structure-property correlations. The following two sections introduce peptide

amphiphiles: PAs and aromatic peptide amphiphiles. These two classes of materials, unlike pure amino acids backbone, may require additional manual synthesis. They consist of amino acids and hydrophobic motifs, such as aliphatic chains, aromatic groups, or heterocyclic compounds. These compounds introduce non-natural compounds into the self-assembled structure and additional functionalities.

1.7.6. Peptide amphiphile (PA)

PA molecules were first reported in the Stupp laboratory in the early 2000s. They self-assemble into long nanofibers and form hydrogel biomaterials with high water content that mimic the ECM. Fiber-forming PA molecules, depicted in **Figure 6**, are comprised of an aliphatic tail with more than 10 carbon atoms, a peptide sequence with a high tendency to form β-sheets, a charged peptide sequence to increase hydrophilicity, followed by a bioactive segment.[40] The length of the hydrophobic tail, the sequence of the structure-forming peptide, and the additional spacers between each segment of PA molecules play important roles in the physicochemical properties and the final self-assembled structure and bioactivity.[41,55,103]

Okur et al. selected a NGF sequence that was coupled to PA molecules. The NGF-binding PA nanofibers stimulated the differentiation of PC12 cells into neuron-like cells and the expression of neuronal markers, such as βIII-tubulin. In addition, the NGF-binding PA nanofibers also supported the survival of sensory DRG neurons and induced axon outgrowth and synaptic connectivity for DRG neurons.[104]

Netrin-1 is a chemotropic factor responsible for axon growth, guidance, and synaptogenesis. Netrin-1 mimic was synthesized on PA molecules and tested on primary neuronal culture, shown in **Figure 10 (a)-(c)**. Conjugated to PA molecules, only cyclic Netrin-1 mimetic PA nanofibers (N1-PA) efficiently activated the receptor and associated signaling pathway in primary mouse cortical neurons. These findings suggest that the Netrin-1 mimetic PA nanofibers can be a potential therapy for SCI repair as well as for diseases or injuries associated with netrin-1 deficiency, such as stroke and Alzheimer's disease.[76]

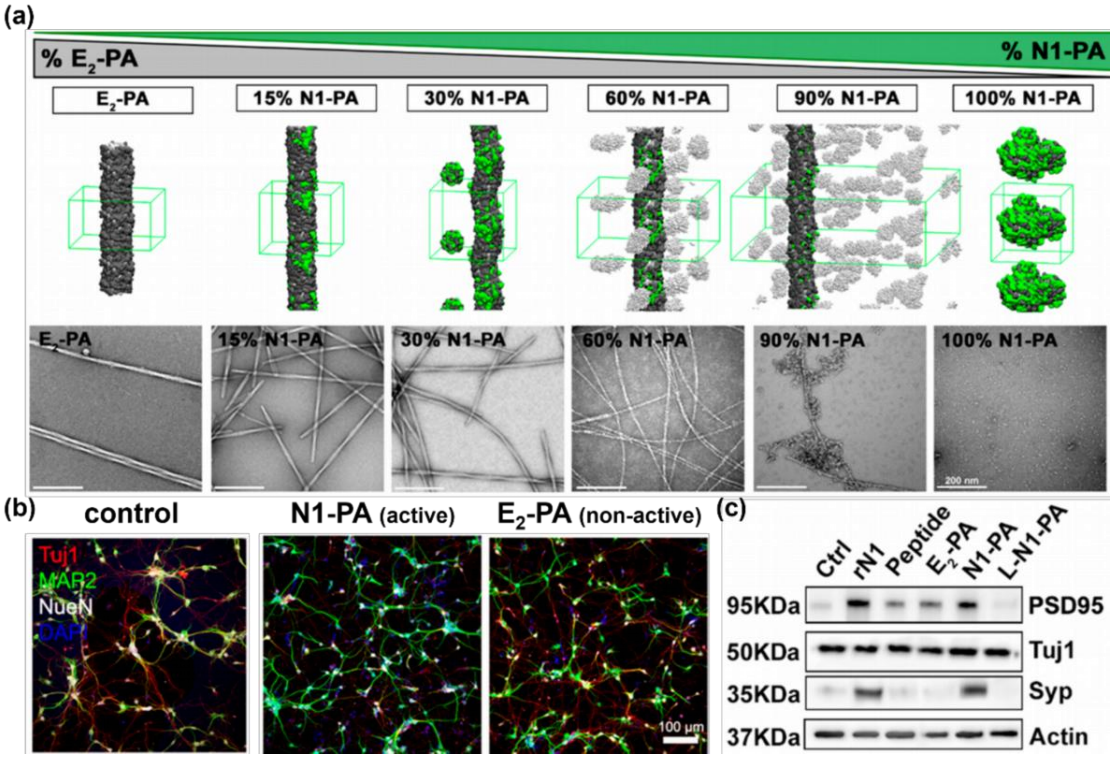

Figure 10. An example of PA SAP for neural repair. (a) Coarse-grained molecular dynamics (CG-MD) simulations suggested that 60% or less of co-assembling ratio of Netrin-1 decorated PA monomer and PA monomer to obtain fiber structure. Meanwhile, the corresponding TEM images of different co-assembly ratios were taken to confirm the results of CG-MD simulation. (b) Representative confocal microscopy images of primary neurons after treated with poly d-lysine coating (control), pure PA (E_2-PA), and N1-PA for one week. (c) Representative Western blot of PSD95, Tuj1, and synaptophysin (Syp) in primary neurons after treatment with poly d-lysine coating, recombinant netrin-1 (rN1, the positive control), netrin-1 mimetic peptide (Peptide), E_2-PA, PA and N1-PA, and linear 15% netrin-1 mimetic peptide modified PA (L-N1-PA) for two weeks. Adapted with permission.[76] Copyright 2023, American Chemical Society.

1.7.7. Aromatic peptide amphiphile

Proteins carry an enormous amount of structural and functional information. The design of aromatic peptide amphiphiles aims to provide a minimalistic and scalable class of materials as an alternative to natural proteins.[105] The general structure of aromatic peptide amphiphiles consists of an aromatic group, a linker, a functional peptide sequence, and the

C-terminus, depicted in **Figure 6**. The aromatic moiety triggers the self-assembly via directional aromatic stacking, also known as π-π stacking, with some commonly used aromatic groups being the derivatives of fluorene, phenyl, naphthalene (Nap), pyrene, etc.[105,106] The N-terminal capping group can be functionalized with heterocyclic capping groups to introduce more functionality; for example, redox-responsive groups and fluorophores.[106,107] The length and chain flexibility of a linker group affect the conformation and the chirality of the assembled structures, and a more linear linker is preferable to allow effective intermolecular aromatic stacking. In a functional peptide sequence, the amino acids also have a significant influence on the assembled structures. For example, the side chain of the amino acids may introduce aromatic groups (F, Y), hydrophobic moieties (V, L), and charged residues (E, D, H, R, and K). The C-terminus, like the carboxylic group, amide group, and methoxycarbonyl group, regulates the self-assembled structures via the hydrophilicity and charges. Moreover, the C-terminus can be further chemically modified to tune the self-assembled structures or introduce additional functions.[105]

The Fmoc protecting groups are ubiquitous in aromatic-modified peptides which form stiff hydrogels with fibrillar nanostructures.[105] Roy's lab co-assembled two laminin mimetic peptides, Fmoc IKVAV and Fmoc YIGSR, creating a self-sorted fiber network in a single hydrogel scaffold. The non-covalent entanglement of the two laminin mimetic peptides provided a neurotrophic niche for C6 glioma cells and SH-SY5Y neuroblastoma cells, which was confirmed by proliferation assay and neurite outgrowth experiments.[72] James et al. reported thiophene-modified peptide sequences that self-assembled into nanofiber hydrogels as an example of heterocyclic end capping groups which can induce self-assembly and introduce conductivity to a SAP system. Despite the successful synthesis and characterization, further biological evaluation is necessary before considering this conductive nanofiber hydrogel as a therapeutic treatment for neural tissue engineering.[108] Another example of heterocyclic end capping groups triggering self-assembly and conferring conductivity to peptide sequences was published by Arioz and colleagues. Tetra(aniline)-modified peptides self-assembled into conductive nanofiber hydrogels to stimulate the differentiation of PC12 cells. Further *in vivo* studies along with thorough

investigation of the mechanism of neural differentiation will pave the way for the application of this conductive SAP hydrogel for neural regeneration.[67]

Interestingly, despite the significant differences in sequence pattern, length, composition, and origin (natural vs. designed), the above-mentioned classes of peptide materials show remarkable similarities in their ability to support neuronal growth. All these peptides tend to form highly anisotropic structures, e.g. nanofibers or fiber bundles, which resemble the morphology of the fibrous ECM proteins. Minimal peptides such as the aromatic peptide amphiphiles are particularly cost effective to produce, but do not show a robust assembly under varying conditions. In contrast, longer peptides such as the RADA family or PAs with longer alkyl chains have the advantage of forming nanofibers in a variety of buffers and supporting a wide range of bioactive epitopes that can be coupled to the peptide without altering the resulting assembled structure. When it comes to designing peptide materials for neural regeneration, an optimal material does not (yet) exist and the pros and cons of each class of materials need to be considered.

Reference:

(1) Lai, Y.; Li, F.; Zou, Z.; Saeed, M.; Xu, Z.; Yu, H. Bio-Inspired Amyloid Polypeptides: From Self-Assembly to Nanostructure Design and Biotechnological Applications. *Appl Mater Today* **2021**, *22*, 100966.

(2) Wei, G.; Su, Z.; Reynolds, N. P.; Arosio, P.; Hamley, I. W.; Gazit, E.; Mezzenga, R. Self-Assembling Peptide and Protein Amyloids: From Structure to Tailored Function in Nanotechnology. *Chem Soc Rev* **2017**, *46* (15), 4661–4708.

(3) Balasco, N.; Diaferia, C.; Morelli, G.; Vitagliano, L.; Accardo, A. Amyloid-Like Aggregation in Diseases and Biomaterials: Osmosis of Structural Information. *Front Bioeng Biotechnol* **2021**, *9*.

(4) Knowles, T. P. J.; Mezzenga, R. Amyloid Fibrils as Building Blocks for Natural and Artificial Functional Materials. *Advanced Materials* **2016**, *28* (31), 6546–6561.

(5) Zhang, S. Discovery and Design of Self-Assembling Peptides. *Interface Focus* **2017**, *7* (6), 20170028.

(6) Hu, X.; Liao, M.; Gong, H.; Zhang, L.; Cox, H.; Waigh, T. A.; Lu, J. R. Recent Advances in Short Peptide Self-Assembly: From Rational Design to Novel Applications. *Curr Opin Colloid Interface Sci* **2020**, *45*, 1–13.

(7) Matiiv, A. B.; Trubitsina, N. P.; Matveenko, A. G.; Barbitoff, Y. A.; Zhouravleva, G. A.; Bondarev, S. A. Structure and Polymorphism of Amyloid and Amyloid-Like Aggregates. *Biochemistry (Moscow)* **2022**, *87* (5), 450–463.

(8) Fitzpatrick, A. W. P.; Debelouchina, G. T.; Bayro, M. J.; Clare, D. K.; Caporini, M. A.; Bajaj, V. S.; Jaroniec, C. P.; Wang, L.; Ladizhansky, V.; Müller, S. A.; MacPhee, C. E.; Waudby, C. A.; Mott, H. R.; De Simone, A.; Knowles, T. P. J.; Saibil, H. R.; Vendruscolo, M.; Orlova, E. V; Griffin, R. G.; Dobson, C. M. Atomic Structure and Hierarchical Assembly of a Cross-β Amyloid Fibril. *Proceedings of the National Academy of Sciences* **2013**, *110* (14), 5468–5473.

(9) Sinha, N. J.; Langenstein, M. G.; Pochan, D. J.; Kloxin, C. J.; Saven, J. G. Peptide Design and Self-Assembly into Targeted Nanostructure and Functional Materials. *Chem Rev* **2021**, *121* (22), 13915–13935.

(10) Nilsson, B. L.; Celebi Torabfam, G.; Dias, C. L. Peptide Self-Assembly into Amyloid Fibrils: Unbiased All-Atom Simulations. *J Phys Chem B* **2024**, *128* (14), 3320–3328.

(11) Yakupova, E. I.; Bobyleva, L. G.; Vikhlyantsev, I. M.; Bobylev, A. G. Congo Red and Amyloids: History and Relationship. *Biosci Rep* **2019**, *39* (1), BSR20181415.

(12) Xue, C.; Lin, T. Y.; Chang, D.; Guo, Z. Thioflavin T as an Amyloid Dye: Fibril

Quantification, Optimal Concentration and Effect on Aggregation. *R Soc Open Sci* **2017**, *4* (1), 160696.

(13) Yang, H.; Yang, S.; Kong, J.; Dong, A.; Yu, S. Obtaining Information about Protein Secondary Structures in Aqueous Solution Using Fourier Transform IR Spectroscopy. *Nat Protoc* **2015**, *10* (3), 382–396.

(14) Greenfield, N. J. Using Circular Dichroism Spectra to Estimate Protein Secondary Structure. *Nat Protoc* **2006**, *1* (6), 2876–2890.

(15) Vilar, M.; Wang, L.; Riek, R. Structural Studies of Amyloids by Quenched Hydrogen–Deuterium Exchange by NMR. In *Amyloid Proteins: Methods and Protocols*; Sigurdsson, E. M., Calero, M., Gasset, M., Eds.; Humana Press: Totowa, NJ, 2012; pp 185–198.

(16) Morris, K. L.; Serpell, L. C. X-Ray Fibre Diffraction Studies of Amyloid Fibrils. In *Amyloid Proteins: Methods and Protocols*; Sigurdsson, E. M., Calero, M., Gasset, M., Eds.; Humana Press: Totowa, NJ, 2012; pp 121–135.

(17) Pitz, M. E.; Nukovic, A. M.; Elpers, M. A.; Alexander-Bryant, A. A. Factors Affecting Secondary and Supramolecular Structures of Self-Assembling Peptide Nanocarriers. *Macromol Biosci* **2022**, *22* (2), 2100347.

(18) Radamaker, L.; Baur, J.; Huhn, S.; Haupt, C.; Hegenbart, U.; Schönland, S.; Bansal, A.; Schmidt, M.; Fändrich, M. Cryo-EM Reveals Structural Breaks in a Patient-Derived Amyloid Fibril from Systemic AL Amyloidosis. *Nat Commun* **2021**, *12* (1), 875.

(19) Heerde, T.; Schütz, D.; Lin, Y.-J.; Münch, J.; Schmidt, M.; Fändrich, M. Cryo-EM Structure and Polymorphic Maturation of a Viral Transduction Enhancing Amyloid Fibril. *Nat Commun* **2023**, *14* (1), 4293.

(20) Wang, L.-Q.; Zhao, K.; Yuan, H.-Y.; Wang, Q.; Guan, Z.; Tao, J.; Li, X.-N.; Sun, Y.; Yi, C.-W.; Chen, J.; Li, D.; Zhang, D.; Yin, P.; Liu, C.; Liang, Y. Cryo-EM Structure of an Amyloid Fibril Formed by Full-Length Human Prion Protein. *Nat Struct Mol Biol* **2020**, *27* (6), 598–602.

(21) Zapadka, K. L.; Becher, F. J.; Gomes dos Santos, A. L.; Jackson, S. E. Factors Affecting the Physical Stability (Aggregation) of Peptide Therapeutics. *Interface Focus* **2017**, *7* (6), 20170030.

(22) Betush, R. J.; Urban, J. M.; Nilsson, B. L. Balancing Hydrophobicity and Sequence Pattern to Influence Self-Assembly of Amphipathic Peptides. *Peptide Science* **2018**, *110* (1), e23099.

(23) Lee, N. R.; Bowerman, C. J.; Nilsson, B. L. Effects of Varied Sequence Pattern on the Self-Assembly of Amphipathic Peptides. *Biomacromolecules* **2013**, *14* (9), 3267–3277.

(24) Wang, S.-T.; Lin, Y.; Spencer, R. K.; Thomas, M. R.; Nguyen, A. I.; Amdursky, N.; Pashuck, E. T.; Skaalure, S. C.; Song, C. Y.; Parmar, P. A.; Morgan, R. M.; Ercius, P.; Aloni, S.; Zuckermann, R. N.; Stevens, M. M. Sequence-Dependent Self-Assembly and Structural Diversity of Islet Amyloid Polypeptide-Derived β-Sheet Fibrils. *ACS Nano* **2017**, *11* (9), 8579–8589.

(25) Sangji, M. H.; Sai, H.; Chin, S. M.; Lee, S. R.; R Sasselli, I.; Palmer, L. C.; Stupp, S. I. Supramolecular Interactions and Morphology of Self-Assembling Peptide Amphiphile Nanostructures. *Nano Lett* **2021**, *21* (14), 6146–6155.

(26) Roy, S.; Javid, N.; Frederix, P. W. J. M.; Lamprou, D. A.; Urquhart, A. J.; Hunt, N. T.; Halling, P. J.; Ulijn, R. V. Dramatic Specific-Ion Effect in Supramolecular Hydrogels. *Chemistry – A European Journal* **2012**, *18* (37), 11723–11731.

(27) Shanbhag, B. K.; Liu, C.; Haritos, V. S.; He, L. Understanding the Interplay between Self-Assembling Peptides and Solution Ions for Tunable Protein Nanoparticle Formation. *ACS Nano* **2018**, *12* (7), 6956–6967.

(28) Miravet, J. F.; Escuder, B.; Segarra-Maset, M. D.; Tena-Solsona, M.; Hamley, I. W.; Dehsorkhi, A.; Castelletto, V. Self-Assembly of a Peptide Amphiphile: Transition from Nanotape Fibrils to Micelles. *Soft Matter* **2013**, *9* (13), 3558–3564.

(29) Yuan, S. C.; Lewis, J. A.; Sai, H.; Weigand, S. J.; Palmer, L. C.; Stupp, S. I. Peptide Sequence Determines Structural Sensitivity to Supramolecular Polymerization Pathways and Bioactivity. *J Am Chem Soc* **2022**, *144* (36), 16512–16523.

(30) Schilling, C.; Mack, T.; Lickfett, S.; Sieste, S.; Ruggeri, F. S.; Sneideris, T.; Dutta, A.; Bereau, T.; Naraghi, R.; Sinske, D.; Knowles, T. P. J.; Synatschke, C. V; Weil, T.; Knöll, B. Sequence-Optimized Peptide Nanofibers as Growth Stimulators for Regeneration of Peripheral Neurons. *Adv Funct Mater* **2019**, *29* (24), 1809112.

(31) Carvalho, I. C.; Mansur, H. S.; Leonel, A. G.; Mansur, A. A. P.; Lobato, Z. I. P. Soft Matter Polysaccharide-Based Hydrogels as Versatile Bioengineered Platforms for Brain Tissue Repair and Regeneration. *Int J Biol Macromol* **2021**, *182*, 1091–1111.

(32) Peressotti, S.; Koehl, G. E.; Goding, J. A.; Green, R. A. Self-Assembling Hydrogel Structures for Neural Tissue Repair. *ACS Biomater Sci Eng* **2021**, *7* (9), 4136–4163.

(33) Doblado, L. R.; Martínez-Ramos, C.; Pradas, M. M. Biomaterials for Neural Tissue Engineering. *Frontiers in Nanotechnology* **2021**, *3*.

(34) Shen, H.; Fan, C.; You, Z.; Xiao, Z.; Zhao, Y.; Dai, J. Advances in Biomaterial-Based Spinal Cord Injury Repair. *Adv Funct Mater* **2022**, *32* (13), 2110628.

(35) Koss, K. M.; Unsworth, L. D. Neural Tissue Engineering: Bioresponsive Nanoscaffolds Using Engineered Self-Assembling Peptides. *Acta Biomater* **2016**, *44*, 2–15.

(36) Peressotti, S.; Koehl, G. E.; Goding, J. A.; Green, R. A. Self-Assembling Hydrogel Structures for Neural Tissue Repair. *ACS Biomater Sci Eng* **2021**, *7* (9), 4136–4163.

(37) Hussey, G. S.; Dziki, J. L.; Badylak, S. F. Extracellular Matrix-Based Materials for Regenerative Medicine. *Nat Rev Mater* **2018**, *3* (7), 159–173.

(38) Tupone, M. G.; d'Angelo, M.; Castelli, V.; Catanesi, M.; Benedetti, E.; Cimini, A. A State-of-the-Art of Functional Scaffolds for 3D Nervous Tissue Regeneration. *Front Bioeng Biotechnol* **2021**, *9*.

(39) Sharma, P.; Pal, V. K.; Roy, S. An Overview of Latest Advances in Exploring Bioactive Peptide Hydrogels for Neural Tissue Engineering. *Biomater Sci* **2021**, *9* (11), 3911–3938.

(40) Sato, K.; Hendricks, M. P.; Palmer, L. C.; Stupp, S. I. Peptide Supramolecular Materials for Therapeutics. *Chem Soc Rev* **2018**, *47* (20), 7539–7551.

(41) Hendricks, M. P.; Sato, K.; Palmer, L. C.; Stupp, S. I. Supramolecular Assembly of Peptide Amphiphiles. *Acc Chem Res* **2017**, *50* (10), 2440–2448.

(42) Yang, C.-Y.; Huang, W.-Y.; Chen, L.-H.; Liang, N.-W.; Wang, H.-C.; Lu, J.; Wang, X.; Wang, T.-W. Neural Tissue Engineering: The Influence of Scaffold Surface Topography and Extracellular Matrix Microenvironment. *J Mater Chem B* **2021**, *9* (3), 567–584.

(43) Chambel, S. S.; Cruz, C. D. Axonal Growth Inhibitors and Their Receptors in Spinal Cord Injury: From Biology to Clinical Translation. *Neural Regen Res* **2023**, *18* (12).

(44) Abbas, W. A.; Ibrahim, M. E.; El-Naggar, M.; Abass, W. A.; Abdullah, I. H.; Awad, B. I.; Allam, N. K. Recent Advances in the Regenerative Approaches for Traumatic Spinal Cord Injury: Materials Perspective. *ACS Biomater Sci Eng* **2020**, *6* (12), 6490–6509.

(45) Barnes, J. M.; Przybyla, L.; Weaver, V. M. Tissue Mechanics Regulate Brain Development, Homeostasis and Disease. *J Cell Sci* **2017**, *130* (1), 71–82.

(46) Wolf, J. A.; Stys, P. K.; Lusardi, T.; Meaney, D.; Smith, D. H. Traumatic Axonal Injury Induces Calcium Influx Modulated by Tetrodotoxin-Sensitive Sodium Channels. *The Journal of Neuroscience* **2001**, *21* (6), 1923.

(47) Mahumane, G. D.; Kumar, P.; du Toit, L. C.; Choonara, Y. E.; Pillay, V. 3D Scaffolds for Brain Tissue Regeneration: Architectural Challenges. *Biomater Sci* **2018**, *6* (11), 2812–2837.

(48) Kristian Franze. *Annu. Rev. Cell Dev. Biol.* **2020**, 36:61–83.

(49) Koser, D. E.; Thompson, A. J.; Foster, S. K.; Dwivedy, A.; Pillai, E. K.; Sheridan, G. K.; Svoboda, H.; Viana, M.; Costa, L. da F.; Guck, J.; Holt, C. E.; Franze, K. Mechanosensing Is Critical for Axon Growth in the Developing Brain. *Nat Neurosci* **2016**, *19* (12), 1592–1598.

(50) Udvary, D.; Harth, P.; Macke, J. H.; Hege, H.-C.; de Kock, C. P. J.; Sakmann, B.; Oberlaender, M. The Impact of Neuron Morphology on Cortical Network Architecture. *Cell Rep* **2022**, *39* (2), 110677.

(51) Vedaraman, S.; Perez-Tirado, A.; Haraszti, T.; Gerardo-Nava, J.; Nishiguchi, A.; De Laporte, L. Anisometric Microstructures to Determine Minimal Critical Physical Cues Required for Neurite Alignment. *Adv Healthc Mater* **2021**, *10* (20), 2100874.

(52) Yang, S.; Zhu, J.; Lu, C.; Chai, Y.; Cao, Z.; Lu, J.; Zhang, Z.; Zhao, H.; Huang, Y.-Y.; Yao, S.; Kong, X.; Zhang, P.; Wang, X. Aligned Fibrin/Functionalized Self-Assembling Peptide Interpenetrating Nanofiber Hydrogel Presenting Multi-Cues Promotes Peripheral Nerve Functional Recovery. *Bioact Mater* **2022**, *8*, 529–544.

(53) Tran, K. A.; Jin, Y.; Bouyer, J.; DeOre, B. J.; Suprewicz, Ł.; Figel, A.; Walens, H.; Fischer, I.; Galie, P. A. Magnetic Alignment of Injectable Hydrogel Scaffolds for Spinal Cord Injury Repair. *Biomater Sci* **2022**, *10* (9), 2237–2247.

(54) Pashuck, E. T.; Duchet, B. J. R.; Hansel, C. S.; Maynard, S. A.; Chow, L. W.; Stevens, M. M. Controlled Sub-Nanometer Epitope Spacing in a Three-Dimensional Self-Assembled Peptide Hydrogel. *ACS Nano* **2016**, *10* (12), 11096–11104.

(55) Álvarez, Z.; Kolberg-Edelbrock, A. N.; Sasselli, I. R.; Ortega, J. A.; Qiu, R.; Syrgiannis, Z.; Mirau, P. A.; Chen, F.; Chin, S. M.; Weigand, S.; Kiskinis, E.; Stupp, S. I. Bioactive Scaffolds with Enhanced Supramolecular Motion Promote Recovery from Spinal Cord Injury. *Science (1979)* **2021**, *374* (6569), 848–856.

(56) Liyanage, W.; Nilsson, B. L. Substituent Effects on the Self-Assembly/Coassembly and Hydrogelation of Phenylalanine Derivatives. *Langmuir* **2016**, *32* (3), 787–799.

(57) Colquhoun, C.; Draper, E. R.; Eden, E. G. B.; Cattoz, B. N.; Morris, K. L.; Chen, L.; McDonald, T. O.; Terry, A. E.; Griffiths, P. C.; Serpell, L. C.; Adams, D. J. The Effect of Self-Sorting and Co-Assembly on the Mechanical Properties of Low Molecular Weight Hydrogels. *Nanoscale* **2014**, *6* (22), 13719–13725.

(58) Raspa, A.; Saracino, G. A. A.; Pugliese, R.; Silva, D.; Cigognini, D.; Vescovi, A.; Gelain, F. Complementary Co-Assembling Peptides: From In Silico Studies to In Vivo Application. *Adv Funct Mater* **2014**, *24* (40), 6317–6328.

(59) Horgan, C. C.; Rodriguez, A. L.; Li, R.; Bruggeman, K. F.; Stupka, N.; Raynes, J. K.; Day, L.; White, J. W.; Williams, R. J.; Nisbet, D. R. Characterisation of Minimalist Co-Assembled Fluorenylmethyloxycarbonyl Self-Assembling Peptide Systems for Presentation of Multiple Bioactive Peptides. *Acta Biomater* **2016**, *38*, 11–22.

(60) Onogi, S.; Shigemitsu, H.; Yoshii, T.; Tanida, T.; Ikeda, M.; Kubota, R.; Hamachi, I. In Situ Real-Time Imaging of Self-Sorted Supramolecular Nanofibres. *Nat Chem* **2016**, *8* (8), 743–

752.

(61) Horgan, C. C.; Rodriguez, A. L.; Li, R.; Bruggeman, K. F.; Stupka, N.; Raynes, J. K.; Day, L.; White, J. W.; Williams, R. J.; Nisbet, D. R. Characterisation of Minimalist Co-Assembled Fluorenylmethyloxycarbonyl Self-Assembling Peptide Systems for Presentation of Multiple Bioactive Peptides. *Acta Biomater* **2016**, *38*, 11–22.

(62) Lu, C.; Wang, Y.; Yang, S.; Wang, C.; Sun, X.; Lu, J.; Yin, H.; Jiang, W.; Meng, H.; Rao, F.; Wang, X.; Peng, J. Bioactive Self-Assembling Peptide Hydrogels Functionalized with Brain-Derived Neurotrophic Factor and Nerve Growth Factor Mimicking Peptides Synergistically Promote Peripheral Nerve Regeneration. *ACS Biomater Sci Eng* **2018**, *4* (8), 2994–3005.

(63) Mammadov, B.; Mammadov, R.; Guler, M. O.; Tekinay, A. B. Cooperative Effect of Heparan Sulfate and Laminin Mimetic Peptide Nanofibers on the Promotion of Neurite Outgrowth. *Acta Biomater* **2012**, *8* (6), 2077–2086.

(64) Kiyotake, E. A.; Martin, M. D.; Detamore, M. S. Regenerative Rehabilitation with Conductive Biomaterials for Spinal Cord Injury. *Acta Biomater* **2022**, *139*, 43–64.

(65) Bierman-Duquette, R. D.; Safarians, G.; Huang, J.; Rajput, B.; Chen, J. Y.; Wang, Z. Z.; Seidlits, S. K. Engineering Tissues of the Central Nervous System: Interfacing Conductive Biomaterials with Neural Stem/Progenitor Cells. *Adv Healthc Mater* **2022**, *11* (7), 2101577.

(66) He, L.; Xiao, Q.; Zhao, Y.; Li, J.; Reddy, S.; Shi, X.; Su, X.; Chiu, K.; Ramakrishna, S. Engineering an Injectable Electroactive Nanohybrid Hydrogel for Boosting Peripheral Nerve Growth and Myelination in Combination with Electrical Stimulation. *ACS Appl Mater Interfaces* **2020**, *12* (47), 53150–53163.

(67) Arioz, I.; Erol, O.; Bakan, G.; Dikecoglu, F. B.; Topal, A. E.; Urel, M.; Dana, A.; Tekinay, A. B.; Guler, M. O. Biocompatible Electroactive Tetra(Aniline)-Conjugated Peptide Nanofibers for Neural Differentiation. *ACS Appl Mater Interfaces* **2018**, *10* (1), 308–317.

(68) Moritz, C.; Field-Fote, E. C.; Tefertiller, C.; van Nes, I.; Trumbower, R.; Kalsi-Ryan, S.; Purcell, M.; Janssen, T. W. J.; Krassioukov, A.; Morse, L. R.; Zhao, K. D.; Guest, J.; Marino, R. J.; Murray, L. M.; Wecht, J. M.; Rieger, M.; Pradarelli, J.; Turner, A.; D'Amico, J.; Squair, J. W.; Courtine, G. Non-Invasive Spinal Cord Electrical Stimulation for Arm and Hand Function in Chronic Tetraplegia: A Safety and Efficacy Trial. *Nat Med* **2024**, *30* (5), 1276–1283.

(69) Ligorio, C.; Mata, A. Synthetic Extracellular Matrices with Function-Encoding Peptides. *Nature Reviews Bioengineering* **2023**, *1* (7), 518–536.

(70) Kaur, H.; Roy, S. Designing Aromatic N-Cadherin Mimetic Short-Peptide-Based Bioactive Scaffolds for Controlling Cellular Behaviour. *J Mater Chem B* **2021**, *9* (29), 5898–5913.

(71) Mehrban, N.; Zhu, B.; Tamagnini, F.; Young, F. I.; Wasmuth, A.; Hudson, K. L.; Thomson, A. R.; Birchall, M. A.; Randall, A. D.; Song, B.; Woolfson, D. N. Functionalized α-Helical Peptide Hydrogels for Neural Tissue Engineering. *ACS Biomater Sci Eng* **2015**, *1* (6), 431–439.

(72) Jain, R.; Roy, S. Controlling Neuronal Cell Growth through Composite Laminin Supramolecular Hydrogels. *ACS Biomater Sci Eng* **2020**, *6* (5), 2832–2846.

(73) Sever, M.; Gunay, G.; Guler, M. O.; Tekinay, A. B. Tenascin-C Derived Signaling Induces Neuronal Differentiation in a Three-Dimensional Peptide Nanofiber Gel. *Biomater Sci* **2018**, *6* (7), 1859–1868.

(74) Lu, J.; Yan, X.; Sun, X.; Shen, X.; Yin, H.; Wang, C.; Liu, Y.; Lu, C.; Fu, H.; Yang, S.; Wang, Y.; Sun, X.; Zhao, L.; Lu, S.; Mikos, A. G.; Peng, J.; Wang, X. Synergistic Effects of Dual-Presenting VEGF- and BDNF-Mimetic Peptide Epitopes from Self-Assembling Peptide Hydrogels on Peripheral Nerve Regeneration. *Nanoscale* **2019**, *11* (42), 19943–19958.

(75) Sarkar, B.; Ma, X.; Agas, A.; Siddiqui, Z.; Iglesias-Montoro, P.; Nguyen, P. K.; Kim, K. K.; Haorah, J.; Kumar, V. A. In Vivo Neuroprotective Effect of a Self-Assembled Peptide Hydrogel. *Chemical Engineering Journal* **2021**, *408*, 127295.

(76) Smith, C. S.; Álvarez, Z.; Qiu, R.; Sasselli, I. R.; Clemons, T.; Ortega, J. A.; Vilela-Picos, M.; Wellman, H.; Kiskinis, E.; Stupp, S. I. Enhanced Neuron Growth and Electrical Activity by a Supramolecular Netrin-1 Mimetic Nanofiber. *ACS Nano* **2023**, *17* (20), 19887–19902.

(77) Rubert Pérez, C. M.; Álvarez, Z.; Chen, F.; Aytun, T.; Stupp, S. I. Mimicking the Bioactivity of Fibroblast Growth Factor-2 Using Supramolecular Nanoribbons. *ACS Biomater Sci Eng* **2017**, *3* (9), 2166–2175.

(78) Wang, T.-W.; Chang, K.-C.; Chen, L.-H.; Liao, S.-Y.; Yeh, C.-W.; Chuang, Y.-J. Effects of an Injectable Functionalized Self-Assembling Nanopeptide Hydrogel on Angiogenesis and Neurogenesis for Regeneration of the Central Nervous System. *Nanoscale* **2017**, *9* (42), 16281–16292.

(79) Hong, J. Y.; Kim, S. H.; Seo, Y.; Jeon, J.; Davaa, G.; Kim, S. H.; Hyun, J. K. Self-Assembling Peptide Gels Promote Angiogenesis and Functional Recovery after Spinal Cord Injury in Rats. *J Tissue Eng* **2022**, *13*, 20417314221086492.

(80) Wu, W.; Jia, S.; Xu, H.; Gao, Z.; Wang, Z.; Lu, B.; Ai, Y.; Liu, Y.; Liu, R.; Yang, T.; Luo, R.; Hu, C.; Kong, L.; Huang, D.; Yan, L.; Yang, Z.; Zhu, L.; Hao, D. Supramolecular Hydrogel Microspheres of Platelet-Derived Growth Factor Mimetic Peptide Promote Recovery from Spinal Cord Injury. *ACS Nano* **2023**, *17* (4), 3818–3837.

(81) Ma, X.; Agas, A.; Siddiqui, Z.; Kim, K.; Iglesias-Montoro, P.; Kalluru, J.; Kumar, V.; Haorah, J. Angiogenic Peptide Hydrogels for Treatment of Traumatic Brain Injury. *Bioact Mater* **2020**, *5* (1), 124–132.

(82) Huettner, N.; Dargaville, T. R.; Forget, A. Discovering Cell-Adhesion Peptides in Tissue Engineering: Beyond RGD. *Trends Biotechnol* **2018**, *36* (4), 372–383.

(83) Hamley, I. W. Small Bioactive Peptides for Biomaterials Design and Therapeutics. *Chem Rev* **2017**, *117* (24), 14015–14041.

(84) Jain, R.; Roy, S. Designing a Bioactive Scaffold from Coassembled Collagen–Laminin Short Peptide Hydrogels for Controlling Cell Behaviour. *RSC Adv* **2019**, *9* (66), 38745–38759.

(85) Lu, J.; Sun, X.; Yin, H.; Shen, X.; Yang, S.; Wang, Y.; Jiang, W.; Sun, Y.; Zhao, L.; Sun, X.; Lu, S.; Mikos, A. G.; Peng, J.; Wang, X. A Neurotrophic Peptide-Functionalized Self-Assembling Peptide Nanofiber Hydrogel Enhances Rat Sciatic Nerve Regeneration. *Nano Res* **2018**, *11* (9), 4599–4613.

(86) Markus, A.; Patel, T. D.; Snider, W. D. Neurotrophic Factors and Axonal Growth. *Curr Opin Neurobiol* **2002**, *12* (5), 523–531.

(87) Delgado, A. C.; Maldonado-Soto, A. R.; Silva-Vargas, V.; Mizrak, D.; von Känel, T.; Tan, K. R.; Paul, A.; Madar, A.; Cuervo, H.; Kitajewski, J.; Lin, C.-S.; Doetsch, F. Release of Stem Cells from Quiescence Reveals Gliogenic Domains in the Adult Mouse Brain. *Science (1979)* **2021**, *372* (6547), 1205–1209.

(88) Gelain, F.; Luo, Z.; Zhang, S. Self-Assembling Peptide EAK16 and RADA16 Nanofiber Scaffold Hydrogel. *Chem Rev* **2020**, *120* (24), 13434–13460.

(89) Chen, J.; Zou, X. Self-Assemble Peptide Biomaterials and Their Biomedical Applications. *Bioact Mater* **2019**, *4*, 120–131.

(90) Raspa, A.; Carminati, L.; Pugliese, R.; Fontana, F.; Gelain, F. Self-Assembling Peptide Hydrogels for the Stabilization and Sustained Release of Active Chondroitinase ABC in Vitro and in Spinal Cord Injuries. *Journal of Controlled Release* **2021**, *330*, 1208–1219.

(91) Pugliese, R.; Marchini, A.; Saracino, G. A. A.; Zuckermann, R. N.; Gelain, F. Cross-Linked Self-Assembling Peptide Scaffolds. *Nano Res* **2018**, *11* (1), 586–602.

(92) Shi, W.; Huang, C. J.; Xu, X. D.; Jin, G. H.; Huang, R. Q.; Huang, J. F.; Chen, Y. N.; Ju, S. Q.; Wang, Y.; Shi, Y. W.; Qin, J. B.; Zhang, Y. Q.; Liu, Q. Q.; Wang, X. B.; Zhang, X. H.; Chen, J. Transplantation of RADA16-BDNF Peptide Scaffold with Human Umbilical Cord Mesenchymal Stem Cells Forced with CXCR4 and Activated Astrocytes for Repair of Traumatic Brain Injury. *Acta Biomater* **2016**, *45*, 247–261.

(93) Kumar, V. A.; Taylor, N. L.; Shi, S.; Wang, B. K.; Jalan, A. A.; Kang, M. K.; Wickremasinghe, N. C.; Hartgerink, J. D. Highly Angiogenic Peptide Nanofibers. *ACS Nano* **2015**, *9* (1), 860–868.

(94) Shashoua, V. E.; Adams, D. S.; Boyer-Boiteau, A.; Cornell-Bell, A.; Li, F.; Fisher, M. Neuroprotective Effects of a New Synthetic Peptide, CMX-9236, in in Vitro and in Vivo Models of Cerebral Ischemia. *Brain Res* **2003**, *963* (1), 214–223.

(95) Rode, S.; Hayn, M.; Röcker, A.; Sieste, S.; Lamla, M.; Markx, D.; Meier, C.; Kirchhoff, F.; Walther, P.; Fändrich, M.; Weil, T.; Münch, J. Generation and Characterization of Virus-Enhancing Peptide Nanofibrils Functionalized with Fluorescent Labels. *Bioconjug Chem* **2017**, *28* (4), 1260–1270.

(96) Rode, S.; Hayn, M.; Röcker, A.; Sieste, S.; Lamla, M.; Markx, D.; Meier, C.; Kirchhoff, F.; Walther, P.; Fändrich, M.; Weil, T.; Münch, J. Generation and Characterization of Virus-Enhancing Peptide Nanofibrils Functionalized with Fluorescent Labels. *Bioconjug Chem* **2017**, *28* (4), 1260–1270.

(97) Heerde, T.; Schütz, D.; Lin, Y.-J.; Münch, J.; Schmidt, M.; Fändrich, M. Cryo-EM Structure and Polymorphic Maturation of a Viral Transduction Enhancing Amyloid Fibril. *Nat Commun* **2023**, *14* (1), 4293.

(98) Yaguchi, A.; Oshikawa, M.; Watanabe, G.; Hiramatsu, H.; Uchida, N.; Hara, C.; Kaneko, N.; Sawamoto, K.; Muraoka, T.; Ajioka, I. Efficient Protein Incorporation and Release by a Jigsaw-Shaped Self-Assembling Peptide Hydrogel for Injured Brain Regeneration. *Nat Commun* **2021**, *12* (1), 6623.

(99) Zhang, W.; Yu, X.; Li, Y.; Su, Z.; Jandt, K. D.; Wei, G. Protein-Mimetic Peptide Nanofibers: Motif Design, Self-Assembly Synthesis, and Sequence-Specific Biomedical Applications. *Prog Polym Sci* **2018**, *80*, 94–124.

(100) Luo, T.; Kiick, K. L. Collagen-Like Peptide Bioconjugates. *Bioconjug Chem* **2017**, *28* (3), 816–827.

(101) Kim, W.; Chaikof, E. L. Recombinant Elastin-Mimetic Biomaterials: Emerging Applications in Medicine. *Adv Drug Deliv Rev* **2010**, *62* (15), 1468–1478.

(102) Nelson, D. W.; Gilbert, R. J. Extracellular Matrix-Mimetic Hydrogels for Treating Neural Tissue Injury: A Focus on Fibrin, Hyaluronic Acid, and Elastin-Like Polypeptide Hydrogels. *Adv Healthc Mater* **2021**, *10* (22), 2101329.

(103) Pashuck, E. T.; Cui, H.; Stupp, S. I. Tuning Supramolecular Rigidity of Peptide Fibers through Molecular Structure. *J Am Chem Soc* **2010**, *132* (17), 6041–6046.

(104) Okur, Z.; Senturk, O. I.; Yilmaz, C.; Gulseren, G.; Mammadov, B.; Guler, M. O.; Tekinay, A. B. Promotion of Neurite Outgrowth by Rationally Designed NGF-β Binding Peptide

Nanofibers. *Biomater Sci* **2018**, *6* (7), 1777–1790.

(105) Fleming, S.; Ulijn, R. V. Design of Nanostructures Based on Aromatic Peptide Amphiphiles. *Chem Soc Rev* **2014**, *43* (23), 8150–8177.

(106) Hamley, I. W. Self-Assembly, Bioactivity, and Nanomaterials Applications of Peptide Conjugates with Bulky Aromatic Terminal Groups. *ACS Appl Bio Mater* **2023**, *6* (2), 384–409.

(107) Martin, A. D.; Thordarson, P. Beyond Fmoc: A Review of Aromatic Peptide Capping Groups. *J Mater Chem B* **2020**, *8* (5), 863–877.

(108) James, E. I.; Jenkins, L. D.; Murphy, A. R. Peptide-Thiophene Hybrids as Self-Assembling Conductive Hydrogels. *Macromol Mater Eng* **2019**, *304* (11), 1900285.

2. Motivation and Conceptual Design

Neurons play a crucial role in transmitting vital electrical and chemical signals within the nervous system. However, when neurons are damaged due to external insults or neurodegenerative diseases, particularly in the central nervous system, they have a limited ability to regenerate due to the convoluted neural environment, neuroinflammation, and scar tissue formation. Conventional treatments, like surgery and small molecules cannot achieve complete functional recovery. Cell therapy is a new therapeutic option, but cell viability and cost hinder the development of this approach. Biomaterial scaffolds provide an alternative means of physically supporting cells and biochemically simulating cellular activity. Scaffolds derived from natural sources have intrinsic bioactivity, but they tend to have issues with batch-to-batch variation and uncontrollable degradation rates. Conversely, scaffolds fabricated from synthetic polymers have high reproducibility and processing plasticity; however, the lack of inherent bioactive motifs and the release of potential cytotoxic degradation compounds limit the use of polymeric scaffolds for neural regeneration. Synthetic peptides, composed of amino acids, combine the advantages of both classes of materials and can be designed to form amyloid-like self-assembling peptides (SAPs). Amyloid-like SAPs form nanostructures that have the potential to serve as an artificial extracellular matrix (ECM) or as scaffolds for neural tissue engineering.

Amyloid-like SAPs can form hierarchical nanostructures under physiological conditions. Different assembled nanostructures can lead to different functionalities, despite having the same peptide sequence. For example, nanofibers are preferable matrix for neural cells, as they resemble fibrous proteins of the ECM. Therefore, it is worthwhile to investigate different factors that influence the self-assembled nanostructures. The versatility of this material class is not only limited to sequence design but also multiple factors that influence the self-assembly morphology, such as concentration, solvent effect, and temperature. However, most published works focus on how cell adhesion epitopes or growth factor mimic-modified SAPs can manipulate neural regeneration. Neural cells are also known to respond to physical cues; therefore, this thesis focuses on investigating various structures of amyloid-like SAPs by molecular binding assays, microscopy, and spectroscopy. Meanwhile, neural cells are tested with these materials. Through the analysis of the physical cues and biological studies, this thesis aims to address the correlation

between the structural effects of amyloid-like SAPs and neural activity. To further elucidate this correlation between structural effects of self-assembled nanostructures and neural cells, the thesis is divided into the three chapters. The first project studies how sequence design affects assembled nanostructures and subsequently influences neural activity. The second project examines how solvent effects and inconspicuous factors such as processing history affect assembled structures and neural activity. The third project presents a strategy for creating a stable amyloid-like SAP substrate on which neural cells can grow. This thesis emphasizes the importance of structure and bioactivity, and is **Figure 2.1.** summarized the conceptual scheme and scope of the three projects.

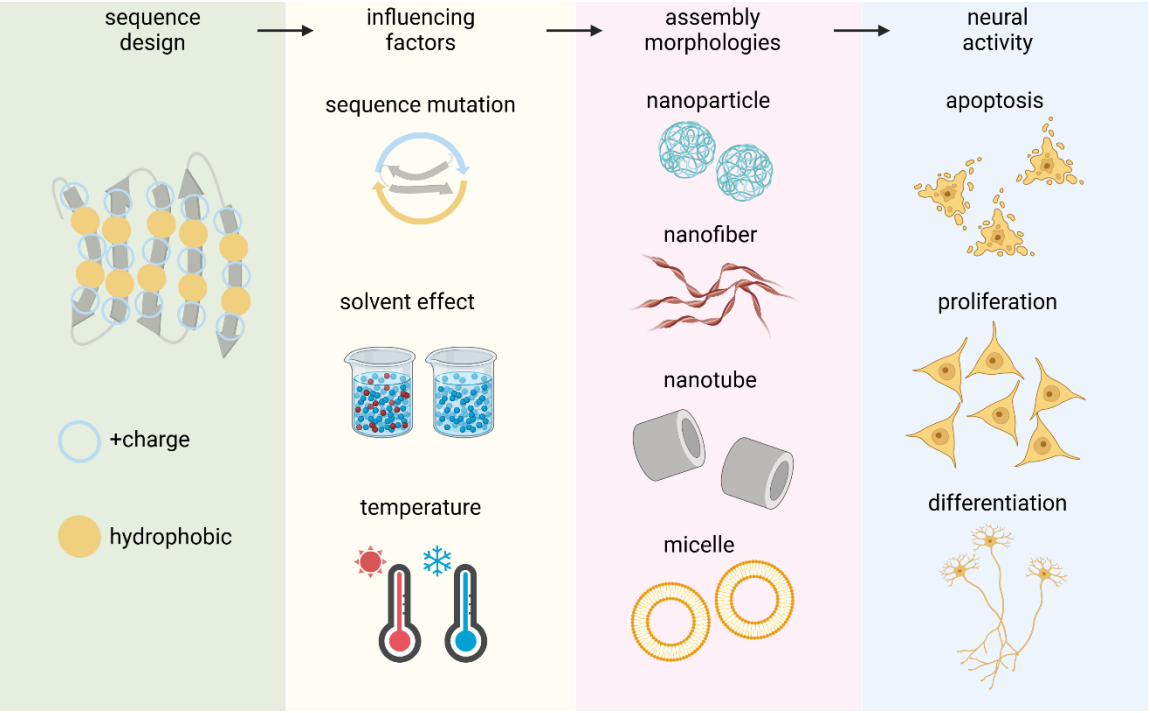

Figure 2.1. The conceptual scheme and scope of this thesis. The amyloid-like self-assembling peptides for neural cells typically contain positively charged amino acids and hydrophobic amino acids to trigger self-assembly. To explore the potential morphologies of this class of materials, various sequential designs and processing plasticity are implemented, such as the solvent and temperature effects. Later, similar amino acid sequences with the same treatment or the same amino acid sequences with different treatments are systematically examined with neural cells to evaluate their structural effects on the cells.

Starting with the most straightforward strategy, **Chapter 3** investigates amyloid-like SAPs derived from enhancing factor C sequence (EF-C) with sequential mutations, i.e. systematic sequence variation. To retain the positively charged property to interact with the negatively charged cell membranes, the hydrophobic cores are systematically modified and grouped according to their chemical identity: sequences with aromatic side chains, sequences with aliphatic side chains, and sequences with relatively weak hydrophobic chains. Nine peptides are designed, and their physicochemical properties and self-assembled morphologies are characterized using Congo Red binding assay, electron microscopy, and infrared spectroscopy. Computational modeling is implemented to gain a more detailed understanding of the self-assembly behavior. Based on the structural investigations, *in vitro* studies of neuroblastoma cells are carried out to determine the relationship between the morphology of self-assembling peptides and their corresponding neural activity. The conceptual scheme of this chapter is illustrated in **Figure 2.2**.

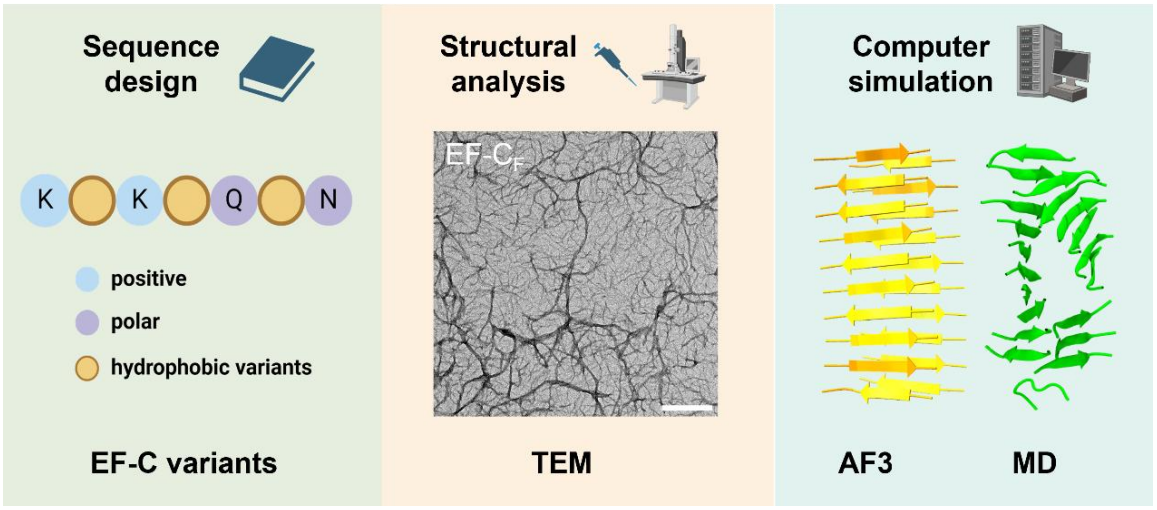

Figure 2.2. The conceptual scheme of Chapter 3. This chapter mainly examines how different hydrophobic groups change the structures of the SAP variants derived from enhancing factor C (EF-C), and studies these structural differences and bioactivity of these variants with neural cells.

Other than sequence design, the solvent effect—including concentration, purity, salts, and so on—is known to play a role in self-assembly behavior. Thus, **in Chapter 4**, the importance of the solvent effect and processing history on the morphologies of amyloid-like SAPs (amyloid beta (Aβ) peptides) are investigated. The physicochemical properties

of the same peptide sequences, produced by different manufacturers, dissolved in different solvents, or tested at different time points, are characterized by the following methods: (1) the molecular binding affinity of an amyloid dye (thioflavin T), (2) the secondary structures of the peptides detected by circular dichroism, and (3) images taken by transmission electron microscopy. Later, these different conditions are tested on neural cells to activate of formyl peptide receptor 1 in order to understand the correlation between the solvent effect and the processing history of amyloid-like SAPs and neural activity. The conceptual design of this chapter is depicted in **Figure 2.3**.

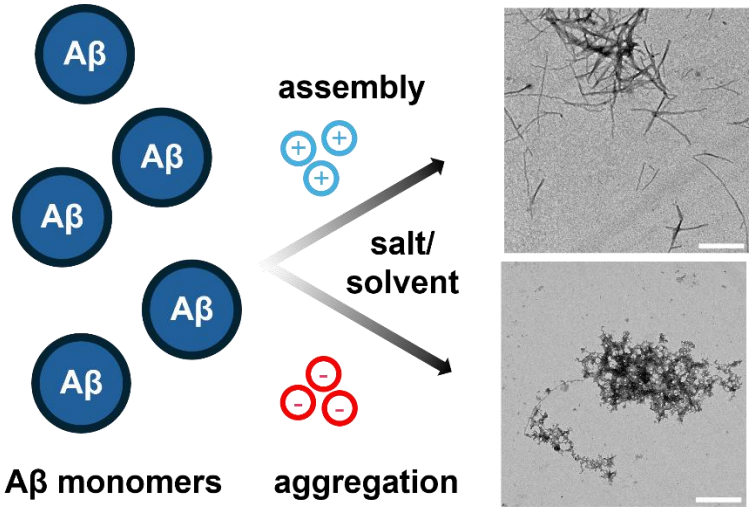

Figure 2.3. The conceptual scheme of Chapter 4. This chapter discusses how the processing history and solvent effect, such as different manufacturers or different buffers for the same peptide sequence, influences the structure of amyloid-like self-assembling peptides.

In order to provide a stable cell culture platform based on amyloid-like SAPs, in **Chapter 5**, one of the EF-C derivatives is immobilized on substrates to investigate its surface functionality. The amyloid-like peptides are modified with vinyl groups, and thiolated substrates are prepared by chemical vapor deposition of 3-mercaptopropyltrimethoxysilane (MPS). Subsequently, the modified peptides are immobilized on the thiolated substrates via the photo-triggered thiol-ene reaction. Surface characterization techniques, such as X-ray photoelectron spectroscopy and time-of-flight secondary ion mass spectrometry, are used to semi-quantify the peptide modification and

assess the potential of this strategy for photopatterning. Contact angle, surface zeta potential, and atomic force microscopy are utilized to examine the surface properties. Last but not least, neural cells are added to the modified substrate to analyze its bioactivity. Figure 2.4. illustrates the concept of this chapter.

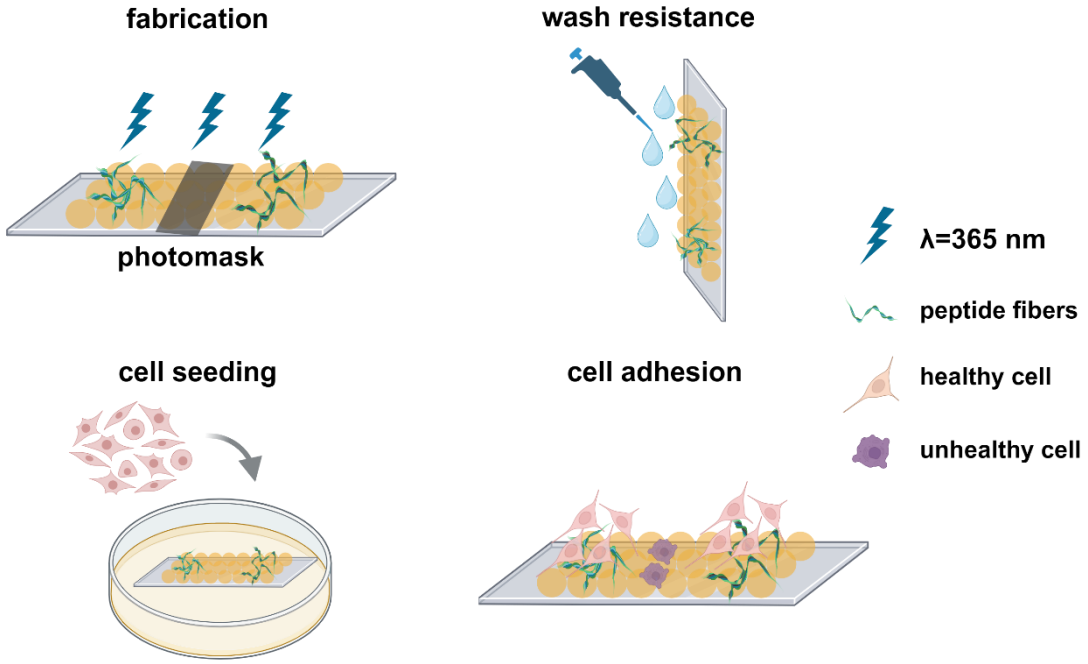

Figure 2.4. The conceptual scheme of Chapter 5. This chapter explores the properties of amyloid-like peptide immobilization on substrates and the potential for fabricating a robust, large-scale, and selective neural cell culture platform.

In summary, this thesis studies the correlation between structural effects of the amyloid-like self-assembling peptides on neural cells. Starting from the sequential variations, other factors influencing the structure of this class of materials are also highlighted. Through proper design of the peptide sequence and comprehensive sample preparation procedure, this work aims to provide insight into the design of amyloid-like self-assembling peptides based on their structural effect, in the hope of accelerating the development of new therapeutic options for neural repair.

3. Design of the Hydrophobic Core of Self-Assembling EF-C Peptide Fibrils for Enhanced Neural Regeneration

This chapter is reproduced from

Yu-Liang Tsai, Primiana Cavallo, Lu Qi, Christopher P. Ender, Julian Link, Katrin Amann-Winkel, Kristina Endres, Christopher V. Synatschke, Torsten John. ChemRxiv, **2024**

DOI: 10.26434/chemrxiv-2024-mzghg

Author

Yu-Liang Tsai, Primiana Cavallo, Qi Lu, Christopher P. Ender, Julian Link, Katrin Amann-Winkel, Kristina Endres, Christopher V. Synatschke, Torsten John

Contribution

Yu-Liang Tsai: Conceptualization, Methodology, Validation, Formal analysis, Investigation, Writing - Original Draft, Writing - Review & Editing, Visualization, Project administration.

Primiana Cavallo: Formal analysis, Investigation, Writing - Review & Editing.

Qi Lu: Investigation.

Christopher P. Ender: Formal analysis, Investigation, Writing - Review & Editing.

Julian Link: Fomal analysis, Investigation, Writing - Review & Editing.

Katrin Amann-Winkel: Methodology, Formal analysis, Writing - Review & Editing; Kristina Endres: Methodology, Formal analysis Writing - Review & Editing; Christopher V. Synatschke: Resources, Writing - Review & Editing, Supervision, Project administration, Funding acquisition.

Torsten John: Conceptualization, Methodology, Formal analysis, Investigation, Writing - Original Draft, Writing - Review & Editing, Visualization, Supervision, Project administration

3.1.Abstract

Neurons have limited self-repair ability, and typical treatment approaches rely on surgery. Hindered by the lack of donor tissues and the complex neural environment, there is great interest in developing biomaterials to support neural regeneration. Self-assembling peptides with fibrous structures mimicking the extracellular matrix have shown great potential as neurosupportive biomaterials. Previously, we identified peptide sequences derived from enhancing factor-C (EF-C) that are neurotrophic without additional supplements. Here, a library of nine EF-C variants is designed by varying the hydrophobic core of the peptide backbone to elucidate their influence on self-assembly and bioactivity. The physicochemical properties of these variants, including secondary structure and morphology, are thoroughly analyzed. Furthermore, molecular dynamics simulations based on AlphaFold 3 models are conducted and provide theoretical insights that explain the differential assembly and stability of EF-C variants. Subsequently, the peptides are tested for bioactivity in a neuroblastoma cell line (SH-SY5Y) to establish structure-property relationships. The structure-forming EF-C variants, particularly those featuring phenylalanine and isoleucine, are neurotrophic towards SH-SY5Y cells, shown by enhanced ATP levels. The combination of experimental and computational methods provides a strategy for the accelerated design of neuro-regenerative peptides.

3.2.Introduction

The complex microenvironment and inhibitory factors resulting from neuroinflammation or scar formation limit the ability of neurons to repair themselves after injury.[1–4] Treatment is usually achieved by reconnecting nerve ends or integrating transplants for larger defects. However, microstructural mismatch at the injury site and limited donor tissue are major obstacles. Surgical repair of neural injuries helps patients to alleviate discomfort, but typically does not result in full neurological recovery,[5–7] and more collaborative and interdisciplinary efforts in neural engineering are needed. As an alternative approach, biomaterials based on polymers, peptides and proteins have been explored. In particular, self-assembling peptides (SAPs) have emerged as a potential treatment for neural repair. SAPs offer a wide variety of biomimetic scaffolds that simultaneously provide different morphologies, structural stability and biological stimuli.[3,10,11] Peptide amphiphiles (PAs), for example, consist of a short peptide sequence conjugated to an aliphatic tail. Stupp *et al.* have systemically developed and thoroughly investigated their molecular design, self-assembly dynamics and hierarchical structure.[8] PAs have been further decorated with various bioactive epitopes and growth factor mimics to improve their potential in *in vitro* and *in vivo* models of neural regeneration[9–12]. Various groups developed and investigated self-assembling multidomain peptides, consisting of alternating hydrophilic and hydrophobic amino acids in the center (usually serine and leucine) and charged amino acids at both termini, as therapeutics for neural repair.[13,14] Wang *et al.* demonstrated that a RADA16 (sequence: RADARADARADARADA) based SAP modified with a growth factor mimic promotes angiogenesis and neurogenesis.[15] Gelain and colleagues provided a comprehensive overview of this class of SAPs as well as their neural regenerative applications.[16]

All of the above-mentioned SAPs share the incorporation of bioactive motifs into the peptide backbones to facilitate neural regeneration. In our previous work, we identified neural active peptide sequences, KIKIQI and KFKFQF, which were variants of enhancing factor-C (EF-C) derived from the glycoprotein $GP120_{417–428}$ of human immunodeficiency virus.[17] These sequences facilitated neuronal growth and adhesion of primary mouse neurons without the presence of epitopes or growth-factor mimics.[18] Our results suggested that bioactive EF-C variants have (1) a strong tendency to form fibers, (2) an alternating

pattern of hydrophobic and positively charged amino acids with a positive net charge, (3) high intermolecular β-sheet contents, and (4) a larger cross-sectional diameter in single fiber atomic force microscopy (AFM) analysis. However, the relationship between the physicochemical properties and molecular structure of the hydrophobic core of the EF-C variants and their bioactivity has not been studied yet.

SAPs are highly versatile and easily tunable, indicating that there are multiple underlying factors, such as charge distribution and chemical nature of peptide side chains, which influence the secondary structure and supramolecular assembly.[19] For example, modifying hydrophobicity and aromaticity of the SAP sequence led to different hydrogelation behavior.[20] Lee *et al.* reported that adjusting the pattern of the SAP sequence changed the self-assembly propensity and morphology.[21] In another example, Cao and coworkers found that varying the side chain size and hydrophobicity gave rise to distinct assembled morphologies and encapsulation efficiencies of molecules.[22] Yuan and colleagues found that tailoring the sequence of PAs induced different self-assembly pathways and cell-material interactions.[23] Comprehensive structural analysis is essential for understanding structure-property relationships. Characterization of SAPs typically involves molecular and microscopic analyses. At the molecular level, binding assays using dyes such as Congo Red[24,25] are characteristic of amyloid-like structures with high β-sheet content. Spectroscopy, including Fourier transform infrared spectroscopy (FT-IR),[26–28] and crystallography, such as X-ray diffraction (XRD), provide additional molecular information.[29,30] At the microscopic level, dynamic light scattering (DLS) is a non-destructive technique to estimate the size distribution of aggregates in solution.[19,31] Electron microscopy, such as scanning electron microscopy (SEM) and transmission electron microscopy (TEM), generates images and characterizes the morphology of SAPs.[19,31]

Currently, the design of functional SAPs heavily relies on iterative experimental studies, which is not always efficient. Therefore, it is beneficial to incorporate theoretical and computational methods to reveal the formation mechanisms of SAPs and accelerate the development and prediction of functional SAPs for biomedical applications.[32–34] An example of an experimental and computational study by Wang *et al.* showed that molecular

dynamics (MD) simulations helped explain the mechanism of how the salt concentration can influence self-assembly behavior observed in experiments.[35] John and colleagues applied MD simulations to dive into the contribution of single amino acids on fiber formation of a sequence from islet amyloid polypeptide.[34] However, predicting the accurate 3D self-assembled structure from amino acid sequences *de novo* is challenging.[36] In this work, we used AlphaFold 3 to predict oligomer and protofibril structures of EF-C variants and applied MD simulations to test the stability of the predicted structures.[37] We rationally designed SAPs derived from EF-C variants with different hydrophobic motifs and analyzed their physicochemical properties. Subsequently, we compared the physicochemical analyses with theoretical prediction. Finally, a human neuroblastoma cell line (SH-SY5Y) was used as a model to study the neural bioactivity of structure-forming SAPs. Herein, we systematically altered the hydrophobic amino acids in the peptide backbones to gain insight into the behavior of these as neural active SAPs, as illustrated in **Figure 3. 1**. We aim to validate that computational predictions can facilitate the design of peptide sequences for achieving neural regeneration.

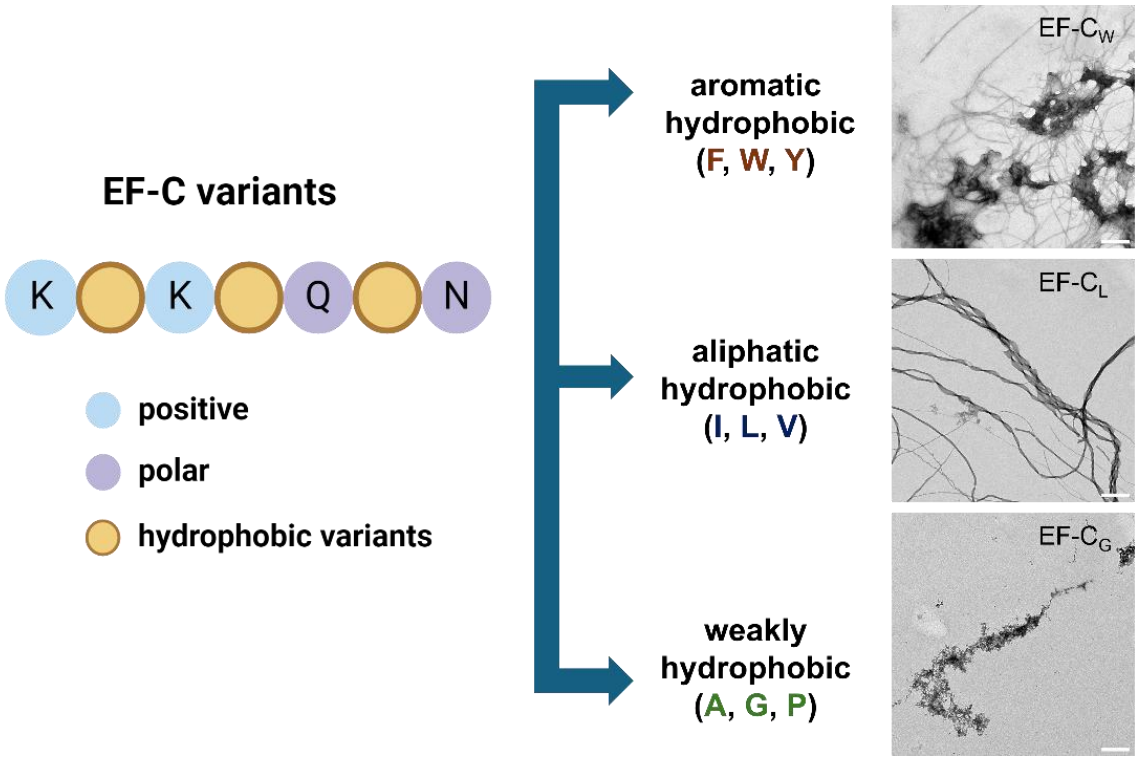

Figure 3.1 A conceptional scheme and TEM images of different hydrophobic motifs affecting the assembled morphology of EF-C variants (scale bar = 500 nm).

3.3.Result and Discussion

3.3.1. Design Strategy and Synthesis of EF-C Variants for Enhanced Neural Regeneration

Starting from the EF-C peptide, we systematically varied the hydrophobic core of the peptide KXKXQXN (X = hydrophobic amino acid). Previous research identified sequences consisting of KIKIQI and KFKFQF, a high propensity to form fibers, a positive net charge, and high intermolecular β-sheet content as important features for neural repair.[18] Several reports also suggested that sidechain chemistry and arrangements of the peptide backbones affected the morphology, stability, and rigidity of SAPs.[20–22,38–41] Inspired by these findings, nine peptide sequences were designed as variants of EF-C. These peptides were synthesized via solid phase peptide synthesis (SPPS) using fluorenylmethyloxycarbonyl (Fmoc)-Asn (trt) Wang resins in an automatic peptide synthesizer, and the sequences and abbreviations of the peptides are listed in **Table 3.1**. All peptides were collected by reversed phase preparative HPLC and characterized by mass spectrometry. The purity of each peptide (>95%) was further confirmed by analytical HPLC. The corresponding spectra are provided in **Figure S3. 1** and **Figure S3. 2**. Further characterization of leucine (EF-C_I) and isoleucine (EF-C_L) variants by ^{1}H-NMR spectroscopy is included in **Figure S3. 3.** To facilitate visualization of the peptide material in cell experiments, rhodamine B (RhB)-labeled EF-C_I was synthesized. Characterization of the labelling agent and product is included in **Figure S3. 4** and **Figure S3. 5**.

Table 1. Overview of EF-C variants with abbreviation, amino acid sequence, and fibril formation properties: conversion rate, IR peaks, XRD (calculated distance *d*), and assembled morphologies based on TEM images.

Abbreviation	Sequence	Conversion rate (%)	IR peaks 2nd deriv. (cm^{-1})	XRD *d* (Å)	Morphology
EF-C_F	KFKFQFN	94	1626, 1694	4.7, 5.17, 5.24, 5.82	linear nanofiber
EF-C_W	KWKWQWN	94	1627, 1667, 1679, 1693	4.61, 4.72, 4.81, 5.06, 5.25, 8.34	linear nanofiber

EF-C_Y	KYKYQYN	60	1605, 1625, 1676	X	no structure
EF-C_I	KIKIQIN	93	1620, 1658, 1678, 1690	4.66, 4.82, 5.17	twisted nanofiber
EF-C_L	KLKLQLN	73	1622, 1643, 1677	4.61, 4.73, 5.16, 5.26	twisted nanofiber
EF-C_V	KVKVQVN	62	1623, 1669 1688	4.64, 5.08, 5.18, 5.67, 5.83	twisted nanofiber
EF-C_A	KAKAQAN	27	1623, 1667, 1692	X	no structure
EF-C_G	KGKGQGN	19	1607, 1667	X	no structure
EF-C_P	KPKPQPN	35	1626, 1678	X	no structure

X stands for no clear signals

To facilitate the visualization of the peptide material in further experiments, rhodamine B (RhB)-labeled EF-C_I was synthesized. The labelling agent RhB-*N*-hydroxysuccinimide ester (RhB-NHS) was synthesized following a previous report,[53] as confirmed by MS and ^{1}H-NMR shown in **Figure S3. 4**. A spacer, aminohexanoic acid, was introduced to link EF-C_I and RhB-NHS so as to diminish chemical influence on the peptide backbone.[54] The final product, RhB-EF-C_I, was collected by preparative HPLC and characterized by MALDI-ToF MS; the corresponding spectra are given in **Figure S3. 5**.

3.3.2. Mechanistic Study of Self-Assembly of EF-C Variants

To experimentally study the self-assembly of the nine EF-C variants, the peptides were incubated following a uniform protocol. Each peptide was initially dissolved in dimethyl sulfoxide (DMSO) due to the high hydrophobicity of the peptides, as previously established,[42,43] followed by dilution in phosphate buffered saline to form 1 mM peptide solutions which were statically incubated at room temperature for 24 hr unless otherwise stated. To establish and verify this protocol for peptide self-assembly, the aggregation concentration was measured by DLS. DLS is a non-invasive technique measuring the Brownian motion of molecules and correlating this motion to the size of the molecules.[44]

After self-assembly of EF-C variants for 24 hr, the derived count rate of scattered light was used to determine the aggregation propensity of the peptides. In **Figure 3. 2 (a)**, five EF-C variants, namely EF-C_F, EF-C_W, EF-C_I, EF-C_L, and EF-C_V, show that their aggregation concentrations are approximately or less than 100 μM, and the average size of aggregates is around 1 μm (not shown). EF-C_I shows significant light scattering at the lowest concentration; thus featuring the highest aggregation propensity. The other four variants, EF-C_Y, EF-C_A, EF-C_G, and EF-C_P, demonstrated little aggregation tendency (**Figure 3.2 (a)**) with the average size of aggregates less than 20 nm (not shown). As expected, sequences with aromatic and aliphatic chains show aggregation tendency except for EF-C_Y. Since DLS is dependent on aggregate shape and morphology, and typically assumes spherical objects for accurate size determination, complementary characterization techniques such as electron microscopy were used to investigate the aggregation and self-assembly behavior of the peptides.[31,44]

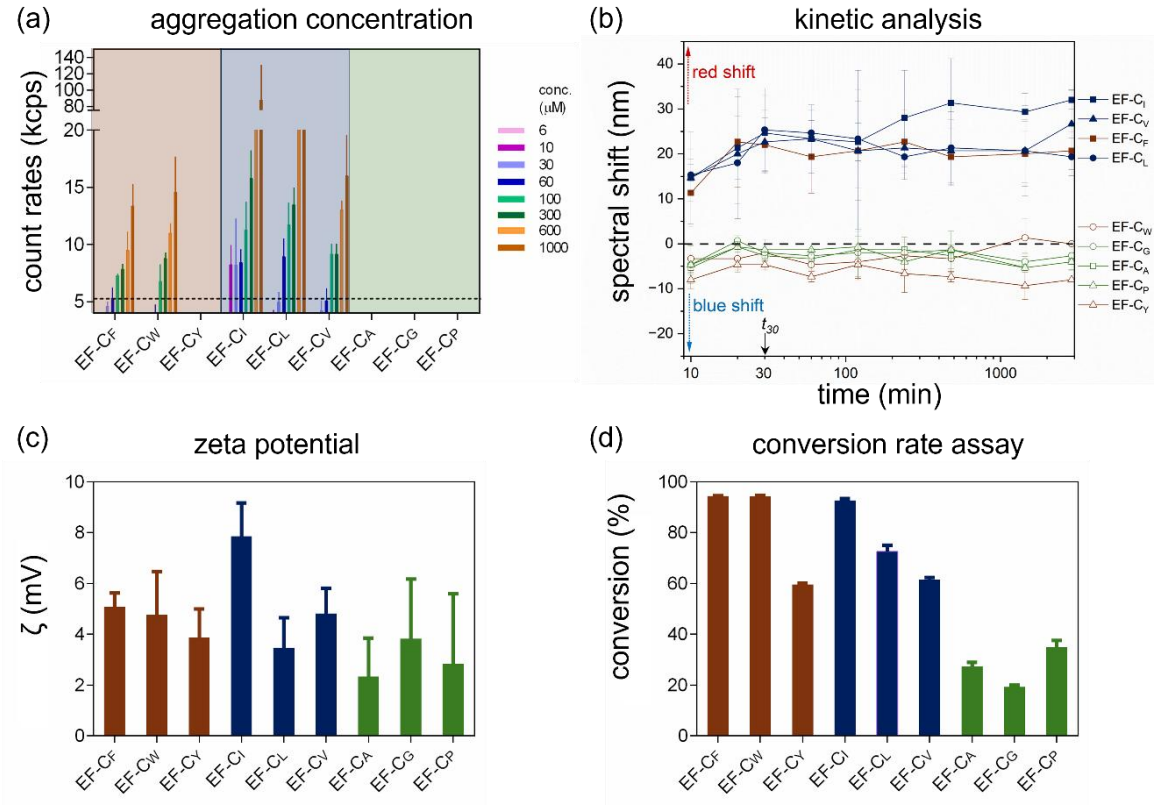

Figure 3. 2. Kinetics and aggregation analysis of EF-C variants. (a) Aggregation concentrations of EF-C variants were determined by DLS, and count rates below the dotted line (5 kcps) were considered as "no aggregation". (b) Characterization of amyloid-like

aggregation kinetics probed by Congo red assay at 1 mM peptide concentration for 2 days (measurement time points: 0 min, 10 min, 20 min, 30 min, 1 hr, 2 hr, 4 hr, 8 hr, 24 hr, and 48 hr). t_{30} stands for the time at which assembly behavior reaches equilibrium. (c) Zeta potential measurements of EF-C variants (100 μM) after 24 hr incubation displayed that the peptides have an overall positive charge. (d) Conversion rates for 1 mM peptide based on a fluorescamine assay showed that EF-C_F, EF-C_W, and EF-C_I had high conversation rates (x > 90%), EF-C_L, EF-C_V, and EF-C_Y had moderate conversation rates (60 % < x < 80 %), and the remaining three variants (EF-C_A, EF-C_G, and EF-C_P,) had low conversation rates (x < 35%). Presented are mean values and standard deviations of the mean.

A Congo red assay was applied to study the kinetics of amyloid-like fibrillar assembly based on the specific orientations of β-sheet-rich structures.[45] Congo red molecules intercalate into the β-sheet structure via hydrogen bonding (H-bonding) and π-π stacking.[46,47] The interaction between Congo red molecules with β-sheet-rich structures leads to a spectral red shift in the Congo red absorption from 498 nm.[45,46] In **Figure 3. 2 (b)**, four EF-C variants, including EF-C_F, EF-C_I, EF-C_L, and EF-C_V, show spectral red shifts at maximum absorption from 498 nm to around 520 nm. For the four variants, the spectral red shift of approximately 20 nm was reached after 30 min and remained relatively stable up to 48 hr, indicating that the assembly process took less than 30 min and remained in equilibrium. There were almost no spectral shifts for EF-C_A, EF-C_G, and EF-C_P, as expected since no aggregation was observed in DLS. Surprisingly, two sequences with aromatic side chains did not demonstrate spectral red shift. EF-C_W did not show any noticeable spectral shift and EF-C_Y displayed a 10 nm blue shift, which may be attributed to the hydroxyl groups of the sequence, inducing strong H-bonding, resulting in different electrostatic interactions between the negatively charged sulfonate groups of Congo red molecules and positively charged peptide backbones,[47] while all peptides studied have an overall negative surface charge as shown in **Figure 3. 2 (c)**.

A conversion rate assay using fluorescamine as a probe was used to estimate the amount of peptide monomers converted into assembled structures.[31] Fluorescamine is highly reactive to primary amines and the excess amount of fluorescamine is degraded within several seconds.[48] EF-C_F, EF-C_W, and EF-C_I demonstrate high conversion rates,

while EF-C_Y, EF-C_L, and EF-C_V perform rather moderately, and the monomers of EF-C_A, EF-C_G, and EF-C_P barely converted into any aggregates or self-assembled structures, following the same trends observed in the DLS study. A summary of the conversion rate assay based on fluorescamine is shown in **Figure 3. 2 (d)** and included in **Table 3. 1**. This approach has an intrinsic limitation in that it recorded the fluorescence intensity of the samples while it is unknown if amine groups are accessible in small aggregates or self-assembled structures, leading to a potential underestimation of the fraction of aggregated molecules. In certain cases, proline and secondary amines are also reactive towards fluorescamine.[48] Thus, conversion rate assays using analytical HPLC were carried out and the results are provided in **Figure S3. 6**. For EF-C_F, EF-C_W, EF-C_I, EF-C_L, and EF-C_V, no peptide signal was observed after the samples were filtrated, suggesting that most of their monomers converted into aggregates or self-assembled structures. On the other hand, the liquid chromatograms of EF-C_Y, EF-C_A, EF-C_G, and EF-C_P were nearly identical before and after filtration, indicating low or no conversion. High conversion rates correlate with high aggregation tendencies, suggesting that DLS, the fluorescamine-based conversion assay, and the analytical HPLC-based conversion rate assay all provide similar trends for the tendency of monomers to aggregate or self-assemble.

In summary, the protocol for peptide self-assembly was established and validated. For the self-assembling sequences, namely EF-C_F, EF-C_W, EF-C_I, EF-C_L, and EF-C_V, 1 mM of peptide was sufficient for aggregation or self-assembly. Thus, 1 mM was selected to investigate the kinetics of each peptide, and the spectral red shift remained stable after 30 min, suggesting that 24 hr of peptide incubation is sufficient to induce peptide aggregation or self-assembly. After 24 hr of incubation, all peptides exhibited a positive surface charge in buffer solution. EF-C_F, EF-C_W, EF-C_I, EF-C_L, and EF-C_V showed high conversion rates. EF-C_A, EF-C_G, and EF-C_P displayed only a little sign of conversion. However, EF-C_Y required further analyses to confirm their aggregation tendency.

3.3.3. Morphology and Secondary Structure Analysis

With a robust protocol for the preparation of self-assembled peptide structures, we then studied the morphologies of all EF-C variants using TEM. The EF-C variants were

first categorized based on their side chains into three groups, (1) EF-C variants with rigid and aromatic side chains in the peptide backbones, which are EF-C_F, EF-C_W, and EF-C_Y, (2) EF-C variants, namely EF-C_I, EF-C_L, and EF-C_V, with flexible and aliphatic side groups in their peptide backbones, and (3) EF-C variants with weakly hydrophobic residues in the peptide backbones, which are EF-C_A, EF-C_G, and EF-C_P, respectively. The summary of morphologies of all EF-C variants based on TEM images is listed in **Table 3. 1**, and representative TEM images of the three groups are shown in **Figure 3. 3 (a, d, g)**. Additional TEM images of all variants are presented on a large scale (2 μm) in **Figure S3. 7**. In the group of peptides carrying aromatic side groups, we found that EF-C_F and EF-C_W display linear fibers and aggregates with short and dense fibrillar networks, shown in **Figure 3. 3 (a)** and **Figure S3. 7 (a, b)**. Surprisingly, EF-C_Y did not form any defined structure despite having aromatic side chains in the peptide backbones, displayed in **Figure S7 (c)**. In group 2, TEM images of sequences with flexible and aliphatic side chains all exhibit long and twisted nanofibers, demonstrated in **Figure 3. 3 (d)** and **Figure S3. 7 (d, e, f)**. In contrast, in the last group, we observed many random pieces or large aggregates in **Figure 3. 3 (g)** and **Figure S3. 7 (g, h, i)**. In our aggregation studies, EF-C_A, EF-C_G, and EF-C_P did not show significant aggregation tendencies or conversion rates, thus, structures observed were most likely the result of drying artifacts.[49] In **Figure S3. 8**, EF-C variants that formed defined structures were further investigated with more detail to confirm the morphological observations. EF-C_L fibrils are particularly twisted like twist rolls, shown in **Figure S3. 8 (d, i)**. We hypothesize that peptide backbones with flexible and aliphatic side groups formed longer and twisted nanofibers because they had less steric hindrance and less directional stacking than those with aromatic groups.

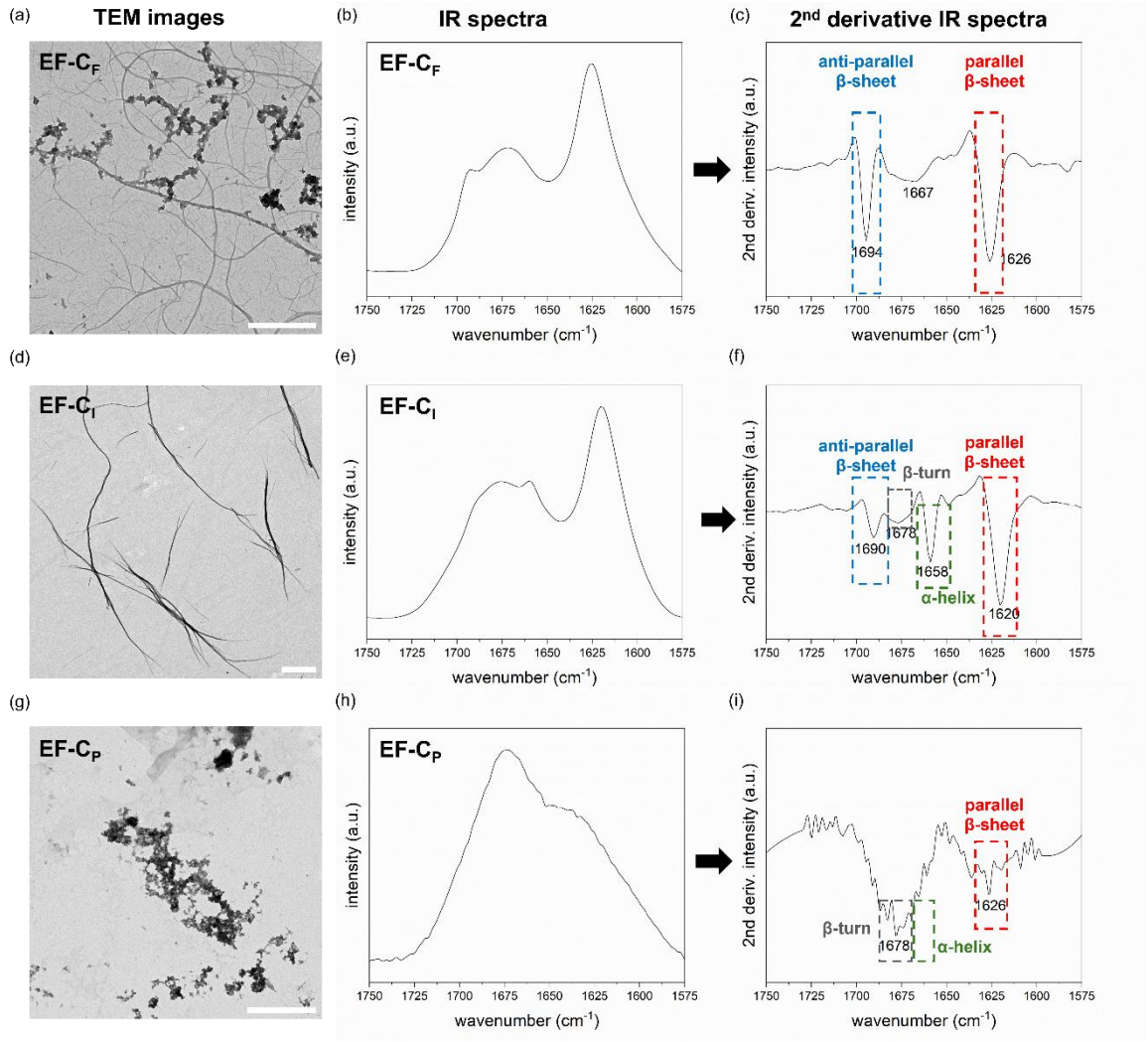

Figure 3. Overview of self-assembled morphologies of EF-C variants studied by TEM and IR. (a) The representative TEM image of EF-C$_F$ reveals linear nanofibers and a small portion of aggregates (scale bar = 1 μm). (b) IR absorption spectrum of EF-C$_F$. (c) There are two distinct sharp peaks at 1626 cm^{-1} and 1694 cm^{-1}, resulting from parallel and antiparallel β-sheets, as shown in the 2nd derivative IR absorption spectrum of EF-C$_F$. (d) The representative TEM image of EF-C$_L$ shows twisted nanofibers (scale bar = 1 μm). (e) IR absorption spectrum of EF-C$_I$. (f) In the 2nd derivative IR absorption spectrum of EF-C$_I$, there is one distinct sharp peak at 1620 cm^{-1} resulting from parallel β-sheets, one peak attributed to α-helix at 1658 cm^{-1}, one broad peak related to β-turn around 1678 cm^{-1}, and another peak associated with anti-parallel β-sheet at 1690 cm^{-1}. (g) The representative TEM image of EF-C$_P$ displays aggregates only (scale bar = 1 μm). (h) IR absorption spectrum of EF-C$_P$. (i) In the 2nd derivative IR absorption spectrum of EF-C$_P$, there is a broad band

between 1640 cm^{-1} to 1680 cm^{-1}, which can be assigned to β-turn, helical, and coil structures.

After analyzing the morphologies of the EF-C variants, we identified EF-C_F, EF-C_W, EF-C_I, EF-C_L, and EF-C_V as the structure-forming sequences, while the other four candidates are non-structure-forming sequences. The structural characteristics of the peptides were evaluated by IR (**Figure 3.3**, **Figure S3. 9**, **10**, **and 11**) and XRD (**Figure S3. 12**) to correlate the secondary structure and molecular packing distance with the assembled morphologies. The obtained IR absorption signals and molecular packing distances calculated from XRD are summarized in **Table 3. 1**. IR spectroscopy is suitable for determining structural characteristics of insoluble protein deposits, such as amorphous aggregates or amyloid fibrils.[50] The advantage of using this technique is its versatility because IR samples can be measured in solution, solid, and thin films.[50,51] To obtain structural information from IR spectroscopy, analysis primarily relies on the absorbance of the amide I band arising mostly from the peptide C=O stretching mode, i.e. roughly from 1600 to 1700 cm^{-1} of the amide functional groups.[50] Second derivative IR spectra are used for broad and unresolved bands to analyze secondary structural motifs, such as α-helices, and parallel and antiparallel β-sheets.[50,52] Correlations between common secondary structures and the frequencies of corresponding amide I bonds are consolidated from previous reports[50–52] and summarized in **Table 3. 2**. As displayed in **Figure 3. 3 (b, c, e, f)** and **Figure S3. 9 and S3. 10 (a, b, d, e, f)**, the IR spectra of the structure-forming sequences, including EF-C_F, EF-C_W, EF-C_I, EF-C_L, and EF-C_V, show a sharp peak around 1625 cm^{-1} and another peak near 1690 cm^{-1}, suggesting that β-sheets are the main secondary structure. In **Figure 3. 3 (h, i)** and **Figure S3. 9 and S3. 10 (c, g, h, i)**, the non-fiber-forming variants, which are EF-C_A, EF-C_G, EF-C_P, and EF-C_Y, have a dominant broad band from 1640 cm^{-1} to 1680 cm^{-1} in the IR spectra, indicating that random coils and α-helices are the primary secondary structures. The deconvoluted IR spectra were calculated using the peaks found in the 2nd derivative, provided in **Figure S3. 11,** and the β-sheet content was calculated accordingly. The data suggest that all structure-forming variants contained more than 68% of β-sheets in the overall secondary structure.

Table 3. 2 Correlations between common secondary structures and the frequency (wave number) of corresponding amide I bonds.

secondary structure	amide I frequencies (cm^{-1})
parallel β-sheets	1615-1643
random (unordered)	1640-1650
α-helix	1650-1670
β-turn	1665-1685
antiparallel β-sheets	1675-1700

Signals from 1600 cm^{-1} to 1620 cm^{-1} can be attributed to different side chains.[50–52]

XRD was used as it offers molecular packing information of amyloid-like peptides. Typical β-sheet patterns in protein chains assemble via H-bonding orthogonal to the fibril direction with a distance of 4.7 Å.[29,53] The intermolecular packing of assembled EF-C variants was detected by XRD, and the packing distances (d) were calculated from the XRD pattern. The XRD diffractograms are provided in **Figure S3. 12**, and the calculated intermolecular distances are listed in **Table 3. 1**. Non-structure-forming sequences did not show any sharp signal that can be simply calculated from the Bragg reflection in the diffractograms (not provided). All fiber-forming peptides had interstrand distances ranging from 4.6 to 5.8 Å featuring amyloid-like peptides, and the differences in the packing distance between β-sheets depended on the size of the side chain groups.[53] Additional packing distances (5.2~6 Å) derived from the Bragg reflections in the XRD pattern might be attributed to intersheet distances.[53] The diffraction data of EF-C_w at 8.34 Å might be explained by the β-sheets involving H-bonding of the glutamine side chains and the secondary amine group on tryptophan side chains,[54] which may be the reason why EF-C_W was not reactive towards Congo red binding assay.

3.3.4. Molecular Modelling and Simulation of EF-C Peptide Fibrils

To obtain a structural model of oligomers and protofibrils of the EF-C peptide variants, we applied AlphaFold 3 (AF3).[55] AF3 enables the prediction of biomolecular interactions of complex structures using diffusion-based machine learning. Here, we used this approach to model the structures of oligomers consisting of four peptide monomers and protofibrils

consisting of twenty peptide monomers (**Figure 3. 4 (a, c, e)** and **Figure S3. 13-14**). Relevant models of the oligomers and protofibrils were selected and used as starting structures for molecular dynamics (MD) simulations. MD simulations sample the dynamics and stability of predicted assemblies in a solvated environment. While instable oligomer and protofibril models disassembled during MD simulation, stable peptide assemblies only presented minor structural rearrangements to optimize their geometry, shown in **Figure 3. 4 (b, d, f)** and **Figure S3. 15** (water molecules not shown for better illustration). Findings on oligomer and protofibril stability were thus indirectly related to the propensity of peptides to form peptide fibrils.[34] Sequences with aliphatic side chains in their backbones (EF-C_I, EF-C_L, and EF-C_V) displayed slightly more twisted nanofibers compared to those with aromatic side chains in their backbones (EF-C_F and EF-C_W), which confirmed our observation in TEM images. To quantify the observed protofibril stability, we analyzed the solvent accessible surface area (SASA), a measure for the surface area of the peptides that was accessible by water. When peptide monomers assembled tightly, this area was small, while free peptide monomers had a large SASA. The non-structural forming ones, EF-C_A, EF-C_G, and EF-C_P, had larger SASAs compared to other EF-C variants, displayed in **Figure 3. 4 (g)** and **Figure S3. 16**. As an additional parameter, the secondary structure content of the peptides was determined (**Figure 3. 4 (h)** and **Figure S3. 17**). It can be clearly seen that EF-C_F, EF-C_W, EF-C_I, EF-C_L, and EF-C_V present the highest β-sheet content (i.e. β-strands and β-bridges in the DSSP classification), while EF-C_A, EF-C_G, and EF-C_P do not have significant β-sheet content.

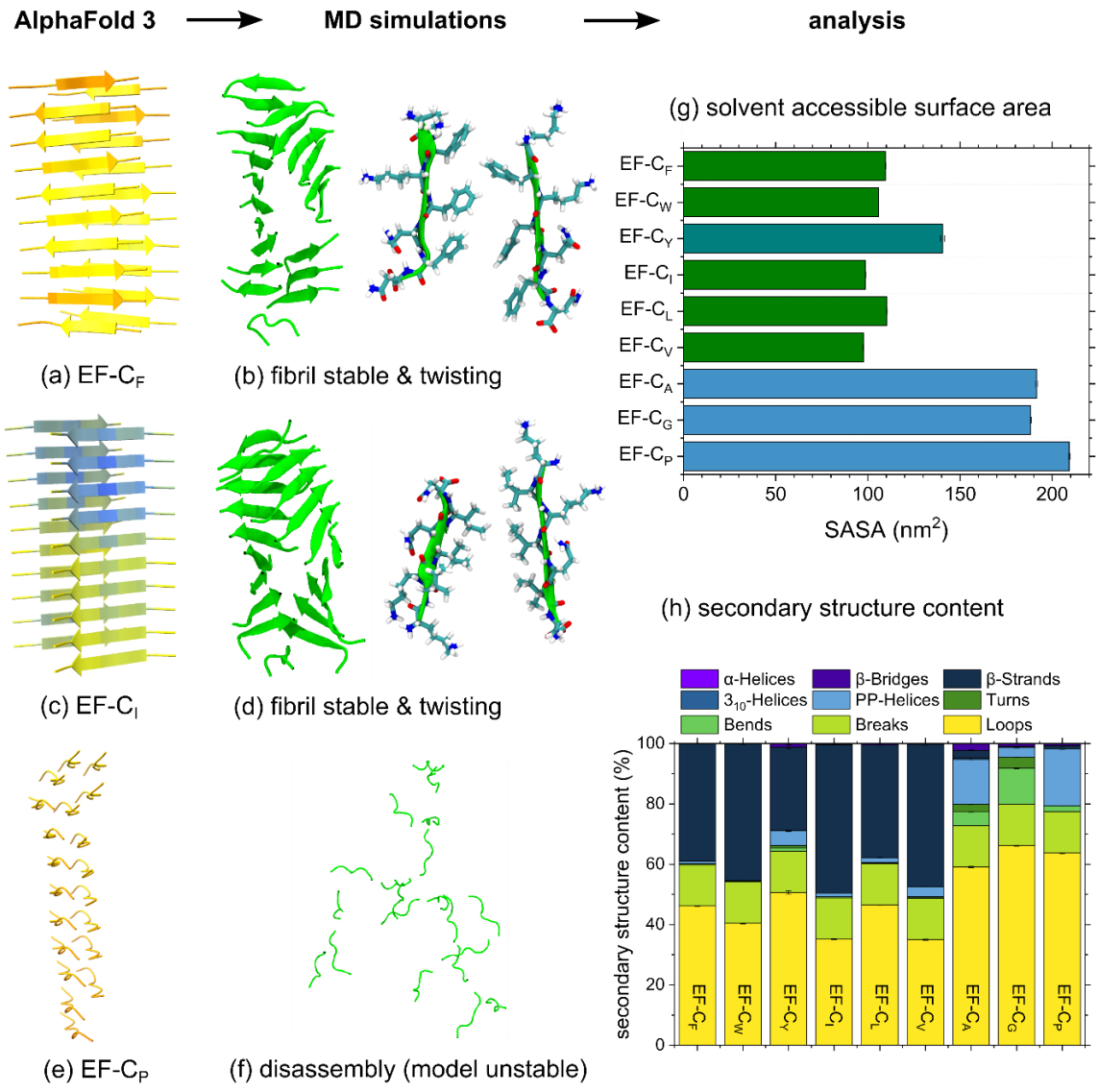

Figure 3. 4 Computational AlphaFold 3 (AF3) modelling and molecular dynamics (MD) simulations of EF-C self-assembly. Structures of early EF-C protofibrils (20mers) were modeled using AF3 (a, c, e) and then studied in all-atom MD simulations. Stable models optimized their geometry by twisting while unstable models collapsed (b, e, f). Analysis of solvent accessible surface area (SASA) (g) and secondary structure content (h) confirmed that stable peptide fibrils, EF-C$_F$, EF-C$_W$, EF-C$_I$, EF-C$_L$, and EF-C$_V$, had relatively high β-sheet content, while EF-C$_A$, EF-C$_G$, and EF-C$_P$ did not have β-sheet content. EF-C$_Y$ showed intermediate β-sheet content. Secondary structures are assigned according to the DSSP classification.[56]

Additional MD simulations were performed with six randomly placed peptide monomers for the fibril-forming sequences. These simulations presented clustering of peptides in all cases (**Figure S3. 18-20**) while anti-parallel and parallel β-sheet dimers and trimers were observed. EF-C_W also formed short-lived β-sheet structures, but these were not dominant within the simulation time. A focused structure of the dimer formed during self-assembly of EF-C_Y is shown in **Figure S3. 21**. Originally, EF-C_Y was presumed to behave and assemble similarly to those EF-C variants with aromatic side chains; however, it showed lower conversion rates and did not present defined structures in TEM images. With the simulation result, we propose that π-π interactions were the driving force to assemble EF-C_Y monomers in proximity but H-bonding between water molecules and lysine cationic amine groups and tyrosine hydroxyl groups became the predominant interaction, leading to the collapse of the assembly. The tyrosine hydroxyl groups of the hydrophobic side chains weakened the hydrophobic core of possible assemblies. In summary, our computational results not only correlated very well with our experimental findings but also provided insights into molecular interactions, which explain the stability of each EF-C variant. Thus, such a computational approach is suitable for screening or even predicting sequences with high propensities to form fibrils.

3.3.5. Correlation of EF-C Fibril Assembly with SH-SY5Y Activities

After biophysical and computational characterization of the self-assembly of the EF-C variants, we investigated correlations between peptide structure and the characteristics of the interaction with neural cells. As reported previously, sequences of alternating hydrophobic and positively charged amino acids preserve the positive surface charges for cell adhesion.[18] Based on our results, systematically switching the hydrophobic core of the peptide backbones did not significantly influence the surface charge while strongly affecting structural parameters. Building upon this, changes in bioactivity, such as proliferation and neurite outgrowth, of SH-SY5Y should be attributed to structural variations. SH-SY5Y cells are a secondary human neuroblastoma cell line that is widely used as a model for analysis of neuronal functions. SH-SY5Y cells were cultivated for 24 hr before adding 50 μM of all EF-C variants (diluted from PBS to culture medium). After incubation with EF-C variants for 24 hr, cell viability was measured using the CellTiter-

Glo assay, which is based on a luminescent signal proportional to the amount of adenosine triphosphate (ATP) present. The doubling time of SH-SY5Y is approximately 27 hr;[57] therefore, the results in **Figure 3. 5 (a)** suggest that non-structure-forming sequences were well tolerated by the cells, but also did not provide a significant benefit over the control. On the other hand, the fiber forming sequences, EF-C_F, EF-C_W, EF-C_I, EF-C_L, and EF-C_V induced higher ATP content in SH-SY5Y, indicating higher cell division and metabolic activity.

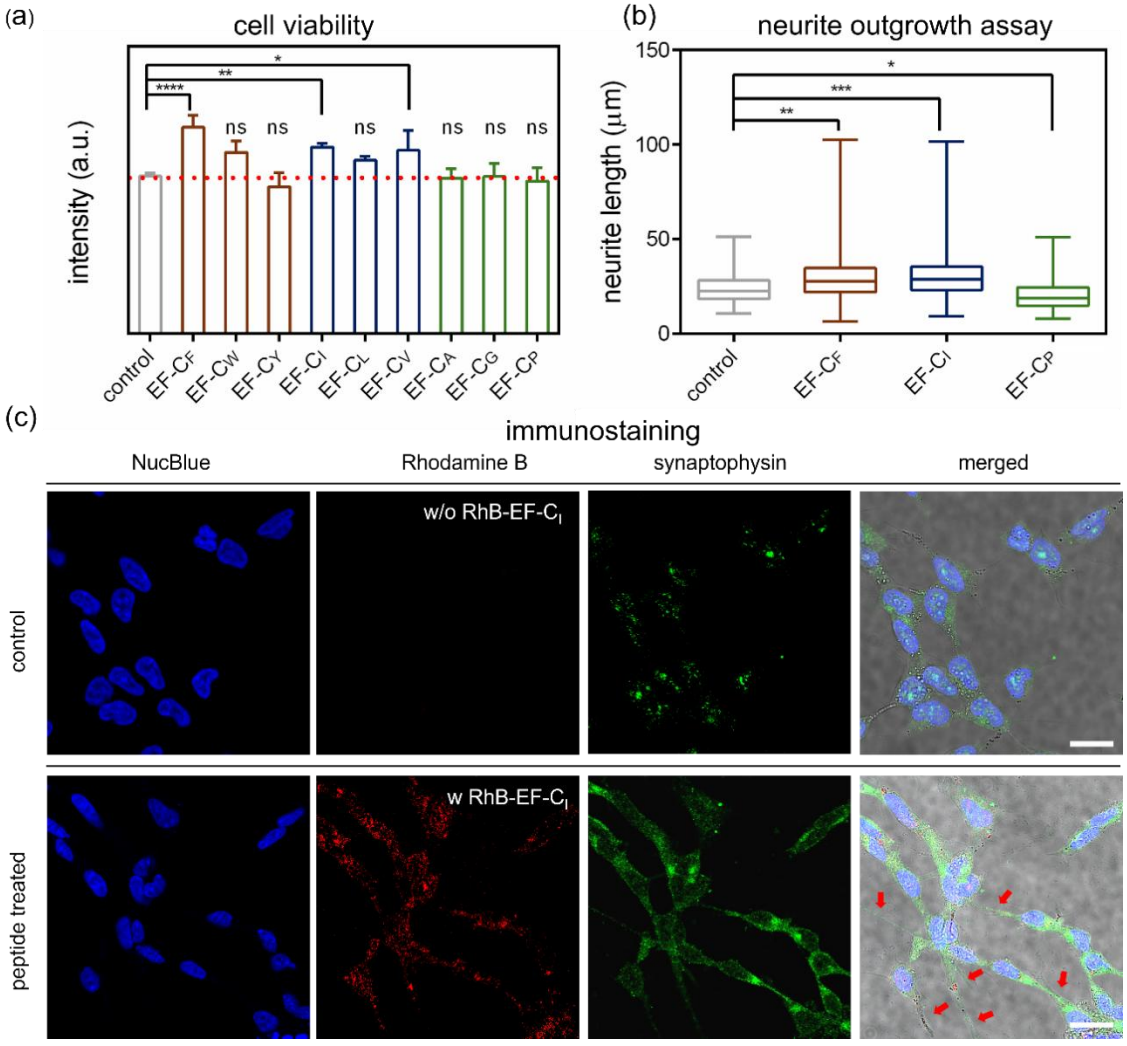

Figure 3. 5 Correlations between EF-C variants and SH-SY5Y cells parameters. (a) The graph represents cell proliferation of SH-SY5Y cells after treatment with EF-C variants for 24 hr. The structure-forming sequences, which are EF-C_F, EF-C_W, EF-C_I, EF-C_L, and EF-C_V, facilitate the proliferation of SH-SY5Y cells, while the other sequences

perform similarly to the solvent control group (*p ≤ 0.05; **p ≤ 0.01; ****p ≤ 0.0001, ns = not significant, N=2, n=6, One-way ANOVA test, Dunnett post hoc test in comparison to the solvent control). (b) One sequence out of each group (aliphatic, non-hydrophobic, and aromatic) was selected to test its ability to stimulate the differentiation of SH-SY5Y. EF-C_F (average neurite length = 29.7 μm and SD = 11.5) and EF-C_I (average neurite length = 30.8 μm and SD = 11.6) slightly promoted neurite outgrowth of SH-SY5Y cells compared to the control group (average neurite length = 24.3 μm and SD = 8.1) and EF-C_P (average neurite length = 20.4 μm and SD = 7.5), in all cases without the presence of any growth factor (*p ≤ 0.05; **p ≤ 0.01; ***p ≤ 0.001, N=2, n=20, One-way ANOVA test, Dunnett post hoc test in comparison to the solvent control). (c) The upper panel demonstrates the solvent control group with immunostained SH-SY5Y. The lower panel shows the interaction of fluorophore-labeled EF-C_I with immunostained SH-SY5Y. The blue channel represents the nucleus (NucBlue), the red channel is the RhB-EF-C_I, the green channel is SH-SY5Y stained with synaptophysin-directed antibody, and the last one is the merged image with red arrows pointing at neurites (scale bar = 20 μm). The brightness and contrast of the fluorescent images of the red and green channels were slightly adjusted for better visualization, and the raw images are provided in **Figure S3. 22**.

In general, the differentiation of SH-SY5Y cells requires phorbol esters, retinoic acid, or growth factors, such as nerve growth factor and brain derived neurotrophic factor.[57–59] A neurite outgrowth assay was performed according to previous work.[60] Three EF-C variants, EF-C_F, EF-C_I, and EF-C_P, of each representing group were chosen to test their potency to induce neural differentiation of SH-SY5Y cells, without adding growth factors. The differentiated SH-SY5Y cells are elongated and distributed randomly on a substrate, while the undifferentiated ones have an unpolarized shape and tend to grow in clusters and on top of one another.[57] Different morphologies of SH-SY5Y cells were seen after incubation with the three variants for 7 d, shown in **Figure S3. 23**. Cell morphologies of the control group (N=2, n=20, average neurite number per image = 5.1 and standard deviation (SD)= 2.0; average neurite length = 24.3 μm and SD = 8.1) and EF-C_P (N=2, n=20, average neurite number per image = 9.4 and SD = 3.6; average neurite length = 20.4 μm and SD = 7.5) were less polarized and fewer neurites were observed. Contrarily, SH-SY5Y cells became more polarized and connected with longer neurites after being treated

with EF-C_F (N=2, n=20, average neurite number per image = 13.8 and SD = 4.1; average neurite length = 29.7 μm and SD = 11.5) and EF-C_I (N=2, n=20, average neurite number per image = 10.4 and SD = 2.6; average neurite length = 30.8 μm and SD = 11.6) , displayed in **Figure 3. 5 (b)**. Indeed, there was no drastic neurite outgrowth observed when cells were treated with structure-forming EF-C variants, such as EF-C_F and EF-C_I. However, only basal medium was used to culture the cells without neurotrophic molecules or growth factors. Therefore, we infer that the structure-forming EF-C variants cannot only boost proliferation but also induce some degree of differentiation of SH-SY5Y cells.

Following the neurite outgrowth assay, immunochemistry was applied to verify the differentiation of SH-SY5Y cells. Synaptophysin is a major protein of the neurotransmitter vesicle membrane, which occurs in presynaptic endings of the central and peripheral nervous systems.[61] In a differentiated state, SH-SY5Y cells express mature neuronal markers such as synaptophysin.[57] On top of the immunostaining of one neuronal marker, we attempted to visualize the interaction of EF-C variants labeled with a RhB fluorophore with neural cells. In the upper panel of **Figure 3. 5 (c)**, untreated medium (DMSO only) served as control group. The nuclei were stained with Hoechst 33342. As expected, no RhB signal was observed, and only moderate expression of synaptophysin was captured based on fluorescent signals of Alexa 488 dye and the morphology of SH-SY5Y was less polarized. Applying the same imaging parameters, co-assembled EF-C_I and RhB-EF-C_I (v/v= 9:1) fibril assemblies showed slight red fluorescent signals in the lower panel of **Figure 3. 5 (c)**. The expression of synaptophysin based on Alexa 488 dye was stronger. In the merged image, SH-SY5Y cells become more polarized and neurite outgrowth, as marked with red arrows, of SH-SY5Y cells was observed, suggesting the neural regenerative potential of EF-C peptide.

In summary, β-sheet-rich SAPs mimic the natural extracellular matrix and provide mechanical support for cell adhesion.[62] Electrostatic forces between positive surface charges of EF-C variants and negatively charged cell membranes play an essential role in the interaction between materials and cells.[18] It is still controversial, though, because some earlier research indicated that amyloid-like structures and fragments are neurotoxic,[63–65] whilst other studies demonstrated that those fibers support neural regeneration.[66–69] Based on our findings, we suggest that SH-SY5Y viability and differentiation are facilitated by

the fiber structure of EF-C peptide variants. The mechanism for triggering SH-SY5Y differentiation remains to be explored. In agreement with previous work, our findings demonstrate that side chain interactions of peptide monomers lead to different supramolecular structures.[20–22,40] Our work, summarized in **Figure 3. 6**, used computational modelling and simulation to predict the assembly and stability of these supramolecular structures which we systematically studied in biophysical experiments and *in vitro* screening. The facilitation of computational modeling and simulation provides a strategy for materials design, which can support the engineering of bioactive assemblies *in silico*. We envision that the combination of computational approaches with biophysical characterization and biological readouts can accelerate the discovery of bioactive materials.

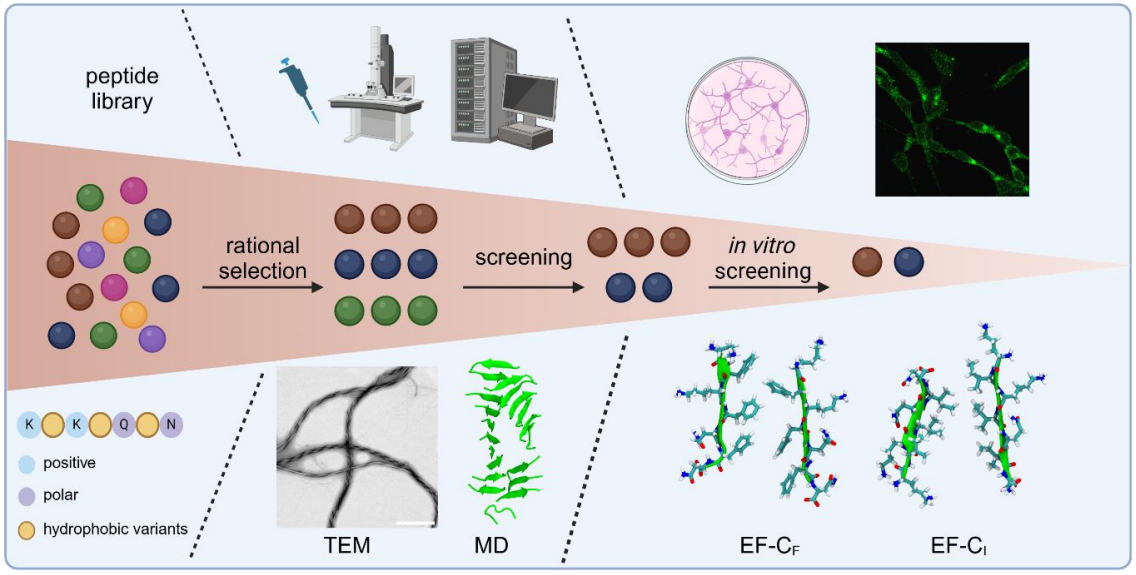

Figure 6. Workflow of peptide fibril materials design. Material structure-property relationships were discovered using biophysical approaches, computational modelling and simulation, and *in vitro* screening (image generated using Biorender).

3.4.Conclusions

We designed a peptide library of EF-C SAPs of varying hydrophobic core with the goal to identify peptide fibrils with enhanced neural regeneration capacity. To achieve this, we used a systematic approach of peptide sequence variation, and each variant was characterized by biophysical imaging and spectroscopic methods. This enabled us to identify fibril-forming sequences and their morphologies. We complemented this with

computational modelling and simulation to obtain molecular level insight into the self-assembly behavior. Our experimental and computational approaches correlated very well and we thus propose that AlphaFold 3 modelling and simulations can accelerate the discovery of functional SAPs for neural regeneration. The bioactivity of each peptide variant was tested in human neuroblastoma cells, and the results suggested that the fibril material structures played a significant role in modulating cell behavior. Our study shows that the development of new peptide sequences for neural regeneration can be accelerated by combining systematic characterization of SAPs with computational modelling and simulation.

3.5.Experimental Procedures

Materials. Fluorenylmethyloxycarbonyl (Fmoc) protected amino acids and ethyl cyano(hydroxyimino) acetate (Oxyma Pure®) were purchased from Novabiochem (Merck KGaA, Darmstadt, Germany). 6-(Fmoc-amino) hexanoic acid was obtained from Alfa Aesar (Thermo Fisher Scientific, Waltham, MA, USA). Fmoc-Asn (Trt) Wang Resin was acquired from Merck KGaA (Darmstadt, Germany). Congo Red, α-cyano-4-hydroxycinnamic acid (CHCA), *N,N′*-diisopropylcarbodiimide (DIC), *N,N*-diisopropylethylamine (DIPEA), dimethyl sulfoxide (DMSO), dimethyl sulfoxide-d_6 (DMSO-d_6), rhodamine B (RhB) triisopropylsilane (TIPS), were bought from Sigma-Aldrich (Burlington, MA, USA). *N,N*-dimethylformamide (DMF, peptide grade), 4-dimethylaminopyridine (DMAP), dichloromethane (DCM), fluorescamine, and 2% uranyl acetate solution were purchased from Thermo Fisher Scientific (Waltham, MA, USA). 25% ammonia solution (NH_4OH), *N*-(3-dimethylaminopropyl)-N-ethyl carbodiimide hydrochloride salt (EDC-HCl), *N*-hydroxysuccinimide (NHS), piperidine (peptide grade), potassium chloride (KCl), silica gel, and trifluoroacetic acid (TFA) were obtained from Carl Roth GmbH + Co. KG (Karlsruhe, Germany). Diethyl ether and acetonitrile (ACN, HPLC grade) were acquired from Honeywell (Charlotte, NC, USA). All chemicals were used upon arrival without further purification. Ultrapure water was obtained by a Millipore purification system (MilliQ, Merck KGaA, Darmstadt, Germany).

Solid State Peptide Synthesis (SPPS). All peptides were synthesized in an automated microwave peptide synthesizer (Liberty Blue™, CEM Corporation, Matthews, NC, USA) from C- to N-terminus by Fmoc-SPPS method using Fmoc-Asn (Trt) Wang Resins with a size of 100-200 mesh. DMF was used as the main washing solvent, and the deprotection solvent consisted of 20% piperidine in DMF. The activator and activator base were namely 0.5 M of DIC and 1.0 M of Oxyma in DMF. The amount of materials and reagents was prepared following the suggestion by Liberty Blue™ software calculation. In brief, the resins were swollen with DMF for 30 min prior to synthesis. The procedure started with Fmoc removal, and the resins were immersed in the deprotection solvent and heated to 75 °C (155 W) for 15 s and 90 °C (30 W) for 50 s, followed by washing with DMF twice. Subsequently, amino acids were coupled from 0.2 M solutions of the respective amino acid

in DMF with the facilitated by an activator and an activator base. The reaction was heated to 75 °C (170 W) for 15 s and 90 °C (30 W) for 110 s, followed by flushing with DMF. Deprotection solvent was added to remove the Fmoc motif after the final coupling. Afterwards, the resin beads were first flushed by DCM and immersed in a cleavage cocktail (95% TFA, 2.5% MilliQ water, 2.5% TIPS) for 2 hr, followed by precipitation in cold diethyl ether and centrifugation to obtain the final precipitate. The amino acids of the peptide sequences are listed in **Table 3. 1**.

Synthesis of *N*-Hydroxysuccinimide Modified Rhodamine B (RhB-NHS). The synthesis of RhB-NHS was conducted based on a previous report.[70] In brief, RhB (1.0 mmol), NHS (1.1 mmol), EDC-HCl (1.1 mmol), and DMAP (0.2 mmol) were dissolved in DCM (5 mL) in a reaction flask wrapped with aluminium foil. The resulting reaction mixture was stirred at room temperature for 4 hr. The compound was purified via silica gel chromatography and was assessed by MALDI-ToF MS on a rapifleX MALDI-ToF/ToF (Bruker, Billerica, MA; USA) and NMR spectroscopy on a Bruker Avance 400 MHz (Bruker, Billerica, MA, USA).

Synthesis of RhB Labeled EF-C Variants. RhB labeled peptides were manually synthesized on resin with a stoichiometry of 1: 2: 4 (peptide: RhB-NHS: DIPEA) in DMF in a peptide reactor (Carl Roth GmbH + Co. KG, Karlsruhe, Germany) wrapped with aluminium foil for 4 hr. Afterwards, resin beads were first rinsed with DCM and immersed in the same cleavage cocktail described previously for 2 hr, followed by precipitation in cold diethyl ether and centrifugation to the final precipitate. A spacer, aminohexanoic acid, was introduced to link EF-C_I and RhB-NHS so as to diminish chemical influence on the peptide backbone.[71]

Purification and Characterization of EF-C Variants. The peptide precipitate was dissolved in a mixture of MilliQ H_2O and ACN and purified by preparative RP-HPLC (Shimadzu, Kyoto, Japan) via a C18 column (Phenomenex Gemini, 5 μm, NX-C18, 110 Å, 150 × 30 mm, Torrance, CA, USA) with a flow rate of 25 mL/min. The solvent gradient of

solvent mixture of ACN/MilliQ with 0.1% TFA or 0.1% NH_4OH began from 0% to 100 % ACN. Fractions of samples were collected based on the retention time monitored with an ultraviolet (UV) absorption detector at 214 nm. The purified samples were lyophilized and stored at -20 °C prior to use.

Samples were identified by MALDI-ToF MS via dried droplet method. Samples were mixed with a saturated solution (MilliQ H_2O/ACN = 1:1) of the matrix CHCA. MALDI-ToF mass spectra were recorded on a rapifleX MALDI-ToF/ToF (Bruker, Billerica, MA, USA).

The purity of the samples was confirmed by analytical RP-HPLC (Shimadzu, Kyoto, Japan), equipped with a C18 column (ZORRBAX Eclipse XDB-C18, 5 μm, 70 Å, 9.4 × 250 mm, Agilent, Santa Clara, CA, USA) with a flow rate of 4 mL/min. A gradient of solvent mixture of ACN/MilliQ with 0.1% TFA or 0.1% NH_4OH began from 5% to 80 % ACN. The samples were monitored at 214 nm UV absorption.

To distinguish between leucine (EF-C_L) and isoleucine (EF-C_I) containing variants, these two variants were dissolved in DMSO-d_6 with a concentration of 3 mg/mL. NMR spectra were recorded on a Bruker Avance 700 MHz (Bruker, Billerica, MA, USA) at room temperature.

Preparation and Characterization of EF-C Self-Assembly

EF-C Self-Assembly. Each peptide powder was dissolved in DMSO (10 mM stock solution) and further diluted into DPBS (phosphate buffered saline without calcium chloride and magnesium chloride, Thermo Fisher Scientific, Waltham, MA, USA) to obtain the incubation concentration of 1 mM at room temperature for 24 hr, unless otherwise stated.

DLS. Aggregation concentrations of self-assembling EF-C variants were evaluated by DLS at room temperature on a Zetasizer Nano ZS (Malvern Instruments, Malvern, UK) based on published procedures.[31] Peptide solutions were diluted from the 10 mM DMSO peptide stock solution into DPBS (1 mM, 600 μM, 300 μM, 100 μM, 60 μM, 30 μM, 10 μM, 6 μM) for 24 hr incubation before measurement. Each measurement was performed in triplicate with 10 measurements per scan. The aggregation concentrations were plotted as

count rates against peptide concentrations with Origin 8.5 (OriginLab, Northampton, MA, USA). It is worth noting that when the derived count rate was below 2 kilo counts per scan (kcps), the instrument usually displays “The sample is too dilute for measurement”. To minimize the bias, we defined no aggregation from the peptides when the derived count rate was lower than 5 kcps.

Congo Red Assay. Congo red assay was employed to study the formation kinetics of amyloid fibers based on a previous report.[58] Congo red molecules align parallel to the fiber axis, which has a β-sheet structure, and induce a red shift in the absorption maximum (498 nm). Therefore, the spectral shift was calculated only based on the absorption maximum of Congo red. The procedure is briefly described as follows: 2 µl of 500 µM Congo red stock solution in DPBS was diluted in 43 µl PBS. 5 µl of 10 mM peptide stock solution was added to obtain a final peptide concentration of 1 mM. The control group consisted of 5 µl DMSO, 2 µl of 500 µM Congo red and 43 µl PBS. 15 µl of each mixture was transferred into a transparent 384-well plate (transparent UV Star, Greiner Bio-One, Kremsmünster, Austria), and the plate was sealed with a transparent seal (Viewseal Sealer, Greiner Bio-One, Kremsmünster, Austria) to prevent evaporation. Absorbance shifts were recorded between 400 and 600 nm at room temperature by a microplate reader (Spark®, Tecan, Männedorf, Switzerland). Analysis was performed in triplicate with 10 time points (0 min, 10 min, 20 min, 30 min, 1 hr, 2 hr, 4 hr, 8 hr, 24 hr, 48 hr), and the spectra were plotted with Origin 2024 (OriginLab, Northampton, MA, USA).

Fluorescence Based Conversion Rate (CR) Assay. The amount of peptide monomers assembled into nanostructures was assessed by a CR assay based on a previous report.[31] In short, 200 µL of 1 mM peptide solution was incubated for 24 hr and 100 µL of peptide solution was centrifuged in a Vivaspin® 500 centrifugal concentrator (3 kDa, Sartorius, Göttingen, Germany) to separate fibers and peptide monomers with a rate at 12,000 g for 60 min at 4 °C. Both filtrated and non-filtrated solutions were lyophilized and dissolved in 30 µL of DMSO. 9 µL of the amine-reactive dye fluorescamine (10 mg/mL in DMSO) was added to the filtrated and non-filtrated ones, followed by incubation in a 384-well plate (black UV Star®, GreinerBio-One, Kremsmünster, Austria) at room temperature for 20 min.

Fluorescence was recorded on a microplate reader (Spark®, Tecan, Männedorf, Switzerland) with excitation at λ= 365 nm and emission at λ= 470 nm (bandwidth = 10 nm and multiple readings per well, 3 × 3). The conversion rate is calculated using equation (1). Each measurement was performed in triplicate and plotted with Prism (GraphPad Software, San Diego, CA, USA).

$$CR = \left[1 - \left(\frac{filtrated\ fluorescence\ intensity}{nonfiltrated\ fluorescence\ intensity}\right)\right]\% \quad (1)$$

Analytical HPLC Based CR Assay. Control groups were peptide powders dissolved in DMSO and MilliQ water at a concentration of 50 μM, and experimental groups were peptide solutions after self-assembly (as described in 'EF-C Self-Assembly.') further diluted in MilliQ water to reach the same concentration, followed by filtration through a 0.2 μm pore size filter. Analytical HPLC with the same conditions described in the previous section were used to check whether the peptide could be detected at 214 nm UV absorption.

Zeta potential (ζ). Zeta-potential measurements were conducted using a Zetasizer Nano ZS (Malvern Instruments, Malvern, UK) to determine the surface charge of aggregated peptides following a previous report.[31] Peptide solutions (60 μL) were diluted in 600 μL of 1 mM KCl solution in 1 mL disposable capillary cells (DTS1060, Zetasizer Nano series, Malvern Instruments, Malvern, UK). Each measurement was performed in triplicate and plotted with Prism (GraphPad Software, San Diego, CA, USA).

TEM. To prepare samples for TEM measurement, 5 μL of peptide solution was deposited on copper grids coated with carbon and formvar layer (300 mesh, Plano GmbH, Wetzlar, Germany) for 10 min. The grids were stained with 2% uranyl acetate solution for 3 min, washed three times and dried with filter paper. Measurements were performed on a Jeol 1400 electron microscope (Tokyo, Japan) with 120 kV acceleration voltage to observe the morphology of self-assembling EF-C variants. Images were processed with Image J.[72]

Attenuated Total Reflectance FT-IR (ATR-FTIR) Spectroscopy. Each peptide solution (200 μL) was lyophilized into powder before measurement. All spectra were acquired with a resolution of 4 cm^{-1} and 64 scans on a Bruker Tensor27 spectrometer (Bruker, Billerica,

MA, USA) with a diamond crystal as ATR element (PIKE MiracleTM FTIR, Madison, WI, USA). The data were plotted with Origin 8.5 (OriginLab, Northampton, MA, USA) and the second derivative of the spectra was calculated using a Savitzky-Golay filter. The β-sheet content was calculated from equation (2) based on the deconvolution area corresponding to the secondary structure and the amide I frequencies (cm^{-1}) listed in **Table 2**.

$$\beta\text{-sheet}\ (\%) = \frac{\beta\text{−sheet area}}{\text{all secondary structure area}} \qquad (2)$$

Powder X-ray Diffraction (XRD). Each peptide solution (300 µL) was lyophilized before measurement. The powders were placed on a zero reflection Si substrate (Crystal Substrates, Traverse City, MI, USA**)** and XRD measurements were performed in θ/θ geometry on a Rigaku SmartLab diffractometer, using a Cu K-α anode (λ = 1.5406 Å) and HyPix-3000 detector. The scanning angle started from 5˚ to 25˚ with a rate of 0.2˚ per min. The data were plotted using Origin 8.5 (OriginLab, Northampton, MA, USA) and molecular packing distances were calculated in the Match!3 (Crystal Impact, Bonn, Germany) software based on equation (3).

$$\lambda = 2d\ sin\ \theta \qquad (3)$$

Modelling of Oligomer and Protofibril Structures Using AlphaFold 3. To obtain a structural model of oligomers and protofibrils of the EF-C peptide variants, we applied AlphaFold 3 (AF3).[55] The AF3 server (https://alphafoldserver.com) provided structural models of the five most likely structures, along with confidentiality scores. Relevant models of the oligomers (4mers) and protofibrils (20mers) were selected and used as starting structures for molecular dynamics (MD) simulations. By default, the top structural model was chosen. When all structural models had similar confidentiality scores, the model that aligned with the other variants has been chosen. In most cases, AF3 predicted 2x2 or 1x4 and 2x10 β-sheets. The AF3 results are subject to the AlphaFold Server Output Terms of Use found at https://alphafoldserver.com/output-terms. AF3 visualizations were performed with UCSF ChimeraX version 1.8, developed by the Resource for Biocomputing, Visualization, and Informatics at the University of California, San Francisco, with support from National Institutes of Health R01-GM129325 and the Office

of Cyber Infrastructure and Computational Biology, National Institute of Allergy and Infectious Diseases.[73] AF3 has been used to predict the structures of peptide oligomers (4mers) and protofibrils (20mers) of nine variants.

Molecular Dynamics (MD) Simulations. Predicted structural models for oligomers and protofibrils from AF3 were used as starting structures for MD simulation. The structures were placed in a cubic box with box lengths of at least 5 nm (4mer, oligomer) or 7 nm (20mer, protofibril), while the minimum distance between solute and box was at least 1 nm. The peptide assemblies were solvated with explicit water using the TIP3P water model[74] and sodium chloride (140 mM) was added as physiological salt and to neutralize the systems. Each system was initially energy minimized using a steepest-descent algorithm. This was followed by equilibration steps with position restrained peptides (k = 1000 kJ mol^{-1} nm^{-2}), first in a NVT ensemble for 100 ps and then in a NPT ensemble for another 100 ps. Each simulation was performed in triplicate with random starting velocities following a Boltzmann distribution at 295 K. All simulations were performed for 200 ns each, while the protofibril systems which showed relatively stable structures after 200 ns were simulated for another 300 ns (total of 500 ns) to confirm structural stability of the AF3 models. The overview of simulations is included in **Table 3. 3**.

Table 3. 3 Overview of MD Simulations with Simulation Times and No. of Replicates.

Peptide Variant	Oligomer Stability (4mer)	Protofibril Stability (20mer)	Oligomer Formation (6 monomers)
EF-C_I	3 x 200 ns	3 x 500 ns	3 x 500 ns
EF-C_A	3 x 200 ns	3 x 500 ns	/
EF-C_G	3 x 200 ns	3 x 200 ns	/
EF-C_V	3 x 200 ns	3 x 500 ns	3 x 500 ns
EF-C_P	3 x 200 ns	3 x 200 ns	/
EF-C_F	3 x 200 ns	3 x 500 ns	3 x 500 ns
EF-C_Y	3 x 200 ns	3 x 500 ns	3 x 500 ns
EF-C_L	3 x 200 ns	3 x 500 ns	3 x 500 ns
EF-C_W	3 x 200 ns	3 x 500 ns	3 x 500 ns

In the above studies, initial fibril structures were based on predictions from AF3. These simulations provided useful insight in the stability of oligomer and protofibril structures. To learn more about oligomer self-assembly, systems with six randomly placed peptide monomers in a cubic box (box length 4 nm) were studied for 500 ns, except for EF-C_A, EF-C_G, and EF-C_P, as they all disassembled in the stability simulations and did not present characteristic fibril formation in the experiments. The monomer peptide structures were extracted from the 20mer protofibril AF3 models. As described above, these systems were also solvated, ions added, energy minimized, and equilibrated before three independent replicates were run.

GROMACS version 2021.7 was used for all MD simulations[75–82] with a time step of 2 fs and the all-atom additive CHARMM36m force field to describe peptides, solvent and ions.[83,84] Periodic boundary conditions were applied. The Verlet cutoff scheme was used for neighbor search. A single cutoff of 1.2 nm was set to calculate electrostatic and van der Waals interactions. A force switch was applied to smoothly switch the van der Waals forces to zero between 1.0 nm and 1.2 nm. Long-range electrostatic interactions beyond the cutoff were described using the Particle-Mesh Ewald (PME) method.[85] All bonds with H-atoms in the peptides were constrained to their equilibrium values using the LINCS algorithm;[86] water molecules were constrained using the SETTLE algorithm.[87] The center of mass translational velocity of the system was removed. The temperatures of peptides, and water and ions, were independently coupled to an external bath at 295 K using the v-rescale thermostat with a relaxation time of 0.1 ps.[88] Isotropic pressure coupling to maintain a pressure of 1 bar was achieved using the Berendsen barostat during equilibration[89] and the Parrinello-Rahman barostat during production MD (relaxation time 2 ps, compressibility of 0.000045 bar^{-1}).[90]

Analysis of MD simulations was achieved using GROMACS tools. The final 10 ns of each simulation trajectory was used for further analysis. To determine the most representative structures of all replicates for each peptide variant, cluster analysis (gmx cluster, gromos method, RMSD cutoff 0.8 nm)[91] was performed and the central structure of the largest cluster was visualized using VMD 1.9.4.[92] Solvent accessible surface areas (SASAs) were calculated using a solvent probe radius of 0.14 nm (gmx sasa).[93,94] The secondary structure content of the EF-C peptide variants was analyzed using the DSSP tool

(Define Secondary Structure of Proteins, gmx dssp in GROMACS version 2024.4) for the last 10 ns of simulation time of all replicates.[56,95]

Cell Viability of Human Neuroblastoma Cells (SH-SY5Y). SH-SY5Y cells (ATCC-CRL-2266 ™) were cultivated at 37 °C, 95% humidity, and 5% CO_2 in Dulbecco's Modified Eagle Medium (DMEM)/ Ham's F-12 Nutrient Mixture (F-12) (Thermo Fisher Scientific, Waltham, MA, USA) with additional 10% fetal bovine serum (FBS) (Thermo Fisher Scientific, Waltham, MA, USA) and 1% penicillin-streptomycin (PS) (Sigma-Aldrich, Burlington, MA, USA) to study cell viability proliferation after treatment with different EF-C variants, and a control group (DMSO only). SH-SY5Y cells were seeded at a density of 10,000 cells/well in a white half area 96-well plate (Greiner Bio-One, Kremsmünster, Austria) and incubated at 37 °C for 24 hr. Peptide solutions were further diluted to 50 μM in culture medium and cells incubated for 24 hr with respective peptide (50 μL medium per well). Cell proliferation measurements were conducted using CellTiter-Glo® Luminescence Cell Viability Assay according to the manufacturer's protocol (Promega, Madison, WI, USA). Reagent (50 μL) was added to each well and the well plate was gently shaken for 10 min in dark at room temperature before measurement.

Neurite Outgrowth Assay. Each well in an 8-well plate (glass bottom, ibidi, Gräfelfing, Germany) was first coated with a thin layer of poly-D-lysine hydrobromide for 1 hr (concentration: 0.1 mg/mL, MW= 70000−150000; Sigma-Aldrich, Burlington, MA, USA), rinsed with DPBS and left dry before use. SH-SY5Y cells were seeded at a density of 80,000 cells/well in the 8 well plate. After 24 hr incubation, cells were incubated with solvent (DMSO only) or 50 μM of peptides, namely EF-C_F, EF-C_I, and EF-C_P, in culture medium. The medium containing peptide solutions was refreshed every two days for 7 d. To enhance the contrast for the contour of neurites under the fluorescent microscope, cells were rinsed with PBS, followed by staining the nuclei by Hoechst 33342 dye (NucBlue, Thermo Fisher Scientific, Waltham, MA, USA) and cell membrane according to the manufacturer's protocol (CellMask™, Deep Red Plasma Membrane Stains, Invitrogen, Thermo Fisher Scientific, Waltham, MA, USA). Afterwards, cells were rinsed with PBS and fixed with 4 % (v/v) PFA (Sigma-Aldrich, Burlington, MA, USA) for 15 min before

imaging under a BZ-X800 microscope (Keyence, Osaka, Germany) utilizing a Plan Fluorite 40X LD PH objective lens. The neurite outgrowth assay was measured based on images taken at 10 random spots from two individual experiments (N=2, n=20), and the quantification of the neurite length was conducted on Image J and Neuron J following previous reports[96–98]. The statistical study was evaluated by One-way ANOVA test and was plotted with Prism (GraphPad Software, San Diego, CA, USA).

Visualization of the Interaction of SH-SY5Y Cells and EF-C SAPs. SH-SY5Y cells were seeded at the same density as described in the neurite outgrowth assay in an 8 well plate (glass bottom, ibidi, Gräfelfing, Germany). After 24 hr incubation, the cells were treated with 50 μM of a peptide solution (10% of RhB labeled EF-C_I and 90 % of unlabeled one) for another 24 hr. After rinsing with PBS, cell nuclei were stained with Hoechst 33342 dye according to the manufacturer's protocol (Thermo Fisher Scientific, Waltham, MA, USA). For immunostaining, cells were rinsed with PBS, fixed with 4 % (v/v) paraformaldehyde (PFA) (Sigma-Aldrich, Burlington, MA, USA) for 15 min, permeabilized with 0.5% (v/v) Triton X-100 (Merck KGaA, Darmstadt, Germany) for 5 min, and blocked with 4 % bovine serum albumin (BSA, Roche, Basel, Switzerland) in PBS for 5 min. The primary antibody synaptophysin (SYN, rabbit anti-SYN, Proteintech, Rosemont, IL, USA) was diluted in PBS (1:200) and added to the samples at 4 C° for 24 hr. After rinsing with PBS, secondary antibody labeled with Alexa 488 (donkey anti-rabbit IgG Alexa Fluor™ Plus 488, Invitrogen, Thermo Fisher Scientific, Waltham, MA, USA) in PBS (1:500) was added to samples at room temperature for 4 hr before imaging.

Visualization of the cell-material interaction was conducted by using a confocal laser scanning microscope, Stellaris 8 FALCON (Leica, Wetzlar, Germany). A 405 nm excitation diode laser was implemented to monitor the nuclei staining with excitation (Ex) at 405 nm and emission (Em) at 425 nm. The immunostaining images were recorded under an Argon diode laser with Ex at 496 nm and Em at 532 nm. The fluorophore labeled EF-C_I was observed with Ex at 546 nm and Em at 700 nm.

3.6.Acknowledgements

The authors would like to acknowledge the financial support from the Deutsche Forschungsgemeinschaft (project number 441734479) and the scientific support from the Biocore, NMR, and Mass Spectrometry facilities at the Max Planck Institute for Polymer Research. T.J. acknowledges financial support from the Alexander von Humboldt Foundation through a Feodor-Lynen Return Fellowship. Computations were performed on the HPC system Raven at the Max Planck Computing and Data Facility.

Table of Content

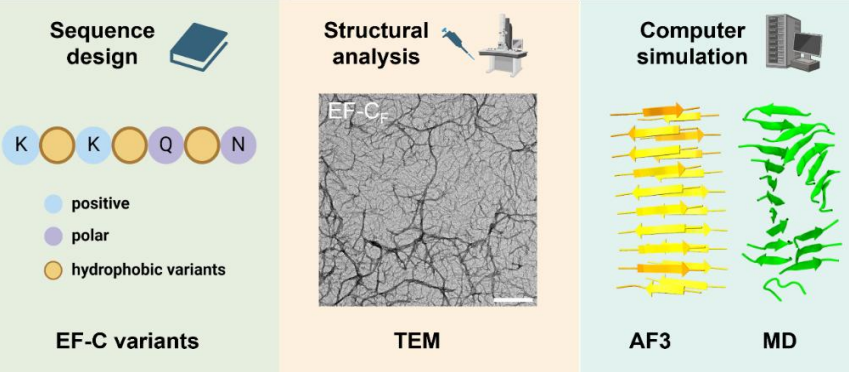

This study reports the design of peptide fibrils with enhanced neural regeneration by systematically varying the hydrophobic core of EF-C-derived peptide variants. We identified those variants with phenylalanine or isoleucine side chains as having high aggregation propensities and performed *in vitro* studies with neuroblastoma cells. The combination of biophysical assays with computational modelling and simulation can accelerate the identification of relationships between the morphology of self-assembling peptides and neural activity.

3.7.References

(1) Tsai, Y.-L.; Song, J.; Shi, R.; Knöll, B.; Synatschke, C. V. A Roadmap of Peptide-Based Materials in Neural Regeneration. *Adv Healthc Mater* **2024**, 2402939.

(2) Abbas, W. A.; Ibrahim, M. E.; El-Naggar, M.; Abass, W. A.; Abdullah, I. H.; Awad, B. I.; Allam, N. K. Recent Advances in the Regenerative Approaches for Traumatic Spinal Cord Injury: Materials Perspective. *ACS Biomater Sci Eng* **2020**, *6* (12), 6490–6509.

(3) Maclean, F. L.; Wang, Y.; Walker, R.; Horne, M. K.; Williams, R. J.; Nisbet, D. R. Reducing Astrocytic Scarring after Traumatic Brain Injury with a Multifaceted Anti-Inflammatory Hydrogel System. *ACS Biomater Sci Eng* **2017**, *3* (10), 2542–2549.

(4) Shen, H.; Fan, C.; You, Z.; Xiao, Z.; Zhao, Y.; Dai, J. Advances in Biomaterial-Based Spinal Cord Injury Repair. *Adv Funct Mater* **2022**, *32* (13), 2110628.

(5) Ng, S. Y.; Lee, A. Y. W. Traumatic Brain Injuries: Pathophysiology and Potential Therapeutic Targets. *Front Cell Neurosci* **2019**, *13*.

(6) Shen, H.; Fan, C.; You, Z.; Xiao, Z.; Zhao, Y.; Dai, J. Advances in Biomaterial-Based Spinal Cord Injury Repair. *Adv Funct Mater* **2022**, *32* (13), 2110628.

(7) Aertker, B. M.; Bedi, S.; Cox, C. S. Strategies for CNS Repair Following TBI. *Exp Neurol* **2016**, *275*, 411–426.

(8) Hendricks, M. P.; Sato, K.; Palmer, L. C.; Stupp, S. I. Supramolecular Assembly of Peptide Amphiphiles. *Acc Chem Res* **2017**, *50* (10), 2440–2448.

(9) Smith, C. S.; Álvarez, Z.; Qiu, R.; Sasselli, I. R.; Clemons, T.; Ortega, J. A.; Vilela-Picos, M.; Wellman, H.; Kiskinis, E.; Stupp, S. I. Enhanced Neuron Growth and Electrical Activity by a Supramolecular Netrin-1 Mimetic Nanofiber. *ACS Nano* **2023**, *17* (20), 19887–19902.

(10) Álvarez, Z.; Kolberg-Edelbrock, A. N.; Sasselli, I. R.; Ortega, J. A.; Qiu, R.; Syrgiannis, Z.; Mirau, P. A.; Chen, F.; Chin, S. M.; Weigand, S.; Kiskinis, E.; Stupp, S. I. Bioactive Scaffolds with Enhanced Supramolecular Motion Promote Recovery from Spinal Cord Injury. *Science (1979)* **2021**, *374* (6569), 848–856.

(11) Álvarez, Z.; Ortega, J. A.; Sato, K.; Sasselli, I. R.; Kolberg-Edelbrock, A. N.; Qiu, R.; Marshall, K. A.; Nguyen, T. P.; Smith, C. S.; Quinlan, K. A.; Papakis, V.; Syrgiannis, Z.; Sather, N. A.; Musumeci, C.; Engel, E.; Stupp, S. I.; Kiskinis, E. Artificial Extracellular Matrix Scaffolds of Mobile Molecules Enhance Maturation of Human Stem Cell-Derived

Neurons. *Cell Stem Cell* **2023**, *30* (2), 219-238.e14.

(12) Motalleb, R.; Berns, E. J.; Patel, P.; Gold, J.; Stupp, S. I.; Kuhn, H. G. In Vivo Migration of Endogenous Brain Progenitor Cells Guided by an Injectable Peptide Amphiphile Biomaterial. *J Tissue Eng Regen Med* **2018**, *12* (4), e2123–e2133.

(13) Ma, X.; Agas, A.; Siddiqui, Z.; Kim, K.; Iglesias-Montoro, P.; Kalluru, J.; Kumar, V.; Haorah, J. Angiogenic Peptide Hydrogels for Treatment of Traumatic Brain Injury. *Bioact Mater* **2020**, *5* (1), 124–132.

(14) Lopez-Silva, T. L.; Cristobal, C. D.; Edwin Lai, C. S.; Leyva-Aranda, V.; Lee, H. K.; Hartgerink, J. D. Self-Assembling Multidomain Peptide Hydrogels Accelerate Peripheral Nerve Regeneration after Crush Injury. *Biomaterials* **2021**, *265*, 120401.

(15) Wang, T.-W.; Chang, K.-C.; Chen, L.-H.; Liao, S.-Y.; Yeh, C.-W.; Chuang, Y.-J. Effects of an Injectable Functionalized Self-Assembling Nanopeptide Hydrogel on Angiogenesis and Neurogenesis for Regeneration of the Central Nervous System. *Nanoscale* **2017**, *9* (42), 16281–16292.

(16) Gelain, F.; Luo, Z.; Zhang, S. Self-Assembling Peptide EAK16 and RADA16 Nanofiber Scaffold Hydrogel. *Chem Rev* **2020**, *120* (24), 13434–13460.

(17) Yolamanova, M.; Meier, C.; Shaytan, A. K.; Vas, V.; Bertoncini, C. W.; Arnold, F.; Zirafi, O.; Usmani, S. M.; Müller, J. A.; Sauter, D.; Goffinet, C.; Palesch, D.; Walther, P.; Roan, N. R.; Geiger, H.; Lunov, O.; Simmet, T.; Bohne, J.; Schrezenmeier, H.; Schwarz, K.; Ständker, L.; Forssmann, W.-G.; Salvatella, X.; Khalatur, P. G.; Khokhlov, A. R.; Knowles, T. P. J.; Weil, T.; Kirchhoff, F.; Münch, J. Peptide Nanofibrils Boost Retroviral Gene Transfer and Provide a Rapid Means for Concentrating Viruses. *Nat Nanotechnol* **2013**, *8* (2), 130–136.

(18) Schilling, C.; Mack, T.; Lickfett, S.; Sieste, S.; Ruggeri, F. S.; Sneideris, T.; Dutta, A.; Bereau, T.; Naraghi, R.; Sinske, D.; Knowles, T. P. J.; Synatschke, C. V; Weil, T.; Knöll, B. Sequence-Optimized Peptide Nanofibers as Growth Stimulators for Regeneration of Peripheral Neurons. *Adv Funct Mater* **2019**, *29* (24), 1809112.

(19) Pitz, M. E.; Nukovic, A. M.; Elpers, M. A.; Alexander-Bryant, A. A. Factors Affecting Secondary and Supramolecular Structures of Self-Assembling Peptide Nanocarriers. *Macromol Biosci* **2022**, *22* (2), 2100347.

(20) Bowerman, C. J.; Liyanage, W.; Federation, A. J.; Nilsson, B. L. Tuning β-Sheet Peptide

Self-Assembly and Hydrogelation Behavior by Modification of Sequence Hydrophobicity and Aromaticity. *Biomacromolecules* **2011**, *12* (7), 2735–2745.

(21) Lee, N. R.; Bowerman, C. J.; Nilsson, B. L. Effects of Varied Sequence Pattern on the Self-Assembly of Amphipathic Peptides. *Biomacromolecules* **2013**, *14* (9), 3267–3277.

(22) Cao, M.; Lu, S.; Zhao, W.; Deng, L.; Wang, M.; Wang, J.; Zhou, P.; Wang, D.; Xu, H.; Lu, J. R. Peptide Self-Assembled Nanostructures with Distinct Morphologies and Properties Fabricated by Molecular Design. *ACS Appl Mater Interfaces* **2017**, *9* (45), 39174–39184.

(23) Yuan, S. C.; Lewis, J. A.; Sai, H.; Weigand, S. J.; Palmer, L. C.; Stupp, S. I. Peptide Sequence Determines Structural Sensitivity to Supramolecular Polymerization Pathways and Bioactivity. *J Am Chem Soc* **2022**, *144* (36), 16512–16523.

(24) Yakupova, E. I.; Bobyleva, L. G.; Vikhlyantsev, I. M.; Bobylev, A. G. Congo Red and Amyloids: History and Relationship. *Biosci Rep* **2019**, *39* (1), BSR20181415.

(25) Klunk, W. E.; Jacob, R. F.; Mason, R. P. [19] Quantifying Amyloid by Congo Red Spectral Shift Assay. In *Methods in Enzymology*; Academic Press, 1999; Vol. 309, pp 285–305.

(26) Byler, D. M.; Susi, H. Examination of the Secondary Structure of Proteins by Deconvolved FTIR Spectra. *Biopolymers* **1986**, *25* (3), 469–487.

(27) Yang, H.; Yang, S.; Kong, J.; Dong, A.; Yu, S. Obtaining Information about Protein Secondary Structures in Aqueous Solution Using Fourier Transform IR Spectroscopy. *Nat Protoc* **2015**, *10* (3), 382–396.

(28) Jackson, M.; Mantsch, H. H. The Use and Misuse of FTIR Spectroscopy in the Determination of Protein Structure. *Crit Rev Biochem Mol Biol* **1995**, *30* (2), 95–120.

(29) Serpell, L. C.; Fraser, P. E.; Sunde, M. [34] X-Ray Fiber Diffraction of Amyloid Fibrils. In *Methods in Enzymology*; Academic Press, 1999; Vol. 309, pp 526–536.

(30) Morris, K. L.; Serpell, L. C. X-Ray Fibre Diffraction Studies of Amyloid Fibrils. In *Amyloid Proteins: Methods and Protocols*; Sigurdsson, E. M., Calero, M., Gasset, M., Eds.; Humana Press: Totowa, NJ, 2012; pp 121–135.

(31) Kaygisiz, K.; Rauch-Wirth, L.; Dutta, A.; Yu, X.; Nagata, Y.; Bereau, T.; Münch, J.; Synatschke, C. V; Weil, T. Data-Mining Unveils Structure–Property–Activity Correlation of Viral Infectivity Enhancing Self-Assembling Peptides. *Nat Commun* **2023**, *14* (1), 5121.

(32) Cao, N.; Huang, K.; Xie, J.; Wang, H.; Shi, X. Self-Assembly of Peptides: The Acceleration by Molecular Dynamics Simulations and Machine Learning. *Nano Today* **2024**, *55*, 102160.

(33) Williams-Noonan, B. J.; Kamboukos, A.; Todorova, N.; Yarovsky, I. Self-Assembling Peptide Biomaterials: Insights from Spontaneous and Enhanced Sampling Molecular Dynamics Simulations. *Chemical Physics Reviews* **2023**, *4* (2), 021304.

(34) John, T.; Bandak, J.; Sarveson, N.; Hackl, C.; Risselada, H. J.; Prager, A.; Elsner, C.; Abel, B. Growth, Polymorphism, and Spatially Controlled Surface Immobilization of Biotinylated Variants of IAPP21–27 Fibrils. *Biomacromolecules* **2020**, *21* (2), 783–792.

(35) Wang, Y.; An, Y.; Shmidov, Y.; Bitton, R.; Deshmukh, S. A.; Matson, J. B. A Combined Experimental and Computational Approach Reveals How Aromatic Peptide Amphiphiles Self-Assemble to Form Ion-Conducting Nanohelices. *Mater Chem Front* **2020**, *4* (10), 3022–3031.

(36) Jumper, J.; Evans, R.; Pritzel, A.; Green, T.; Figurnov, M.; Ronneberger, O.; Tunyasuvunakool, K.; Bates, R.; Žídek, A.; Potapenko, A.; Bridgland, A.; Meyer, C.; Kohl, S. A. A.; Ballard, A. J.; Cowie, A.; Romera-Paredes, B.; Nikolov, S.; Jain, R.; Adler, J.; Back, T.; Petersen, S.; Reiman, D.; Clancy, E.; Zielinski, M.; Steinegger, M.; Pacholska, M.; Berghammer, T.; Bodenstein, S.; Silver, D.; Vinyals, O.; Senior, A. W.; Kavukcuoglu, K.; Kohli, P.; Hassabis, D. Highly Accurate Protein Structure Prediction with AlphaFold. *Nature* **2021**, *596* (7873), 583–589.

(37) John, T.; Rampioni, A.; Poger, D.; Mark, A. E. Molecular Insights into the Dynamics of Amyloid Fibril Growth: Elongation and Lateral Assembly of GNNQQNY Protofibrils. *ACS Chem Neurosci* **2024**, *15* (4), 716–723.

(38) Monera, O. D.; Sereda, T. J.; Zhou, N. E.; Kay, C. M.; Hodges, R. S. Relationship of Sidechain Hydrophobicity and α-Helical Propensity on the Stability of the Single-Stranded Amphipathic α-Helix. *Journal of Peptide Science* **1995**, *1* (5), 319–329.

(39) Pashuck, E. T.; Cui, H.; Stupp, S. I. Tuning Supramolecular Rigidity of Peptide Fibers through Molecular Structure. *J Am Chem Soc* **2010**, *132* (17), 6041–6046.

(40) Wang, K.; Keasling, J. D.; Muller, S. J. Effects of the Sequence and Size of Non-Polar Residues on Self-Assembly of Amphiphilic Peptides. *Int J Biol Macromol* **2005**, *36* (4), 232–240.

(41) De Leon Rodriguez, L. M.; Hemar, Y.; Cornish, J.; Brimble, M. A. Structure–Mechanical Property Correlations of Hydrogel Forming β-Sheet Peptides. *Chem Soc Rev* **2016**, *45* (17), 4797–4824.

(42) John, T.; Piantavigna, S.; Dealey, T. J. A.; Abel, B.; Risselada, H. J.; Martin, L. L. Lipid Oxidation Controls Peptide Self-Assembly near Membranes through a Surface Attraction Mechanism. *Chem Sci* **2023**, *14* (14), 3730–3741.

(43) Hayn, M.; John, T.; Bandak, J.; Rauch-Wirth, L.; Abel, B.; Münch, J. Hybrid Materials From Peptide Nanofibrils and Magnetic Beads to Concentrate and Isolate Virus Particles. *Adv Funct Mater* **2024**, *34* (27), 2316260.

(44) Stetefeld, J.; McKenna, S. A.; Patel, T. R. Dynamic Light Scattering: A Practical Guide and Applications in Biomedical Sciences. *Biophys Rev* **2016**, *8* (4), 409–427.

(45) Hamsici, S.; White, A. D.; Acar, H. Peptide Framework for Screening the Effects of Amino Acids on Assembly. *Sci Adv* **2024**, *8* (3), eabj0305.

(46) Yakupova, E. I.; Bobyleva, L. G.; Vikhlyantsev, I. M.; Bobylev, A. G. Congo Red and Amyloids: History and Relationship. *Biosci Rep* **2019**, *39* (1), BSR20181415.

(47) Kumar, V.; Patel, D.; Pal, H.; Kuperkar, K. A Comprehensive Insight on H-Type Aggregation in Congo Red-Surfactant Systems Revealed through Spectroscopic and Electrochemical Study Unified with a Simulation Framework. *Physical Chemistry Chemical Physics* **2019**, *21* (28), 15584–15594.

(48) Udenfriend, S.; Stein, S.; Böhlen, P.; Dairman, W.; Leimgruber, W.; Weigele, M. Fluorescamine: A Reagent for Assay of Amino Acids, Peptides, Proteins, and Primary Amines in the Picomole Range. *Science (1979)* **1972**, *178* (4063), 871–872.

(49) Korpanty, J.; Gnanasekaran, K.; Venkatramani, C.; Zang, N.; Gianneschi, N. C. Organic Solution-Phase Transmission Electron Microscopy of Copolymer Nanoassembly Morphology and Dynamics. *Cell Rep Phys Sci* **2022**, *3* (3).

(50) Seshadri, S.; Khurana, R.; Fink, A. L. [36] Fourier Transform Infrared Spectroscopy in Analysis of Protein Deposits. In *Methods in Enzymology*; Academic Press, 1999; Vol. 309, pp 559–576.

(51) Calero, M.; Gasset, M. Featuring Amyloids with Fourier Transform Infrared and Circular Dichroism Spectroscopies. In *Amyloid Proteins: Methods and Protocols*; Sigurdsson, E. M., Calero, M., Gasset, M., Eds.; Humana Press: Totowa, NJ, 2012; pp 53–68.

(52) Moran, A.; Mukamel, S. The Origin of Vibrational Mode Couplings in Various Secondary Structural Motifs of Polypeptides. *Proceedings of the National Academy of Sciences* **2004**, *101* (2), 506–510.

(53) Makin, O. S.; Serpell, L. C. Structures for Amyloid Fibrils. *FEBS J* **2005**, *272* (23), 5950–5961. https://doi.org/https://doi.org/10.1111/j.1742-4658.2005.05025.x.

(54) Watanabe, T.; Terada, K.; Takemura, S.; Masunaga, H.; Tsuchiya, K.; Lamprou, A.; Numata, K. Chemoenzymatic Polymerization of L-Serine Ethyl Ester in Aqueous Media without Side-Group Protection. *ACS Polymers Au* **2022**, *2* (3), 147–156.

(55) Abramson, J.; Adler, J.; Dunger, J.; Evans, R.; Green, T.; Pritzel, A.; Ronneberger, O.; Willmore, L.; Ballard, A. J.; Bambrick, J.; Bodenstein, S. W.; Evans, D. A.; Hung, C.-C.; O'Neill, M.; Reiman, D.; Tunyasuvunakool, K.; Wu, Z.; Žemgulytė, A.; Arvaniti, E.; Beattie, C.; Bertolli, O.; Bridgland, A.; Cherepanov, A.; Congreve, M.; Cowen-Rivers, A. I.; Cowie, A.; Figurnov, M.; Fuchs, F. B.; Gladman, H.; Jain, R.; Khan, Y. A.; Low, C. M. R.; Perlin, K.; Potapenko, A.; Savy, P.; Singh, S.; Stecula, A.; Thillaisundaram, A.; Tong, C.; Yakneen, S.; Zhong, E. D.; Zielinski, M.; Žídek, A.; Bapst, V.; Kohli, P.; Jaderberg, M.; Hassabis, D.; Jumper, J. M. Accurate Structure Prediction of Biomolecular Interactions with AlphaFold 3. *Nature* **2024**, *630* (8016), 493–500.

(56) Kabsch, W.; Sander, C. Dictionary of Protein Secondary Structure: Pattern Recognition of Hydrogen-Bonded and Geometrical Features. *Biopolymers* **1983**, *22* (12), 2577–2637.

(57) Kovalevich, J.; Langford, D. Considerations for the Use of SH-SY5Y Neuroblastoma Cells in Neurobiology. In *Neuronal Cell Culture: Methods and Protocols*; Amini, S., White, M. K., Eds.; Humana Press: Totowa, NJ, 2013; pp 9–21.

(58) Agholme, L.; Lindström, T.; Kågedal, K.; Marcusson, J.; Hallbeck, M. An In Vitro Model for Neuroscience: Differentiation of SH-SY5Y Cells into Cells with Morphological and Biochemical Characteristics of Mature Neurons. *Journal of Alzheimer's Disease* **2010**, *20*, 1069–1082.

(59) Bilginer Kartal, R.; Arslan Yildiz, A. Exploring Neuronal Differentiation Profiles in SH-SY5Y Cells through Magnetic Levitation Analysis. *ACS Omega* **2024**, *9* (13), 14955–14962.

(60) Mitchell, P. J.; Hanson, J. C.; Quets-Nguyen, A. T.; Bergeron, M.; Smith, R. C. A Quantitative Method for Analysis of in Vitro Neurite Outgrowth. *J Neurosci Methods* **2007**, *164* (2), 350–362.

(61) García-Mesa, Y.; García-Piqueras, J.; Cuendias, P.; Cobo, R.; Martín-Cruces, J.; Feito, J.; García-Suarez, O.; Biedma, B. M.; Vega, J. A. Synaptophysin Is a Selective Marker for

Axons in Human Cutaneous End Organ Complexes. *Annals of Anatomy - Anatomischer Anzeiger* **2022**, *243*, 151955.

(62) Levin, A.; Hakala, T. A.; Schnaider, L.; Bernardes, G. J. L.; Gazit, E.; Knowles, T. P. J. Biomimetic Peptide Self-Assembly for Functional Materials. *Nat Rev Chem* **2020**, *4* (11), 615–634.

(63) Mrdenovic, D.; Pieta, I. S.; Nowakowski, R.; Kutner, W.; Lipkowski, J.; Pieta, P. Amyloid β Interaction with Model Cell Membranes – What Are the Toxicity-Defining Properties of Amyloid β? *Int J Biol Macromol* **2022**, *200*, 520–531.

(64) Bystrenova, E.; Bednarikova, Z.; Barbalinardo, M.; Albonetti, C.; Valle, F.; Gazova, Z. Amyloid Fragments and Their Toxicity on Neural Cells. *Regen Biomater* **2019**, *6* (2), 121–127.

(65) Nguyen, H. L.; Linh, H. Q.; Krupa, P.; La Penna, G.; Li, M. S. Amyloid β Dodecamer Disrupts the Neuronal Membrane More Strongly than the Mature Fibril: Understanding the Role of Oligomers in Neurotoxicity. *J Phys Chem B* **2022**, *126* (20), 3659–3672.

(66) Sawaya, M. R.; Hughes, M. P.; Rodriguez, J. A.; Riek, R.; Eisenberg, D. S. The Expanding Amyloid Family: Structure, Stability, Function, and Pathogenesis. *Cell* **2021**, *184* (19), 4857–4873.

(67) Chen, G.; Xu, T.; Yan, Y.; Zhou, Y.; Jiang, Y.; Melcher, K.; Xu, H. E. Amyloid Beta: Structure, Biology and Structure-Based Therapeutic Development. *Acta Pharmacol Sin* **2017**, *38* (9), 1205–1235.

(68) Mathes, T. G.; Monirizad, M.; Ermis, M.; de Barros, N. R.; Rodriguez, M.; Kraatz, H.-B.; Jucaud, V.; Khademhosseini, A.; Falcone, N. Effects of Amyloid-β-Mimicking Peptide Hydrogel Matrix on Neuronal Progenitor Cell Phenotype. *Acta Biomater* **2024**, *183*, 89–100.

(69) Tycko, R. Amyloid Polymorphism: Structural Basis and Neurobiological Relevance. *Neuron* **2015**, *86* (3), 632–645. https://doi.org/10.1016/j.neuron.2015.03.017.

(70) Chen, X.; Wu, Q.; Henschke, L.; Weber, G.; Weil, T. An Efficient and Versatile Approach for the Preparation of a Rhodamine B Ester Bioprobe Library. *Dyes and Pigments* **2012**, *94* (2), 296–303.

(71) Rudat, B.; Birtalan, E.; Vollrath, S. B. L.; Fritz, D.; Kölmel, D. K.; Nieger, M.; Schepers, U.; Müllen, K.; Eisler, H.-J.; Lemmer, U.; Bräse, S. Photophysical Properties of

Fluorescently-Labeled Peptoids. *Eur J Med Chem* **2011**, *46* (9), 4457–4465.

(72) Schneider, C. A.; Rasband, W. S.; Eliceiri, K. W. NIH Image to ImageJ: 25 Years of Image Analysis. *Nat Methods* **2012**, *9* (7), 671–675.

(73) Meng, E. C.; Goddard, T. D.; Pettersen, E. F.; Couch, G. S.; Pearson, Z. J.; Morris, J. H.; Ferrin, T. E. UCSF ChimeraX: Tools for Structure Building and Analysis. *Protein Science* **2023**, *32* (11), e4792.

(74) Jorgensen, W. L.; Chandrasekhar, J.; Madura, J. D.; Impey, R. W.; Klein, M. L. Comparison of Simple Potential Functions for Simulating Liquid Water. *J Chem Phys* **1983**, *79* (2), 926–935.

(75) Van Der Spoel, D.; Lindahl, E.; Hess, B.; Groenhof, G.; Mark, A. E.; Berendsen, H. J. C. GROMACS: Fast, Flexible, and Free. *J Comput Chem* **2005**, *26* (16), 1701–1718.

(76) Lindahl; Abraham; Hess; der Spoel, van. GROMACS 2021.7 Source Code. Zenodo January 2023.

(77) Berendsen, H. J. C.; van der Spoel, D.; van Drunen, R. GROMACS: A Message-Passing Parallel Molecular Dynamics Implementation. *Comput Phys Commun* **1995**, *91* (1), 43–56.

(78) Lindahl, E.; Hess, B.; van der Spoel, D. GROMACS 3.0: A Package for Molecular Simulation and Trajectory Analysis. *Molecular modeling annual* **2001**, *7* (8), 306–317.

(79) Páll, S.; Abraham, M. J.; Kutzner, C.; Hess, B.; Lindahl, E. Tackling Exascale Software Challenges in Molecular Dynamics Simulations with GROMACS. In *Solving Software Challenges for Exascale*; Markidis, S., Laure, E., Eds.; Springer International Publishing: Cham, 2015; pp 3–27.

(80) Abraham, M. J.; Murtola, T.; Schulz, R.; Páll, S.; Smith, J. C.; Hess, B.; Lindahl, E. GROMACS: High Performance Molecular Simulations through Multi-Level Parallelism from Laptops to Supercomputers. *SoftwareX* **2015**, *1–2*, 19–25.

(81) Hess, B.; Kutzner, C.; van der Spoel, D.; Lindahl, E. GROMACS 4: Algorithms for Highly Efficient, Load-Balanced, and Scalable Molecular Simulation. *J Chem Theory Comput* **2008**, *4* (3), 435–447.

(82) Pronk, S.; Páll, S.; Schulz, R.; Larsson, P.; Bjelkmar, P.; Apostolov, R.; Shirts, M. R.; Smith, J. C.; Kasson, P. M.; van der Spoel, D.; Hess, B.; Lindahl, E. GROMACS 4.5: A High-Throughput and Highly Parallel Open Source Molecular Simulation Toolkit. *Bioinformatics* **2013**, *29* (7), 845–854.

(83) Huang, J.; Rauscher, S.; Nawrocki, G.; Ran, T.; Feig, M.; de Groot, B. L.; Grubmüller, H.; MacKerell, A. D. CHARMM36m: An Improved Force Field for Folded and Intrinsically Disordered Proteins. *Nat Methods* **2017**, *14* (1), 71–73.

(84) Huang, J.; MacKerell Jr, A. D. CHARMM36 All-Atom Additive Protein Force Field: Validation Based on Comparison to NMR Data. *J Comput Chem* **2013**, *34* (25), 2135–2145.

(85) Essmann, U.; Perera, L.; Berkowitz, M. L.; Darden, T.; Lee, H.; Pedersen, L. G. A Smooth Particle Mesh Ewald Method. *J Chem Phys* **1995**, *103* (19), 8577–8593.

(86) Hess, B.; Bekker, H.; Berendsen, H. J. C.; Fraaije, J. G. E. M. LINCS: A Linear Constraint Solver for Molecular Simulations. *J Comput Chem* **1997**, *18* (12), 1463–1472.

(87) Miyamoto, S.; Kollman, P. A. Settle: An Analytical Version of the SHAKE and RATTLE Algorithm for Rigid Water Models. *J Comput Chem* **1992**, *13* (8), 952–962.

(88) Bussi, G.; Donadio, D.; Parrinello, M. Canonical Sampling through Velocity Rescaling. *J Chem Phys* **2007**, *126* (1), 014101.

(89) Berendsen, H. J. C.; Postma, J. P. M.; van Gunsteren, W. F.; DiNola, A.; Haak, J. R. Molecular Dynamics with Coupling to an External Bath. *J Chem Phys* **1984**, *81* (8), 3684–3690.

(90) Parrinello, M.; Rahman, A. Polymorphic Transitions in Single Crystals: A New Molecular Dynamics Method. *J Appl Phys* **1981**, *52* (12), 7182–7190.

(91) Daura, X.; Gademann, K.; Jaun, B.; Seebach, D.; van Gunsteren, W. F.; Mark, A. E. Peptide Folding: When Simulation Meets Experiment. *Angewandte Chemie International Edition* **1999**, *38* (1–2), 236–240.

(92) Humphrey, W.; Dalke, A.; Schulten, K. VMD: Visual Molecular Dynamics. *J Mol Graph* **1996**, *14* (1), 33–38.

(93) Bondi, A. Van Der Waals Volumes and Radii. *J Phys Chem* **1964**, *68* (3), 441–451.

(94) Eisenhaber, F.; Lijnzaad, P.; Argos, P.; Sander, C.; Scharf, M. The Double Cubic Lattice Method: Efficient Approaches to Numerical Integration of Surface Area and Volume and to Dot Surface Contouring of Molecular Assemblies. *J Comput Chem* **1995**, *16* (3), 273–284.

(95) Gorelov, S.; Titov, A.; Tolicheva, O.; Konevega, A.; Shvetsov, A. DSSP in GROMACS: Tool for Defining Secondary Structures of Proteins in Trajectories. *J Chem Inf Model* **2024**, *64* (9), 3593–3598.

(96) Meijering, E.; Jacob, M.; Sarria, J.-C. F.; Steiner, P.; Hirling, H.; Unser, M. Design and Validation of a Tool for Neurite Tracing and Analysis in Fluorescence Microscopy Images. *Cytometry Part A* **2004**, *58A* (2), 167–176.

(97) Meijering, E. Neuron Tracing in Perspective. *Cytometry Part A* **2010**, *77A* (7), 693–704.

(98) Abramoff, M.; Magalhães, P.; Ram, S. J. Image Processing with ImageJ. *Biophotonics International* **2003**, *11*, 36–42.

3.8.Supporting Information

Design of the Hydrophobic Core of Self-Assembling EF-C Peptide Fibrils for Enhanced Neural Regeneration

Yu-Liang Tsai, Primiana Cavallo, Qi Lu, Christopher P. Ender, Julian Link, Katrin Amann-Winkel, Kristina Endres, Christopher V. Synatschke, and Torsten John**

Y.-L. Tsai, P. Cavallo, Q. Lu, C. P. Ender, J. Link, K. Amann-Winkel, K. Endres, C. V. Synatschke, T. John
Max Planck Institute for Polymer Research, Ackermannweg 10, 55128 Mainz, Germany
E-mail: synatschke@mpip-mainz.mpg.de

K. Amann-Winkel
Institute for Physics, Johannes Gutenberg University Mainz, Staudingerweg 7, 55128 Mainz, Germany

K. Endres
Department of Psychiatry and Psychotherapy, University Medical Center Mainz, Johannes Gutenberg University Mainz, 55131 Mainz, Germany

K. Endres
Faculty of Computer Sciences and Microsystems Technology, Kaiserslautern University of Applied Sciences, Amerikastr.1, 66482 Zweibrücken, Germany

T. John
School of Science, Constructor University, Campus Ring 1, 28759 Bremen, Germany
E-mail: tjohn@constructor.university

Table of Content

Supporting References

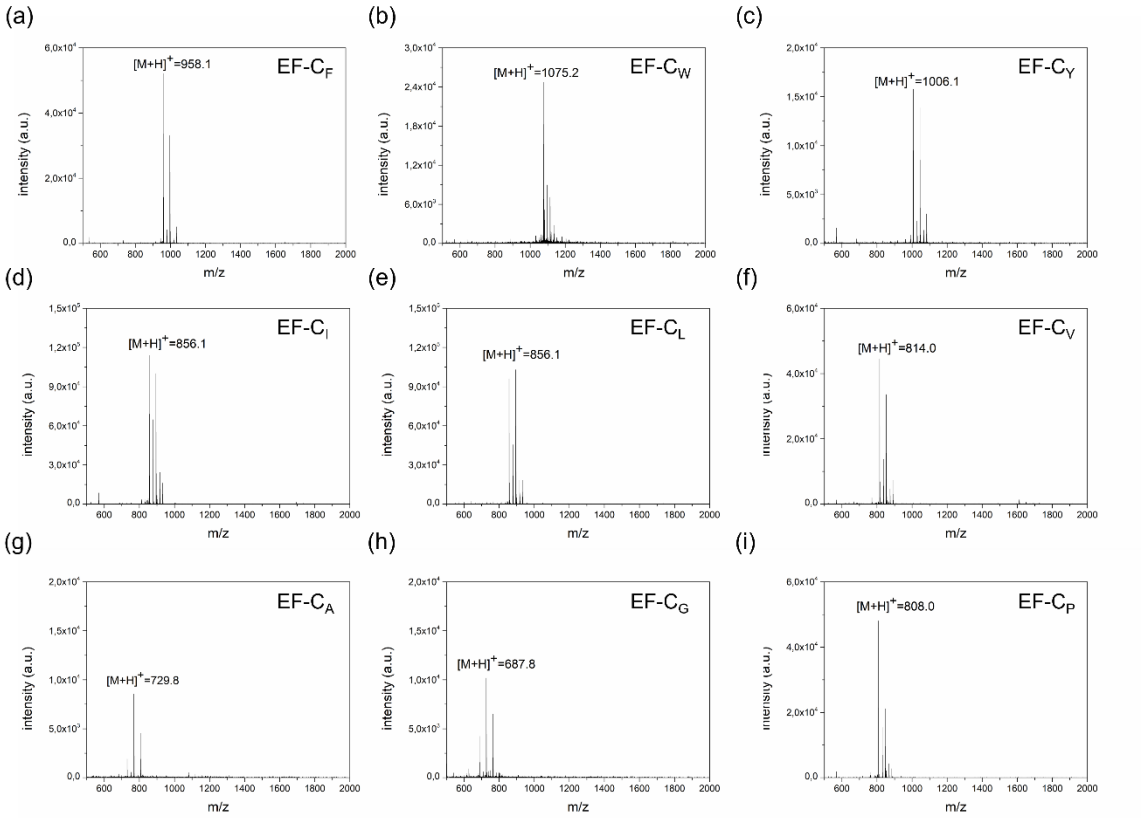

Figure S3. 1 Mass spectra of EF-C variants measured by MALDI-ToF MS. (a) $[M+H]^+ = 958.1$ was detected for EF-C_F (theoretical MW = 958.1). (b) $[M+H]^+ = 1075.2$ was detected for EF-C_W (theoretical MW = 1075.2). (c) $[M+H]^+ = 1006.1$ was detected for EF-C_Y (theoretical MW = 1006.1). (d) $[M+H]^+ = 856.1$ was detected for EF-C_I (theoretical MW= 856.1). (e) $[M+H]^+ = 856.1$ was detected for EF-C_L (theoretical MW = 856.1). (f) $[M+H]^+ = 814.0$ was detected for EF-C_V (theoretical MW = 814.0). (g) $[M+H]^+ = 729.8$ was detected for EF-C_A (theoretical MW = 729.8). (h) $[M+H]^+ = 687.7$ was detected for EF-C_G (theoretical MW = 687.8). (i) $[M+H]^+ = 808.0$ was detected for EF-C_P (theoretical MW = 807.9).

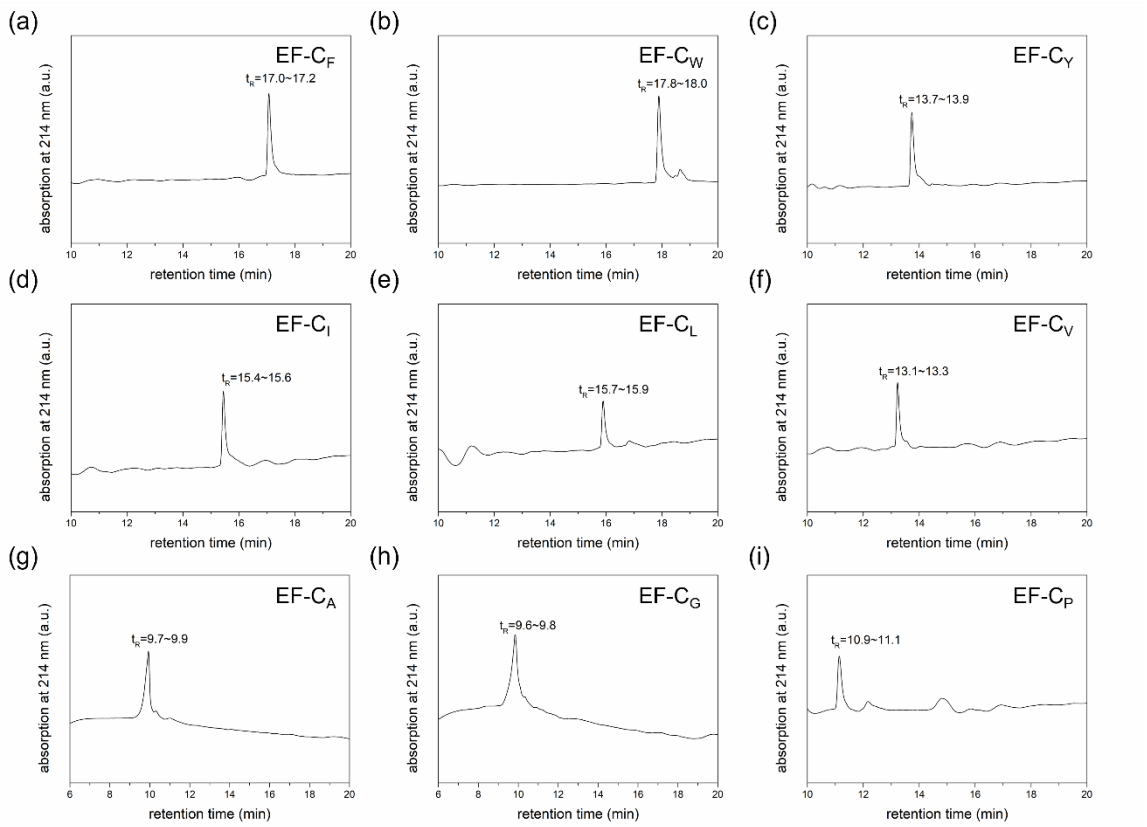

Figure S3. 2 Liquid chromatograms of EF-C variants. (a) HPLC trace of EF-C_F in an acidic condition with a retention time (t_R) = 17.0–17.2 min. (b) HPLC trace of EF-C_W in an acidic condition with t_R = 17.8–18.0 min. (c) HPLC trace of EF-C_Y in an acidic condition with t_R = 13.7–13.9 min. (d) HPLC trace of EF-C_I in an acidic condition with t_R of 15.4–15.6 min. (e) HPLC trace of EF-C_L in an acidic condition with t_R = 15.7–15.9 min. (f) HPLC trace of EF-C_V in an acidic condition with t_R = 13.1–13.3 min. (g) HPLC trace of EF-C_A in a basic condition with a t_R = 9.7–9.9 min. (h) HPLC trace of EF-C_G in a basic condition with a t_R = 9.6–9.8 min. (i) HPLC trace of EF-C_P in an acidic condition with t_R = 10.9–11.1 min.

Given that the hydrophobic side groups of leucine (EF-C_I) and isoleucine (EF-C_L) are isomers with almost identical mass spectra and liquid chromatography profiles, distinguishing between these two peptides required more techniques such as ^{1}H-NMR spectroscopy. While the ^{1}H-NMR spectra of both species showed minor differences in the aliphatic region (compare **Figure S3. 3 (a) and (b)**), utilizing 2D proton correlation ^{1}H-NMR spectroscopy (COSY) differentiated the peptides due to the characteristic pattern of the respective amino acids, shown in **Figure S3. 3 (c) and (d)**.

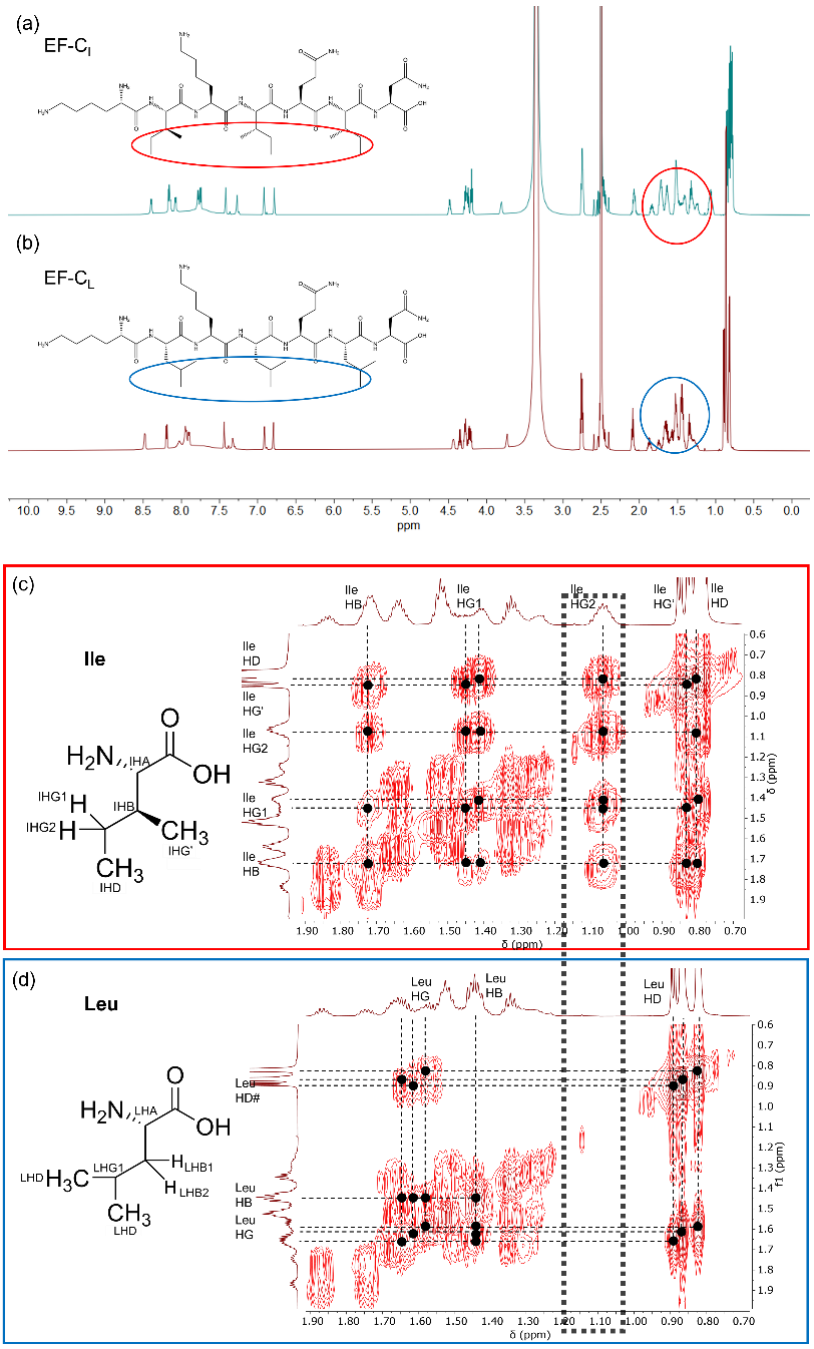

Figure S3. 3 NMR spectra of EF-C$_L$ and EF-C$_I$. (a) ^{1}H-NMR spectrum of EF-C$_L$. (b) ^{1}H-NMR spectrum of EF-C$_I$. (c) 2D-NMR correlation spectrum of EF-C$_L$. (d) 2D-NMR correlation spectrum of EF- C$_I$. (DMSO-D$_6$, 298K, 700 MHz)

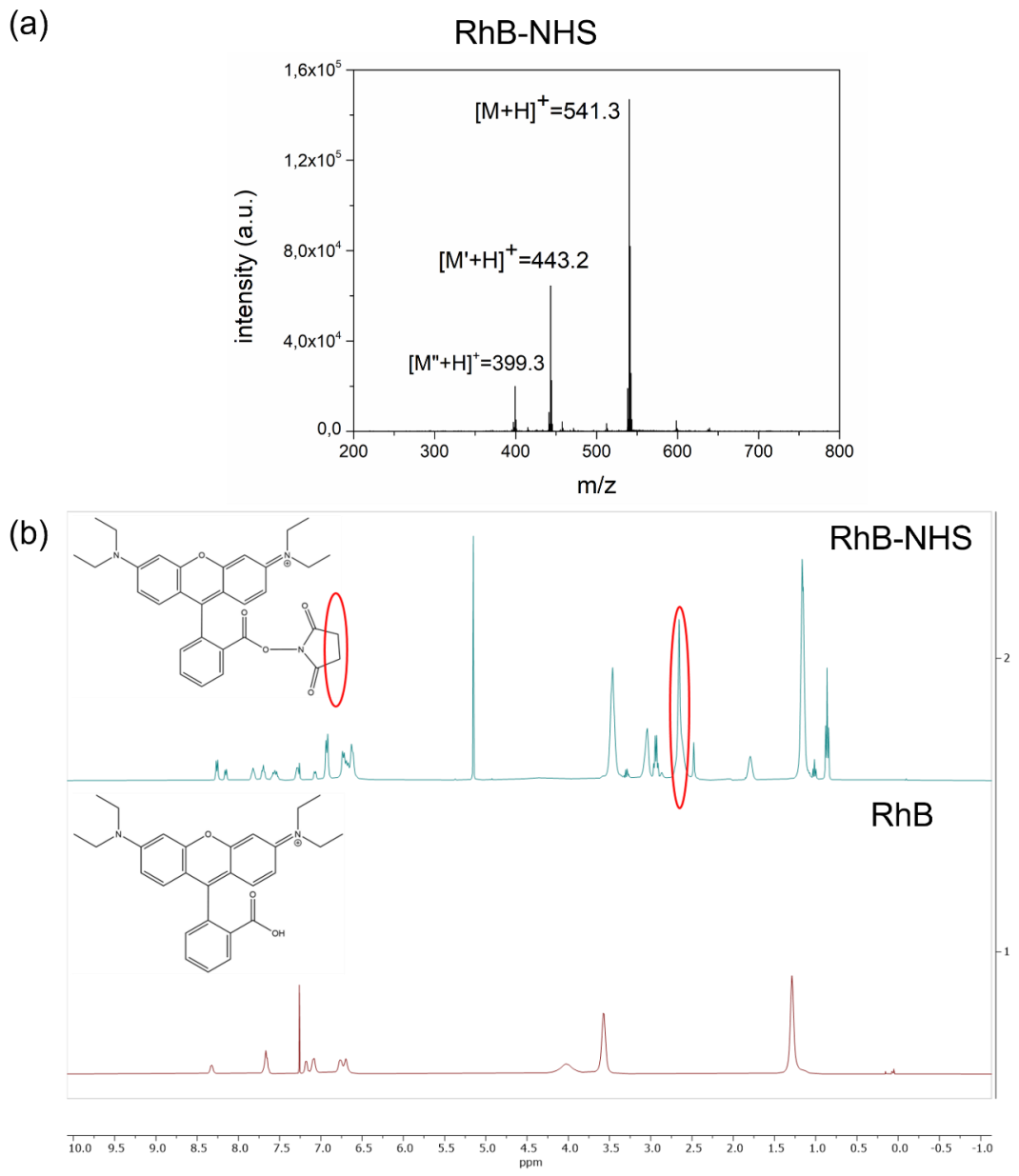

Figure S3. 4 Mass spectrum and ^{1}H-NMR spectra of RhB-NHS. (a) Mass spectrum of RhB-NHS was measured by MALDI-ToF MS with $[M+H]^{+}$= 541.3 (theoretical MW = 540.6), while the other two signals $[M'+H]^{+}$ and $[M''+H]^{+}$ were non-fluorescent spirolactams, which could be explained by a previous report.[1] (b) A sharp signal at 2.7 ppm is the characteristic signal for the NHS motif in the spectrum of RhB-NHS, while there is no such signal in the spectrum of RhB, indicating the successful modification of the NHS group. ($CDCl_3$, 298K, 400 MHz).

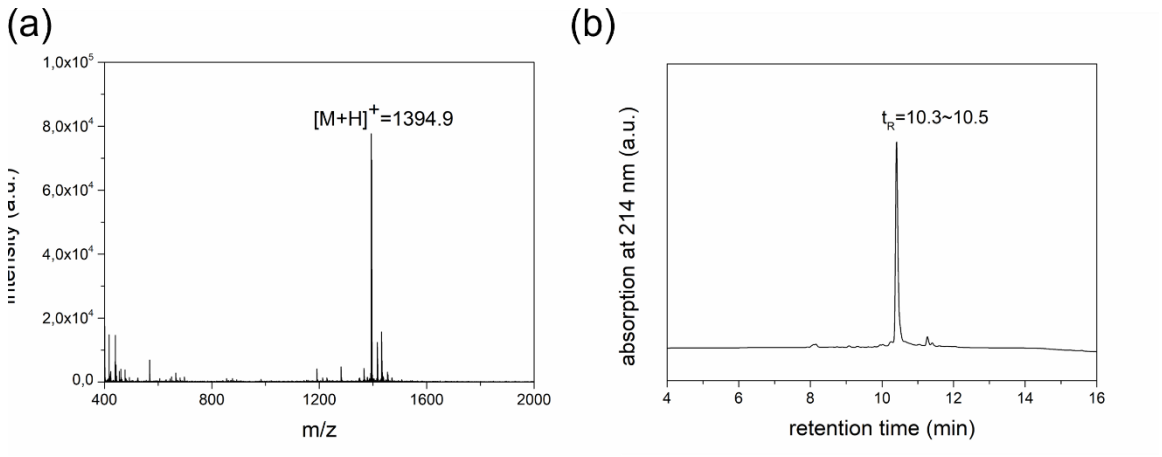

Figure S3. 5 Mass spectrum and LC chromatogram of RhB-EF-C$_I$. (a) Mass spectrum of RhB-EF-C$_I$ was measured by MALDI-TOF MS with $[M+H]^+$ = 1394.9 (theoretical MW = 1394.8). (b) HPLC trace of RhB-EF-C$_I$ in an acidic condition with t_R = 10.3–10.5 min.

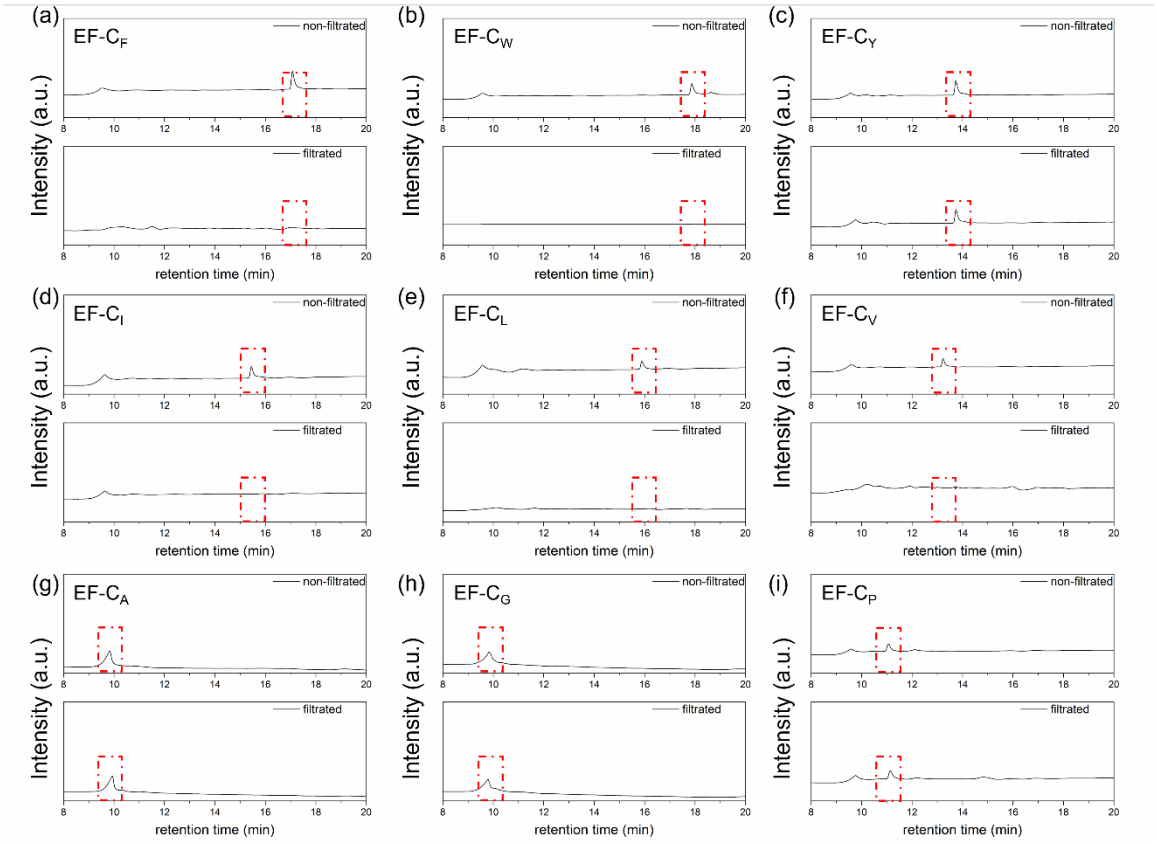

Figure S3. 6 Conversion rate assay of self-assembled EF-C variants based on analytical liquid chromatograms measured at 214 nm absorption. (a) The upper panel of the non-filtrated sample of EF-C$_F$ shows the peptide signal, while the lower one displays no signal after filtration. (b) The upper chromograph of the non-filtered sample of EF-C$_W$ shows the peptide signal, while the lower one displays no signal after filtering. (c) Both of the panels of EF-C$_Y$ show a signal. (d) The upper panel of the non-filtrated EF-C$_I$ shows the peptide signal, and the lower panel displays no signal after filtration. (e) The upper panel of the non-filtered sample of EF-C$_L$ shows the peptide signal, while the lower one displays no signal after filtering. (f) The upper panel of the non-filtrated sample of EF-C$_V$ shows the peptide signal, while the lower one displays no signal after filtration. (g) Both panels of EF-C$_A$ show a signal with or without filtration. (h) Both panels of EF-C$_G$ display a signal with or without filtration. (i) Both panels of EF-C$_P$ show the peptide signal with or without filtration.

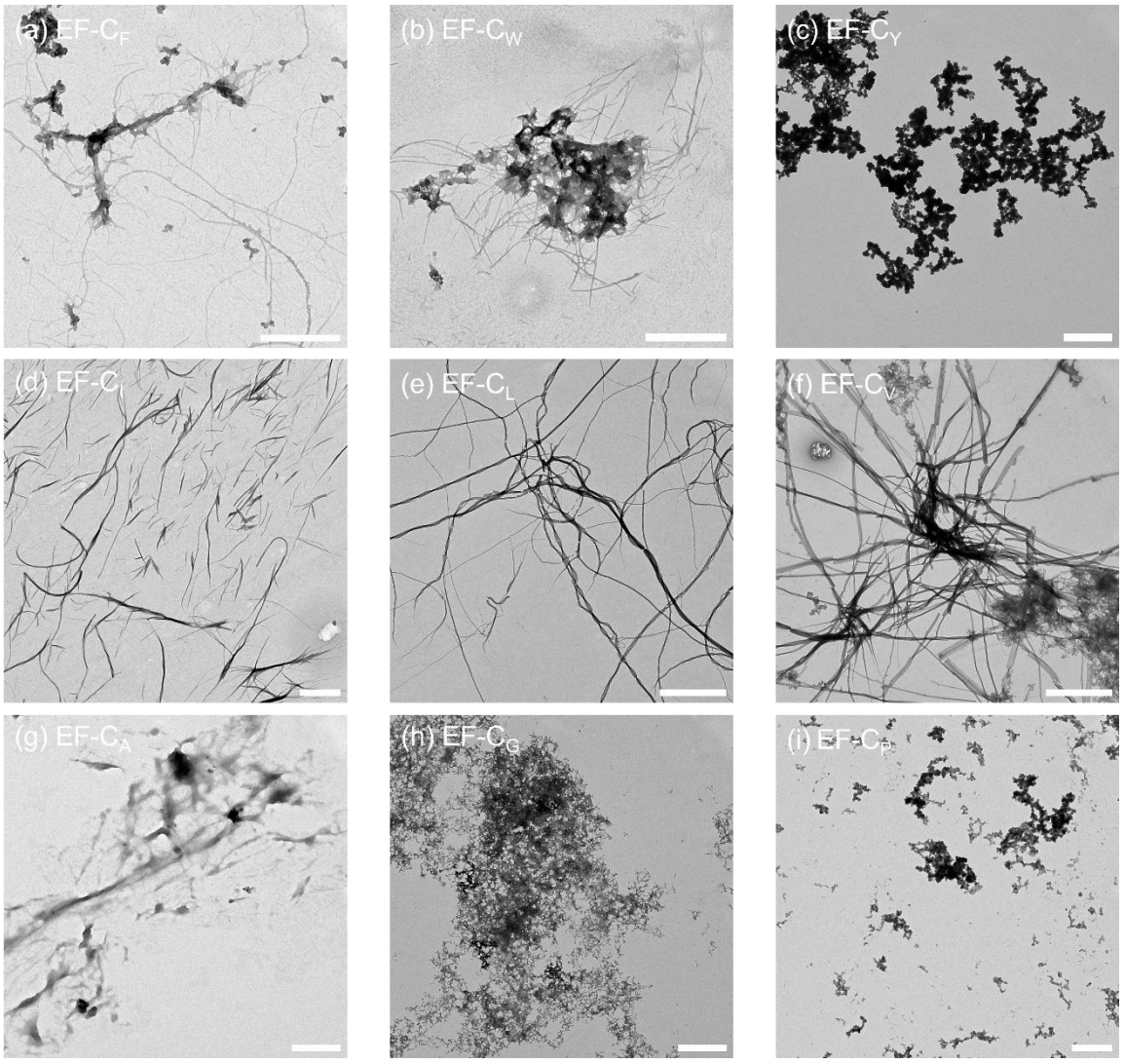

Figure S3. 7 TEM images of EF-C variants on a large scale. (a) TEM image of EF-C_F. (b) TEM image of EF-C_W. (c) TEM image of EF-C_Y. (d) TEM image of EF-C_I. (e) TEM image of EF-C_L. (f) TEM image of EF-C_V. (g) TEM image of EF-C_A. (h) TEM image of EF-C_G. (i)TEM image of EF-C_P (All scale bars = 2 μm).

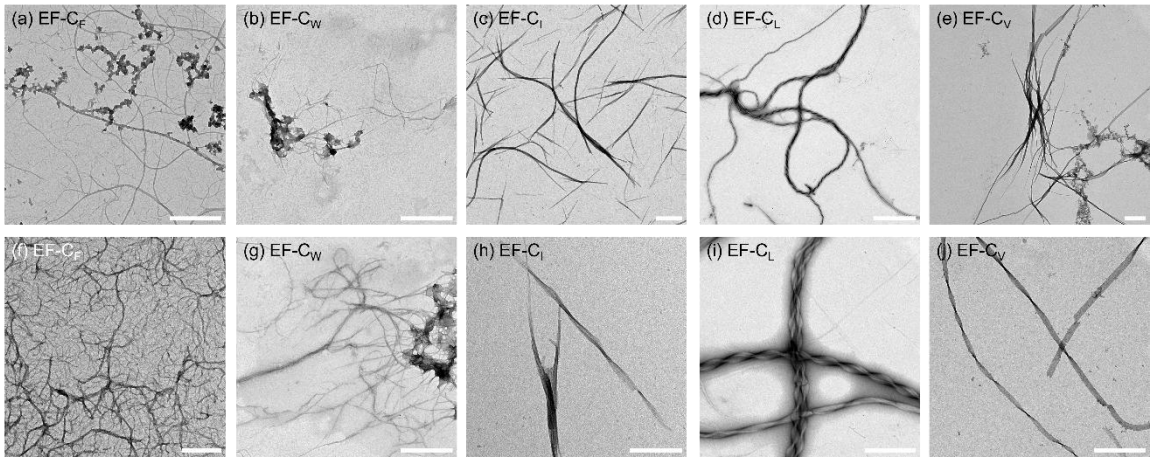

Figure S3. 8 TEM images of the assembled morphologies of EF-C variants on small scales. (a, b, c, d, e) TEM images of EF-C_F, EF-C_W, EF-C_I, EF-C_L, and EF-C_V with scale bars of 1 μm. (f, h, i, j) TEM images of EF-C_F, EF-C_I, EF-C_L, and EF-C_V with scale bars of 250 nm. (g) A TEM image of EF- C_W with scale bars of 500 nm.

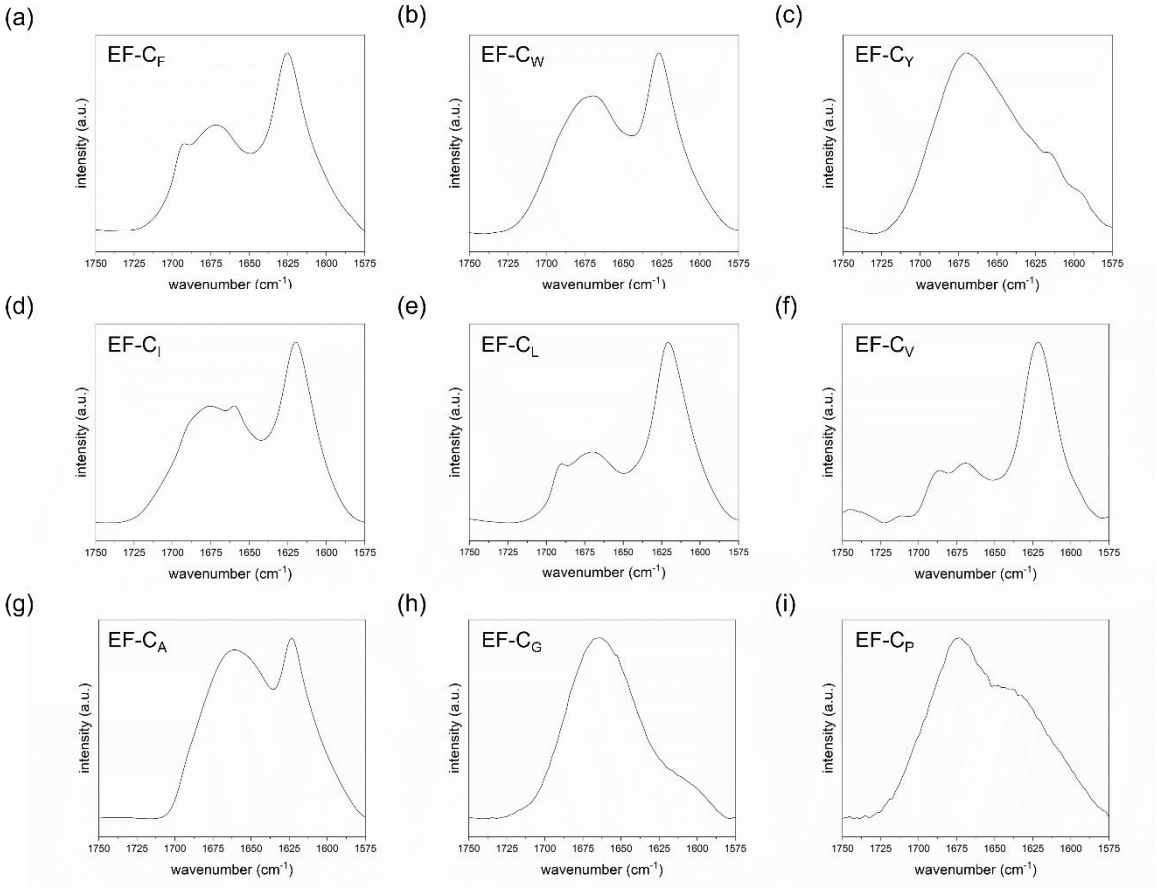

Figure S3. 9 IR spectra of EF-C variants. (a) EF-C$_F$. (b) EF-C$_W$. (c) EF-C$_Y$. (d) EF-C$_I$. (e) EF-C$_L$. (f) EF-C$_V$. (g) EF-C$_A$. (h) EF-C$_G$. (i) EF-C$_P$.

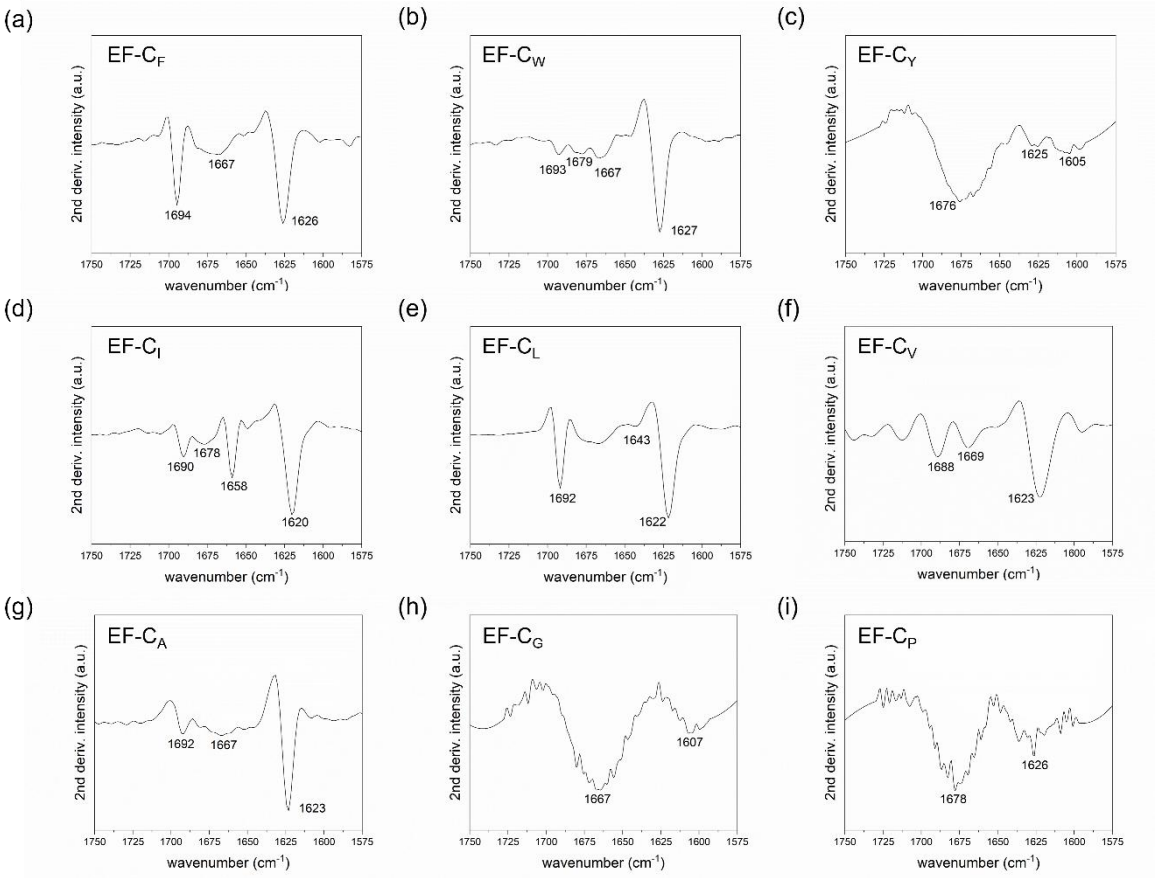

Figure S3. 10 Second derivative IR spectra of EF-C variants. (a) EF-C_F. (b) EF-C_W. (c) EF-C_Y. (d) EF-C_I. (e) EF-C_L. (f) EF-C_V. (g) EF-C_A. (h) EF-C_G. (i) EF-C_P.

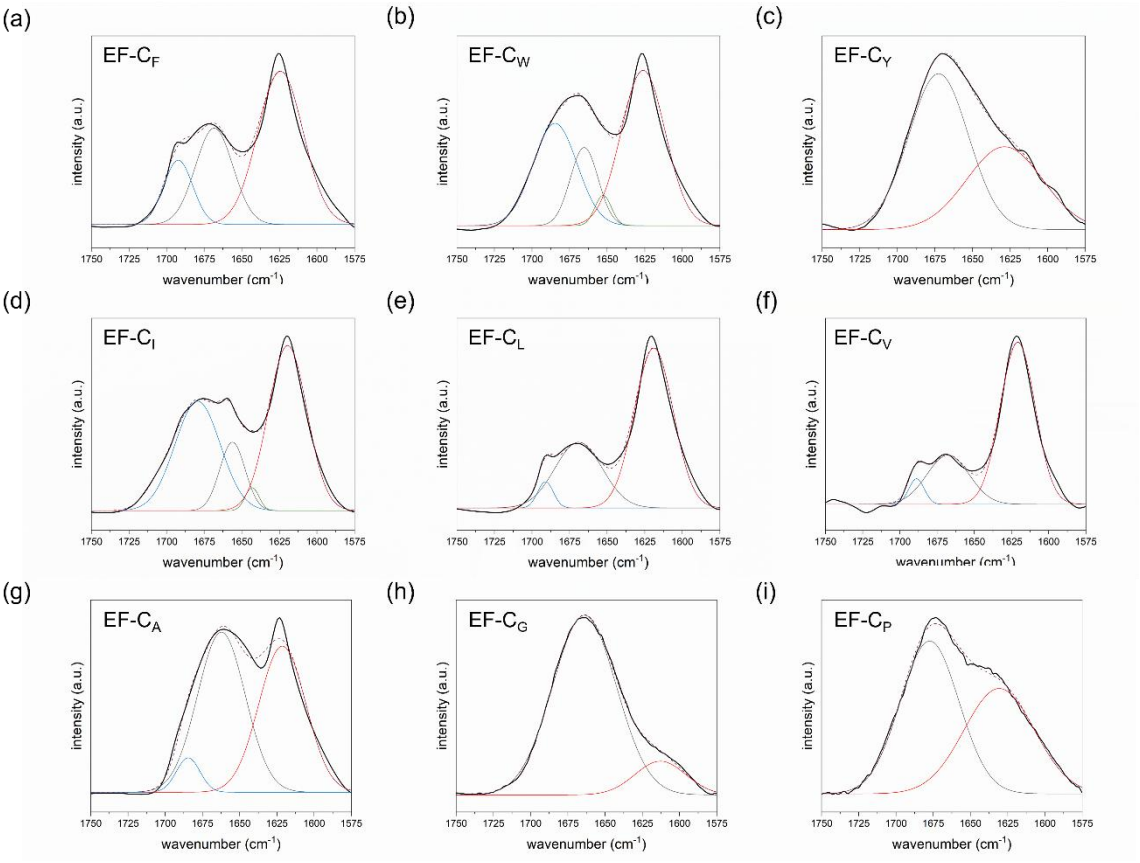

Figure S3. 11 Deconvoluted IR spectra of EF-C variants. Black lines are the IR spectra, and the brown dotted line are the deconvoluted according to the 2nd derivative IR spectra. Red lines represent the signal contributed from parallel β-sheets (1615-1643 cm^{-1}), green lines show the signal derived from random coil and α-helix (1640-1670 cm^{-1}), gray lines display the signal stemming from β-turn (1665-1685 cm^{-1}), and blue lines exhibit the signal originating from anti- parallel β-sheets (1675-1700 cm^{-1}). (a) Deconvoluted IR spectrum of EF-C$_F$ with relative β-sheets of 71.0%. (b) Deconvoluted IR spectrum of EF-C$_W$ with relative β-sheets of 80.8%. (c) Deconvoluted IR spectrum of EF-C$_Y$ with relative β-sheets of 40.3%. (d) Deconvoluted IR spectrum of EF-C$_I$ with relative β-sheets of 84.7%. (e) Deconvoluted IR spectrum of EF-C$_L$ with relative β-sheets of 68.0%. (f) Deconvoluted IR spectrum of EF-C$_V$ with relative β-sheets of 74.2% (g) Deconvoluted IR spectrum of EF-C$_A$ with relative β-sheets of 50.1%. (h) Deconvoluted IR spectrum of EF-C$_G$ with relative β-sheets of 13.1%. (i) Deconvoluted IR spectrum of EF-C$_P$ with relative β-sheets of 45.3%.

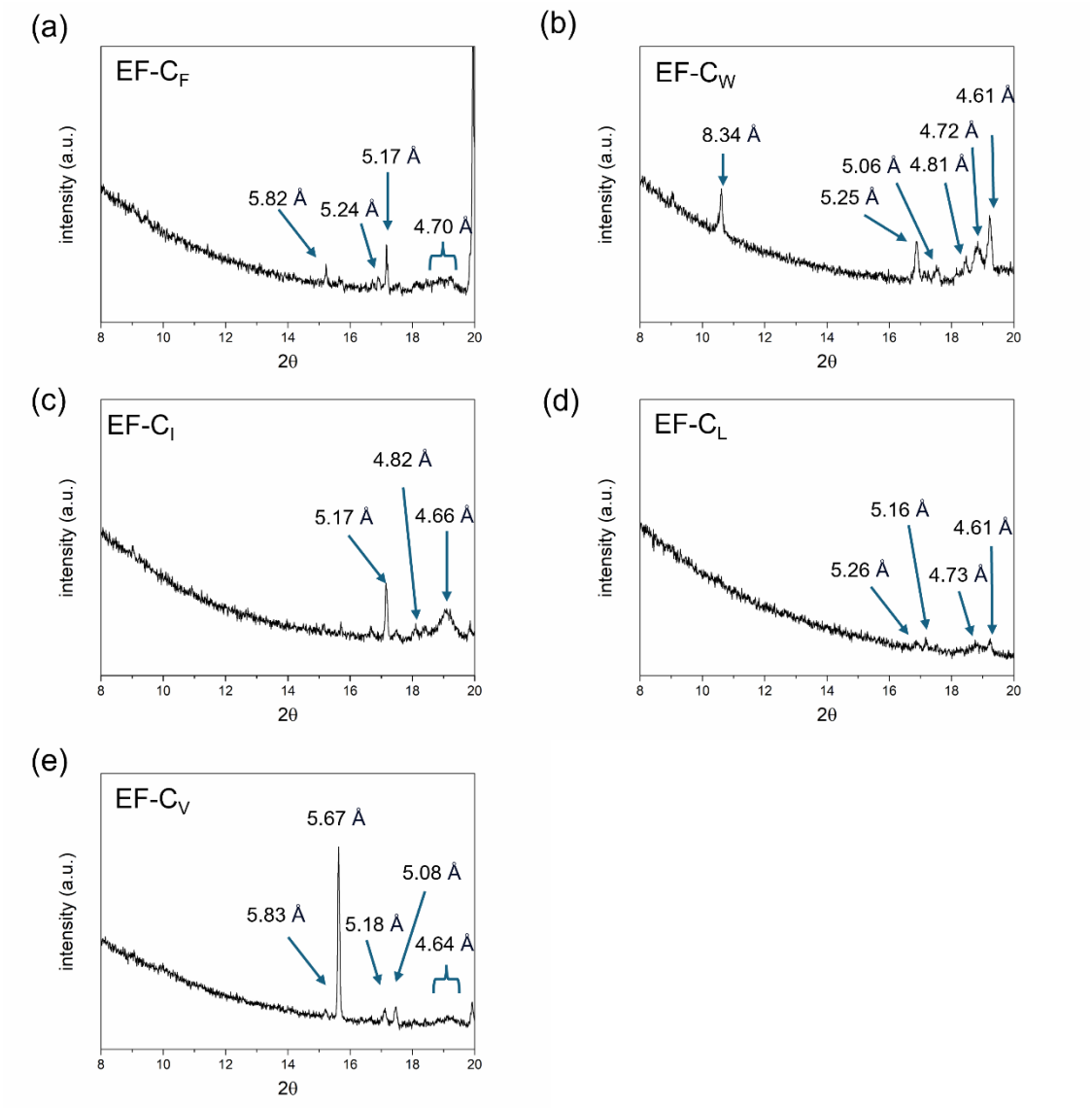

Figure S3. 12 XRD diffractograms of self-assembled EF-C variants with assigned molecular packaging distances. (a) The XRD diffractogram of EF-C_F and the correlated molecular packing distances at 4.7, 5.17, 5.24, and 5.82 Å. (b) The XRD diffractogram of EF-C_W and the analogized molecular packing distances at 4.61, 4.72, 4.81, 5.06, 5.25, and 8.34 Å. (c) The XRD diffractogram of EF-C_I and the corresponding molecular packing distances at 4.66, 4.82, and 5.17 Å. (d) The XRD pattern of EF-C_L and the associated molecular packing distances at 4.61, 4.73, 5.16, and 5.26 Å. (e) The XRD pattern of EF-C_V and the relevant molecular packing distances at 4.64, 5.08, 5.18, 5.67, and 5.83 Å.

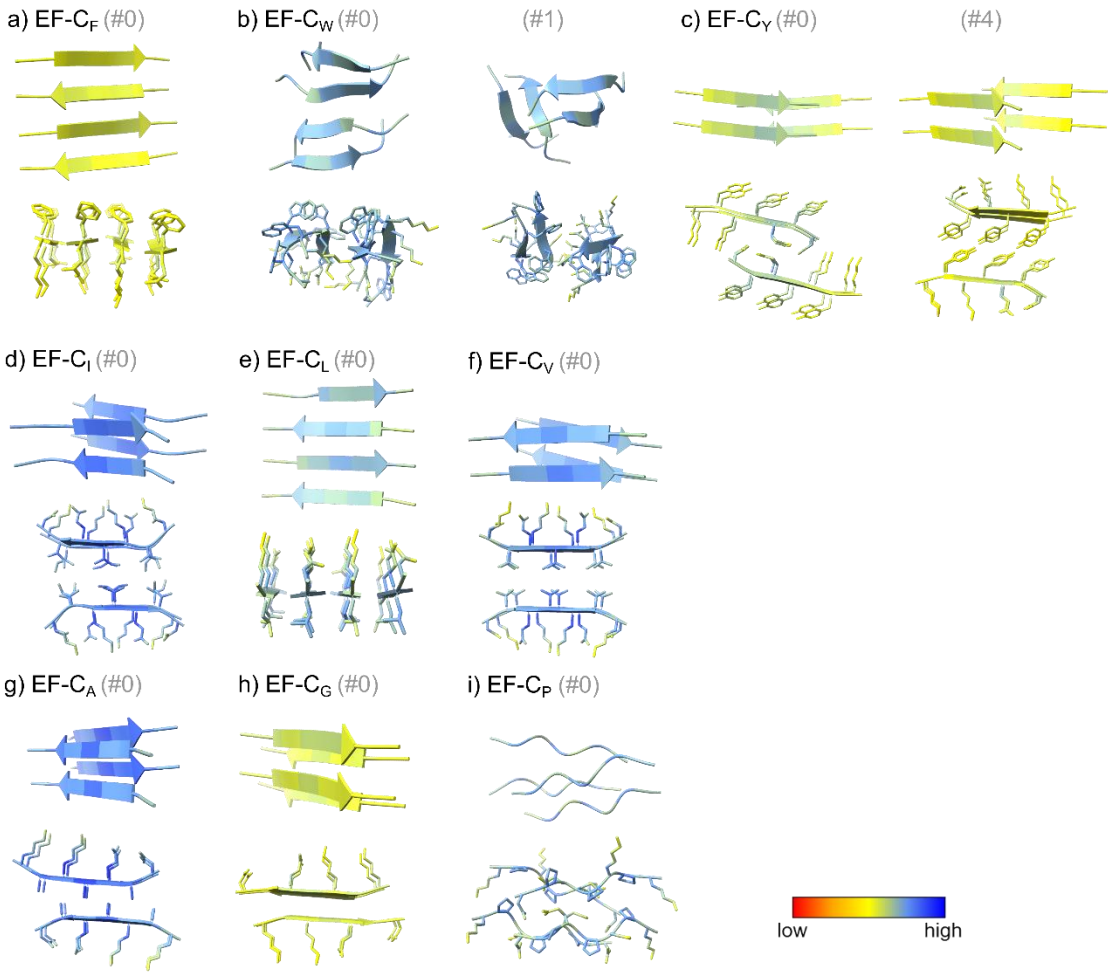

Figure S3. 13 Structural models for peptide oligomers (4mers) of nine EF-C variants using AF3. Local confidence values (predicted local distance difference test, pLDDT) are used as color coding. Low confidence regions are shown in red/yellow, high confidence regions in blue. While the top model (highest confidence, #0) has been used for MD simulations by default, for some peptides, another model (e.g. #1, #4) with very similar confidence has been considered as this showed consistence in hydrophobic side chains to the core.

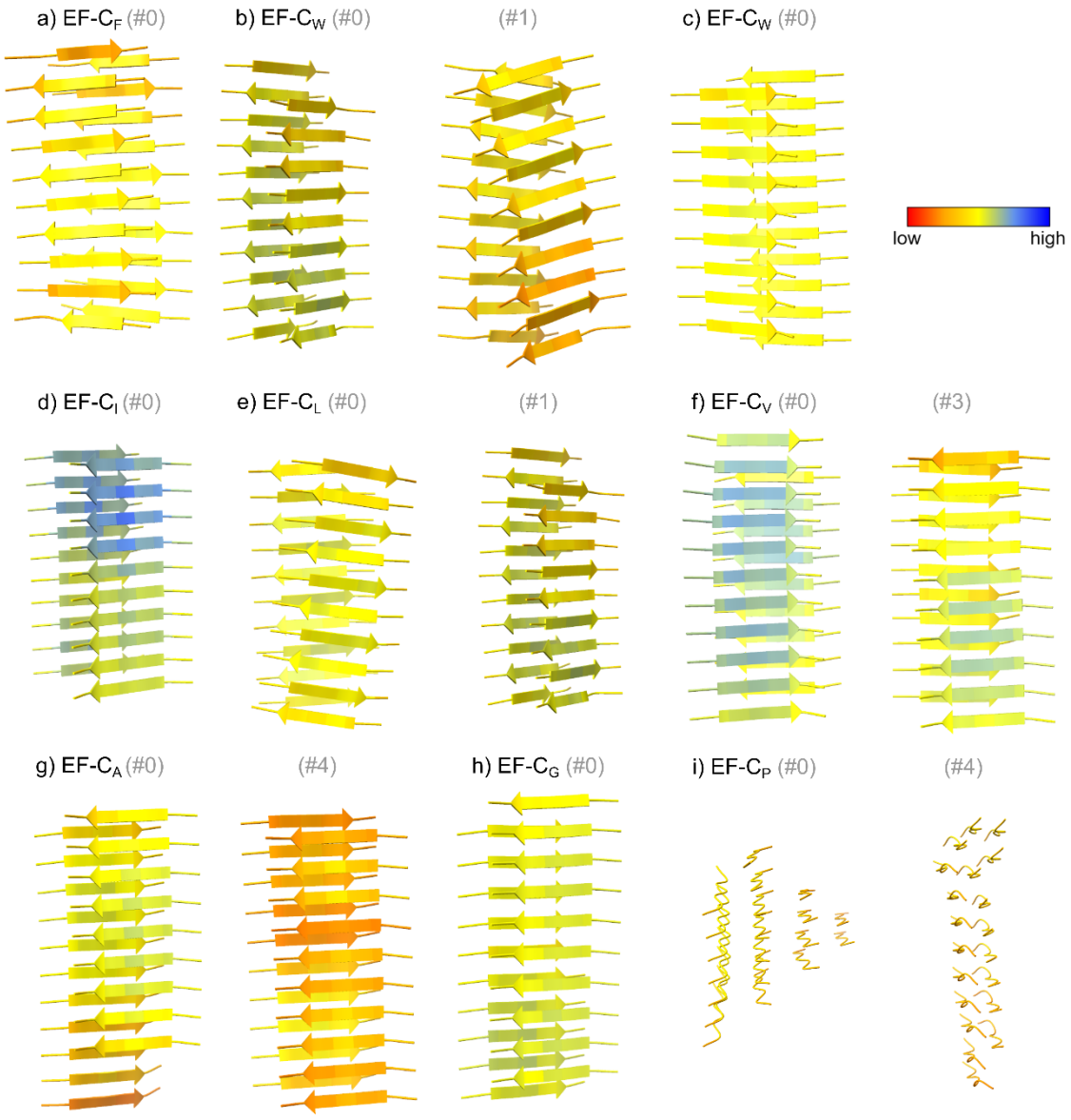

Figure S3. 14 Structural models for peptide protofibrils (20mers) of nine EF-C variants using AF3. Local confidence values (predicted local distance difference test, pLDDT) are used as color coding. Low confidence regions are shown in red/yellow, high confidence regions in blue. While the top model (highest confidence, #0) has been used for MD simulations by default, for some peptides, another model (e.g. #1, #3, #4) with very similar confidence has been considered as this showed consistence in two-stranded sheets or twisting.

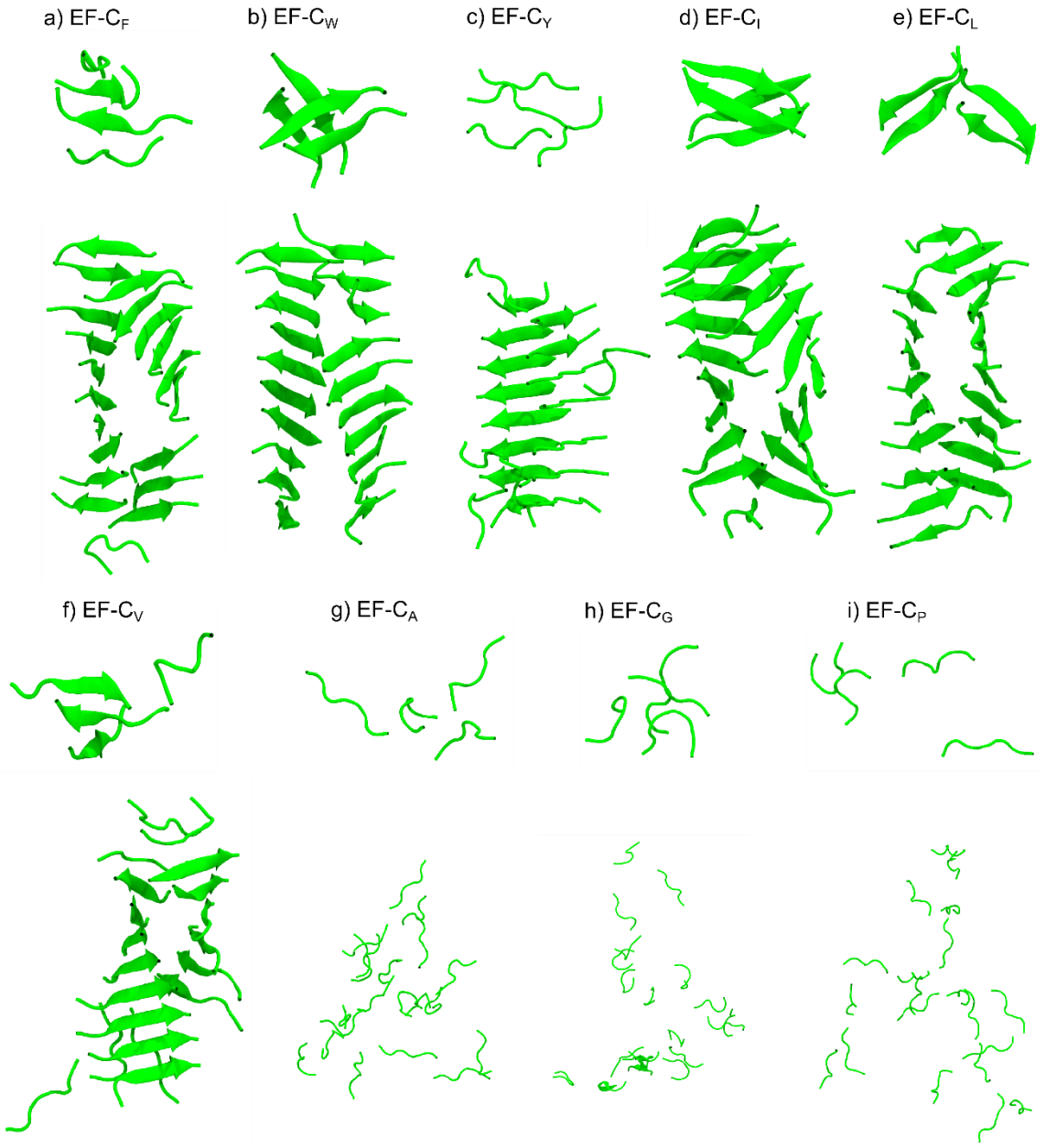

Figure S3. 15 Representative structures of peptide oligomers (4mers) and protofibrils (20mers) of nine EF-C variants. Structures represent the central structures of the largest cluster of structures during the final 10 ns of MD simulations of three replicates each. Clustering was performed using the gromos method with RMSD cutoff of 0.8 nm in GROMACS. Structures either disassembled during MD, representing unstable AF3 starting models, or stabilized their structures by twisting.

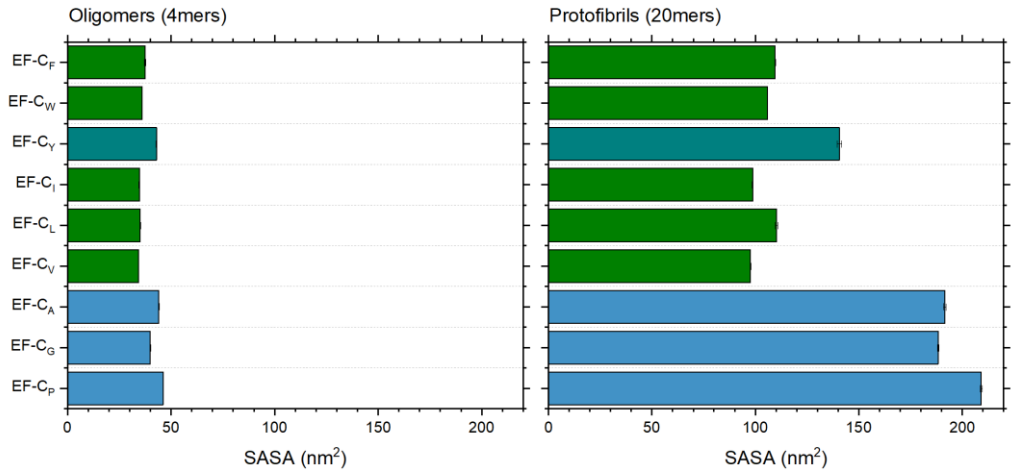

Figure S3. 16 Solvent Accessible Surface Areas (SASAs) of EF-C oligomers (4mer) and protofibrils (20mers). The SASA of a tightly packed self-assembled oligomer or protofibril is smaller than the SASA of a loosely packed structure or unclustered peptide monomers. Means with standard errors are shown.

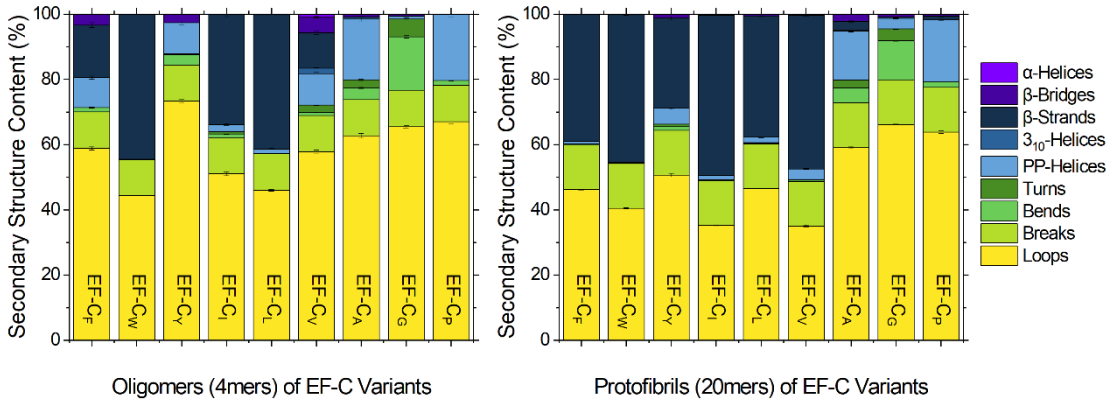

Figure S3. 17 Secondary structure content of EF-C oligomers (4mer) and protofibrils (20mers). The average secondary structures (and standard errors) were determined for the last 10 ns simulation time of all replicates.

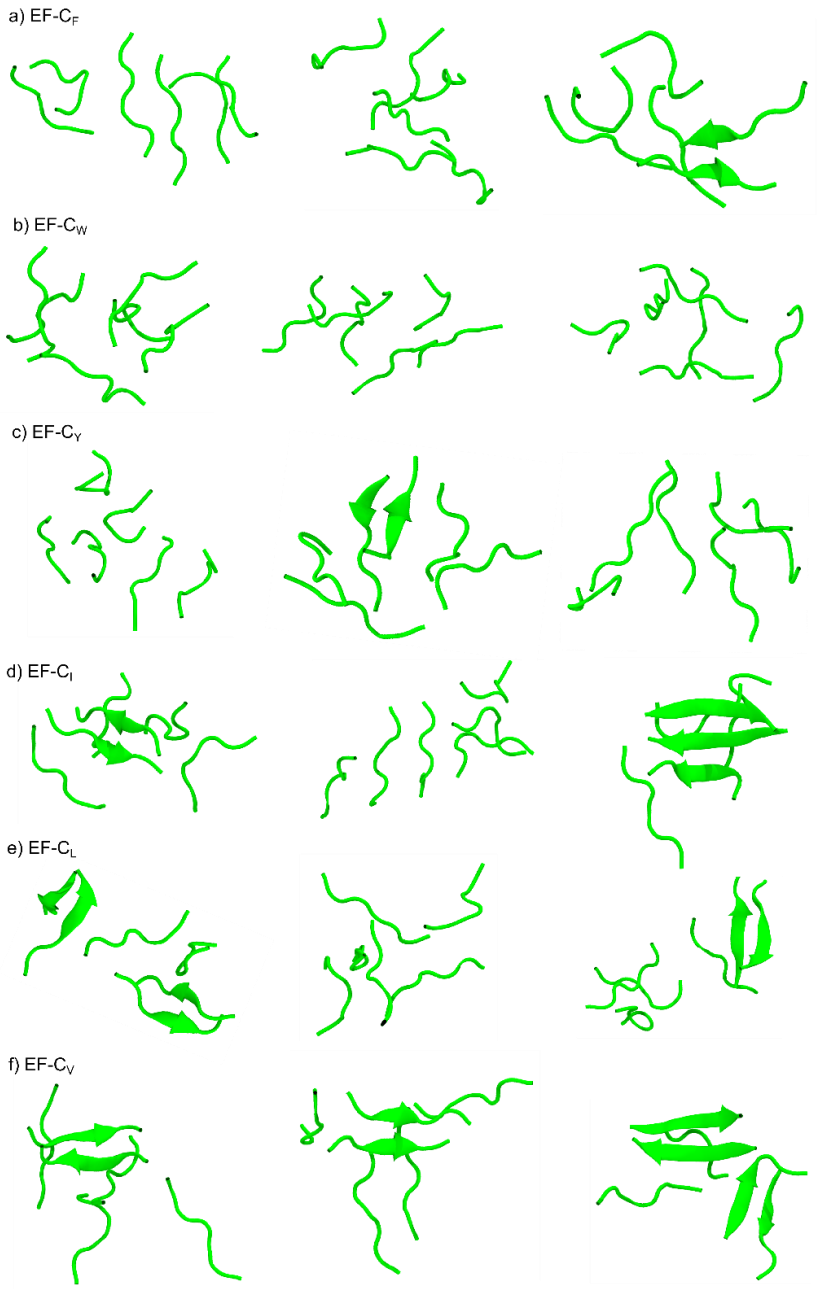

Figure S3. 18 Self-assembled peptide structures of fibril-forming EF-C variants. Structures represent the central structures of the three largest clusters of the self-assembly of six monomers during the final 10 ns of MD simulations of three replicates each. Clustering was performed using the gromos method with RMSD cutoff of 0.8 nm in GROMACS. Formation of dimers and trimers indicates early oligomers while not all peptides transformed their secondary structure within the simulation time such as EF-C$_W$.

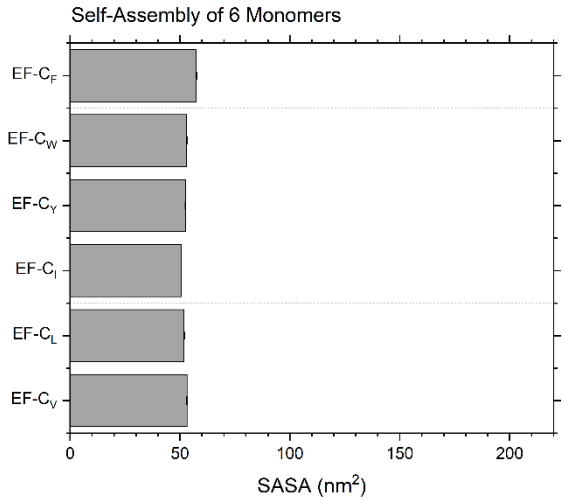

Figure S3. 19 Solvent Accessible Surface Areas (SASAs) of EF-C self-assembled structures with six monomers. All fibril-forming EF-C variants clustered during self-assembly and reached similar SASAs within 500 ns simulation time. Means with standard errors are shown.

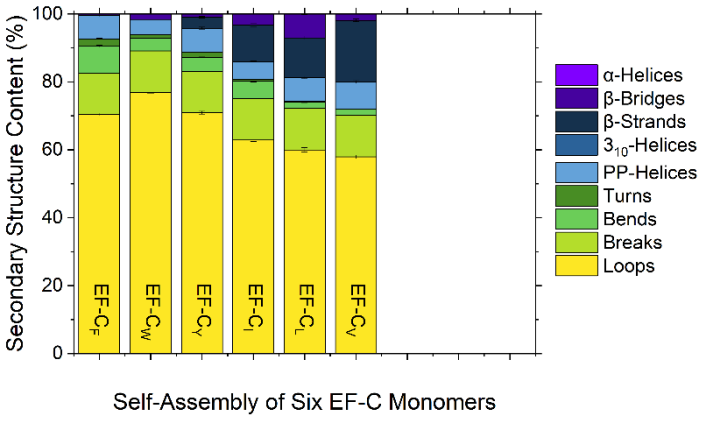

Figure S3. 20 Secondary structure content of EF-C self-assembled structures with six monomers. The average secondary structures (and standard errors) were determined for the last 10 ns simulation time of all replicates.

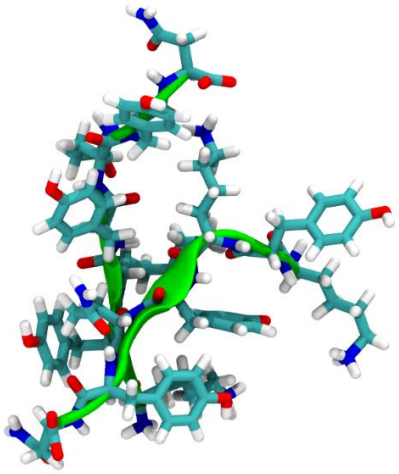

Figure S3. 21 Structural representation of dimer of EF-C$_Y$ (KYKYQYN) formed during self-assembly. Tyrosine and lysine residues are both directed outwards with proximity between cationic lysine amine groups and aromatic tyrosine residues.

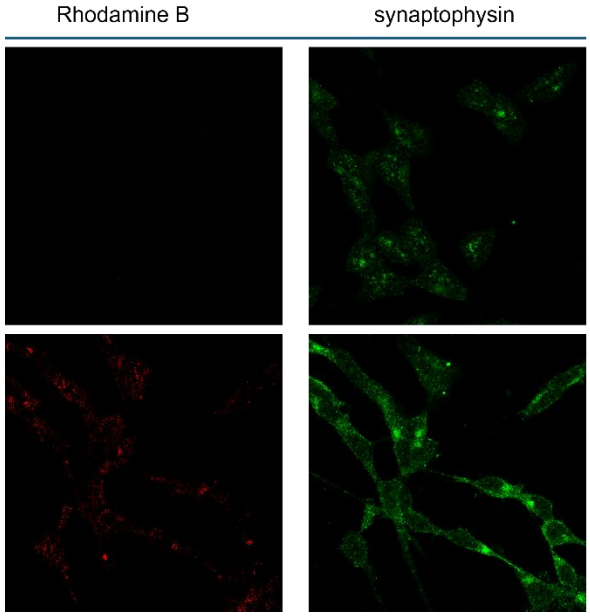

Figure S3. 22. Raw data of fluorescence images of immunostaining in Figure 5 (c).

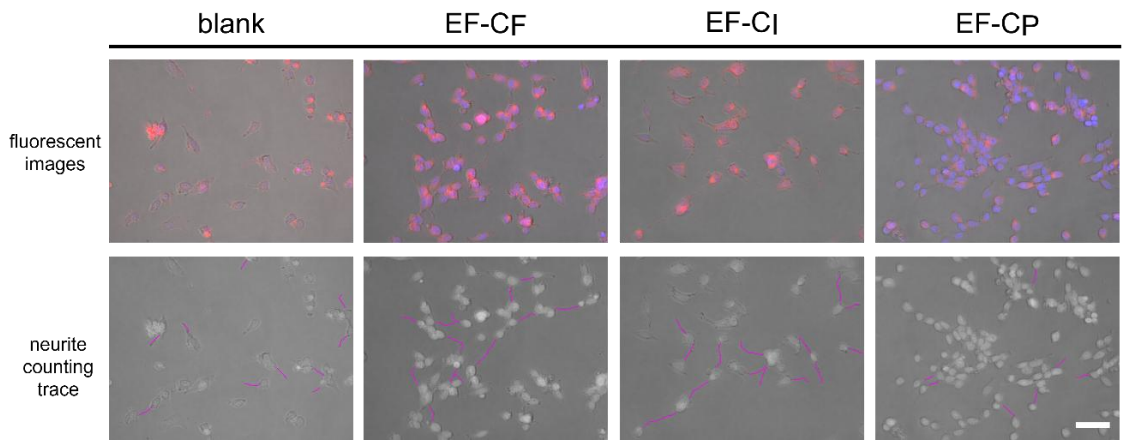

Figure S3. 22 Examples of neurite counting traces. The upper panels show the fluorescent images of SH-SY5Y cells stained with nuclei (NucBlue) and cell membranes (Deep Red Plasma Membrane). Based on the fluorescent images above, neurites were marked in pink, measured, and calculated from the images in the lower panels based on previous reports (scale bar = 50 μm).[2–4]

Supporting References

(1) Birtalan, E.; Rudat, B.; Kölmel, D. K.; Fritz, D.; Vollrath, S. B. L.; Schepers, U.; Bräse, S. Investigating Rhodamine B-Labeled Peptoids: Scopes and Limitations of Its Applications. *Biopolymers* **2011**, *96* (5), 694–701.

(2) Abramoff, M.; Magalhães, P.; Ram, S. J. Image Processing with ImageJ. *Biophotonics International* **2003**, *11*, 36–42.

(3) Meijering, E.; Jacob, M.; Sarria, J.-C. F.; Steiner, P.; Hirling, H.; Unser, M. Design and Validation of a Tool for Neurite Tracing and Analysis in Fluorescence Microscopy Images. *Cytometry Part A* **2004**, *58A* (2), 167–176.

(4) Meijering, E. Neuron Tracing in Perspective. *Cytometry Part A* **2010**, *77A* (7), 693–704.

4. Amyloid Beta and its Naturally Occurring N-Terminal Variants are Potent Activators of Human and Mouse Formyl Peptide Receptor 1

This chapter is reproduced in part with permission from
Lukas Busch, Zukaa al Taleb, ***Yu-Liang Tsai***, Vu Thu Thuy Nguyen, Qi Lu, Christopher V. Synatschke, Kristina Endres, Bernd Bufe, *J. Biol. Chem.* (2022) 298(12) 102642, https://doi.org/10.1016/j.jbc.2022.102642. Copyright 2022, Elsevier.

Author:
Lukas Busch, Zukaa al Taleb, ***Yu-Liang Tsai***, Vu Thu Thuy Nguyen, Qi Lu, Christopher V. Synatschke, Kristina Endres, Bernd Bufe

Contribution:
Lukas Busch: investigation, formal analysis, methodology, writing–original draft
Zukaa al Taleb: investigation, formal analysis, methodology, writing–original draft
Yu-Liang Tsai: investigation, formal analysis (CD, TEM) methodology, writing–original draft
Vu Thu Thuy Nguyen: investigation, methodology
Qi Lu: investigation
Christopher V. Synatschke: supervision
Kristina Endres: methodology, writing–original draft, supervision
Bernd Bufe: methodology, writing–original draft

4.1.Abstract

Formyl peptide receptors (FPRs) may contribute to inflammation in Alzheimer's disease through interactions with neuropathological Amyloid beta (Aβ) peptides. Previous studies reported activation of FPR2 by $Aβ_{1-42}$, but further investigation of other FPRs and Aβ variants is needed. This study provides a comprehensive overview of the interactions of mouse and human FPRs with different physiologically relevant Aβ-peptides using transiently transfected cells in combination with calcium imaging. We observed that, in addition to hFPR2, all other hFPRs also responded to $Aβ_{1-42}$, $Aβ_{1-40}$, and the naturally occurring variants $Aβ_{11-40}$ and $Aβ_{17-40}$. Notably, $Aβ_{11-40}$ and $Aβ_{17-40}$ are very potent activators of mouse and human FPR1, acting at nanomolar concentrations. Buffer composition and aggregation state are extremely crucial factors that critically affect the interaction of Aβ with different FPR subtypes. To investigate the physiological relevance of these findings, we examined the effects of $Aβ_{11-40}$ and $Aβ_{17-40}$ on the human glial cell line U87. Both peptides induced a strong calcium flux at concentrations that are very similar to those obtained in experiments for hFPR1 in HEK cells. Further immunocytochemistry, qPCR, and pharmacological experiments verified that these responses were primarily mediated through hFPR1. Chemotaxis experiments revealed that $Aβ_{11-40}$ but not $Aβ_{17-40}$ evoked cell migration, which argues for a functional selectivity of different Aβ peptides. Together, these findings provide the first evidence that not only hFPR2 but also hFPR1 and hFPR3 may contribute to neuroinflammation in Alzheimer's disease through an interaction with different Aβ variants

4.2.Introduction

Alzheimer's disease (AD) is a complex neurodegenerative disorder with a heterogeneous pathobiology leading to progressive dementia with death as an inevitable outcome, generally within 5 to 12 years after symptom onset.[1] While there is an urgent need for therapies that may prevent or slow the progression of AD, no unequivocal treatment is currently available.[2] A better understanding of the molecular mechanisms underlying AD can help to identify new strategies to develop such treatments. The discovery that extracellular amyloid beta (Aβ) depositions[3] and intracellular accumulation of hyperphosphorylated tau[4,5] are common neuro pathological hallmarks of all AD forms were significant advances that helped to clarify several key aspects of the underlying pathology. Although these discoveries are already more than 3 decades old, the precise impact of Aβ on neuroinflammation and neurodegeneration is still incompletely understood.[2] Major challenges in Aβ-research comprise the complex peptide processing involving multiple proteases,[6] the challenging physiochemical properties of the resulting fragments that permit a formation of different oligomeric structures,[7] and the pleiotropic physiological effects of Aβ peptides on neurons, glia, and immune cells.[8,9]

Aβ is produced by a sequential cleavage of an amyloid pre cursor protein (APP) by β- and γ-secretase.[10] Cleavage can occur at several sites, which results in the predominant pro duction of peptides ending at position 38, 40, or 42 of the Aβ domain.[10,11] APP processing is somewhat imprecise and thus, depending on the specific (patho)physiological conditions, several additional longer and shorter Aβ variants in varying concentrations can occur.[6,12] Many of them tend to form β sheet conformations that are prone to self-aggregate into different dimers, trimers, and tetramers, higher-order oligomers, protofibrils, and ultimately, typical 8-nm amyloid fibrils.[7] There is clear evidence that the precise composition of these aggregates has a strong impact on their neurotoxicity[7,13] and that different Aβ variants can trigger varying amounts of detrimental pro-inflammatory activities in astrocytes and microglia.[14,15] Their biochemical properties can vary significantly depending on the microenvironment in which they are generated, their amino acid composition, and their carboxyl terminus.[13,16] This makes the precise assessment of the Aβ structure for the etiology of AD extremely difficult.

Microglia are a key factor for AD. In a healthy brain, they provide tropic support to neurons while simultaneously surveying the central nervous system for pathological stimuli.[14,17] Upon activation, they undergo morphological changes and assume a reactive phenotype where they cease their supportive role.[14] Instead, they obtain phagocytic and inflammatory functions, start to produce pro-inflammatory cytokines and chemokines such as IL-1β, IL-6, IL-8, and TNFα, and generate oxidative stress through the release of nitric oxide and reactive oxygen species.[14,18] Small oligomeric variants of Aβ are potent activators of microglia hat led to more severe neurotoxic outcomes than larger variants.[19,20] It is therefore crucial to understand how different Aβ variants interact with microglia to produce these neurotoxic effects. Unfortunately, interactions between Aβ and microglial cells are highly complex because Aβ acts through multiple pathways including TREM2 (Triggering receptor expressed on myeloid cells 2), TRPM2 (Transient receptor potential cation channel, subfamily M, member 2),[21] scavenger receptors such as CD36, MARCO (Macrophage re ceptor with collagenous structure), and RAGE (receptor for advanced glycation endproducts),[22] and pattern recognition receptors (PRR) such as Toll-like receptors,[23] NOD-like receptors,[24] and FPRs (formyl peptide receptors).[12]

The activation of PRRs by Aβ has become a recent focus in AD research because they have a special ability to potently trigger the reactive state.[14,25] Among these PRRs, FPRs are one of the promising targets for AD research.[12] They belong to a small gene family of G protein–coupled receptors with three members in humans and seven in mice.[26] FPRs are primarily expressed in the innate and adaptive immune system, where they contribute to the detection and elimination of bacterial pathogens.[27–30] However, they are also expressed in a number of cell types in the brain such as microglia, astrocytes, and some specific subsets of neurons.[31–35] Several independent lines of evidence support a significant contribution of FPRs to the pathological progression of AD. First, FPRs are highly upregulated in reactive glial cells at the site of senile plaques in human AD patients.[36] Second $A\beta_{1–42}$ induced a decrease of cAMP and an induction of ERK phosphorylation in rat microglia and astrocytes, which was inhibited by the syn thetic FPR antagonist WRW4.[35,37] Third, FPR2-dependent recognition of $A\beta_{1-42}$ led to the induction of oxidative stress, the release of pro-inflammatory cytokines, and chemotaxis of neutrophils and murine glial cells.[36,38-41] Fourth, in vitro expression studies demonstrated that $A\beta_{1–42}$ can

induce calcium mobilization and ERK signaling in cell lines that were transfected with human and murine FPR2.[35,36,38] In addition, FPRs mediate the intracellular uptake of $A\beta_{1-42}$ in primary murine glia and in in vitro FPR expression systems.[37,42–44] Last but not least, treatment with the FPR antagonist Boc2 significantly ameliorated typical symptoms of AD such as cognitive impairment, decreased neuronal density, and Aβ plaque accumulation in an AD mouse model.[46]

Despite these promising results, several key aspects of the interactions between Aβ and the different FPR variants are still insufficiently understood. For example, most studies on the interaction of Aβ with FPRs so far nearly exclusively focused on the role of FPR2. However, the human (h) gene family comprises the three members, hFPR1, hFPR2, and hFPR3. Thus, the potential of the other variants to interact with Aβ has not been extensively examined. Next, the murine (m) gene family comprises seven family members: mFpr1, mFpr2, mFpr3, mFpr-rs3, mFpr-rs4, mFrp-rs6, mFpr-rs7.[46] The only mouse gene that has a clear genetic ortholog inside the human gene family is mFpr1, which has a common ancestor with hFPR1.[47,48] All others are paralogs, which evolved independently after the split of the human and mouse species,[46] which makes it questionable to which extent data from mouse models can be transferred to humans. Finally, the interactions of FPRs with Aβ were nearly exclusively studied for $A\beta_{1-42}$, while data on the responses to other naturally occur ring Aβ variants are lacking.

To address these questions, we used in vitro expression of human and mouse FPRs in HEK293T cells in combination with high-throughput measurements of intracellular calcium mobilization to systematically investigate the interactions between different Aβ variants with all human receptors and to compare their response with those of the relevant mouse receptors. In summary, these data provide the first clear evidence for a contribution of FPR1 and FPR3 to Aβ detection and identify N abridged Aβ fragments as a previously unknown potent group of activators for FPRs. Our results reveal that in addition to mFpr2 and hFPR2, also mFpr1, hFPR, and hFPR3 are capable to interact with $A\beta_{1-42}$. Next, we can show that the solvent composition and manufacturer of the peptides critically influence the activation of FPRs by $A\beta_{1-42}$. These variations likely depend on a different structural composition of Aβ from different sources. Furthermore, we demonstrate that human and mouse FPRs are also activated by $A\beta_{1-40}$ and N-terminally abridged variants such as $A\beta_{11-}$

$_{40}$ and $A\beta_{17-40}$. Noteworthy, FPR1 is able to detect these peptides with up to 30-times higher sensitivity than $A\beta_{1-42}$ and that these peptides induce calcium flux and chemotaxis in glial U87 cells that is likely mediated by hFPR1.

4.3.Result and Discussion

4.3.1. Activation of Formyl Peptide Receptors by Aβ is not Restricted to FPR2

We first investigated the ability of the human receptors hFPR1, hFPR2, and hFPR3 and their mouse counterparts' mFpr1, mFpr2, and mFpr3 to detect Aβ. The further four existing mouse receptors mFpr-rs3, mFpr-rs4, mFrp-rs6, mFpr-rs7 were excluded from the analysis because they are not expressed in the brain[48] and likely do not mediate classical immune functions[49] but are responsible for the detection of yet largely unknown olfactory cues.[49,50] We first monitored changes in intracellular calcium levels of HEK293T cells transiently transfected with one of the different FPRs after application of $A\beta_{1-42}$. Consistent with previous reports,[36,38] we observed that $A\beta_{1-42}$ induced Ca^{2+} flux at low micromolar concentrations through mouse and human FPR2 (**Fig 4. 1A**). Surprisingly, we also observed a similar or even higher amount of activation of mFpr1, hFPR1, and hFPR3, whereas mFpr3 and mock-transfected negative controls did not respond. These data suggest that in addition to hFPR2, all other human FPRs are also able to respond to $A\beta_{1-42}$. Noteworthy, subsequent concentration response tests showed that mouse and human FPR1 were even more sensitive and had a higher signal amplitude than any other receptor (**Fig 4. 1B**). Next, we also noticed some important differences between murine and human FPRs. First, we found that mFpr1 responded with an approximately tenfold higher sensitivity to $A\beta_{1-42}$ than mFPR2, whereas the responses of human FPR1 were just slightly better than that the ones of hFPR2. This raises the possibility that mFpr1 might be more relevant for the physiological responses to $A\beta_{1-42}$ in mouse models than its human ortholog. Second, we found an activation of human FPR3 by $A\beta_{1-42}$ but did not detect a corresponding signal of its mouse counterpart. In summary, the observed species-dependent variations argue for a diverging importance of the different FPR paralogs for Aβ detection and signal transduction in between humans and mice, which should be further examined.

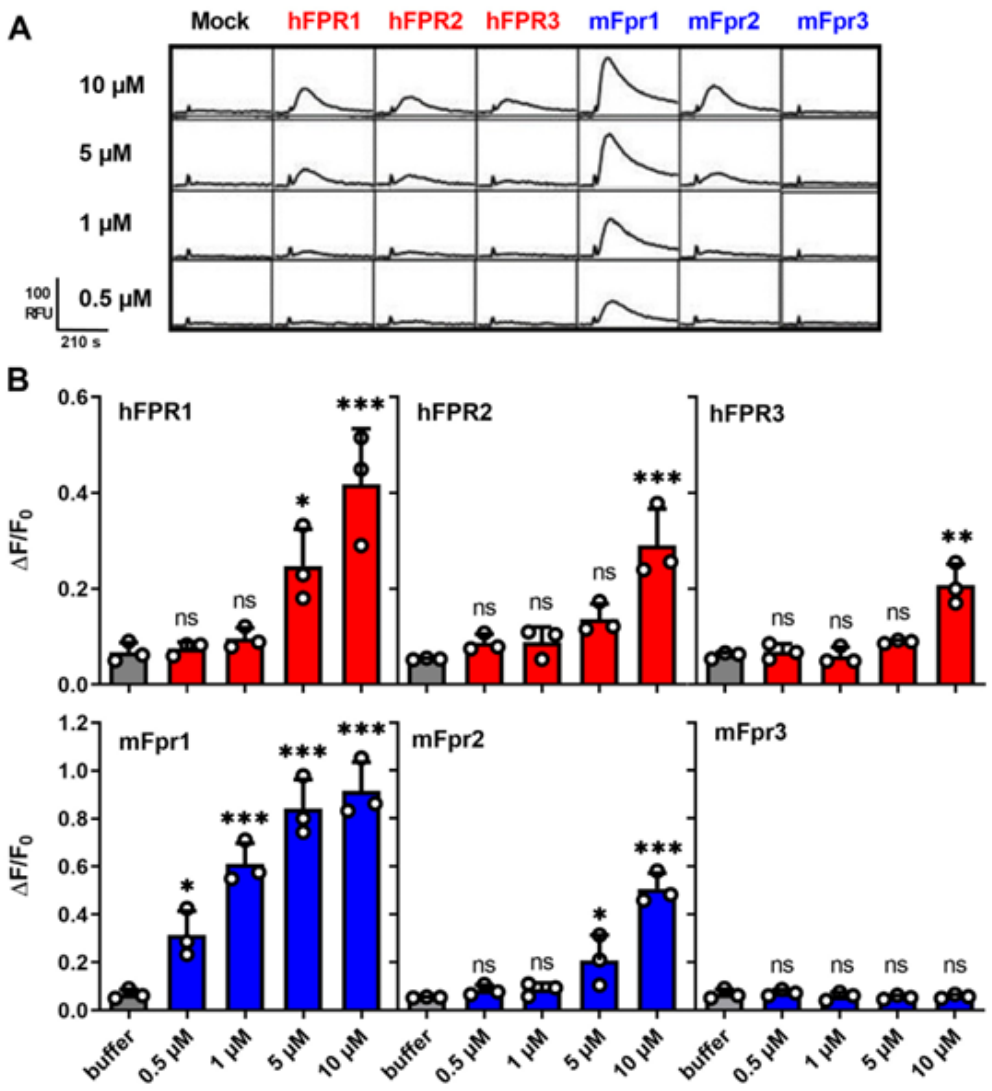

Figure 4. 1 Aβ1-42 activates all human FPRs. (A) Representative Ca^{2+} traces of HEK293T cells transiently transfected with FPR plasmids or an empty vector (mock) after stimulation with Aβ1-42 obtained from P&E. (B) Mean peak Ca^{2+} responses of human (red) and mouse (blue) FPRs upon stimulation with different concentrations of Aβ1-42. Buffer (gray) denotes responses to the assay buffer without Aβ1-42. Bars represent mean values of three independent experiments (n = 3) carried out as technical duplicates (N = 2). All Error bars, S.D.; One-way ANOVA test, Dunnett post hoc test; *p ≤ 0.05; **p ≤ 0.01; ***p ≤ 0.001; ns, no significance. Aβ, amyloid beta; FPR, Formyl peptide receptor. Copyright 2022, Elsevier.

4.3.2. Solvent and Supplier Variations can Critically Influence FPR Responses to Aβ

A detailed comparison of our results with other publications revealed some inconsistencies in the current literature. While our observation that $A\beta_{1\text{-}42}$ induces Ca^{2+} flux through human and mouse FPR2 in micromolar concentrations is in accordance with all previous studies,[36,38] our study is the first to report of an activation of hFPR3. Next, our notion that mouse and human FPR1 are activated by $A\beta_{1\text{-}42}$ is in line with the results reported by Le et al. and Slowik et al.[35,42] However, in these studies, the hFPR1 responses were far less pronounced and a study by Tiffany et al. even failed to detect any activation of mouse and human FPR1. A careful comparison of the methods used in these and other reports for possible explanations revealed three major potential sources. First, researchers frequently use dimethyl sulfoxide (DMSO) to dissolve $A\beta_{1\text{-}42}$, which can be critical in the case of FPRs because DMSO is an agonist for FPR1 and FPR2 and may therefore affect the $A\beta_{1\text{-}42}$-evoked signals.[49] Second, varying types of physiological assay buffers and solvents were used, which might be critical in the case of $A\beta_{1\text{-}42}$ because this peptide tends to form diverse kinds of aggregates in different assay buffers.[20,51,52] Third, $A\beta_{1\text{-}42}$ was obtained from different sources, which raises the possibility that variations in the production processes may have influenced the peptide aggregation status. We therefore decided to carefully investigate the influence of these factors on the FPR responses. To examine the impact of peptide synthesis on the receptor responses, we ordered four additional $A\beta_{1\text{-}42}$ peptides from three additional sources (Anaspec, Sigma-Aldrich, and Synpeptide) and compared them to the peptide that we obtained from our initial supplier Peptides & Elephants (P&E). A second peptide from Anaspec that was hexafluoroisopropanol (HFIP) treated was used as positive control for aggregation because this peptide is known to readily form aggregates. Using a thioflavinT (ThT) assay (**Fig 4. 2A**), we first compared the aggregation status 10 min after dissolving the peptides with their kinetics over the course of the next 2 hours because we estimated that this would be the maximal time span to perform our calcium imaging experiments. We already observed clear differences between the four supposedly identical peptides in the 10 min after dissolving them in our assay buffer. In comparison to the peptide from P&E, $A\beta_{1\text{-}42}$ from Synpeptide and Sigma-Aldrich showed an approximately 30% to 50% lower aggregate content, whereas the non-HFIP–treated peptide from Anaspec was approximately 30%

more pre-aggregated. The kinetics in the first 2 h revealed that the aggregation control with the HFIP-treated peptide showed the expected increase, whereas the status of $A\beta_{1-42}$ from Sigma-Aldrich and Synpeptide did not drastically change. The non-HFIP–treated Anaspec peptide even showed a reduction of fluorescence. In transmission electron microscopy (TEM, **Fig S4. 1A**), $A\beta_{1-42}$ from P&E, Synpeptide, and the HFIP-treated Anaspec peptide displayed a somewhat similar amorphous morphology, while the non-HFIP–treated Anaspec peptide seemed to directly form long fibers, which may explain the high starting fluorescence in our ThT assay. Together, these results indicate a considerable amount of heterogeneity in the secondary and tertiary structure of peptides from different sources. In line with this, Ca^{2+} flux measurements also revealed clear differences in the response pattern of mouse and human FPRs to these peptides (**Fig 4. 2 B and C and S4. 1B**). $A\beta_{1-42}$ from Sigma Aldrich elicited a similar response pattern as that of P&E. However, it failed to activate hFPR1. When using $A\beta_{1-42}$ from Synpeptide, the responses of hFPR1 and hFPR2 were lost. The non-HFIP–treated peptide from Anaspec potently activated mFpr1 but failed to activate any other mouse or human FPR, whereas the HFIP-treated version weakly activated hFPR3, mFpr1, and mFpr2. Thus, variations in the manufacturing process are critical factors that are capable to strongly affect the activation pattern of FPRs. To evaluate the secondary structure of our peptides, we next performed CD spectroscopy on $A\beta_{1-42}$ peptides from P&E, Synpeptide, and the two variants from Anaspec, all dissolved in the assay buffer C1 (**Fig 4. 2D** and **S4. 1C**). All tested peptides showed similar proportions of α-helix and β-sheet but differed in the amount of β-turns and unstructured sequences. In comparison with the two different Anaspec peptides that elicited only relatively weak calcium responses, the $A\beta_{1-42}$ peptides from P&E and Synpeptide, which were able to more robustly activate FPRs, displayed significantly elevated β turn proportions. This suggests that increased proportions of β-turn conformation in Aβ peptides may improve their interaction with FPRs. We next examined the influence of different assay buffers on FPR signals. To this end, we first compared the FPR responses to $A\beta_{1-42}$ from P&E dissolved in our assay buffer C1 with those of the two frequently used buffers Hank's balanced salt solution (HBSS) and Tris–NaCl (**Fig 4. 2E**). We detected the most robust activation of human and mouse FPRs in C1. The use of Tris–NaCl lead to an approximately 50% and 20% reduction of the signal amplitude of hFPR1- and hFPR2-based response, respectively

but did not significantly alter the responses of hFPR3. Use of HBSS, by contrast, resulted in a complete loss of nearly all FPR responses. Interestingly, this was clearly correlated with a strong reduction in the capability to form aggregates (**Fig 4. 2F**). Furthermore, we even observed that a longer storage of the dissolved peptides in the freezer can affect the response pattern (**Fig S4. 2**). Next, we carefully examined the effect of the commonly used solvent DMSO on the $A\beta_{1-42}$ response pattern of the individual FPRs (**Fig S4. 3**). Again, we observed a number of subtle changes in the FPR response patterns that were difficult to predict because they largely depended on a specific combi nation of receptor subtype and peptide source. For example, DMSO diminished the hFPR1 response to $A\beta_{1-42}$ from P&E by 40%, whereas it increased the response of hFPR3 by 32%. Despite these variations, our data clearly demonstrate that mFpr1 and hFPR3 were activated under almost all conditions. However, the overall activation pattern of FPRs showed considerable alterations that depend on manufacturing source, assay buffer conditions, storage time, and the pretreatment of $A\beta_{1-42}$ with different solvents. Thus, there is a clear need for standardization and careful description of all **Experimental procedures**.

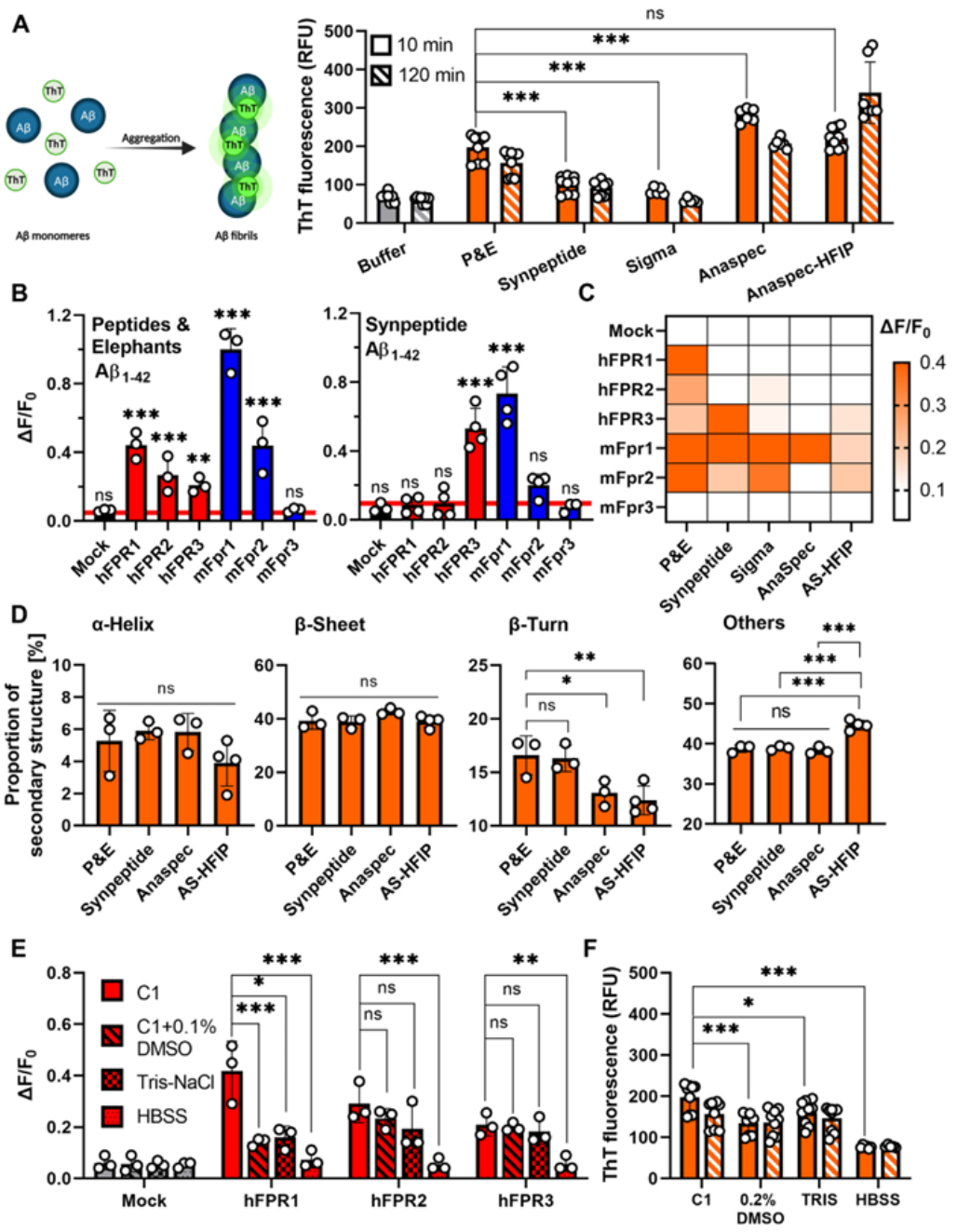

Figure 4. 2 Manufacturer- and solvent-effects on FPR activation by Aβ1-42. (A) left: Schematic depiction of ThT aggregation assay. Right: Mean fluorescence of 22.5 µM Aβ1-42 in C1 buffers from different manufacturers in a ThT aggregation assay during the first 10 min (clear bars) versus fluorescence after 120 min (striped bars). Buffer refers to ThT fluorescence without addition of peptides (gray bars). All n = 3, N = 3, except for Sigma and Anaspec with n = 2, N = 3; One-way ANOVA test, Dunnett post hoc test. (B) Mean Ca^{2+} peak responses of human (red) or mouse (blue) FPRs to 10 µM of Aβ1-42 peptides

obtained from Peptides & Elephants (P&E) and Synpeptide; n = 3, N = 2, One-way ANOVA test, Dunnett post hoc test in comparison to respective buffer controls. (C) Heat map of mean Ca^{2+} responses of FPRs elicited by $A\beta_{1-42}$ peptides obtained from five different manufacturers. The scale ranges from white (no response) to deep orange ($\Delta F/F0 \geq 0.4$). Responses are shown in **Figure S4. 1B**. (D) Secondary structure composition of four $A\beta_{1-42}$ peptides analyzed by circular dichroism (CD) spectroscopy; n = 3, N = 1; One-way ANOVA test, Tukey post hoc test. (E) Mean Ca^{2+} peak responses of cells transfected with human FPRs (red) or mock (gray) towards 5 µM $A\beta_{1-42}$ dissolved in the respective buffers; n = 3, N = 1, One-way ANOVA test, Dunnett post hoc test. (F) Comparison of ThT fluorescence of $A\beta_{1-42}$ (P&E) dissolved in either C1, dimethyl sulfoxide (DMSO), Tris–NaCl, or HBSS. All assays were performed in the respective buffers. For experiments with peptides predissolved in DMSO, assays were conducted in C1 with a final concentration of DMSO: 0.2% (V/V). One-way ANOVA test, Dunnett post hoc test. All Error bars, S.D.; *$p \leq 0.05$; **$p \leq 0.01$; ***$p \leq 0.001$; ns, no significance. Aβ, amyloid beta; FPR, Formyl peptide receptor; ThT, thioflavin T. Copyright 2022, Elsevier.

4.3.3. N-Abridged Aβ-Fragments are Potent Activators of Mouse and Human FPR1

Under *in vivo* conditions, not only $A\beta_{1-42}$ but several other fragments such as $A\beta_{1-40}$, $A\beta_{11-40}$, and $A\beta_{17-40}$ are also generated during the cleavage of APP and its subsequent processing.[12,53,54] Thus, it is conceivable that FPRs can also interact with some of these fragments. To test this hypothesis, we investigated the response of FPRs to the commonly found $A\beta_{1-40}$ the N-abridged variants $A\beta_{11-40}$ and $A\beta_{17-40}$ and the C-terminally abridged fragments $A\beta_{1-10}$ and $A\beta_{1-16}$ (**Fig 4. 3A**). We observed that longer C-terminal deletions tend to be detrimental for the activation of FPRs because fragments such as $A\beta_{1-10}$ and $A\beta_{1-16}$ failed to induce any Ca^{2+} mobilization. In sharp contrast, the two tested N abridged variants $A\beta_{11-40}$ and $A\beta_{17-40}$ elicited responses on all FPRs that we could previously activate with the full-length $A\beta_{1-42}$. Unlike the responses to the full-length $A\beta_{1-42}$, the FPR responses to these shorter fragments seemed to be less prone to manufacturer-dependent variations (**Fig S4. 4**). Surprisingly, N-terminal deletions tended to strongly improve the interaction with FPR1. Concentration response curves revealed that mouse and human FPR1 could detect both N abridged fragments with more than 10-fold higher sensitivity than the full-length

peptide Aβ$_{1-42}$. (**Fig 4. 3 B and C**). Mouse and human FPR2 only responded to micromolar concentrations of these peptides (**Fig 4. 3B**). The observation that Aβ$_{11-40}$ and Aβ$_{17-40}$ can already induce an activation of mouse and human FPR1 at 30 to 100 nanomolar concentration raises the possibility that the detection of these short fragments through FPR1 might be even more relevant for the physiological response than the activation of FPR2 by longer Aβ at micromolar concentration.

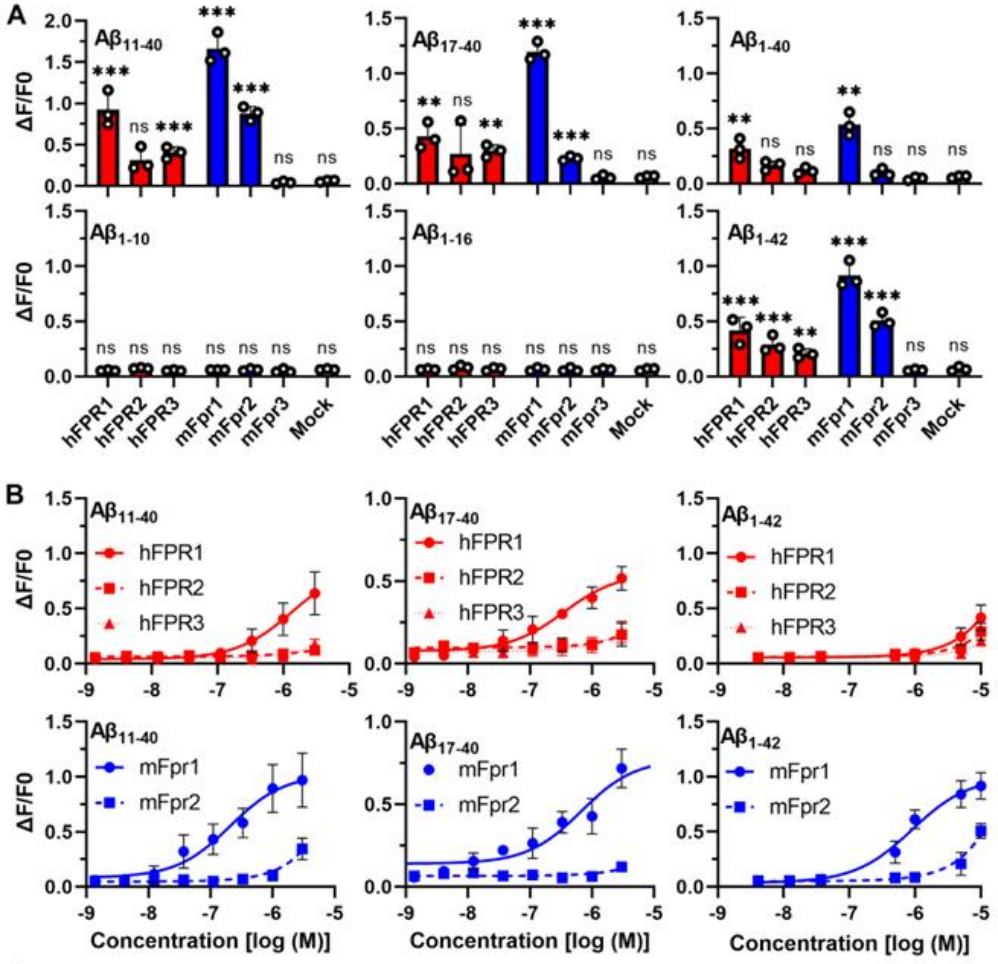

	Aβ$_{17-40}$	Aβ$_{11-40}$	Aβ$_{1-40}$	Aβ$_{1-42}$
hFPR1	100 nM	100 nM	3 µM	3 µM
hFPR2	1 µM	1 µM	3 µM	3 µM
hFPR3	1 µM	1 µM	3 µM	3 µM
mFpr1	30 nM	30 nM	500 nM	500 nM
mFpr2	1 µM	1 µM	5 µM	3 µM
mFpr3	/	/	/	/

Figure 4. 3 Naturally occurring N-abridged Aβ fragments activate FPR1 tenfold better than $Aβ_{1-42}$. (A) Comparison of mean Ca^{2+} peak responses of human (red) or mouse (blue) FPRs to a stimulation with 10 µM $Aβ_{1-40}$ and $Aβ_{1-42}$ or 5 µM of the natural occurring N-abridged variants $Aβ_{11-40}$ and $Aβ_{17-40}$ or with 10 µM of the C-abridged variants $Aβ_{1-10}$ and $Aβ_{1-16}$. Colored bars indicate responses of human (red) or mouse (blue) FPRs, n = 3, N = 1. (B) Concentration response curves of selected variants, n = 3, N = 1. (C) Left: scheme indicating the size and location of the different Aβ variants. Right: Table depicting the proposed 3D-structures and thresholds for minimal detectable activation during Ca^{2+} imaging of the responding Aβ variants. All Error bars, S.D. One-way ANOVA test, Dunnett post hoc test; **p ≤ 0.01; ***p ≤ 0.001; ns, no significance. Aβ, amyloid beta; FPR, Formyl peptide receptor. Copyright 2022, Elsevier.

4.3.4. N-Abridged Aβ Variants are Potent Activators for a Human Glia Cell Line

So far, our study focused on the characterization of the FPR pharmacology in an in vitro over-expression–based system. Despite the strength of this system to dissect responses of the individual FPRs to Aβ, we cannot exclude that differences in the signal transduction system of HEK293T cells or the overexpression of the receptors may affect our pharmacological results. We therefore sought to validate our results in a more biologically relevant setting. To this end, we examined the responses elicited by $Aβ_{11-40}$ and $Aβ_{17-40}$ in U87 cells (**Fig 4. 4**) that are commonly used as a human glial cell model and are known for their natural expression of FPRs.[55,56] We first used reverse transcription polymerase chain reaction and reverse transcription quantitative polymerase chain reaction to examine the expression of the individual FPRs in these cells. Our data revealed that these cells show high mRNA levels of hFPR1 but only a very modest expression of hFPR2 and hFPR3 (**Fig 4. 5A and S4. 6A and S4. 7**). Immunocytochemistry with receptor subtype specific antibodies (**Fig 4. 5B and S4. 5**) confirmed a robust expression of hFPR1 and lower amounts of hFPR2. Interestingly, hFPR3 showed a relatively abundant protein amount despite low amounts of mRNA which is consistent with similar findings for mFpr3 expression in mouse immune cells.[57]

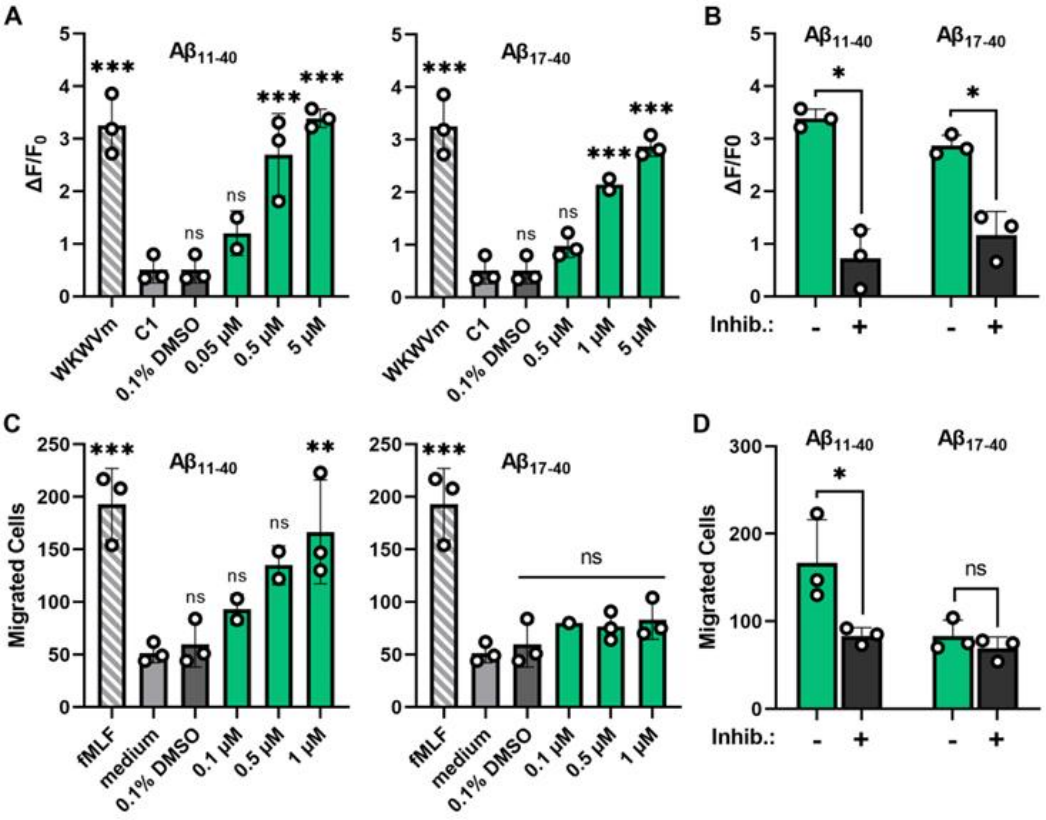

Figure 4. 4 N-abridged Aβ peptides induce hFPR1-dependent responses in glial U87 cells. (A) Mean Ca^{2+} peak responses of U87 cells after stimulation with different concentrations of $A\beta_{11-40}$ or $A\beta_{17-40}$. Striped bars indicate the response towards 10 µM of the positive control WKWVm-NH_2, light gray and dark gray bars indicate negative controls; n = 3, N = 1. (B) Comparison of the Ca^{2+} responses upon stimulation with either 5 µM $A\beta_{11-40}$ or $A\beta_{17-40}$ alone (green bars) or in the presence of 10 µM of the competitive FPR-antagonist tBoc2 (black bars); n = 3, N = 1. (C) Dose-dependent chemotaxis of U87 cells upon stimulation with either $A\beta_{11-40}$ or $A\beta_{17-40}$. Each bar represents the number of cells that migrated through a porous membrane towards the respective stimuli. Green bars indicate migration towards N-abridged fragments, striped bars display migration towards the positive control 1 µM fMLF, light gray bars show migration without stimuli, and dark gray bars represent the response to 0.1% DMSO, n = 3, N = 1. (D) Migration of U87 cells that were either untreated (green bars) or treated with 10 µM tBoc2 (black bars) towards 1 µM of $A\beta_{11-40}$ or $A\beta_{17-40}$; n = 3, N = 1. All Error bars, S.D. One-way ANOVA test, Dunnett post

hoc test for A and C and t test for B and D; *p ≤ 0.05; **p ≤ 0.01; ***p ≤ 0.001; ns, no significance. Aβ, amyloid beta; FPR, Formyl peptide receptor. Copyright 2022, Elsevier.

Calcium imaging experiments revealed that a stimulation with $A\beta_{11-40}$ and $A\beta_{17-40}$ resulted in a pronounced activation of U87 cells (**Fig 4. 4 A and B**) that were closely similar to the typical FPR time kinetics[49] observed in the transfected HEK cells (**Fig 4. 1**). In chemotaxis experiments, only $A\beta_{11-40}$ but not $A\beta_{17-40}$ induced migration of these cells (**Fig 4. 4 C and D**). Both the calcium signals and the chemotaxis were FPR dependent because a co-application of tBoc2, which is a competitive antagonist of FPR1 and FPR2 but does not inhibit FPR3 (**Fig S4. 6B**), completely abolished the responses. To address the question which FPR exactly is responsible for the observed results, we first compared the U87 concentration response curves of $A\beta_{11-40}$ and $A\beta_{17-40}$ with those of FPR-transfected HEK293T cells. We found them to be remarkably similar to hFPR1 (**Fig 4. 5C**). Next, we used receptor subtype-specific activators to test which receptor can trigger a calcium signal. To this end, we challenged U87 cells and hFPR-transfected HEK293T cells with two bacterial signal peptides SP6 and SP4 at concentrations where they would only activate either hFPR1 or hFPR2, respectively.[49] Of note, both compounds would not activate hFPR3 (**Fig S4. 6C**). In line with our previous notion that responses to the N-abridged Aβ variants likely depend on hFPR1, the U87 cells only responded to the hFPR1 specific SP6 stimulus with a calcium signal but not to the hFPR2-specific SP4 stimulus (**Fig 4. 5D and S4. 6C**). Next, we performed cross-desensitization experiments, which showed that responses of U87 cells towards $A\beta_{17-40}$ were absent after pre-application of the FPR1-specific agonist SP6 but were not influenced by pre-application of the FPR2-specific agonist SP4 (**Fig 4. 5E**). Finally, in the chemotaxis assay, U87 cells only migrated towards the FPR1-specific SP6 but not towards the FPR2-specific SP4 (**Fig 4. 5F**). Taken together, these experiments strongly argue that the sensitive calcium and chemotaxis responses of U87 to N-abridged Aβ variants depend on an activation of hFPR1.

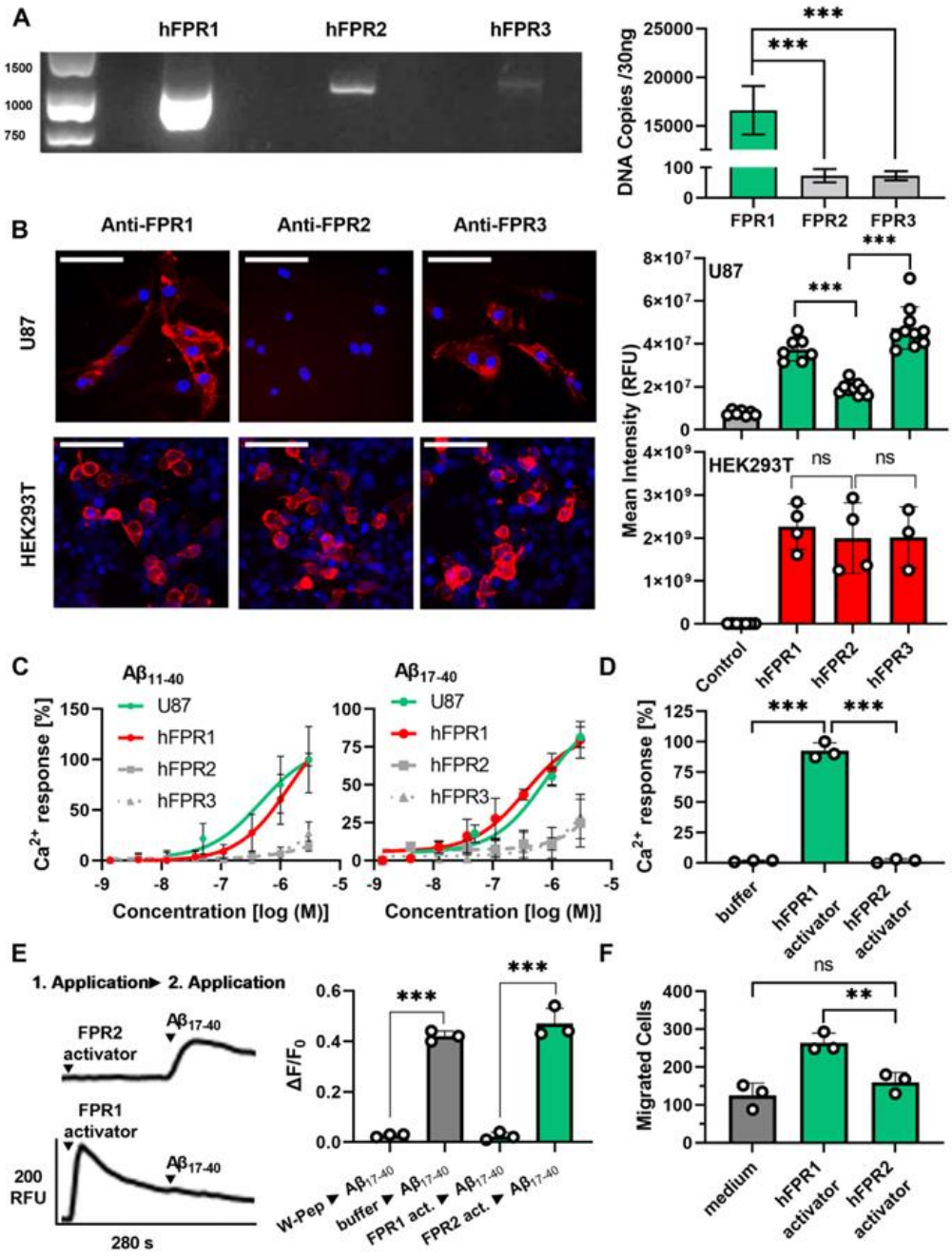

Figure 4. 5 The activation of U87 cells by N-abridged Aβ peptides depends on hFPR1. (A) PCR experiments show that U87 cells contain high mRNA levels of hFPR1 but only low amounts of FPR2 and FPR3. Left: Representative image of gel electrophoresis after reverse transcription polymerase chain reaction with primers for all hFPRs. Right: Quantification of complementary DNA for all FPRs obtained through reverse transcription quantitative polymerase chain reaction, n = 5, N = 2. Details on the primer efficiency, specificity, and linearity are given in **Figures S4. 6 and S4. 7**. One-way ANOVA test,

Dunnett post hoc test. (B) Left: representative immunocytochemistry staining of U87 cells and transfected HEK293T cells with FPR subtype–specific antibodies (red) and nuclei staining (blue). For visibility, brightness and contrast were adjusted for U87 cells and HEK293T cells differently; for absolute intensity comparison pictures with equal settings for exposure time, brightness and contrast pictures are shown in **Figure S4. 5**. Scale bars indicate 100 µm. Right: Quantification of the mean FPR staining in U87 cells (green) in comparison to FPR-transfected HEK293T cells (red). Analysis was performed on images acquired with the same settings. n = 2, N =5 for U87 cells and n = 2, N = 2 for HEK293T cells. Evidence for closely similar staining intensities of FPR1 and FPR2 by the used protocols is shown in **Figure S4. 5**. One-way ANOVA test, Tukey post hoc test. (C) The concentration-dependent Ca^{2+} responses of HEK293 cells and U87 cells towards the N-abridged fragments $A\beta_{11-40}$ and $A\beta_{17-40}$ reveal a clear correlation with the hFPR1 response, n = 3, N = 1. (D) U87 cells respond to the potent hFPR1 activator SP6 (10 nM) but not to a potent hFPR2 agonist SP4 (10 nM) in calcium imaging experiments, n = 3, N = 3. One-way ANOVA test, Dunnett post hoc test. E, Cross desensitization experiment of U87 cells show that the Ca^{2+} responses towards $A\beta_{17-40}$ are abolished by the FPR1 activator SP6 but not by the hFPR2 agonist SP4. Representative Ca^{+} traces (left) and mean Ca^{2+} peak responses (right) to a secondary $A\beta_{17-40}$ stimulus after pre-application of SP4 or SP6 as a first stimulus, n = 1, N = 3; t test. (F) U87 migrate towards the hFPR1-stimulus SP6 (10 nM) but do not respond to the hFPR2 agonist SP4 (10 nM), n = 3, N = 1. One way ANOVA test, Tukey post hoc test. All Error bars, S.D. *$p \leq 0.05$, **$p \leq 0.01$, ***$p \leq 0.001$; ns, no significance. Aβ, amyloid beta; FPR, Formyl peptide receptor.

4.4.Conclusions

In summary, our study provides a systematic overview over the capability of different mouse and human FPRs to interact with Aβ in different buffer systems. To our knowledge, we are the first to report an activation of hFPR3 by Aβ and the first to identify N-abridged Aβ fragments as activators of FPRs. Moreover, our data show that hFPR1 and its mouse ortholog mFpr1 can recognize N-terminally abridged fragments such as $A\beta_{11-40}$ and $A\beta_{17-40}$ at drastically lower concentrations than longer peptides such as $A\beta_{1-40}$ and $A\beta_{1-42}$, which raises the possibility that FPR1 might be more relevant for the pro-inflammatory

physiological responses to Aβ than FPR2. Interestingly, several independent lines of evidence from literature are highly consistent with this hypothesis. First, FPR1 is already expressed at the resting state of glial cells and is further upregulated during their transformation into the reactive state.[58] Next, mFpr1 is highly upregulated in the cortex and hippocampus of transgenic APP/PS1 mice, which are a commonly used AD animal model.[35] Moreover, FPR1 has been shown to mediate typical pro-inflammatory effects in glial cells that are also commonly observed in AD such as generation of oxidative stress, release of inflammatory cytokines and chemokines, and the induction of cell migration,[14,35] whereas several reports suggest an anti-inflammatory role of FPR.[41,43,59] Next, treatment of APP/PS1 mice with the competitive FPR antagonist tBoc2 that preferentially binds to FPR1[26] leads to reduced microglia reactivity, decreased neuronal pathology, and improved cognitive performance.[45] Taken together, these findings strongly support our notion that FPR1 and other FPR variants contribute to neuro inflammation of AD through their ability to sense different Aβ variants. Of note, this contribution might be rather complex because we here observed that abridged variants sometimes trigger partially different signaling pathways (e.g., calcium signaling only for $A\beta_{17\text{-}40}$ or calcium signaling and migration for $A\beta_{11\text{-}40}$) likely through exclusive activation of the identical receptor. Next, a given Aβ peptide will show a concentration dependent interaction with different FPR receptors. Finally, other pro- and anti-inflammatory FPR ligands such as Annexin A1,[43,60] Lipoxin A 4,[61,62] Resolvin,[62] or mitochondrial peptides[63] may further modulate these signals depending on their local concentration. However, the observed 10- to 30-fold higher affinity of FPR1 to N-abridged fragments insinuates that such fragments might be of high pathological relevance for AD if they occur under physiological conditions in sufficient concentrations. Indeed, several studies suggest that $A\beta_{11\text{-}40/42}$ is present in the cerebrospinal fluid at similar concentrations as $A\beta_{1\text{-}42}$ and is furthermore an integral part of senile plaques.[53,64,65] $A\beta_{17\text{-}40/42}$ is thought to occur at 4-fold higher rates than $A\beta_{1\text{-}42}$ and $A\beta_{11\text{-}40/42}$, however, its exact quantification is difficult and therefore often disregarded.[54] In accordance with our data, both $A\beta_{11\text{-}40}$ and $A\beta_{17\text{-}40}$ were shown to activate glial cells, which is associated with the neurotoxic effects seen in AD.[52,65] Moreover, our observation that $A\beta_{11\text{-}40}$– but not $A\beta_{17\text{-}40}$– induced chemotaxis of U87 cells is in line with previous results that show that $A\beta_{17\text{-}40/42}$ and $A\beta_{17\text{-}43}$ only lead to a partial activation of human glial cells.[52,66]

Thus, to the best of our knowledge, our data are consistent with a model in which recognition of these N abridged Aβ variants via FPR1 could thus occur under physiological conditions. Finally, our results clearly demonstrate that the precise FPR responses towards different Aβ variants are highly subjectable to solvent- and manufacturer-dependent effects. Factors such as the secondary structure, 3D conformation, and aggregation therefore seem to be of high importance for the precise activation pattern, and different receptor subtypes seem to prefer different peptide structures or exposed surfaces. Multiple previous studies have already shown that different buffer systems and solvents can critically influence properties of Aβ such as its aggregation kinetics and the structure of its aggregates.[20,51,52] For example, Szczepanik et al.[52] observed differences in Aβ-dependent cytokine release depending on the solvent of their peptides. We assume that variations within our measurements occur due to the formation of aggregates and fibers captured by TEM images and variations in the secondary structure as indicated by our CD. In accordance with this idea, in previous studies, both monocytes and microglia lost FPR dependent signaling with progressing aggregation of $A\beta_{1-42}$.[36,67] Of note, it is conceivable that chemical modifications of the peptide, for example, oxidation of methionine at position 35, racemization, or isomerization may contribute to the functional differences that we observed for an identical peptide in different buffer systems. This needs to be further examined. However, our data also show that it is necessary to develop a generally accepted standardized protocol for the investigation of FPR-related effects on Aβ peptides. In many fields, the use of similar assay conditions has thus improved the reproducibility and quality of data.[20] Based on our current results, we would like to recommend the following protocol (see **Fig 4. 6**). We propose to validate any observed Aβ effects with a peptide from second supplier. Next, we would like to encourage researchers to also include negative results with peptides from other sources. All experiments should be performed using single use aliquots from a freshly dissolved frozen stock. Next, any stocks that are stored should be examined for "aging" effects. We also suggest the use of low complexity buffer systems such as our C1 buffer and avoid cosolvents such as DMSO if possible. In case DMSO or other cosolvents are used, their effects on aggregation and physiological response need to be controlled and reported. All experiments should be performed within the same standardized time in order to have a similar amount of aggregation. Finally, we suggest to always include

at least some data on the aggregation status and time kinetics of the peptides in a given buffer system, which can be easily done with simple inexpensive methods such as ThT assays. Moreover, we would like to encourage a very detailed description of all experimental conditions that may affect the aggregation as Supporting material. Especially, the peptide source including lot numbers, purity, used solvents, precise assay buffer composition, pH, incubation time, storage time, storage conditions, and final concentration of cosolvents in an assay should be reported because this all can critically influence the results.

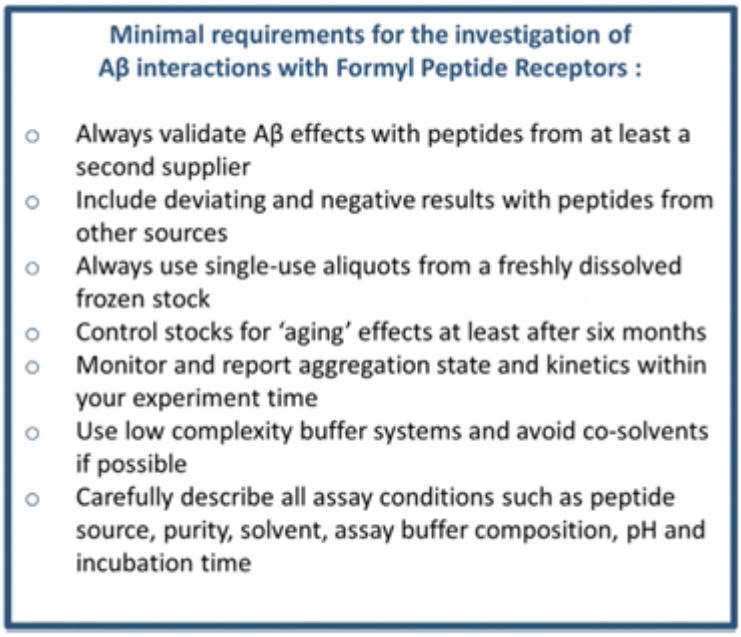

Figure 4. 6 Minimal requirements for the investigation of Aβ interactions with FPRs. Aβ, amyloid beta; FPR, Formyl peptide receptor. Copyright 2022, Elsevier.

4.5.Experimental Procedures

Cloning of human and murine FPR genes. Human hFPR1, hFPR2, and hFPR3 and murine mFpr1, mFpr2, and mFpr3 were amplified from genomic human or C57BL/6J murine DNA, respectively and subcloned into pcDNA3.1$^{(+)}$ (Invitrogen) as previously described.[49]

Ligands and chemicals. Purity of all peptides was at least >95%. Details on manufacturer, Catalog numbers, lot numbers, exact purity of all peptides, solvents, and storage conditions are given in **Table S4. 1**. The amino acid composition of all Aβ peptides corresponded to the human WT sequence. $A\beta_{1-42}$ peptides were purchased from Anaspec/MoBiTec, Peptides&Elephants, and Sigma-Aldrich or synthesized by Synpeptide. All $A\beta_{1-42}$ peptides were dissolved at 30 μM in C1 assay buffer (130 mM NaCl, 10 mM Hepes, 5 mM KCl, 2 mM $CaCl_2$, pH 7.2, all purchased from Carl Roth). To fully dissolve the peptides in C1, they were placed in an ultrasonic bath for usually 5 to 10 min at room temperature until all precipitates had vanished. Peptides dissolved in an aqueous solution were then aliquoted for single use, immediately stored at −20 °C, and used up within 6 weeks because longer storage may affect the results. If not otherwise stated, experiments were performed with $A\beta_{1-42}$ dissolved in C1. For selected experiments (**Table S4. 1**) where we investigated the effects of different solvents $A\beta_{1-42}$ from Anaspec/MoBiTec, P&E, and Synpeptide were dissolved at 5 mM in DMSO (Sigma-Aldrich), $A\beta_{1-42}$ from P&E was additionally dissolved at 30 μM in HBSS (140 mM NaCl, 5 mM KCl, 1 mM $CaCl_2$, 0.4 mM magnesium sulfate heptahydrate, 0.5 mM magnesium chloride hexahydrate, 0.3 mM sodium phosphate dihydrate, 0.4 mM potassium phosphate, 4 mM sodium bicarbonate, pH 7.2, all purchased from Carl Roth) or Tris–NaCl (50 mM Tris, 150 mM NaCl, pH 7.2). Peptides in HBSS or Tris–NaCl were dissolved in an ultrasonic bath as described above. HFIP-pretreated $A\beta_{1-42}$ (in the main text referred to as Anaspec-HFIP) was purchased as AggreSure $A\beta_{1-42}$ from Anaspec/MoBiTec and dissolved at 5 mM in DMSO for calcium imaging experiments or in Tris–NaCl (50 mM Tris, 150 mM NaCl, pH 7.2) for aggregation assays. $A\beta_{1-40}$, $A\beta_{1-10}$, and $A\beta_{1-16}$ were purchased from Anaspec/ MoBiTec. The $A\beta_{17-40}$ peptide used throughout the main text was purchased from Anaspec/MoBiTec and validated with $A\beta_{17-40}$ peptides from Sigma-Aldrich and Synpeptide. $A\beta_{11-40}$ was obtained from Peptides&Elephants. $A\beta_{1-10}$ and $A\beta_{1-16}$ were dissolved in C1 as a 1 mM stock solution and $A\beta_{1-40}$ at 30 μM as

described above. Due to their high hydrophobicity, $A\beta_{11-40}$ and $A\beta_{17-40}$ were dissolved in DMSO at 5 mM. Tert Boc-FLFL (tBoc2) was purchased from Bachem and dissolved in DMSO at 30 mM. f-MLFYFS (Psy-SP6) and f-MAMKKL (Sal-SP4) were obtained from VCPBIO and dissolved at 10 mM in DMSO (Psy-SP6) or at 1 mM in C1 (SP4), respectively. WKWMVm-NH_2 and WKWMVm-CHO were purchased from Proteogenix and VCPBIO, respectively, and dissolved as 1 Mm stock solutions in C1. fMLF was purchased from Sigma Aldrich and also dissolved at 1 mM in C1. All peptides were thawed at room temperature approximately 1 h before each functional experiment, as this time was needed to prepare the compound plates for each measurement.

Cell culture and transient transfections. HEK293T cells (ATCC) were cultured in Dulbecco's Modified Eagle's medium (DMEM, Biowest) supplemented with 10% (v/v) heat-inactivated fetal calf serum (FCS, Pan Biotech), 1 unit/ml penicillin-streptomycin (Biowest), and 2 mM L-glutamine (Biowest) until 80% confluence. For transfection, approximately 2000 cells were seeded in each well of poly-D-lysine–coated (PDL) (10 µg/ml in PBS, Sigma) black optical 96-well µCLEAR-plates (Greiner Bio-One). Cells were transfected after 24 h using jetPEI (Polyplus-transfection SA) with 0.125 µg of DNA plasmids encoding the respective receptors and equal amounts of a plasmid encoding the G protein subunit Gα16 since this subunit is needed to trigger FPR-dependent calcium signals in HEK293 cells.[49,68] The medium of transfected cells was changed 24 h after transfection. For mock transfections, the proportion of the FPR containing plasmids were substituted by an empty pcDNA3.1 vector. U87 MG cells (CLS) were cultured in Minimum Essential medium (Biowest) supplemented with 10% (v/v) heat-inactivated FCS (Pan Biotech), 1 unit/ml penicillin-streptomycin (Biowest), 2mML-glutamine (Biowest), and 1unit/ml non-essential amino acids (Biowest) until 50 to 60% confluence. For calcium imaging and immunostaining, on average 2500 cells were seeded in each well of PDL-coated (10 µg/ml in PBS, Sigma) black optical 96 well µCLEAR-plates (Greiner Bio-One).

Calcium imaging. Cell population responses of transfected HEK293T cells and U87 cells were recorded using a Flexstation III microplate reader (Molecular Devices). Briefly, cells were incubated with 2 µM Calbryte 520 AM (AAC Bioquest) for 2 h at room temperature

in C1 assay buffer with 5 mM glucose (Carl Roth). Before each experiment, cells were rinsed three times with C1. Experiments with HEK293T cells were conducted 48 h after transfection, while experiments with U87 cells were performed 24 h after seeding. Acquisition of baseline fluorescence was performed for 25 s before ligand application, and cell population response was measured for 125 s after application. Responsiveness of cells was controlled by the appropriate buffer and solvent controls and with 10 µM WKWMVm-NH_2 or WKWMVm-CHO as those ligands are potent activators of all three human and mouse FPRs.[49]

Chemotaxis assays. Cell migration assays were performed and analyzed with an IncuCyte S3 Life Cell Imaging System (EssenBio Science). Briefly, U87 cells were harvested and resuspended in Minimum Essential medium (Biowest) supplemented with 0.5% (v/ v) heat-inactivated FCS (Pan Biotech), 1 unit/ml penicillin streptomycin (Biowest), 2 mM L-glutamine (Biowest), and 1 unit/ml non-essential amino acids (Biowest). Approximately, 1000 cells were placed into the top chamber of each well of a 96-well ClearView Plate (EssenBioscience). Chemoattractants were mixed in 200 µl medium and then placed in the corresponding bottom chambers. Image acquisition was performed hourly for 24 h on both sides of a membrane separating the top and bottom chambers. Subsequent analysis was performed using the IncuCyte S3 software.

Immunostaining. Approximately, 2000 HEK293T cells or 3500 U87 cells were seeded in each well of a PDL-coated black optical 96-well µCLEAR-plate (Greiner Bio-One). Transient transfection of HEK293T cells was performed as described above. Twenty four hours after transfection, cells were fixated with 4% [v/v] methanol-free paraformaldehyde (Polyscience Inc) in PBS for 30 min at RT and afterward rinsed with PBS. After blocking with 5% [v/v] FCS in PBS for 30 min at RT, primary antibodies diluted in blocking solution were applied to the cells and incubated over night at 4 °C. Hereby, monoclonal antibodies for hFPR1 (R&D Systems, MAB3744, 1 µg/ml), hFPR2 (Santa Cruz Biotechnology, sc-57141, 0.2 µg/ml), and hFPR3 (R&D Systems, MAB3896, 1 µg/ml) were used. Cells were rinsed three times with PBS and subsequently treated with 2 µg/ml polyclonal alpaca anti-mouse antibody conjugated with Alexa Fluor 568 (Invitrogen) and 2 µM Hoechst 33342

(Thermo Fisher) for 60 min at RT. Image acquisition was performed with a Molecular Devices ImageXpress Micro confocal microscope and analyzed using MetaXpress software (Molec ular Devices).

PCR analysis. Total RNA was isolated using AnalytikJena innuPREP RNA Kit according to the manufacturer's protocol. Reverse transcription was carried out using 30 ng of total RNA and Superscript II Reverse Transcriptase (ThermoFisher Scientific). Initial reverse transcription polymerase chain reaction experiments were performed using DreamTaq DNA polymerase (ThermoFisher Scientific) with primers (Sigma-Aldrich) comprising the full coding region with complementary DNA (cDNA) obtained from 0.3 ng total RNA in a total reaction volume of 20 µl. PCR conditions were as follows: 95 °C for 3 min, 35 cycles at 95 °C for 30 s, 64 °C for 30 s, and 72 °C for 60 s, followed by a final extension of 72 °C for 10 min. qPCRs were performed with the Biozym Blue S'Green qPCR Kit according to the MIQE guidelines.[69] Reverse transcription quantitative polymerase chain reaction reactions were carried out with cDNA obtained from 0.15 ng total RNA as duplicates in 20 µl total reaction volume. PCR conditions were as follows: 95 °C for 3min, 32 cycles at 95 °C for 5s, 66 °C for 10s, and 66 °C for 10 s. Representative samples of all PCR products were assessed by gel electrophoresis and sequencing for their quality. Absolute quantification of DNA copies was calculated according to the specific standard curves supplemented in **Figure S4. 6**. For qPCR for calibration curves, a dilution series of a sequenced and purified PCR product in 2 ng/µl yeast tRNA (Sigma Aldrich) was used. In addition, relative quantifications for a house keeping gene were performed using GAPDH. All PCRs were performed in a TOPical T-Gradient thermocycler (Biometra). Primer sequences are given in **Table S4. 2.**

ThT aggregation assay. For the experiments in C1 buffer, $A\beta_{1-42}$ peptides were dissolved as 30 µM stock solutions. For experiments with different buffers, $A\beta_{1-42}$ from P&E was dissolved either at 5 mM in DMSO or at 30 µM in HBSS or Tris–NaCl as described above. HFIP-treated $A\beta_{1-42}$ was dissolved at 5 mM in DMSO and measured in C1 with a final concentration of 0.2% [v/v] DMSO. ThT (Sigma-Aldrich) stock solutions were dissolved at 1 mM in the respective buffer, sterile filtered with 0.2 µM pore membranes, and stored

at −20 °C. Aβ peptides were combined with ThT stocks to produce working solutions with final concentrations of 22.5 μM $A\beta_{1-42}$ and 250 μM ThT in the respective buffer. Fluorescence measurements were carried out as 100 μl triplicates in black optical 384-well μCLEAR-plates (Greiner Bio-One) at 37 °C with excitation at 440 nm and emission at 484 nm in a FlexStation III microplate reader within 15 min after thawing of the peptides. Signals were measured in intervals of 60 s for 120 min and were shaken for 3 s before each read.

Binding assay. Approximately, 2000 HEK293T cells were seeded in each well of a PDL-coated black optical 96-well plate and transfected as described above. Forty eight hours after transfection, cells were treated with 1 μM of FITC-labeled WKWVm-NH2 and 20 μM Hoechst 33342 diluted in DMEM and incubated for 30 min at 37 °C and 5% CO_2. Cells were then rinsed ten times with C1. Image acquisition was performed with a Molecular Devices ImageXpress Micro confocal microscope and analyzed using MetaXpress software (Molecular Devices)

CD spectroscopy. Thirty micromolar of $A\beta_{1-42}$ dissolved in C1 were sonicated for 10 min before CD measurement. CD spectra were recorded (JASCO J-1500 spectrometer) in a 1 mm High Precision Cell (Hellma Analytics). Data were processed in Spectra Analysis by JASCO and were plotted by Origin.

Transmission electron microscopy. Thirty micromolar of $A\beta_{1-42}$ peptide solution was first incubated for 24 h and then deposited on Formvar/carbon film–coated copper grids (Plano GmbH). Samples were then stained with 4% uranyl acetate. Subsequently, TEM images were acquired (JEOL 1400 Transmission Electron Microscope) and then processed in ImageJ.

Statistical methodology. Statistical significances were calculated using either the unpaired student's t-test with assumption of Gaussian distribution or one-way ANOVA with Dunnett's or Tukey's multiple comparisons post hoc analysis. Calculations were performed using GraphPad Prism 9.2.

4.6.Acknowledgments

We thank Karl-Herbert Schäfer (University of Applied Sciences Kaiserslautern, Zweibrücken) for providing $A\beta_{1-42}$ in pilot studies and for helpful discussions. The 3D models in **Figure 4. 3C** were created using the software Virtual Molecular Dynamics (VMD)[70] based on the structure described by Crescenzi and colleagues.[71] The ThT assay figure was created using BioRender.com and exported under a paid subscription.

4.7.References

(1). Alzheimer Association. 2019 Alzheimer's disease facts and figures. *Alzheimer's Dement*. **2019,** 15, 321–387.

(2). Long, J. M.; Holtzman, D. M. Alzheimer disease: an update on pathobiology and treatment strategies. *Cell* **2019**, 179, 312–339.

(3). Masters, C. L.; Simms, G.; Weinman, N. A.; Multhaup, G.; McDonald, B. L.; Beyreuther, K. Amyloid plaque core protein in Alzheimer disease and Down syndrome. *Proc. Natl. Acad. Sci. U. S. A*. **1985**, 82, 4245–4249.

(4). Grundke-Iqbal, I., Iqbal, K., Tung, Y. C., Quinlan, M., Wisniewski, H. M., and Binder, L. I. Abnormal phosphorylation of the microtubule associated protein tau (tau) in Alzheimer cytoskeletal pathology. *Proc. Natl. Acad. Sci. U. S. A*. **1986**, 83, 4913–4917.

(5). Kosik, K. S.; Joachim, C. L.; Selkoe, D. J. Microtubule-associated protein tau (τ) is a major antigenic component of paired helical filaments in Alzheimer disease. *Proc. Natl. Acad. Sci. U. S. A*. **1986**, 83, 4044–4048.

(6). Zetterberg, H.; Blennow, K.; Hanse, E. Amyloid β and APP as biomarkers for Alzheimer's disease. *Exp. Gerontol.* **2010**, 45,23–29.

(7). Masters, C. L.; Selkoe, D. J. Biochemistry of amyloid β-protein and amyloid deposits in Alzheimer disease. *Cold Spring Harb. Perspect. Med*. **2012**, 2, a006262.

(8). Akiyama, H.; Barger, S.; Barnum, S.; Bradt, B.; Bauer, J.; Cole, G. M.; Cooper, N. R.; Eikelenboom, P.; Emmerling, M.; Fiebich, B. L.; Finch, C. E.; Frautschy, S.; Griffin, W.S.T.; Hampel, H.; Hull, M.; Landreth, G.; Lue, L.-F.; Mrak, R.; Mackenzie, I. R.; McGeer, P. L.; O'Banion, M.; Pachter, J.; Pasinetti, G.; Plata–Salaman, C.; Rogers, J.; Rydel, R.; Shen, Y.; Streit, W.; Strohmeyer, R.; Tooyoma, I.; Muiswinkel, F. L. V.; Veerhuis, R.; Walker, D.; Webster, S.; Wegrzyniak, B.; Wenk, G.; Wyss–Coray, T. Inflammation and Alzheimer's disease. *Neurobiol. Aging* **2000**, 21, 383–421.

(9). Ries, M.; Sastre, M. Mechanisms of Aβ clearance and degradation by glial cells. *Front. Aging Neurosci*. **2016**, 8, 160.

(10). Haass, C.; Kaether, C.; Thinakaran, G.; Sisodia, S. Trafficking and proteolytic processing of APP. *Cold Spring Harb. Perspect. Med*. **2012**, 2, a006270.

(11). Steiner, H.; Fukumori, A.; Tagami, S.; Okochi, M. Making the final cut: pathogenic amyloid-β peptide generation by γ-secretase. *Cell Stress* **2018**, 2, 292–310.

(12). Busch, L.; Vieten, S.; Brödel, S.; Endres, K.; Bufe, B. Emerging contributions of formyl peptide receptors to neurodegenerative diseases. *Biol. Chem.* **2022**, 403,27–41.

(13). Shea, D.; Hsu, C. C.; Bi, T. M.; Paranjapye, N.; Childers, M. C.; Cochran, J.; Tomberlin, C. P.; Wang, L.; Paris, D.; Zonderman, J.; Varani, G.; Link, C. D.; Mullan, M.; Daggett, V. α-Sheet secondary structure in amyloid β-peptide drives aggregation and toxicity in Alzheimer's disease. *Proc. Natl. Acad. Sci. U. S. A.* **2019**,116, 8895–8900.

(14). Leng, F.; Edison, P. Neuroinflammation and microglial activation in Alzheimer disease: Where do we go from here? *Nat. Rev. Neurol.* **2021**, 17, 157–172.

(15). Guzman-Martinez, L.; Maccioni, R. B.; Andrade, V.; Navarrete, L. P.; Pastor, M. G.; Ramos-Escobar, N. Neuroinflammation as a common feature of neurodegenerative disorders. *Front. Pharmacol.* **2019**, 10, 1008.

(16). Haass, C.; Selkoe, D. J. Soluble protein oligomers in neuro degeneration: lessons from the Alzheimer's amyloid β-peptide. *Nat. Rev. Mol. Cell Biol.* **2007**, 8, 101–112.

(17). Nimmerjahn, A.; Kirchhoff, F.; Helmchen, F. Neuroscience: resting microglial cells are highly dynamic surveillants of brain parenchyma in vivo. *Science* **2005**, 308, 1314–1318.

(18). Rodríguez-Gómez, J. A.; Kavanagh, E.; Engskog-Vlachos, P.; Engskog, M. K. R.; Herrera, A. J.; Espinosa-Oliva, A. M.; Joseph, B., Hajji, N.; Venero, J. L.; Burguillos, M. A. Microglia: agents of the CNS pro-inflammatory response. *Cells* **2020**, 9, 1717.

(19). Tolar, M.; Hey, J.; Power, A.; Abushakra, S. Neurotoxic soluble amyloid oligomers drive Alzheimer's pathogenesis and represent a clinically validated target for slowing disease progression. *Int. J. Mol. Sci.* **2021**, 22, 6355.

(20). Dahlgren, K. N.; Manelli, A. M.; Stine, W. B.; Baker, L. K.; Krafft, G. A.; LaDu, M. J. Oligomeric and fibrillar species of amyloid-β peptides differentially affect neuronal viability. *J. Biol. Chem.* **2002**, 277, 32046–32053.

(21). Wang, J.; Jackson, M. F.; Xie, Y. F. Glia and TRPM2 channels in plasticity of central nervous system and Alzheimer's diseases. *Neural Plast.* **2016**, 1680905.

(22). Wilkinson, K.; Khoury, El. J. Microglial scavenger receptors and their roles in the pathogenesis of Alzheimer's disease. *Int. J. Alzheimers. Dis.* **2012**, 1–10.

(23). Fiebich, B. L.; Batista, C. R. A.; Saliba, S. W.; Yousif, N. M.; de Oliveira, A. C. P. Role of microglia TLRs in neurodegeneration. *Front. Cell. Neurosci.* **2018**, 12, 1–10.

(24). Heneka, M. T.; Kummer, M. P.; Stutz, A.; Delekate, A.; Schwartz, S.; Vieira-Saecker, A.; Griep, A.; Axt, D.; Remus, A.; Tzeng, T.-C.; Gelpi, E.; Halle, A.; Korte, M.; Latz, E.; Golenbock, D. T. NLRP3 is activated in Alzheimer's disease and contributes to pathology in APP/PS1 mice. *Nature* **2012**, 493, 674–678.

(25). Doens, D.; Fernández, P. L. Microglia receptors and their implications in the response to amyloid β for Alzheimer's disease pathogenesis. *J. Neuroinflammation* **2014**, 11,48.

(26). Ye, R. D.; Boulay, F.; Wang, J. M.; Dahlgren, C.; Gerard, C.; Parmentier, M.; Serhan, C. N.; Murphy, P. M. International union of basic and clinical pharmacology. LXXIII. Nomenclature for the formyl peptide receptor (FPR) family. *Pharmacol. Rev.* **2009**, 61, 119–161.

(27). Bloes, D. A.; Kretschmer, D.; Peschel, A. Enemy attraction: bacterial agonists for leukocyte chemotaxis receptors. *Nat. Rev. Microbiol.* **2015**, 13, 95–104.

(28). Dahlgren, C.; Gabl, M.; Holdfeldt, A.; Winther, M.; Forsman, H. Basic characteristics of the neutrophil receptors that recognize formylated peptides, a danger-associated molecular pattern generated by bacteria and mitochondria. *Biochem. Pharmacol.* **2016**, 114, 22–39.

(29). Migeotte, I.; Communi, D.; Parmentier, M. Formyl peptide receptors: a promiscuous subfamily of G protein-coupled receptors controlling immune responses. *Cytokine Growth Factor Rev.* **2006**, 17, 501–519.

(30). Bufe, B.; Zufall, F. The sensing of bacteria: emerging principles for the detection of signal sequences by formyl peptide receptors. *Biomol. Concepts* **2016**, 7, 205–214.

(31). Brandenburg, L. O.; Konrad, M.; Wruck, C. J.; Koch, T.; Lucius, R.; Pufe, T. Functional and physical interactions between formyl peptide-receptors and scavenger receptor MARCO and their involvement in amyloid beta 1-42-induced signal transduction in glial cells. *J. Neurochem.* **2010**, 113, 749–760.

(32). Becker, E. L., Forouhar, F. A., Grunnet, M. L., Boulay, F., Tardif, M., Bormann, B. J., Sodja, D.; Ye, R. D.; Woska Jr, J. R.; Murphy, P. M. Broad immunocytochemical localization of the formylpeptide receptor in human organs, tissues, and cells. *Cell Tissue Res* **1998**, 292, 129–135.

(33). Cattaneo, F.; Guerra, G.; Ammendola, R. Expression and signaling of formyl-peptide receptors in the brain. *Neurochem. Res.* **2010**, 35, 2018–2026.

(34). Colucci, M.; Stefanucci, A.; Mollica, A.; Aloisi, A. M.; Maione, F.; Pieretti, S. New insights on formyl peptide receptor type 2 involvement in nociceptive processes in the spinal cord. *Life (Basel)* **2022**, 12, 500.

(35). Slowik, A.; Merres, J.; Elfgen, A.; Jansen, S.; Mohr, F.; Wruck, C. J.; Pufe, T.; Brandenburg, L. Involvement of formyl peptide receptors in receptor for advanced glycation end products (RAGE)- and amyloid beta 1-42-induced signal transduction in glial cells. *Mol. Neurodegener.* **2012**, 7,1.

(36). Le, Y.; Gong, W.; Tiffany, H. L.; Tumanov, A.; Nedospasov, S.; Shen, W.; Dunlop, N. M.; Gao, J.-L.; Murphy, P. M.; Oppenheim, J. J.; Wang, J. M. Amyloid B 42 activates a G-protein-coupled chemo attractant. *J. Neurosci.* **2001**, 21,2–6.

(37). Brandenburg, L. O.; Konrad, M.; Wruck, C.; Koch, T.; Pufe, T.; Lucius, R. Involvement of formyl-peptide-receptor-like-1 and phospholipase D in the internalization and signal transduction of amyloid beta 1-42 in glial cells. *Neuroscience* **2008**, 156, 266–276.

(38). Tiffany, H. L.; Lavigne, M. C.; Cui, Y. H.; Wang, J. M.; Leto, T. L.; Gao, J. L.; Murphy, P. M. Amyloid-β induces chemotaxis and oxidant stress by acting at formylpeptide receptor 2, a G protein-coupled receptor expressed in phagocytes and brain. *J. Biol. Chem.* **2001**, 276, 23645–23652.

(39). Lorton, D.; Schaller, J.; Lala, A.; De Nardin, E. Chemotactic like receptors and Aβ peptide induced responses in Alzheimer's disease. *Neurobiol. Aging* **2000**, 21, 463–473.

(40). Cui, Y.; Le, Y.; Yazawa, H.; Gong, W.; Wang, J. M. Potential role of the formyl peptide receptor-like 1 (FPRL1) in inflammatory aspects of Alzheimer's disease. *J. Leukoc. Biol.* **2002**, 72, 628–635.

(41). Wickstead, E. S.; Karim, H. A.; Manuel, R. E.; Biggs, C. S.; Getting, S. J.; McArthur, S. Reversal of β-amyloid-induced microglial toxicity in vitro by activation of Fpr2/3. *Oxid. Med. Cell. Longev.* **2020**, 2139192.

(42). Yazawa, H.; Yu, Z.-X.; Takeda, K.; Le, Y.; Gong, W.; Ferrans, V. J.; Oppenheim, J. J.; Li, C. C.; Wang, J. M. β Amyloid peptide (Aβ 42) is internalized via the G-protein coupled receptor FPRL1 and forms fibrillar aggregates in macrophages 1. *FASEB J.* **2001**, 15, 2454–2462.

(43). Zhang, S.; Gong, H.; Ge, Y.; Ye, R. D. Biased allosteric modulation of formyl peptide receptor 2 leads to distinct receptor conformational states for pro- and anti-inflammatory signaling. *Pharmacol. Res.* **2020**, 161, 105117.

(44). Kong, Y.; Ruan, L.; Qian, L.; Liu, X.; Le, Y. Norepinephrine promotes microglia to uptake and degrade amyloid β peptide through upregulation of mouse formyl peptide receptor 2 and induction of insulin-degrading enzyme. *J. Neurosci.* **2010**, 30, 11848–11857.

(45). Schröder, N.; Schaffrath, A.; Welter, J. A.; Putzka, T.; Griep, A.; Ziegler, P.; Brandt, E.; Samer, S.; Heneka, M. T.; Kaddatz, H.; Zhan, J.; Kipp, E.; Pufe, T.; Tauber, S. C.; Kipp, M.; Brandenburg, L. O. Inhibition of formyl peptide receptors improves the outcome in a mouse model of Alzheimer disease. *J. Neuroinflammation* **2020**, 17, 1–15.

(46). Gao, J. L.; Chen, H.; Filie, J. D.; Kozak, C. A.; Murphy, P. M. Differential expansion of the N-formylpeptide receptor gene cluster in human and mouse. *Genomics* **1998**, 51, 270–276.

(47). Liberles, S. D.; Horowitz, L. F.; Kuang, D.; Contos, J. J.; Wilson, K. L.; Siltberg-Liberles, J.; Liberles, D. A.; Buck, L. B. Formyl peptide receptors are candidate chemosensory receptors in the vomeronasal organ. *Proc. Natl. Acad. Sci. U. S. A.* **2009**, 106, 9842–9847.

(48). Boillat, M.; Carleton, A.; Rodriguez, I. From immune to olfactory expression: Neofunctionalization of formyl peptide receptors. *Cell Tissue Res* **2021**, 383, 387–393.

(49). Bufe, B.; Schumann, T.; Zufall, F. Formyl peptide receptors from immune and vomeronasal system exhibit distinct agonist properties. *J. Biol. Chem.* **2012**, 287, 33644–33655.

(50). Bufe, B.; Teuchert, Y.; Schmid, A.; Pyrski, M.; Pérez-Gómez, A.; Eisenbeis, J.; Timm, T.; Ishii, T.; Lochnit, G.; Bischoff, M.; Mombaerts, P.; Leinders-Zufall, T., Zufall, F. Bacterial MgrB peptide activates chemoreceptor Fpr3 in mouse accessory olfactory system and drives avoidance behaviour. *Nat. Commun.* **2019**, 10, 4889.

(51). Nichols, M. R.; Moss, M. A.; Reed, D. K.; Hoh, J. H.; Rosenberry, T. L. Amyloid-beta aggregates formed at polar-nonpolar interfaces differ from amyloid-beta protofibrils produced in aqueous buffers. *Microsc. Res. Tech.* **2005**, 67, 164–174.

(52). Szczepanik, A.M.; Rampe, D.; Ringheim, G. E. Amyloid β peptide fragments p3 and p4 induce pro-inflammatory cytokine and chemokine production in vitro and in vivo. *J. Neurochem.* **2001**, 77, 304–317.

(53). Näslund, J., Schierhorn, A., Hellman, U., Lannfelt, L., Roses, A. D., Tjernberg, L. O., Silberring, J.; Grandy, S. E.; Winblad, B.; Greengard, P. Relative abundance of Alzheimer Aβ amyloid peptide variants in Alzheimer disease and normal aging. *Proc. Natl. Acad. Sci. U. S. A.* **1994**, 91, 8378–8382.

(54). Kuhn, A. J.; Raskatov, J. Is the p3 peptide (Aβ17-40, Aβ17-42) relevant to the pathology of Alzheimer's disease? *J. Alzheimers Dis* **2020**, 74, 43–53.

(55). Boer, J. C.; van Marion, D. M.; Joseph, J. V.; Kliphuis, N. M.; Timmer Bosscha, H.; van Strijp, J. A. G.; de Vries, E. G. E.; den Dunnen, W. F. A.; Kruyt, F. A. E.; Walenkamp, A. M. E. Microenvironment involved in FPR1 expression by human glioblastomas. *J. Neurooncol.* **2015**, 123,53–63.

(56). Boer, J. C.; Domanska, U. M.; Timmer-Bosscha, H.; Boer, I. G.; de Haas, C. J.; Joseph, J. V.; Kruyt, F. A. E.; de Vries, E. G. E.; den Dunnen, W. F. A.; van Strijp, J. A. G.; Walenkamp, A. M. E. Inhibition of formyl peptide receptor in high-grade astrocytoma by CHemotaxis Inhibitory Protein of S. aureus. *Br. J. Cancer* **2013**, 108, 587–596.

(57). Stempel, H.; Jung, M.; Pérez-Gómez, A.; Leinders-Zufall, T.; Zufall, F.; Bufe, B. Strain-specific loss of Formyl peptide receptor 3 in the murine vomeronasal and immune systems. *J. Biol. Chem*. **2016**, 291, 9762–9775.

(58). Calvello, R.; Cianciulli, A.; Porro, C.; Moda, P.; De Nuccio, F.; Nicolardi, G.; Giannotti, L.; Panaro, M. A.; Lofrumento, D. D. Formyl peptide receptor (Fpr)1 modulation by resveratrol in an lps-induced neuroinflammatory animal model. *Nutrients* **2021**, 13, 1418.

(59). Wickstead, E. S.; Irving, M. A.; Getting, S. J.; McArthur, S. Exploiting formyl peptide receptor 2 to promote microglial resolution: a new approach to Alzheimer's disease treatment. *FEBS J.* **2021**, 289, 1801–1822.

(60). Walther, A.; Riehemann, K.; Gerke, V. A novel ligand of the formyl peptide receptor: annexin I regulates neutrophil extravasation by interacting with the FPR. *Mol. Cell* **2000***,* 5, 831–840.

(61). Filep, J. G. Biasing the lipoxin A4/formyl peptide receptor 2 pushes inflammatory resolution. *Proc. Natl. Acad. Sci. U. S. A.* **2013**, 110, 18033–18034.

(62). Serhan, C. N.; Chiang, N.; Van Dyke, T. E. Resolving inflammation: Dual anti-inflammatory and pro-resolution lipid mediators. *Nat. Rev. Immunol.* **2008**, 8, 349–361.

(63). Gröper, J.; König, G. M.; Kostenis, E.; Gerke, V.; Raabe, C. A.; Rescher, U. Exploring biased agonism at FPR1 as a means to encode danger sensing. *Cells* **2020**, 9, 1054.

(64). Seubert, P.; Vigo-Pelfrey, C.; Esch, F.; Lee, M.; Dovey, H.; Davis, D.; Sinha, S.; Schlossmache, M.; Whaley, J.; Swindlehurst, C.; McCormack, R.; Wolfert, R.; Selkoe, D.; Lieberburg, I.; Schenk, D. Isolation and quantification of soluble Alzheimer's beta-peptide from biological fluids. *Nature* **1992**, 359, 325–327.

(65). Barritt, J. D.; Younan, N. D.; Viles, J. H. N-terminally truncated amyloid-β (11-40/42) cofibrillizes with its full-length counterpart: implications for Alzheimer's disease. *Angew. Chem. Int. Ed. Engl.* **2017**, 56, 9816–9819.

(66). Giulian, D.; Haverkamp, L. J.; Yu, J. H.; Karshin, W.; Tom, D.; Li, J.; Kirkpatrick, J.; Kuo, Y-. M.; Roher, A. E. Specific domains of beta-amyloid from Alzheimer plaque elicit neuron killing in human microglia. *J. Neurosci.* **1996**, 16, 6021–6037.

(67). Heurtaux, T.; Michelucci, A.; Losciuto, S.; Gallotti, C.; Felten, P.; Dorban, G.; Grandbarbe, L.; Morga, E.; Heuschling, P. Microglial activation depends on beta-amyloid conformation: role of the formylpeptide receptor 2. *J. Neurochem.* **2010**, 114, 576–586.

(68). Offermanns, S.; Simon, M. I. G alpha 15 and G alpha 16 couple a wide variety of receptors to phospholipase C. *J. Biol. Chem.* **1995**, 270, 15175–15180.

(69). Bustin, S. A.; Benes, V.; Garson, J. A.; Hellemans, J.; Huggett, J.; Kubista, M.; Mueller, R.; Nolan, T.; Pfaffl, M. W.; Shipley, G. L.; Vandesompele, J.; Wittwer, C. T. The MIQE guidelines: minimum information for publication of quantitative real-time PCR experiments. *Clin. Chem.* **2009**, 55, 611–622.

(70). Humphrey, W.; Dalke, A.; Schulten, K. Vmd: visual molecular dynamics. *J. Mol. Graph.* **1996**, 14, 33–38.

(71). Crescenzi, O.; Tomaselli, S.; Guerrini, R.; Salvadori, S.; D'Ursi, A. M.; Temussi, P. A.; Picone, D. Solution structure of the Alzheimer amyloid β-peptide (1–42) in an apolar microenvironment. *Eur. J. Biochem.* **2002**, 269, 5642–5648.

4.8.Supporting Information

Amyloid beta and its naturally occurring N-terminal variants are potent activators of human and mouse formyl peptide receptor 1

Lukas Busch[1], Zukaa al Taleb[1], ***Yu-Liang Tsai***[2], Vu Thu Thuy Nguyen[3], Qi Lu[2], Christopher V. Synatschke[2], Kristina Endres[3], Bernd Bufe[1,*]

[1]Department of Informatics and Microsystems Technology, University of Applied Sciences Kaiserslautern, Zweibrücken, Germany.
[2]Department Synthesis of Macromolecules, Max Planck Institute for Polymer Research, Mainz, Germany.
[3]Department of Psychiatry and Psychotherapy, University Medical Centre of the Johannes Gutenberg-University, Mainz, Germany.

* Corresponding Author
E-mail: bernd.bufe@hs-kl.de

Table S4. 1 Details of all used Aβ peptides. The table details the manufacturers, catalog and lot numbers and purity of all Aβ peptides that were used within this work. CaI: Calcium Imaging, ChT: Chemotaxis, ThT: ThT Aggregation Assay. Buffer compositions are detailed in the **Experimental procedures**.

Name	Manufacturer	Catalog#	Lot#	Purity	Stock conc. and solvent	Max. End conc. in Assay
Aβ 1-10	Anaspec	AS-64478	2055677	96%	1 mM / C1	CaI: 10 µM
Aβ 1-16	Anaspec	AS-24225	n.n.	96%	1 mM / C1	CaI: 10 µM
Aβ 1-40	Anaspec	AS-24235	2158441	96%	30 µM / C1	CaI: 10 µM
Aβ 1-40	Anaspec	AS-24235	2056942	95%	30 µM / C1	CaI: 10 µM
Aβ 1-42	Peptides & elephants	EP10060	2206R05	95.50%	5 mM / DMSO 30 µM / C1 30 µM / Tris-NaCl 30 µM / HBSS	CaI: 10 µM ChT: 10 µM ThT: 22.5 µM
Aβ 1-42	Anaspec	AS-20276	2155092	95%	5 mM / DMSO 30 µM / C1	CaI: 10 µM ThT: 22.5 µM
Aβ 1-42	Synpeptide	custom synthesis		95%	5 mM / DMSO 30 µM / C1	CaI: 10 µM ChT: 10 µM ThT:22.5 µM
Aβ 1-42	Sigma-Aldrich	PP69	3760648	95%	30 µM / C1	CaI: 10 µM ThT: 22.5 µM
Aβ 11-40	Peptides & elephants	EP10013	0206U02	95.10%	5 mM DMSO	CaI: 5 µM ChT: 1 µM
Aβ 17-40	Anaspec	AS-22813	2156695	98%	5 mM DMSO	CaI: 5 µM ChT: 5 µM
Aβ 17-40	Synpeptide	custom synthesis		95%	5 mM DMSO	CaI: 5 µM
Aβ 17-40	Sigma-Aldrich	A4848	117K1109	91%	5 mM DMSO	CaI: 5 µM

Table S4. 2 Details of all primers used for PCR experiments and Reverse Transcriptase. Accession numbers and primer sequences which were used for RT-PCR, RT-qPCR and during Reverse Transcriptase.

Accession No.	Gene	Official Full Name	Oligonucleotide sequence
Reverse Transcription primers			
n.n.	n.n.	CDS (Smart)	5-AGCAGTGGTAACAACGCAGAGTA CTTTTTTTTTTTTTTTTTTTTTTTTTTTTVN
n.n.	n.n.	SMART II	5- AAGCAGTGGTAACAACGCAGAGTA CGCGGG
RT-PCR Primer			
NM_002029.4	hFPR1	Homo sapiens formyl peptide receptor 1 (FPR1), transcript variant 2, mRNA	5-AAAGAATTCAAGCTTCCTGCAGGCGC CACCATGGAGACAAATTCCTCTCTCCC-3 5-TTGGATATCGCGGCCGCAAGAGCTCA CTTTGCCTGTAACTCCACCTCTGC-3
NM_001005738	hFPR2	Homo sapiens formyl peptide receptor 2 (FPR2), transcript variant 2, mRNA	5-AAAGAATTCAAGCTTCCTGCAGGCGCC ACCATGGAAACCAACTTCTCCACTCCTC-3 5-TTGGATATCGCGGCCGCAAGAGCTCA CATTGCCTGTAACTCAGTCTCTGCA-3
NM_002030.5	hFPR3	Homo sapiens formyl peptide receptor 3	5-AAAGAATTCAAGCTTCCTGCAGGCGCC ACC ATGGAAACCAACTTCTCCATTCCT-3 5-TTGGATATCGCGGCCGCAAGAGCTCA CATTGCTTGTAACTCCGTCTCCTC-3
RT-qPCR primers			

NM_002029.4	hFPR1	Homo sapiens formyl peptide receptor 1 (FPR1), transcript variant 2, mRNA	5-GGGTCCTCTCCTTTGTCGCAGCA-3 5-GGCGGGAAGGGCGTGGATCA-3
NM_001005738	hFPR2	Homo sapiens formyl peptide receptor 2 (FPR2), transcript variant 2, mRNA	5-GCTTGCCGATGTCCATTGTTGCCA-3 5-GGCCAGGGAGCTCGTTGGGT-3
NM_002030.5	hFPR3	Homo sapiens formyl peptide receptor 3	5-TCAGCGTGCCTATGTCCATCA-3 5-ACCACAGCAGCGAAGACACG-3
NM_002046.7	hGAPDH	Homo sapiens glyceraldehyde-3-phosphate dehydrogenase	5-GAAGGTGAAGGTCGGAGTC-3 5-GAAGATGGTGATGGGATTTC-3

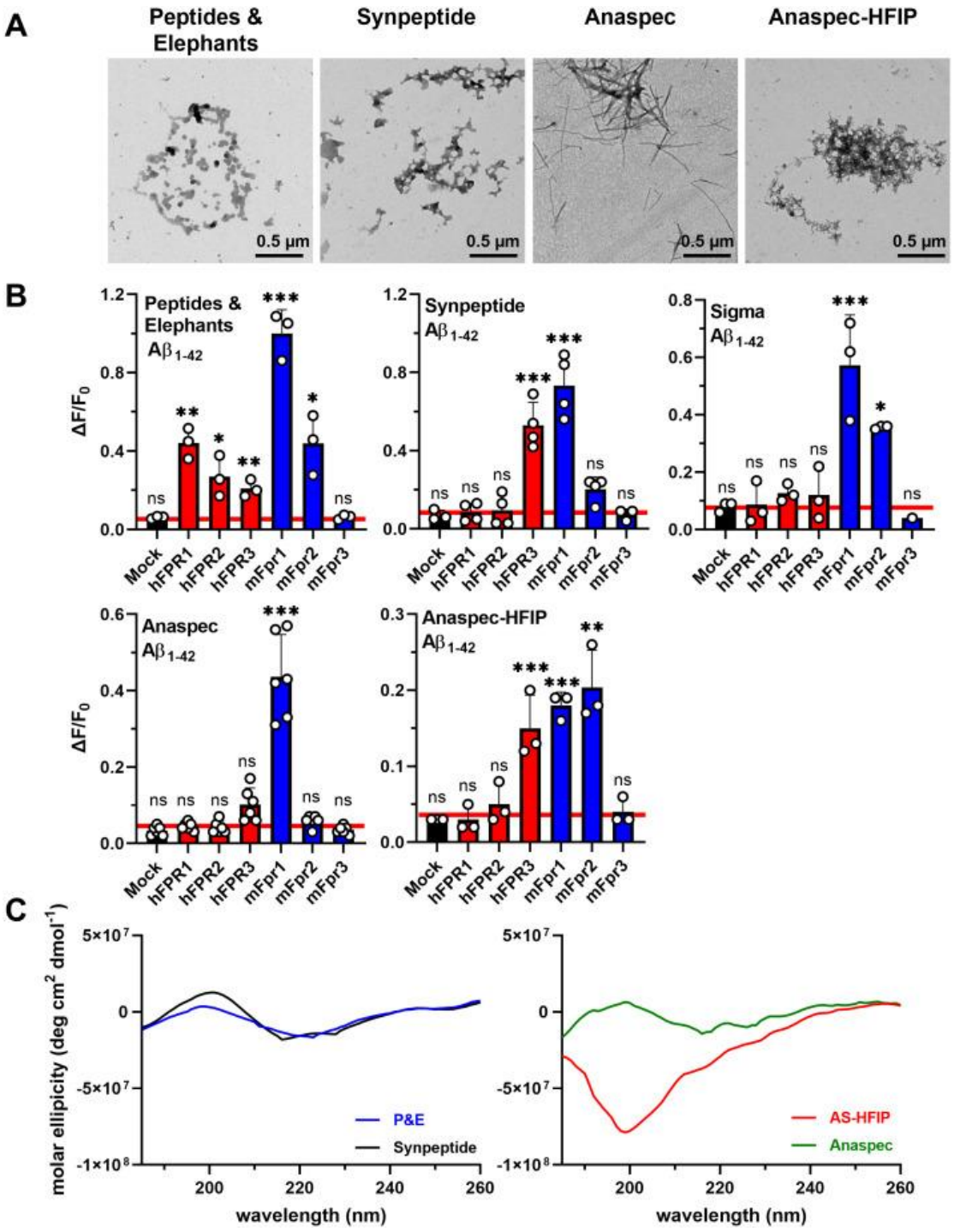

Figure S4. 1 Manufacturer-dependent FPR activation by Aβ1-42. (A) Representative TEM images of Aβ1-42 obtained from either Peptides&Elepehants (P&E), Synpeptide, or Anaspec show different types of aggregates. AS-HFIP refers to a commercially available HFIP-treated peptide from Anaspec. Scale bars indicate 0.5 µm. (B) Mean Ca^{2+} peak responses of FPR-transfected HEK293T cells after stimulation with 10 µM Aβ1-42 obtained

from different manufacturers. Colored bars indicate the response of human (red) or mouse (blue) FPRs, n=3, N=2. Data correspond to the heat map shown in **Fig 4. 2B**. Bar graphs for P&E and Synpeptide are shown again for the sake of comparability. (C) complete CD spectra of all four $A\beta_{1\text{-}42}$ displayed in **Figure 4. 2**. N=3. All Error bars, S.D.; One-way ANOVA test, Dunnett post hoc test; ∗, $p \leq 0.05$; ∗∗, $p \leq 0.01$; ∗∗∗, $p \leq 0.001$; ns, no significance. Copyright 2022, Elsevier.

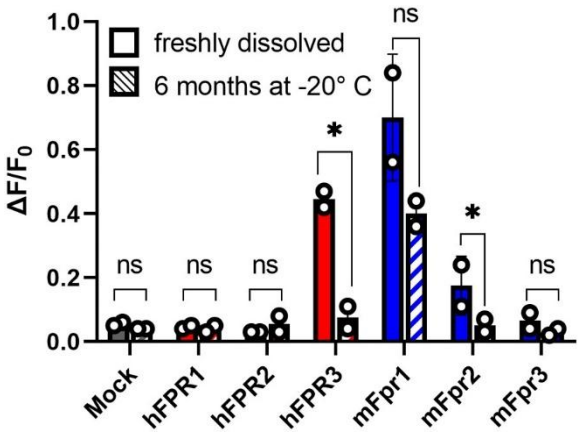

Figure S4. 2 Alterations of FPR responses to $A\beta_{1\text{-}42}$ after extended storage. Comparison of the Ca2+ responses of human (red) or mouse (blue) FPRs to 10 μM $A\beta_{1\text{-}42}$ (Synpeptide) that were either freshly dissolved in the assay buffer C1 (clear bars) or had been stored in C1 at -20° C for 6 months without freeze-thaw cycles (striped bars), n=1, N=2. All Error bars, S.D.; ∗, $p \leq 0.05$; ns, no significance. Copyright 2022, Elsevier.

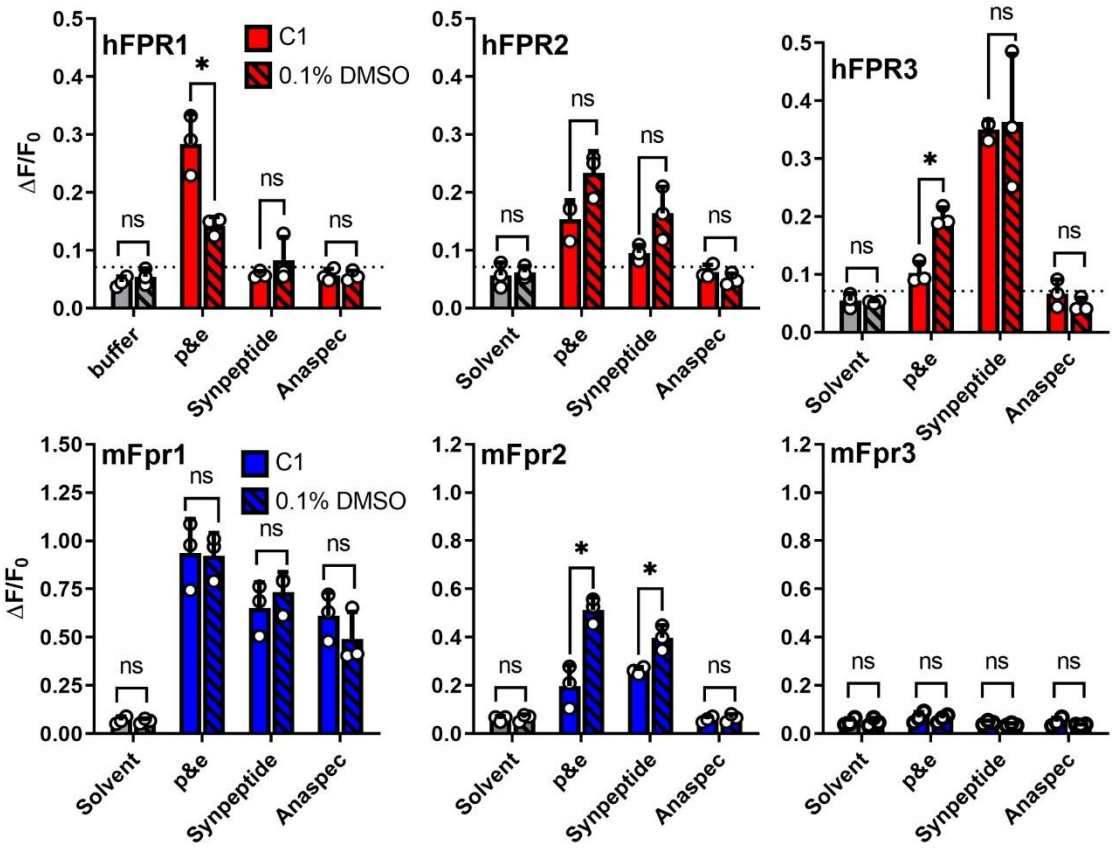

Figure S4. 3 DMSO influences FPR activation by Aβ1-42. Mean Ca^{2+} peak responses of human (red) or mouse (blue) FPRs to 5 μM of Aβ1-42 peptides obtained from P&E, Synpeptide or Anaspec dissolved in either DMSO (striped bars) or C1 (clear bars), n=3, N=2. All Error bars, S.D.; ∗, $p \leq 0.05$; ns, no significance. Copyright 2022, Elsevier.

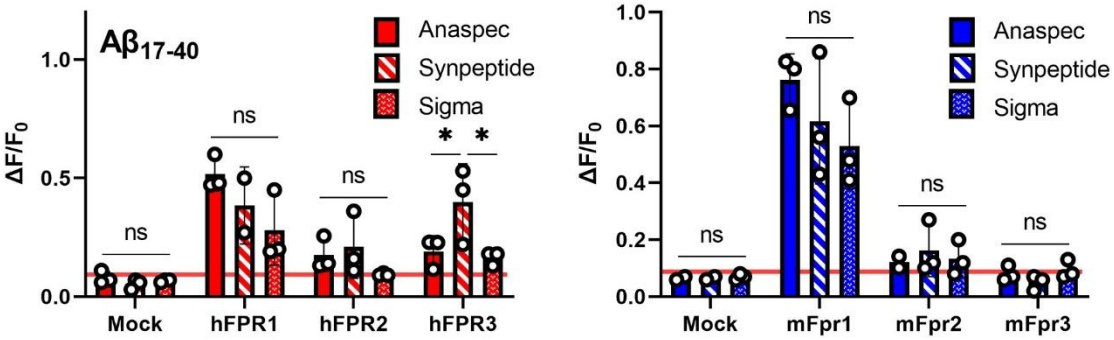

Figure S4. 4 Aβ17-40 is less susceptible to manufacturer-dependent effects than full length Aβ. Mean Ca^{2+} peak responses of FPR-transfected HEK293T cells to 5 μM of Aβ17-40 from three different manufacturers. Clear bars, Aβ17-40 from Anaspec. Striped bars, Aβ17-40 from Synpeptide. Dotted bars: Aβ17-40 from Sigma-Aldrich, n=3, N=1. All Error bars,

S.D.; One-way ANOVA test, Dunnett post hoc test; ∗, $p \leq 0.05$; ns, no significance Copyright 2022, Elsevier.

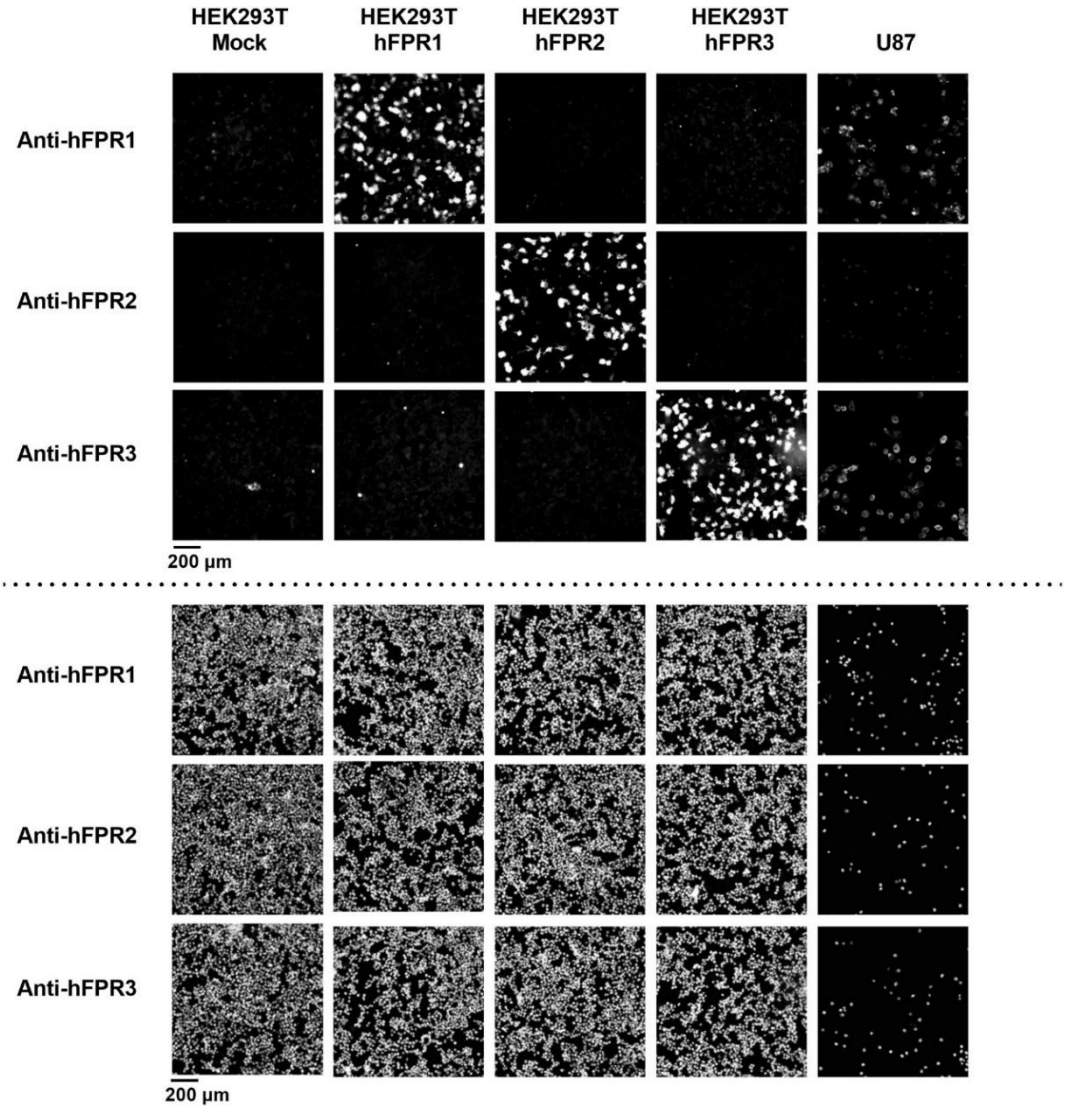

Figure S4. 5 Validation of immunofluorescence staining with FPR subtype-specific antibodies. Top: Comparison of immunofluorescence staining intensity of FPR-transfected HEK293T and U87 cells with receptor subtype specific antibodies. The hFPR1 (1 µg/ml), hFPR2 (0.2 µg/ml) and hFPR3 (1 µg/ml) antibodies were used. Note that the absolute staining intensities of all hFPRs in HEK293T cells were highly similar, however a strong reduction of hFPR2 staining in U87 cells is observed. No cross reactivity was detected. All images were acquired with the same settings and are displayed with the same illumination, brightness and contrast. Evidence for similar cell surface expression and production rates

for hFPR1 and hFPR2 can be found in supporting **Fig S4. 8**. Bottom: corresponding nuclei staining with Hoechst 33342 demonstrating a comparable amount of total cell number in all visual fields. Copyright 2022, Elsevier.

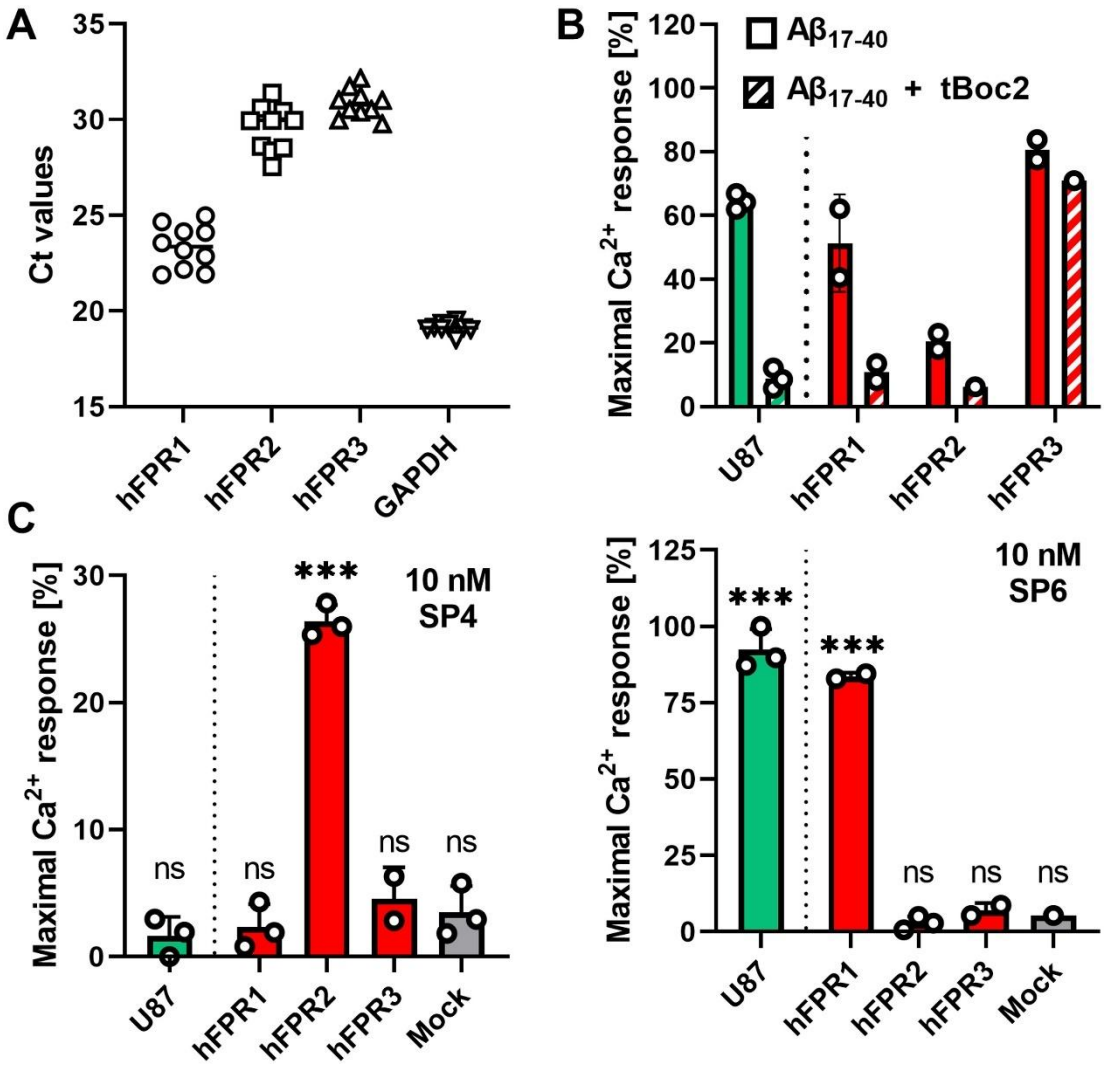

Figure S4. 6 FPR1 is the dominant receptor in U87 cells. (A) Ct values of all human FPRs from the RNA of U87 cells obtained through RT-qPCR, n=5, N=2. B, Ca^{2+} responses of U87 cells (green) or FPR-transfected HEK293T cells (red) towards 5 µM $A\beta_{17-40}$ with (clear bars) or without (striped bars) co-application of 10 µM tBoc2. Signals were normalized to responses of the respective cells towards 10 µM WKYMVm, n=1, N=2 for HEK293T cells and N=3 for U87 cells. (C) Mean Ca^{2+} peak responses of U87 cells (green) or FPR-transfected HEK293T cells (red) that were treated with 10 nM SP4 (left) or 10 nM

SP6 (right), n=1, N=3. All Error bars, S.D. One-way ANOVA test, Dunnett post hoc test; *, $p \leq 0.05$, **, $p \leq 0.01$, ***, $p \leq 0.001$; ns, no significance. Copyright 2022, Elsevier.

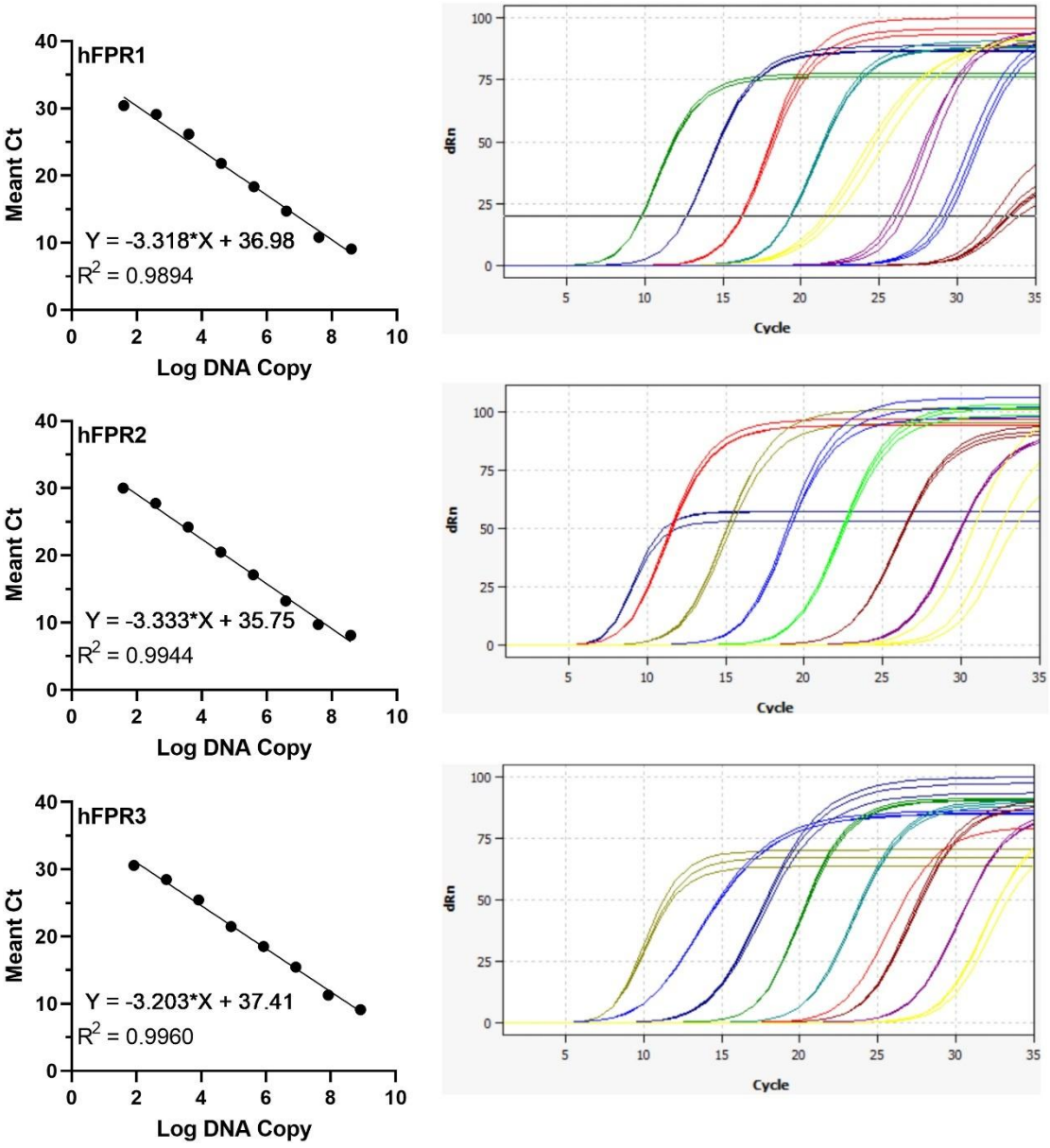

Figure S4. 7. Validation of RT-qPCR primers for all human FPRs. Left: mean standard curves, regression line, and amplification efficiency (n =3, N=3) generated by using a 10-fold serial dilution of a target DNA template starting with 0,1 ng of a purified and sequenced PCR product in t-RNA. Ct values were plotted against the log of template quantity for each dilution. Representative PCR products for all primer sets were controlled

by gel electrophoresis and sequencing for their specificity. Right: A representative data set of an amplification curve from these dilution series for each primer. Copyright 2022, Elsevier.

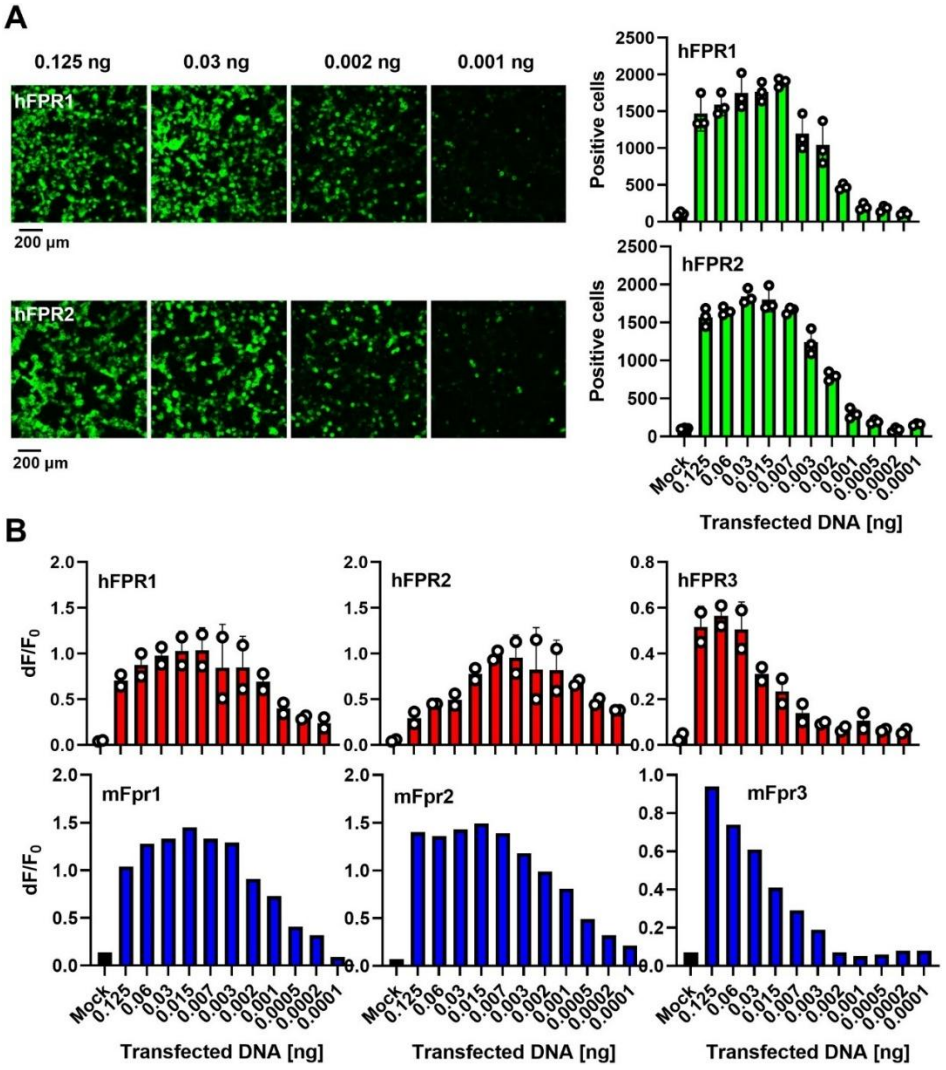

Figure S4. 8. Evidence for similar cell surface expression and calcium responses of FPR1 and FPR2 in HEK293T cells. (A) HEK293T cells were transfected with varying amounts of plasmid DNA for hFPR1 or hFPR2 and subsequently treated with 1 µM of FITC-labeled WKWVm-NH_2 to monitor their cell surface expression. Left: representative images of treated cells transfected with different DNA amounts Right: quantitative analysis of positively stained cells. Note that cell surface expression of both receptors upon dilution is reduced in a similar manure. Error bars, S.D. n=1, N=3. (B) Mean Ca^{2+} peak responses of HEK293T cells transfected with decreasing amounts of human (red) or mouse (blue) FPR plasmid DNA. FPR1 and 2 of each species were treated with 1 µM of WKWVm-NH2

and FPR3-transfected cells with 30 μM of WKWVm-CHO. Note that the amount of FPR 1 and 2 DNA can be diminished by more than 10fold without a strong reduction of the signal amplitudes. Copyright 2022, Elsevier.

5. Peptide photoimmobilization by thiol-ene chemistry for enhancing neural cell adhesion

This chapter is reproduced from

Yu-Liang Tsai, Sotiria Moschopoulou-Triantafyllidou, Sa'id Albarqawi, Jiyao Yu, Tommaso Marchesi D'Alvise, Lothar Veith, Rüdiger Berger, Christopher V. Synatschke. Chemrxiv 2025, DOI**:** 10.26434/chemrxiv-2025-3t1tl.

Contribution:

Yu-Liang Tsai: Conceptualization, Methodology, Validation, Formal analysis, Investigation, Writing - Original Draft, Writing - Review & Editing, Visualization, Project administration.

Sotiria Moschopoulou-Triantafyllidou: Formal analysis, Investigation, Writing - Review & Editing

Sa'id Albarqawi: Formal analysis, Investigation

Jiyao Yu: Formal analysis, Investigation, Writing - Review & Editing

Tommaso Marchesi D'Alvise: Formal analysis, Investigation

Lothar Veith: Formal analysis, Investigation, Writing - Review & Editing

Rüdiger Berger: Formal analysis, Investigation, Writing - Review & Editing

Christopher V. Synatschke: Resources, Writing - Review & Editing, Supervision, Project administration, Funding acquisition.

Peptide photoimmobilization by thiol-ene chemistry for enhanced neural cell adhesion

Yu-Liang Tsai[1], Sotiria Moschopoulou-Triantafyllidou[1], Jiyao Yu[1], Sa'id Albarqawi[2], Tommaso Marchesi D'Alvise[1], Lothar Veith[1], Rüdiger Berger[2], Christopher V. Synatschke[1,*]

1. Max Planck Institute for Polymer Research, Synthesis of Macromolecules, Ackermannweg 10, 55128 Mainz, Germany
2. Max Planck Institute for Polymer Research, Physics at interfaces, Ackermannweg 10, 55128 Mainz, Germany

* Corresponding Author

E-mail: synatschke@mpip-mainz.mpg.de

5.1. Abstract

Neurological diseases and neural injuries are prevalent but difficult to treat because of the complexity of the neural environment. To unravel this complexity, simple cell culture models are required that allow the study of individual aspects of the neural environment under defined conditions. In this work, we developed stable coatings of bioactive peptides via photoimmobilization through thiol-ene reaction on glass substrates suitable for long-term culture of neural cells. The substrates were modified with thiol groups via chemical vapor deposition to obtain a large and homogeneous layer, followed by immobilization of neural active peptides bearing vinyl groups. Subsequently, human neuroblastoma cells were shown to stably adhere and grow on the modified substrates. The results establish a facile fabrication route for large-scale (cm^2), patternable, and peptide-functionalized substrates for the culturing of neural cell adhesion without additional antifouling treatment.

Keywords: surface modification, photopatterning, thiol-ene reaction, neural cell adhesion

5.2. Introduction

Protein and peptide immobilization on substrates through covalent bonds provides an effective way to introduce new functionalities to the substrate, such as adhesion, biocompatibility, anti-fouling, or biosensing.[1–5] Additionally, having a solid support can improve the stability of the target proteins and peptides.[6] With proper orientation of the target molecules on substrates, it is possible to maximize the selectivity and reactivity by exposing the binding domain or the bioactive site in the solutions.[7] To generate large biomolecule-modified substrates, photopatterning holds the advantage of large scale and rapid fabrication which is beneficial for high-throughput analysis in cell culture, e.g., when developing neural regeneration strategies. Among various photopatterning techniques, the photochemistry of olefins and thiols, which is commonly known as the thiol-ene reaction, has many advantages, such as regiospecificity, mild reaction conditions, absence of heavy-metals, and high yield.[3,8–10] Jonkheijm et al. demonstrated that thiol-ene photochemistry could form stable thioether bonds to immobilize proteins with high precision on glass slides in physiological buffers.[8] Herein, we aim to combine the advantages of thiol-ene photochemistry and bioactive peptides to rapidly create a large-scale and robust platform for neural cell adhesion. The bioactive peptide sequence, KIKIQIN, is derived from a self-assembling amyloid-like peptide consisting of amphiphilic 12-amino acid, termed enhancing factor C (EF-C). The EF-C peptide and its derivates were employed to enhance retroviral gene transfer[11] and peripheral nerve repair.[12] Previous work has established that the self-assembling structure plays an important role in the functionality, but little attention has been paid to the functionality of such materials on substrates. Herein, the EF-C derived peptide sequence was selectively immobilized on substrates by thiol-ene photochemistry, as depicted in **Figure 5. 1**, to build a robust neuronal cell culture platform.

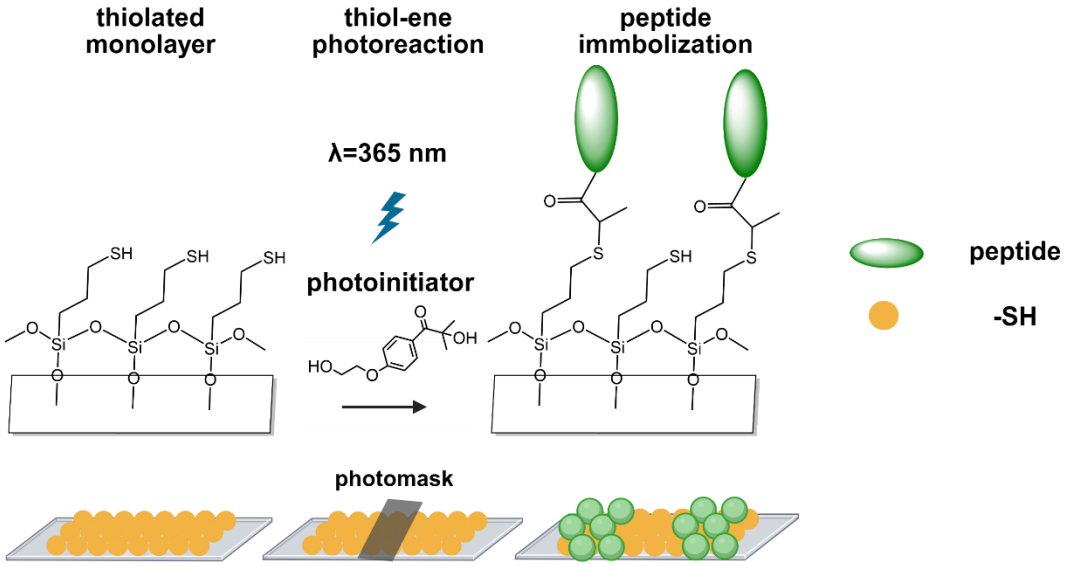

Figure 5. 1. Chemical reaction scheme and conceptual design of the peptide surface modification. The fabrication process of peptide immobilization on the substrate started with chemical vapor deposition (CVD) to generate a thiol layer on a glass substrate, followed by photon-activated thiol-ene reaction with acrylated peptides (sequence: Acr-KIKIQIN). (This image was created using ChemDraw and BioRender).

Surface characteristics such as hydrophilicity, surface charges, surface topography, and surface energy, can influence cellular behavior such as achieving cell adhesion, cell migration, directing morphological changes, activating signaling pathways, and inducing differentiation.[4,5,13–17] Cells respond to these features, provided by their surroundings at multiple scales from the macroscale down to the nanoscale.[18] Neuronal cells, in particular, are responsive to physical cues that direct neuronal cell faith.[19–23] For instance, Zhang et al. covalently patterned peptide sequences derived from laminin in a gradient manner on poly (D,L-lactide-co-caprolactone) (PLCL) films. The micropatterns and peptide gradient on the PLCL films improved the directional growth of mouse Schwann cells.[24] Tomba et al. reported that glial cells responded to the stiffness on different substrates, i.e., they favored cell adhesion and proliferation on stiffer fibronectin substrates but softer poly-L-lysine/laminin substrates.[22] Vedaraman and colleagues reported that using two-photon lithography techniques to design periodic and anisometric patterned clues can create a high-

throughput platform for neurite alignment.[23]

Different methods for the fabrication of topographic features have been developed, including the use of peptide photopatterning and self-assembling peptides (SAP), allowing the investigation of neural behavior. For example, SAPs can provide biomimetic complex structures for neural cells attachment.[17,19] Yang et al. fabricated an aligned nanofiber composed of fibrin and SAPs to stimulate the outgrowth of rat Schwann cells and the functional recovery in a peripheral nerve injury in rats.[25] In addition, 3D printing is one technique to generate aligned and functional network for neural tissue engineering.[26,27] Indeed, photopatterning, SAPs, electrospun fibers, and 3D printed constructs, can create complex matrices that mimic neural cell niches. However, the above-mentioned techniques alone cannot rapidly fabricate large-scale and patterned substrate to direct neuronal cell behavior.[15]

In this work, we aim to immobilize the bioactive peptide sequence, KIKIQIN, via thiol-ene photochemistry and investigate its functionality on the modified surfaces. We characterize the physical and chemical properties of the acrylated KIKIQIN peptide and verify the potential of photo-immobilization of this bioactive sequence on substrates. Finally, cell adhesion assay of a human neuroblastoma cell (SH-SY5Y) is used to test the functionality of the photo-immobilized peptide to achieve a robust neuronal cell culture platform.

5.3. Result and Discussion

5.3.1. Chemical Characterization of Peptide-Modified Substrates

To achieve peptide photoimmobilization on substrates by thiol-ene photochemistry, we chose KIKIQIN as this peptide has previously been shown to facilitate neuronal adhesion on glass substrate.[12] The peptide was synthesized using SPPS followed by on-resin acrylation at the N-terminus and the chemical structure of Acr-KIKIQIN is provided in **Figure S. 1**. The resulting Acr-KIKIQIN was cleaved off the resin and purified by RP-HPLC and confirmed by MALDI-ToF MS (**Figure S5. 1)**.

Next, glass and silicon substrates were modified with MPS via vapor deposition to

introduce thiol groups on the surface, followed by photoinitiated thiol-ene reaction with the Acr-KIKIQIN. A simple strip-patterned photomask, depicted in **Figure 5. 2 (a)**, was used for photopatterning of the Acr-KIKIQIN on the thiolated substrates. The chemical characterization of the modified substrates was carried out by XPS, where the differences between thiolated and peptide-modified substrates could be easily distinguished in the obtained spectra. In the C1s spectra of the thiolated substrate shown in **Figure 5. 2 (b)**, the brown dashed line was attributed to the C-C bonds at 284.9 eV, the blue dotted line was assigned to the C-O bonds at 286.8 eV, and the green dashed line was correlated to the C=O bonds at 289. 2 eV. In contrast, the C1s spectra of the peptide-modified substrates, shown in **Figure 5. 2 (c)**, showed additional signals corresponding to the C-N bonds at 286.2 eV (dark yellow dashed line). There are significant differences in these two C1s spectra in the intensity of the signal at 288~ 289 eV attributed to the C=O bonds and a subtle difference at 286.2 eV assigned to the C-N and C-O bonds. The profound signals from C=O bonds and C-N bonds are typical signals from peptide bonds, which served as a strong indication of peptide immobilization on the substrate. The elemental composition analysis was performed using the deconvoluted spectra and is summarized in **Table 5. 1**.

Table 5. 1 Elemental composition analysis of thiolated and peptide-modified silicon wafers based on their XPS spectra.

	Element content (wt%)			
Samples	C 1s	O 1s	N 1s	S 2p
Thiolated	36.7	40.7	0.9	21.7
Peptide	49.7	32.9	6.7	10.7

Next, ToF-SIMS was applied to investigate the chemical composition of the substrate and provide further evidence of successful peptide modification. Because both MPS and peptide contain significant amount of aliphatic groups, peptide-associated signals were mainly originating from aliphatic amines (C-N signals), while thiolated-associated signals were from fragments containing sulfur in combination with carbon and hydrogen. In **Figure 5. 2 (a-h) and Figure S5. 2 (a, b)**, ToF-SIMS images from photopatterned peptide-modified substrates in positive and negative ions are presented. A semi-quantitative analysis of the relevant ionic signals is presented in **Table 5. 2**. As expected, non-illuminated regions primarily showed signals that originate from thiol-groups of the MPS, confirming that coupling of peptide in non-illuminated areas is negligible. In contrast, illuminated areas showed strong signals (10-fold higher intensity compared to non-illuminated areas) related to peptide fragment, confirming the successful coupling and photopatterning of the substrate.

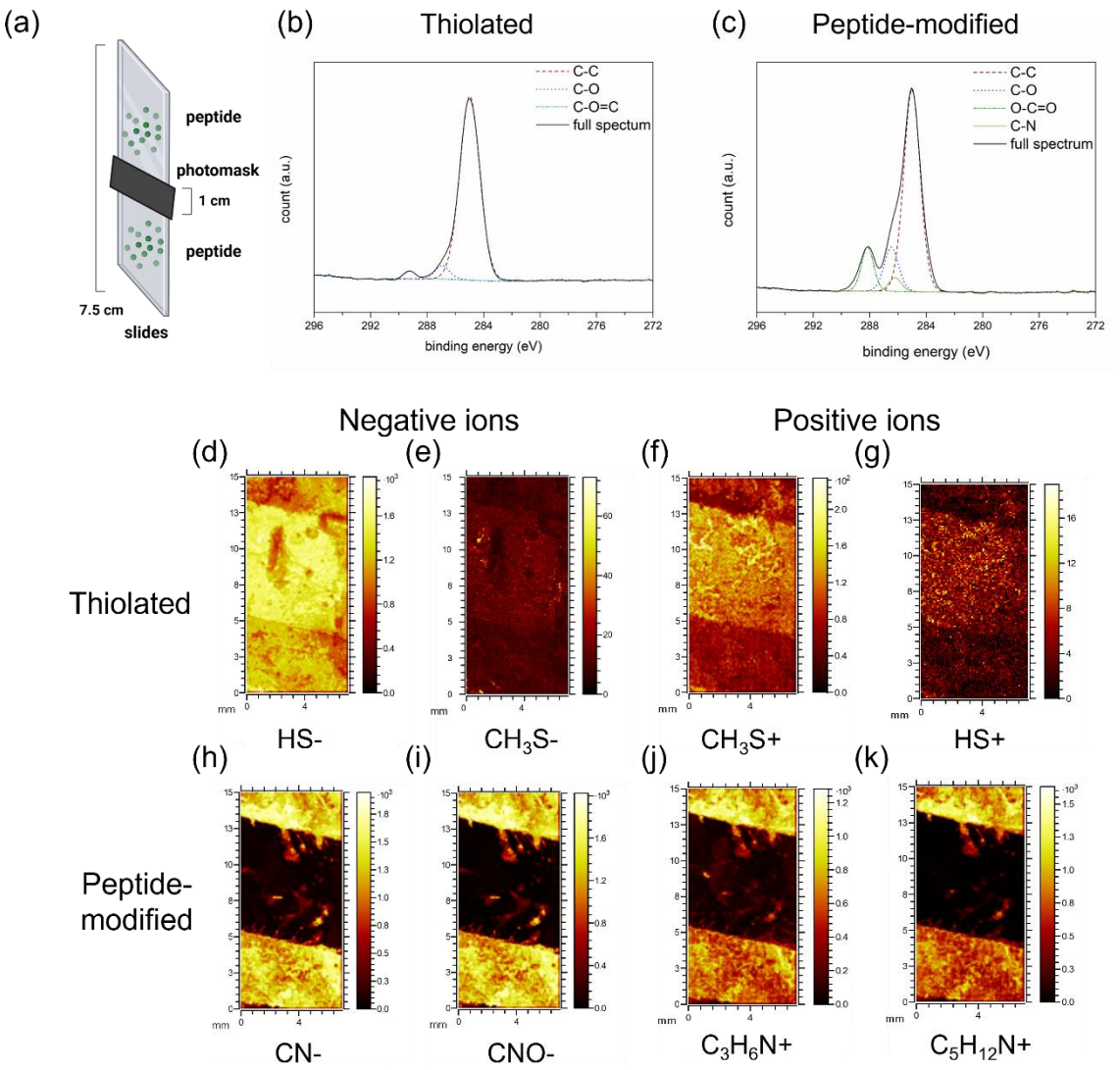

Figure 5. 2. Surface chemical characterization of thiolated and peptide-modified substrates. (a) Scheme of peptide photopatterning on the thiolated glass slides. (This image was created using BioRender). (b) High-resolution narrow scan of C1s of the thiolated side of the substrate and the deconvoluted spectra for the probable chemical species. (c) High-resolution narrow scan of C1s of the peptide-modified side of the substrate and the deconvoluted spectra for the probable chemical species. (d-g) Representative ToF-SIMS chemical maps of the thiolated substrates, with (HS^-, CH_3S^-, CH_3S^+, and HS^+). (h-k) Representative ToF-SIMS chemical maps of the peptide-modified substrates (CN^-, CNO^-, $C_3H_6N^+$, and $C_5H_{12}N^+$).

Additionally, the signal of $[M+H]^+$=924.5 m/z in **Figure S5. 3**, which matched the

molecular weight of Acr-KIKIQIN, was also captured by ToF-SIMS, indicating the successful peptide modification on the substrate

Table 5. 2 Semi-quantitative analysis of relevant ionic signals detected by ToF-SIMS (unit: area normalized by total shots)

Negative	Mass (u)	Thiol	Peptide	Postive	Mass (u)	Thiol	Peptide
CN^-	26.00	2.48E-01	1.75E+00	$C_3H_6N^+$	56.05	7.23E-03	4.73E-01
CNO^-	42.00	1.58E-01	1.89E+00	$C_5H_{12}N^+$	86.10	8.90E-03	5.13E-01
HS^-	32.98	9.74E-01	4.78E-01	HS^+	32.98	3.46E-03	6.73E-04
CH_3S^-	47.00	2.74E-02	1.37E-02	CH_3S^+	47.00	7.62E-02	2.94E-02

The color bars indicate the relative intensity of the capture ions on the thiolated side and peptide-modified side of the substrate.

In short, both XPS spectra and ToF-SIMS suggested the successful peptide immobilization on the substrate, and the ToF-SIMS images demonstrated successful photopatterning of Acr-KIKIQIN on thiolated substrates.

5.3.2. Physical Characterization of Peptide-Modified Substrates

The functionalization with peptides should lead to a change in the surface properties of the samples, ideally providing a beneficial surface for cells to attach. Next, we characterized the surface properties of the modified substrates in more detail and compared them to non-functionalized and thiolated substrates. Wetting analysis was tested by a contact angle goniometer and determined to be 44˚ ± 3˚, 56˚ ± 2˚, 56˚ ± 2˚, and 65˚ ± 2˚ for the thiolated and (0.05 mg/mL, 0.1 mg/ mL, and 0.5 mg/mL) peptide-modified substrates, respectively. The increase in hydrophobicity with increasing peptide concentration was expected as more peptides with aliphatic side chains were immobilized on the substrate.

In surface zeta potential measurements, the modification of the substrate with peptide can be observed in **Figure S5. 4**. While there was no change in the surface zeta potential at pH = 7.4 when modifying the glass substrate with MPS (-66 mV for both glass and

thiolated substrates), with increasing peptide concentration, an increase in the surface zeta potential from – 63 mV for the lowest tested peptide concentration up to – 44 mV for the highest tested peptide concentration was observed. The increase in surface zeta potential could be attributed to multiple amine groups on lysine in the peptide sequence.

We further analyzed the surface morphology of the thiol and peptide-modified Si-substrate surfaces by scanning force microscopy (**Figure 5. 3** and **Figure S5. 5)**. Surprisingly, we found fiber-like structures on the surface, which had a height up to 30 nm and a width up to 100 nm. A statistical analysis of several images and 46 fibers revealed that most fibers had a height between 2-3 nm. The length of the fibers is in a range of hundreds of nanometers to several micrometers, indicating multiple hierarchies of assembly.

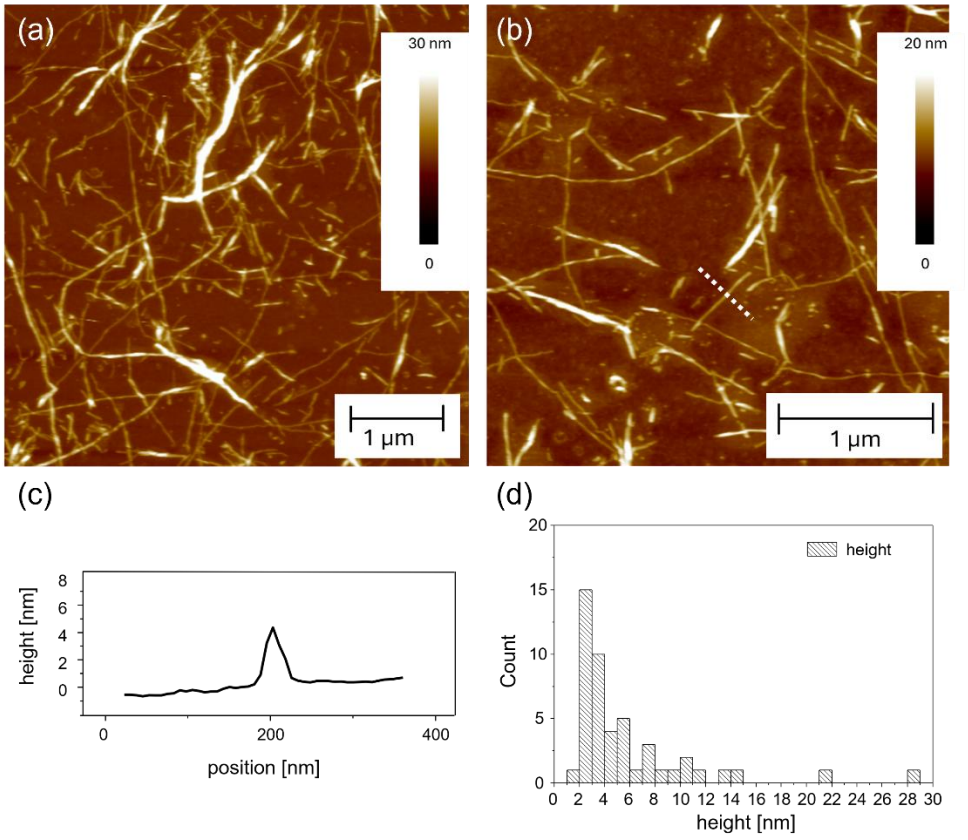

Figure 5. 3. Surface morphology of the peptide-modified substrates. (a, b) Two representative of SFM topography images of peptide-modified substrates (peptide concentration: 0.2 mg/mL). (c) Topography profile across a peptide nanofiber indicated by the white dotted line (b). We took the full width at half maximum as representative value for the width of a nanofiber. (d) Statistical analysis of the height of peptide nanofibers on

the peptide-modified substrates.

Many factors, such as surface charge, surface topography, chemical templating, and the presence of molecules play a role in surface self-assembly.[31–34] Although the exact surface-mediated self-assembly mechanism is unclear, we speculate that Arc-KIKIQIN was first immobilized on the thiolated layer as a nucleation site, followed by supramolecular peptide assembly, which is similar to previous works, i.e. where peptides assembled on highly oriented pyrolytic graphites,[35] N-hydroxysuccinimide modified glasses,[36] maleimide-modified poly(acrylic acid) substrates,[37] and azide-modified wafers.[38]

5.3.3. Neural Cell Adhesion

In previous studies on peptides of similar sequences to KIKIQIN, the so-called EF-C peptide and its derivates, they were found to have biological activity as they improved retroviral gene transfer[11] and enabled peripheral nerve repair.[12] Drop casting was used to prepare peptide-coated substrates for the *in vitro* tests as part of these biological assays. However, drop casting has several drawbacks, such as drying effects leading to inhomogeneous peptide concentrations and insufficient with long-term stability when immersing the coating in buffers or cell culture medium. Therefore, substrates that were photo-coupled with Acr-KIKIQIN were tested for their ability to provide a long-term and stable neural cell culture platform. Cell adhesion of a neuroblastoma cell line, SH-SY5Y, was quantified by the number of cells adhering to the substrates in two separate individual experiments and 10 random images were analyzed from each experiment. For better visualization and to facilitate cell counting, cell nuclei were stained with NucBlue to provide stronger contrast. In **Figure 5. 4 (a)**, a regular glass slide, the thiolated substrate as well as drop casted sample, which underwent the same washing step, showed low number adhered cells, while a clear increase in attached cells was observed with increasing peptide concentration, demonstrating that the cell-adhesive properties of KIKIQIN remain after covalent attachment to the substrate. Furthermore, the peptide-modified substrates showed highly homogeneous coverage with cells over the whole substrate (**Figure S5. 6**). However, the number of adherent cells did not correlate linearly with the concentration of peptide modification. We speculated that this was due to the capacity of cell adhesion receptor and

interface functionality.[39]

In **Figure 5. 4 (b)**, a conceptual scheme demonstrated the cell adhesion after seeding on the photopatterned substrate. In **Figure 5. 4 (c)**, a stitched overview image shows significantly larger number of adherent cells on the peptide-modified part (0.1 mg/mL) compared to the thiolated part of the substrate. Furthermore, clear differences in cell morphology are visible in the enlarged med in images, shown in **Figure 5. 4 (d, e)**. While cells growing on the thiolated side of substrate have a round shape, typically associated with an epithelial-like phenotype and poor viability,[40,41] the cells growing on the peptide-modified side of the substrate are spreading out and have a pyramidal shaped morphology, which is associated with a neuronal phenotype of SH-SY5Y cells.[40] **Figure 5. 4 (f) and Figure 5. 4 (g)** are the fluorescent images of the enlarged in images. In **Figure 5. 4 (g)**, green fluorescent signals were observed from the Alexa 488 dye, which was from the secondary antibody against the expression of a neuronal marker, synaptophysin,[42] whereas there was no green fluorophore in **Figure 5. 4 (f)**. In short, the thiolated area showed fewer cells adhering and with a rounded morphology indicating that the unhealthy cells would detach or undergo apoptosis during prolonged cell culture. In contrast, the peptide-modified substrates showed a large number of healthy, spreading cells, demonstrating the suitability of the Acr-KIKIQIN peptide as a coating for long-term neuronal cell culture.

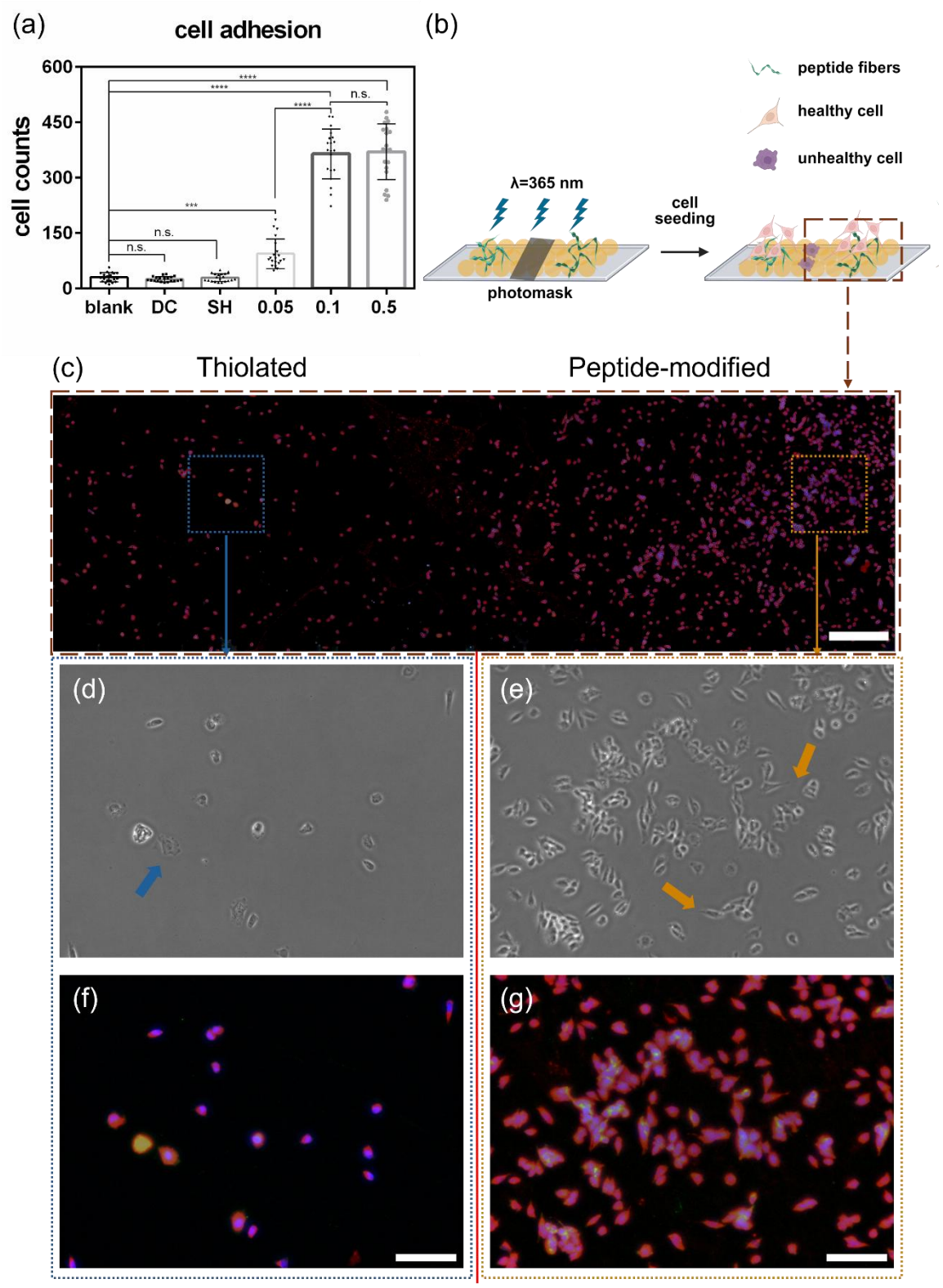

Figure 5. 4. SH-SY5Y cell line in vitro assay. (a) Cell adhesion assay showed that the regular glass (blank), peptide drop casted glass (DC), and thiolated glass (SH) had few cells

adhered to the substrate, and the number of cell increased as the concentration of peptide modification increased (**$p \leq 0.01$; ****$p \leq 0.0001$, ns = not significant, N=2, n=20, One-way ANOVA test). (b) A conceptual scheme of peptide photopatterning for modulating cell adhesion (This image was created using BioRender). (c) Overview image (stitched) of patterned substrate with thiolated side (left) and peptide-modified (0.1 mg/mL) (right), with a scale bar of 600 μm (d) A brightfield image of zoomed in region showing few and rounded (blue arrow) cells on thiolated side of the substrate. (e) A brightfield image of zoomed in region showing many spreading cells (orange arrow) on the peptide-modified side of the substrate. (f) A fluorescent images of zoomed in region on thiolated side of the substrate. (g) A fluorescent images of zoomed in region on the peptide-modified side of the substrate. Fluorescent images were acquired from stained samples with nuclei in blue, cell membrane in red, and neuronal-like expression in green (scale bar = 100 μm).

5.4.Conclusions

An easily fabricated, large-scale, and robust platform for neural cell culture was developed that can accelerate the development of drug screening for neural-related diseases and neural tissue engineering. Here, a neuro-active peptide sequence was covalently attached to substrates via a photo-triggered thiol-ene reaction, to provide robust coatings that promote cell adhesion. Surface chemical analysis showed that peptides could be selectively patterned on the substrate. Interestingly, SFM measurements showed that the immobilized peptides formed fibrous structures with dimensions in nanometer in height and micrometer in length, but the underlying mechanism for this behavior remains to be explored. Finally, superior cell adhesion of SH-SY5Y was demonstrated on the peptide-modified substrates, where increasing amounts of immobilized peptides showed an increase in the number of cells attaching to the surface and directing their morphology from an endothelial type to a neuronal type, when compared to non-peptide-coated controls. Through photopatterning, our method allows us to structure the substrate and direct where cell adhesion can occur. This approach has the potential to create a robust and selective neural culture platform.

5.5. Experimental Procedures

Materials

N,N-Dimethylformamide (DMF), dichloromethane (DCM), 2-propanol, piperidine, and trifluoroacetic acid (TFA) were bought from Carl Roth GmbH + Co. KG. Acetonitrile (ACN, HPLC grade), acetone, diethyl ether, and toluene were obtained from Honeywell. Fluorenylmethyloxycarbonyl (Fmoc) protected amino acids, Fmoc-Asn (Trt) Wang resin, and ethyl cyano(hydroxyimino) acetate (Oxyma Pure®) were purchased from Novabiochem. α-Cyano-4-hydroxycinnamic acid (CHCA), *N,N′*-diisopropylcarbodiimide (DIC), *N,N*-diisopropylethylamine (DIPEA), dimethyl sulfoxide (DMSO), 2-Hydroxy-4′-(2-hydroxyethoxy)-2-methylpropiophenone (Irgacure 2959), and triisopropylsilane (TIPS) were acquired from Sigma-Aldrich. Acrylic acid anhydride (AA), and (3-mercaptopropyl) trimethoxysilane (MPS) were bought from TCI Deutschland GmbH. Dithiothreitol was purchased from VWR. All chemicals were used without further purification, unless otherwise noted. Ultrapure water was obtained by using a purification system (MilliQ, Merck KGaA).

Solid Phase Peptide Synthesis (SPPS) and Peptide Acrylation

Peptide synthesis (KIKIQIN) was performed in an automated microwave peptide synthesizer (Liberty Blue™, CEM Corporation) from C- to N-terminus by Fmoc-SPPS method using Fmoc-Asn (Trt) Wang resin with 100-200 mesh size. DMF was used as the main wash solvent, and DMF with 20% piperidine was the deprotection solvents. The amount of materials and reagents was prepared according to the calculation suggested by the software of Liberty Blue™. In brief, the Wang resin was swelled in DMF for 30 mins prior to the synthesis. Routinely single amino acid coupling was applied unless otherwise stated. The procedure started from Fmoc removal by immersing the resin in the deprotection solvent and heating to 75 °C (155 W) for 15 s and 90 °C (30 W) for 50 s, followed by twice DMF washing. Subsequently, amino acids were coupled using a 0.2 M solution of respective amino acid in DMF with the addition of activator and activator base. The reaction was heated to 75 °C (170 W) for 15 s and 90 °C (30 W) for 110 s, followed by final deprotection step and flushing with DMF. Acylation of peptide (Acr-KIKIQIN) was conducted on resin with a stoichiometry of 1: 2: 4 (peptide: AA: DIPEA) in DMF in a

peptide reactor (Carl Roth GmbH + Co. KG) by shaking for 4 hr at room temperature. Afterwards, resin beads were first rinsed with DCM and immersed in a cleavage cocktail (95% TFA, 2.5% MilliQ water, 2.5% TIPS) for 2 hr, followed by precipitation in cold diethyl ether and centrifugation to obtain the crude peptide.

Purification and Characterization of Acylated Peptide

The crude peptide was dissolved in a mixture of MilliQ water and ACN and purified by reversed phase liquid chromatography (RP-HPLC, Shimadzu) through a C18 column (Phenomenex Gemini, 5 μm, NX-C18, 110 Å, 150 × 30 mm) with a flow rate of 25 mL/min. The solvent gradient of a mixture of ACN/MilliQ with 0.1% TFA started from 10% to 100% ACN. Fractions of samples were collected according to the retention time detected by an ultraviolet (UV) absorption detector at 214 nm. Collected samples were identified by matrix-assisted laser desorption/ionization time-of-flight mass spectrometry (MALDI-ToF MS) via dried droplet method. Samples were mixed with a saturated solution (MilliQ water /ACN = 1:1) of the matrix CHCA. The mass spectra were recorded on a rapifleX MALDI-ToF/ToF (Bruker). The purified samples were lyophilized and stored at -20 °C until further use.

Substrate Thiolation

Thiolation of the substrate was conducted by vapor deposition based on a previous report.[28] Glass slides (microscope slides, Epredia) for cell experiments and silicon wafers (P/ Boron, <100>, Si-Mat) for physicochemical analysis were cleaned by sonication in 2-propanol for 30 min. Afterwards, the substrates were rinsed with MilliQ water and dried with a N_2 stream. Clean substrates and a Teflon bottle with an open vial containing 0.5 ml of MPS were placed in a desiccator. The desiccator was purged with N_2 stream, sealed, and placed in a 90 °C oven for 1 hr. Subsequently, the substrates were rinsed with toluene followed by acetone and then dried using a N_2 stream.

Peptide Photoimmobilization on Thiolated Substrates

Different concentrations (0.5 mg/mL, 0.1 mg/mL, and 0.05 mg/mL) of peptide powders were dissolved in a solvent mixture of MilliQ water (90%) and ACN (10%). Photoinitiator,

Irgacure 2959, was solubilized in the same solvent mixture with a concentration of 1 mg/mL. Peptide and photoinitiator solutions were mixed and applied to the thiolated substrates for 5 min of ultraviolet (UV) irradiation (1.6 mW/cm^2). The peptide-immobilized substrates were washed with DMSO and MilliQ water and then dried with a N_2 stream prior to further experiments.

X-ray Photoelectron Spectroscopy (XPS)

XPS was conducted using a Kratos Axis UltraDLD spectrometer (Kratos) using an Al Kα excitation source with a photon energy of 1486.6 eV. Each sample was measured at three different spots, and data were processed by the CasaXPS software and plotted by Origin.

Time of Flight Secondary Ion Mass Spectrometry (ToF-SIMS)

ToF-SIMS experiments were performed using a TOF.SIMS5 (NCS) instrument (IONTOF GmbH) with 30 keV Bi_3^+ primary ions. Large area images were acquired using 30 keV Bi_3 primary ions rastering a total area of 7 x 15 mm^2 in spectrometry mode at a current of 0.18 pA and a cycle time of 150 µs (mass range up to 1800 m/z) leading to imaging data sets with pixel sizes of 3.3x3.3 $µm^2$. Mass calibration was facilitated using ubiquitous aliphatic hydrocarbon species.

Contact Angle Measurement

The wettability of the substrates was analyzed by measuring static contact angles using the sessile drop method (DataPhysics OCA 35 contact angle goniometer). Triplicate measurements were performed by deposing 10 µl of MiliiQ water on three different spots per substrate. The data were processed within the software of DataPhysics.

Surface Zeta Potential

Zeta potential measurements were conducted using a SurPASS electrokinetic analyzer (Anton Paar GmbH) to evaluate the surface charge properties of the thiolated and peptide-modified substrates under physiological conditions (pH 7.4). A 1 mM KCl solution served as the electrolyte, while 0.1 M HCl and 0.1 M NaOH were used to adjust the pH. Samples were mounted in a clamping cell with the channel height adjusted to approximately 100

µm. Electrokinetic flow was induced by linearly ramping the differential pressure from 0 to 300 mbar, and the streaming potential was recorded as a function of applied pressure. Each sample was measured in triplicate and the data were plotted using Prism.

Scanning Force Microscopy (SFM)

The surface morphology of the thiolated and the peptide-modified substrate was measured by SFM (Dimension Icon, Nanoscope 5 controller, Software 9.7r1sr8) operated in soft tapping mode at a scan speed of around 1 Hz with 512 pixels per line and 512 lines. We used cantilevers with a nominal resonance frequency of 300 kHz and a nominal spring constant of 26 N/m (OTESPA, OPUS made by µ mash). All images were plane corrected by an offset and a tilt (1^{st} order polynomial). The height of fibers was determined from surface profiles.

Cell Culture of Human Neuroblastoma Cells (SH-SY5Y)

SH-SY5Y cells (ATCC- CRL-2266 ™) were cultivated at 37 °C, 95% humidity, and 5% CO_2 in Dulbecco's Modified Eagle Medium (DMEM)/ Ham's F-12 Nutrient Mixture (F-12) (Thermo Fisher Scientific) with additional 10% fetal bovine serum (FBS), 1 % GlutaMax (Thermo Fisher Scientific), and 1% penicillin-streptomycin (PS) (Sigma-Aldrich) to study cell adhesion on thiolated and peptide-modified glass slides.

Cell Adhesion Assay

Cells were seeded on the thiolated, peptide drop-cast (washed with DMSO and MilliQ prior to cell seeding), and peptide-modified substrates at a density of 100,000 cells/cm^2 for 72 hr. Culture medium was changed every 24 hr before observation. For better visualization and quantification, cell nuclei were stained with blue fluorophore (NucBlue™ Live ReadyProbes™ Reagent and cell membranes were stained red fluorophore (Invitrogen™ CellMask™ DeepRed Plasma Membrane Stain**)** according to the manufacturer's protocol (Thermo Fisher Scientific). For immunostaining, cells were rinsed with PBS, fixed with 4 % (v/v) paraformaldehyde (PFA, Sigma-Aldrich) for 10 min, permeabilized with 0.5% (v/v) Triton X-100 (Merck KGaA) for 5 min, and blocked with 4 % bovine serum albumin (BSA, Roche) in PBS for 5 min. The primary antibody synaptophysin (SYN, rabbit anti-SYN,

Proteintech) was diluted in PBS (1:1000) and added to the samples at 4 C° for 24 hr. After rinsing with PBS, secondary antibody labeled with Alexa 488 (donkey anti-rabbit IgG Alexa Fluor™ Plus 488, Invitrogen, Thermo Fisher Scientific) in PBS (1:1000) was added to samples at room temperature for 4 hr before imaging. The images were taken using a BZ-X800 microscope (Keyence) utilizing a Plan Fluorite 20X LD PH objective lens. The built-in "Navigation" and "Stitching" functions of the microscopy were used to visualize larger area. Image files were processed with NIH Image J software and the "analyze particles" function was used to measure the total number of cells in a determined area.[29,30] Statistical analysis was performed using the one-way ANOVA test and plotted using Prism.

5.6. Acknowledgements

The authors are grateful for the financial support of the funding by the Deutsche Forschungsgemeinschaft (project number 441734479) and the cooperation program of the Fraunhofer and Max Planck. J. Y. is gratefully for the support from the China Scholarship Council. The authors appreciate Leon Prädel for XPS measurements, Helma Burg for SFM measurement, and the scientific support from Biocore and Mass Spectrometry facilities at the Max Planck Institute for Polymer Research. The authors thank the Microscopy & Histology Core Facility at the Institute of Molecular Biology (IMB), Mainz, Germany, for assistance with bioimaging processing.

5.7.References

(1) Majhi, S.; Arora, A.; Mishra, A. Surface Immobilization of a Short Antimicrobial Peptide (AMP) as an Antibacterial Coating. *Materialia (Oxf)* **2019**, *6*, 100350.

(2) Hasan, A.; Lee, K.; Tewari, K.; Pandey, L. M.; Messersmith, P. B.; Faulds, K.; Maclean, M.; Lau, K. H. A. Surface Design for Immobilization of an Antimicrobial Peptide Mimic for Efficient Anti-Biofouling. *Chemistry – A European Journal* **2020**, *26* (26), 5789–5793.

(3) Wu, J.-T.; Huang, C.-H.; Liang, W.-C.; Wu, Y.-L.; Yu, J.; Chen, H.-Y. Reactive Polymer Coatings: A General Route to Thiol-Ene and Thiol-Yne Click Reactions. *Macromol Rapid Commun* **2012**, *33* (10), 922–927.

(4) Cai, S.; Wu, C.; Yang, W.; Liang, W.; Yu, H.; Liu, L. Recent Advance in Surface Modification for Regulating Cell Adhesion and Behaviors. *Nanotechnol Rev* **2020**, *9* (1), 971–989.

(5) Azizi, L.; Turkki, P.; Huynh, N.; Massera, J. M.; Hytönen, V. P. Surface Modification of Bioactive Glass Promotes Cell Attachment and Spreading. *ACS Omega* **2021**, *6* (35), 22635–22642.

(6) Santos, J. C. S. dos; Barbosa, O.; Ortiz, C.; Berenguer-Murcia, A.; Rodrigues, R. C.; Fernandez-Lafuente, R. Importance of the Support Properties for Immobilization or Purification of Enzymes. *ChemCatChem* **2015**, *7* (16), 2413–2432.

(7) Li, M.; Cheng, F.; Li, H.; Jin, W.; Chen, C.; He, W.; Cheng, G.; Wang, Q. Site-Specific and Covalent Immobilization of His-Tagged Proteins via Surface Vinyl Sulfone–Imidazole Coupling. *Langmuir* **2019**, *35* (50), 16466–16475.

(8) Jonkheijm, P.; Weinrich, D.; Köhn, M.; Engelkamp, H.; Christianen, P. C. M.; Kuhlmann, J.; Maan, J. C.; Nüsse, D.; Schroeder, H.; Wacker, R.; Breinbauer, R.; Niemeyer, C. M.; Waldmann, H. Photochemical Surface Patterning by the Thiol-Ene Reaction. *Angewandte Chemie International Edition* **2008**, *47* (23), 4421–4424.

(9) Bertin, A.; Schlaad, H. Mild and Versatile (Bio-)Functionalization of Glass Surfaces via Thiol−Ene Photochemistry. *Chemistry of Materials* **2009**, *21* (24), 5698–5700.

(10) Hoyle, C. E.; Bowman, C. N. Thiol–Ene Click Chemistry. *Angewandte Chemie International Edition* **2010**, *49* (9), 1540–1573.

(11) Yolamanova, M.; Meier, C.; Shaytan, A. K.; Vas, V.; Bertoncini, C. W.; Arnold, F.; Zirafi, O.; Usmani, S. M.; Müller, J. A.; Sauter, D.; Goffinet, C.; Palesch, D.; Walther, P.; Roan, N. R.; Geiger, H.; Lunov, O.; Simmet, T.; Bohne, J.; Schrezenmeier, H.; Schwarz, K.; Ständker, L.; Forssmann, W.-G.; Salvatella, X.; Khalatur, P. G.; Khokhlov, A. R.; Knowles, T. P. J.; Weil, T.; Kirchhoff, F.; Münch, J. Peptide Nanofibrils Boost Retroviral Gene Transfer and Provide a Rapid Means for Concentrating Viruses. *Nat Nanotechnol* **2013**, *8*

(2), 130–136.

(12) Schilling, C.; Mack, T.; Lickfett, S.; Sieste, S.; Ruggeri, F. S.; Sneideris, T.; Dutta, A.; Bereau, T.; Naraghi, R.; Sinske, D.; Knowles, T. P. J.; Synatschke, C. V; Weil, T.; Knöll, B. Sequence-Optimized Peptide Nanofibers as Growth Stimulators for Regeneration of Peripheral Neurons. *Adv Funct Mater* **2019**, *29* (24), 1809112.

(13) Amani, H.; Arzaghi, H.; Bayandori, M.; Dezfuli, A. S.; Pazoki-Toroudi, H.; Shafiee, A.; Moradi, L. Controlling Cell Behavior through the Design of Biomaterial Surfaces: A Focus on Surface Modification Techniques. *Adv Mater Interfaces* **2019**, *6* (13), 1900572.

(14) Abbas, W. A.; Ibrahim, M. E.; El-Naggar, M.; Abass, W. A.; Abdullah, I. H.; Awad, B. I.; Allam, N. K. Recent Advances in the Regenerative Approaches for Traumatic Spinal Cord Injury: Materials Perspective. *ACS Biomater Sci Eng* **2020**, *6* (12), 6490–6509.

(15) Yang, C.-Y.; Huang, W.-Y.; Chen, L.-H.; Liang, N.-W.; Wang, H.-C.; Lu, J.; Wang, X.; Wang, T.-W. Neural Tissue Engineering: The Influence of Scaffold Surface Topography and Extracellular Matrix Microenvironment. *J Mater Chem B* **2021**, *9* (3), 567–584.

(16) Mahumane, G. D.; Kumar, P.; du Toit, L. C.; Choonara, Y. E.; Pillay, V. 3D Scaffolds for Brain Tissue Regeneration: Architectural Challenges. *Biomater Sci* **2018**, *6* (11), 2812–2837.

(17) Abbas, W. A.; Ibrahim, M. E.; El-Naggar, M.; Abass, W. A.; Abdullah, I. H.; Awad, B. I.; Allam, N. K. Recent Advances in the Regenerative Approaches for Traumatic Spinal Cord Injury: Materials Perspective. *ACS Biomater Sci Eng* **2020**, *6* (12), 6490–6509.

(18) Stevens, M. M.; George, J. H. Exploring and Engineering the Cell Surface Interface. *Science (1979)* **2005**, *310* (5751), 1135–1138.

(19) Tsai, Y.-L.; Song, J.; Shi, R.; Knöll, B.; Synatschke, C. V. A Roadmap of Peptide-Based Materials in Neural Regeneration. *Adv Healthc Mater* **2024**, 2402939.

(20) Cho, Y.; Choi, Y.; Seong, H. Nanoscale Surface Coatings and Topographies for Neural Interfaces. *Acta Biomater* **2024**, *175*, 55–75.

(21) Simitzi, C.; Ranella, A.; Stratakis, E. Controlling the Morphology and Outgrowth of Nerve and Neuroglial Cells: The Effect of Surface Topography. *Acta Biomater* **2017**, *51*, 21–52.

(22) Tomba, C.; Migdal, C.; Fuard, D.; Villard, C.; Nicolas, A. Poly-l-Lysine/Laminin Surface Coating Reverses Glial Cell Mechanosensitivity on Stiffness-Patterned Hydrogels. *ACS Appl Bio Mater* **2022**, *5* (4), 1552–1563.

(23) Vedaraman, S.; Perez-Tirado, A.; Haraszti, T.; Gerardo-Nava, J.; Nishiguchi, A.; De Laporte, L. Anisometric Microstructures to Determine Minimal Critical Physical Cues Required for Neurite Alignment. *Adv Healthc Mater* **2021**, *10* (20), 2100874.

(24) Zhang, D.; Li, Z.; Shi, H.; Yao, Y.; Du, W.; Lu, P.; Liang, K.; Hong, L.; Gao, C. Micropatterns and Peptide Gradient on the Inner Surface of a Guidance Conduit Synergistically Promotes Nerve Regeneration in Vivo. *Bioact Mater* **2022**, *9*, 134–146.

(25) Yang, S.; Zhu, J.; Lu, C.; Chai, Y.; Cao, Z.; Lu, J.; Zhang, Z.; Zhao, H.; Huang, Y.-Y.; Yao, S.; Kong, X.; Zhang, P.; Wang, X. Aligned Fibrin/Functionalized Self-Assembling Peptide Interpenetrating Nanofiber Hydrogel Presenting Multi-Cues Promotes Peripheral Nerve Functional Recovery. *Bioact Mater* **2022**, *8*, 529–544.

(26) Cadena, M.; Ning, L.; King, A.; Hwang, B.; Jin, L.; Serpooshan, V.; Sloan, S. A. 3D Bioprinting of Neural Tissues. *Adv Healthc Mater* **2021**, *10* (15), 2001600.

(27) Yan, Y.; Li, X.; Gao, Y.; Mathivanan, S.; Kong, L.; Tao, Y.; Dong, Y.; Li, X.; Bhattacharyya, A.; Zhao, X.; Zhang, S.-C. 3D Bioprinting of Human Neural Tissues with Functional Connectivity. *Cell Stem Cell* **2024**, *31* (2), 260-274.e7.

(28) Harant, A. W.; Khire, V. S.; Thibodaux, M. S.; Bowman, C. N. Thiol−Ene Photopolymer Grafts on Functionalized Glass and Silicon Surfaces. *Macromolecules* **2006**, *39* (4), 1461–1466.

(29) Abramoff, M.; Magalhães, P.; Ram, S. J. Image Processing with ImageJ. *Biophotonics International* **2003**, *11*, 36–42.

(30) Schneider, C. A.; Rasband, W. S.; Eliceiri, K. W. NIH Image to ImageJ: 25 Years of Image Analysis. *Nat Methods* **2012**, *9* (7), 671–675.

(31) Gras, S. L. Chapter 6 - Surface- and Solution-Based Assembly of Amyloid Fibrils for Biomedical and Nanotechnology Applications. In *Advances in Chemical Engineering*; Koopmans, R. J., Ed.; Academic Press, 2009; Vol. 35, pp 161–209.

(32) Kinge, S.; Crego-Calama, M.; Reinhoudt, D. N. Self-Assembling Nanoparticles at Surfaces and Interfaces. *ChemPhysChem* **2008**, *9* (1), 20–42.

(33) Yang, B.; Adams, D. J.; Marlow, M.; Zelzer, M. Surface-Mediated Supramolecular Self-Assembly of Protein, Peptide, and Nucleoside Derivatives: From Surface Design to the Underlying Mechanism and Tailored Functions. *Langmuir* **2018**, *34* (50), 15109–15125.

(34) Vigier-Carrière, C.; Boulmedais, F.; Schaaf, P.; Jierry, L. Surface-Assisted Self-Assembly Strategies Leading to Supramolecular Hydrogels. *Angewandte Chemie International Edition* **2018**, *57* (6), 1448–1456.

(35) Zheng, Y.; Yu, L.; Zou, Y.; Yang, Y.; Wang, C. Steric Dependence of Chirality Effect in Surface-Mediated Peptide Assemblies Identified with Scanning Tunneling Microscopy. *Nano Lett* **2019**, *19* (8), 5403–5409.

(36) Ku, S. H.; Park, C. B. Highly Accelerated Self-Assembly and Fibrillation of Prion Peptides

on Solid Surfaces. *Langmuir* **2008**, *24* (24), 13822–13827.

(37) Vigier-Carrière, C.; Garnier, T.; Wagner, D.; Lavalle, P.; Rabineau, M.; Hemmerlé, J.; Senger, B.; Schaaf, P.; Boulmedais, F.; Jierry, L. Bioactive Seed Layer for Surface-Confined Self-Assembly of Peptides. *Angewandte Chemie International Edition* **2015**, *54* (35), 10198–10201.

(38) Dugger, J. W.; Webb, L. J. Fibrillar Structures Formed by Covalently Bound, Short, β-Stranded Peptides on Self-Assembled Monolayers. *Langmuir* **2015**, *31* (11), 3441–3450.

(39) Hauck, C. R. Cell Adhesion Receptors – Signaling Capacity and Exploitation by Bacterial Pathogens. *Med Microbiol Immunol* **2002**, *191* (2), 55–62.

(40) Kovalevich, J.; Langford, D. Considerations for the Use of SH-SY5Y Neuroblastoma Cells in Neurobiology. In *Neuronal Cell Culture: Methods and Protocols*; Amini, S., White, M. K., Eds.; Humana Press: Totowa, NJ, 2013; pp 9–21.

(41) Shipley, M. M.; Mangold, C. A.; Szpara, M. L. Differentiation of the SH-SY5Y Human Neuroblastoma Cell Line. *JoVE* **2016**, No. 108, e53193.

(42) García-Mesa, Y.; García-Piqueras, J.; Cuendias, P.; Cobo, R.; Martín-Cruces, J.; Feito, J.; García-Suarez, O.; Biedma, B. M.; Vega, J. A. Synaptophysin Is a Selective Marker for Axons in Human Cutaneous End Organ Complexes. *Annals of Anatomy - Anatomischer Anzeiger* **2022**, *243*, 151955.

5.8. Supporting information

Peptide photoimmobilization by thiol-ene chemistry for enhanced neural cell adhesion

Yu-Liang Tsai[1], Sotiria Moschopoulou-Triantafyllidou[1], Jiyao Yu[1], Sa'id Albarqawi[2], Tommaso Marchesi D'Alvise[1], Lothar Veith[1], Rüdiger Berger[2], Christopher V. Synatschke[1,*]

3. Max Planck Institute for Polymer Research, Synthesis of Macromolecules, Ackermannweg 10, 55128 Mainz, Germany
4. Max Planck Institute for Polymer Research, Physics at Interfaces, Ackermannweg 10, 55128 Mainz, Germany

* Corresponding Author

E-mail: synatschke@mpip-mainz.mpg.de

Table of Content

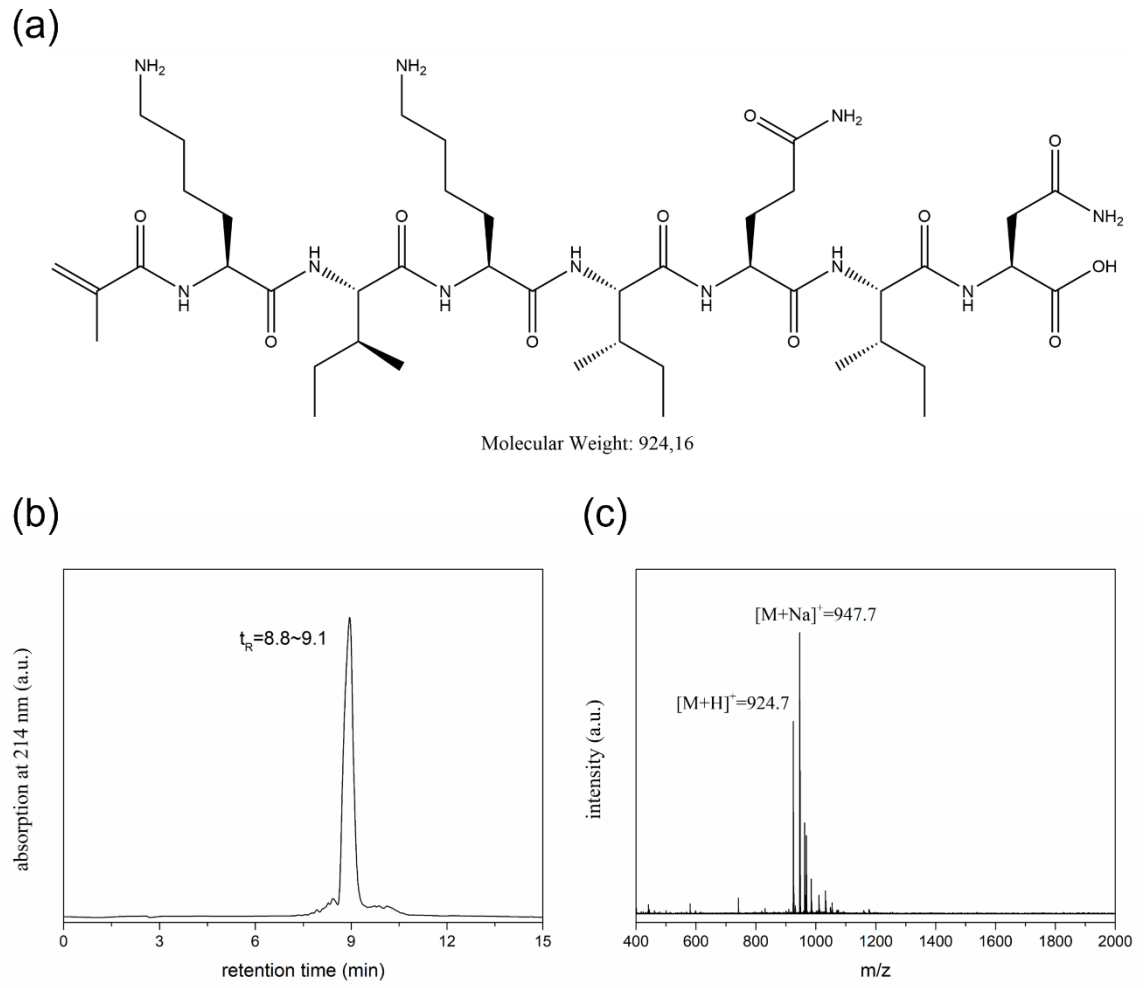

Figure S5. 1. Chemical structure and purity analysis of acrylated peptide, Acr-KIKIQIN. (a) Chemical structure of Acr-KIKIQIN. (b) HPLC trace of the acrylated peptide in an acidic condition with a retention time (t_R) = 8.8– 9.1 min. (c) MALDI-ToF-MS of Acr-KIKIQIN showing expected product signals assigned to $[M+H]^+$ =924.7 m/z and $[M+Na]^+$ = 947.7 were detected (theoretical MW = 924.2).

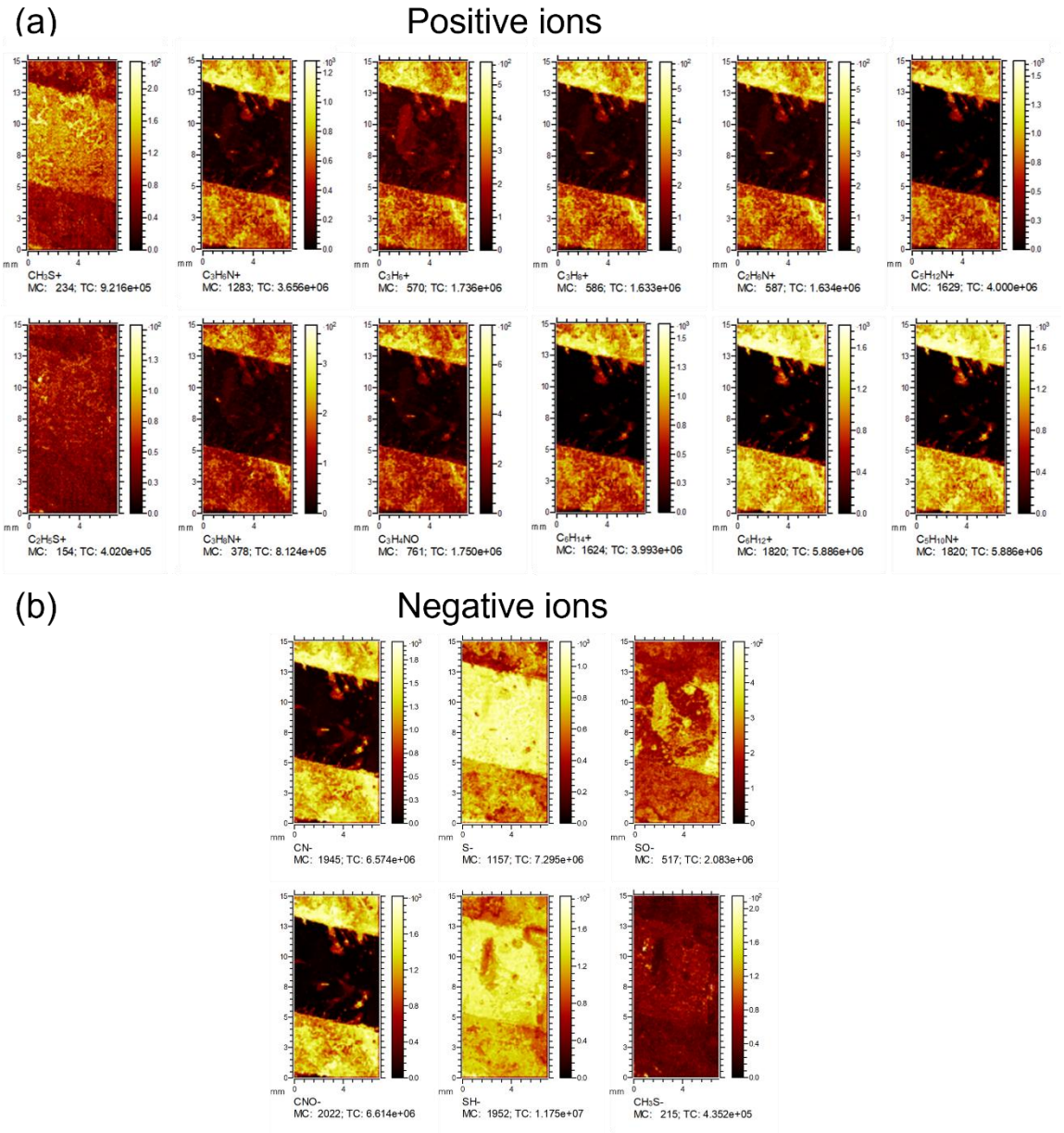

Figure S5. 2. ToF-SIMS images of the photopatterned peptide-modified substrates. (a) Positive ions of ToF-SIMS images, including (CH_3S^+, $C_3H_6N^+$, $C_3H_6^+$, $C_3H_8^+$, $C_2H_6N^+$, $C_5H_{12}N^+$, $C_2H_5S^+$, $C_3H_8N^+$, C_3H_4NO, $C_6H_{14}^+$, $C_6H_{12}^+$, and $C_5H_{10}N^+$). (b) Negative ions of ToF-SIMS images, including (CN^-, S^-, SO^-, CNO^-, SH^-, and CH_3S^-). MC stands for maxium counts (per pixel) and TC represents total counts (in image).

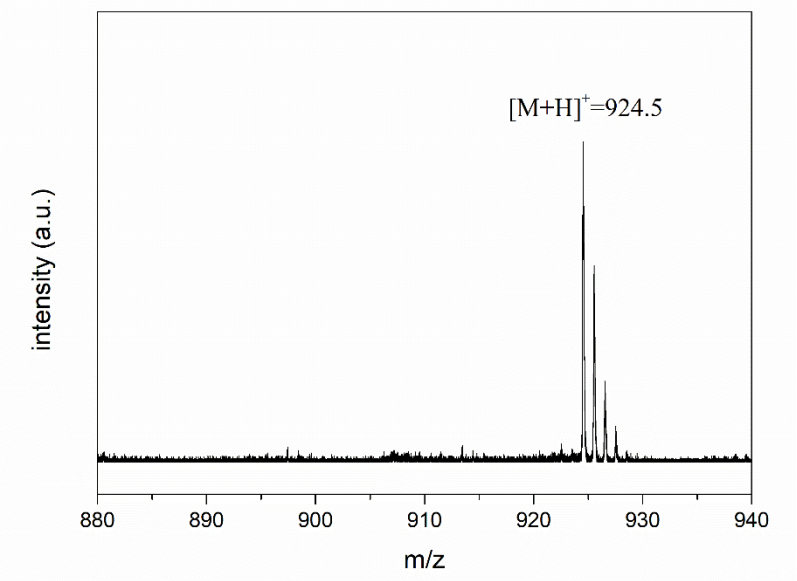

Figure S5. 3. ToF-SIMS of the peptide modified substrate. $[M+H]^+$=924.5 m/z was detected (theoretical MW = 924.2) on the peptide modified substrate.

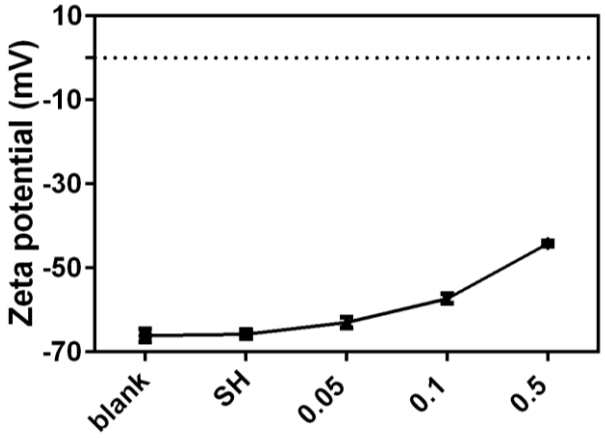

Figure S5. 4. Surface zeta potential of different substrates. Blank was bare glass (-66.11 ± 1.58 mV), and SH represented the thiolated glasses (-65.78 ± 0.72 mV), and 0.05 mg/mL (-62.98 ± 1.28 mV), 0.1 mg/mL (-57.31 ± 1.14), and 0.5 mg/mL (-44.17 ± 0.60) indicates the peptide concentrations (mg/mL) used for coating.

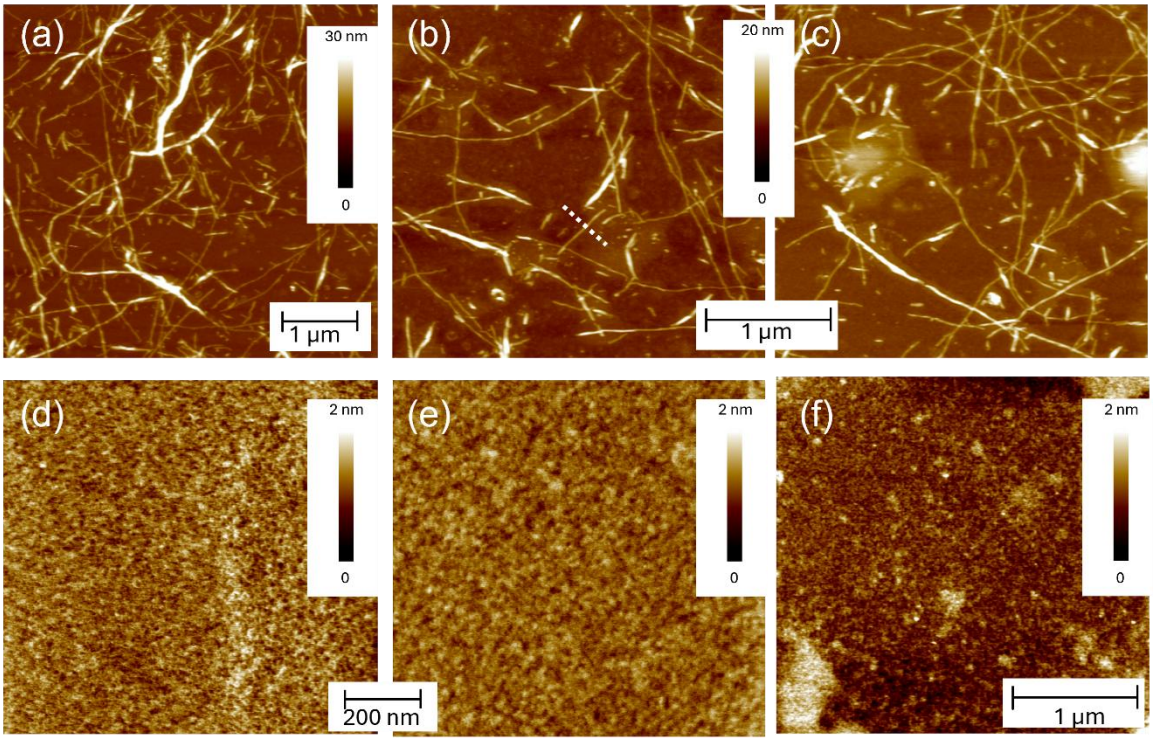

Figure S5. 5. SFM images of photopatterned peptide-modified substrates at three different spots. (a, b, c) Peptide nanofibers are visible on the peptide-modified substrates in the SFM images. (d, e, f). Smooth surfaces without defined nanostructure are visible on the thiolated substrates in the SFM images.

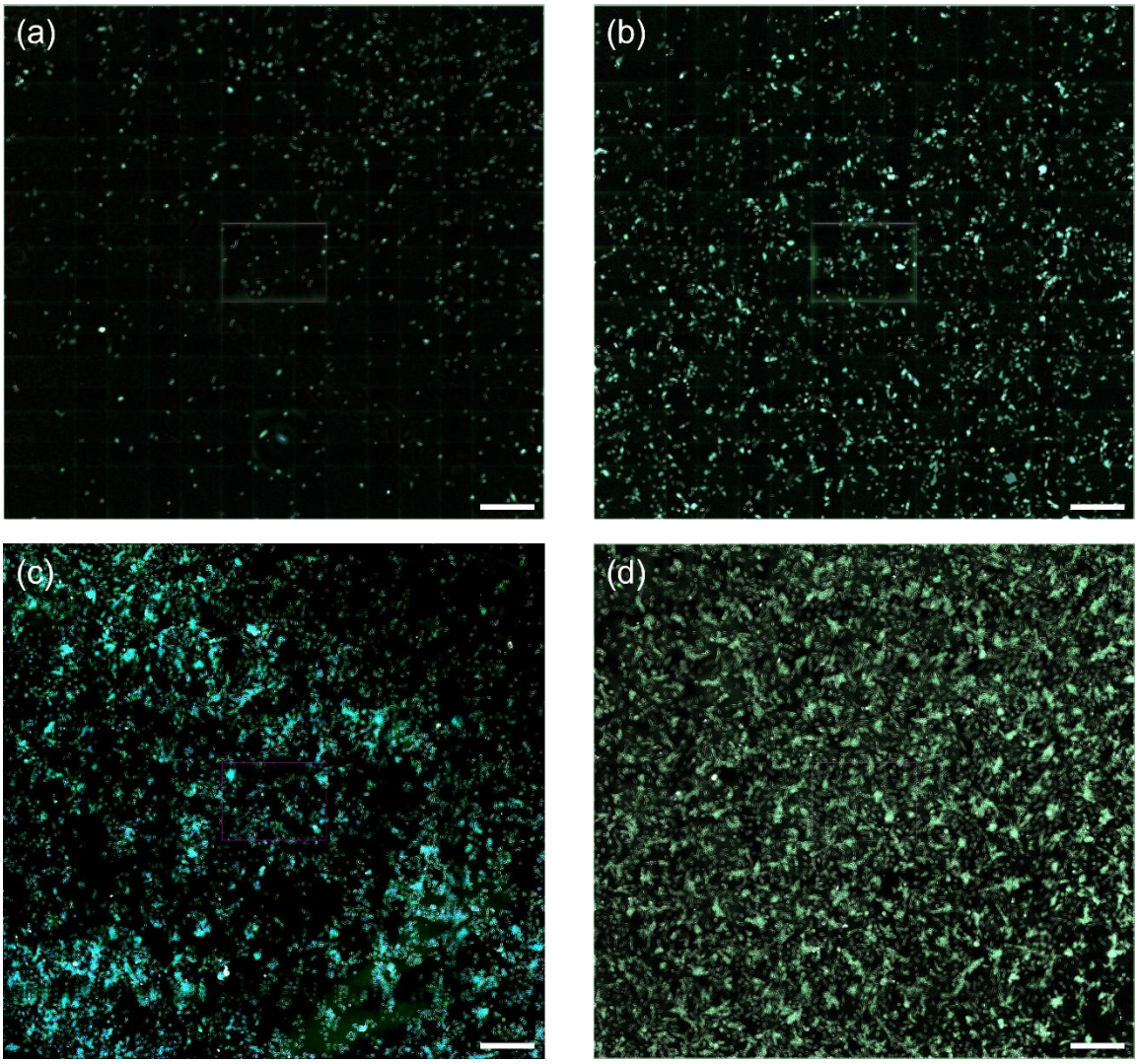

Figure S5. 6. Large scale, stitched images of SH-SY5Y cell adhesion on different substrates. (a) Cell adhesion on the thiolated substrates. (b) Cell adhesion on the peptide (0.05 mg/mL) modified substrate. (c) Cell adhesion on the peptide (0.1 mg/mL) modified substrate. (d) Cell adhesion on the peptide (0.5 mg/mL) modified substrate. Cells were stained with NucBlue and secondary antibody labeled with Alexa 488, and the acquired images were processed with ImageJ by subtracting background with the parameter "rolling ball radius of 50 pixels". Scale bars represent a distance of 500 μm.

6. Summary and Outlook

Amyloid-like SAPs are a class of materials that assemble into supramolecular nanostructures and have high resistance to degradation under physiological conditions, making them intriguing templates for biomedical applications. The assembled nanostructures of amyloid SAPs, especially nanofibers, resemble the ECM of the complex neural tissue environments. Several factors influence the assembled nanostructure. First, the sequence design of amyloid-like SAPs is one of the most intuitive factors determining assembly morphologies because of charge distribution and hydrophobicity profile. In contrast, the effects of external factors, such as ionic strength, temperature, additives, interfacial chemistry, and sample processing on the assembled structure have not been studied as extensively. Other than the convoluted neural environment, neural cells are sensitive to their surroundings and many physical properties, including matrix stiffness, roughness, and topography, can control neural cell fate. Therefore, the scope of this thesis focuses on how intrinsic and extrinsic factors alter the self-assembly behavior of SAPs and determine their morphologies, which further influence neural cell behavior.

As previously mentioned, sequence mutation is the most common method for achieving structural changes in SAPs and modulating their functions. In Chapter 3, the amino acid sequences of amyloid-like SAPs, specificially of derivates of EF-C, were systematically changed based on their hydrophobic cores. Initially, nine peptide sequences were categorized into three groups: aromatic, aliphatic, and weakly hydrophobic. The physicochemical properties of each variant, such as aggregation concentration, assembly kinetics, and conversion rates were characterized. Self-assembled morphologies were analyzed by electron microscopy. Sequences containing aliphatic side chains behaved similarly to sequences containing aromatic side chains except for the sequence with tyrsine, which did not form assembled nanostructure. This exception could be explained by computational modeling and simulation, such as stability test and analysis of solvent accessible surface area. Further in vitro studies showed that neuroblastoma cells proliferated and differentiated better when treated with the structure-forming SAPs. These results suggested that the fibril material structures played an important role in modulating cell behavior, which highlights the importance of structure-property correlation. Combining computational approaches with biophysical characterization and biological

readouts is anticipated to accelerate the discovery of new peptide sequences for neural regeneration.

Other than the sequence of a peptide, minor variations in the sample composition may affect the assembly behavior of amyloid-like SAPs, a feature often overlooked by researchers. In Chapter 4, the solvent effect on the morphology and neural activity of amyloid-like SAPs, amyloid beta (Aβ) peptides, was systematically investigated. The same peptide sequences, $A\beta_{1\text{-}42}$, dissolved in different solvents, incubated in different assay buffers, and tested at different time points resulted in differences in the biological response, namely the activation of FPR1 on neural cells. These experimental results were consistent with those of other research groups. Surprisingly, the same peptide of high purity (> 98%) produced by four different manufacturers using the same preparation protocol also led to different FPR activities. Although the variations between samples from different manufacturers were so small that they were often overlooked, the four peptides of the same sequence showed different ThT binding affinities and significantly different secondary structures as well as self-assembly morphology observed by TEM. These results highlighted that the processing history of the peptide influenced the structures of amyloid-like SAPs and their neural activity. The findings in this chapter served as a non-trivial reminder to researchers to always pay close attention to experimental conditions, including peptide purity, solvents, buffers, pH, incubation time, and peptide sources.

The previous two chapters demonstrate that neural cells, indeed, respond to structural differences in amyloid-like SAPs, such as EF-C derived and Aβ peptides. However, some cellular behaviors such as differentiation require long-term observation. Therefore, it is of interest to build a stable substrate derived from amyloid-like SAPs for neural cells. In Chapter 5, the goal was to create a platform that is easily fabricable, selective, large-scale, and robust for neural cell culture. To generate this platform, the photo-triggered thiol-ene reaction was selected to connect peptides to a glass substrate. The sample preparation process began with the thiolation of glass slides via chemical vapor deposition of MPS and the acylation of amyloid-like SAPs. The modified peptides were then photoimmobilized onto thiolated substrates. Results from surface chemical analyses, including XPS and ToF-SIMS, confirmed the peptide modification of the surface. ToF-SIMS images showed that the modification was homogeneous and had the potential for photopatterning, given further

optimization. Contact angle and surface zeta potential measurements provided additional evidence of a successful peptide modification. AFM images of nanofiber structures revealed that the modified peptides underwent surface-mediated self-assembly and were not randomly distributed. Last but not least, neuroblastoma cells adhered significantly better to the peptide-modified substrates than to the thiolated substrates. This phenomenon demonstrated the potential of amyloid-like SAPs to be selectively immobilized via a photo-triggered thiol-ene reaction. These nanofibers facilitated neural cell adhesion as reported in the previous literature. The results presented in this chapter demonstrate a simple method for creating a large-scale, robust platform for neural cell culture that allows for the growth of large numbers of cells on well-defined surfaces.

Overall, this thesis examined the factors that influence the self-assembly structure of amyloid-like SAPs, focusing primarily on peptide sequence, solvent effect, and surface chemistry. Chapter 3 pointed out that computational simulation of materials could rationalize the design of biological experiments. Chapter 4 emphasized the need to handle amyloid-like SAPs with caution to minimize frequently overlooked variables. Chapter 5 presented a new strategy for building a stable platform based on amyloid-like SAPs for long-term neural cell culture. hese three chapters presented different amyloid-like SAP structures, which were reflected in different neural activities. This reiterates the importance of the structure-property relationship between amyloid-like SAPs and neural cells, as illustrated in **Figure 6.1**.

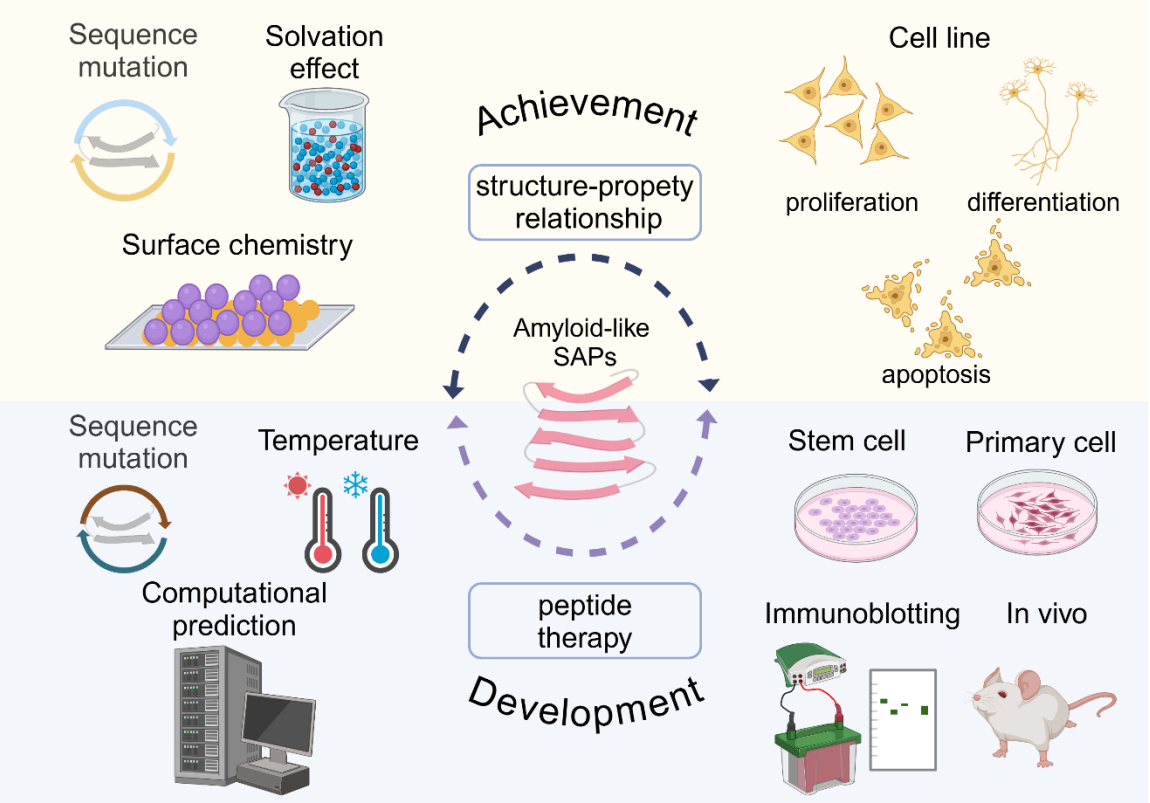

Figure 6.1. The scheme of the overall achievement (top panel) and the future development (bottom panel) in this thesis. The top panel illustrates three parameters each from material and biological perspectives. Factors such as hydrophobic group mutation, solvent effect, and surface immobilization influence the self-assembled structure of amyloid-like SAPs. Preliminary biological readouts, i.e. proliferation, differentiation, apoptosis, are selected to evaluate the correlation between material structure and bioactivity. The bottom panel depicts that other sequence mutation and temperature may be the potential parameters worth investigating with the facilitation of computational modeling. Using more sensitive cell sources, e.g. stem cells or primary neurons, increases the reliability of biological study. Understanding the biological mechanisms such as immunoblotting is a critical milestone before moving on to *in vivo* studies.

The ultimate goal is to develop therapeutic amyloid-like SAPs for treating neural diseases and injuries. This thesis provides a fundamental understanding of the correlation between structure-forming amyloid-like SAPs and the cultivation of neural cell lines. Additionally, this thesis introduced a new methodology for building a robust amyloid-like

SAP substrate for neural cells. However, many hurdles remain before SAPs can be realized as therapeutics. From a material perspective, sequential mutations should encompass more than hydrophobic interactions. For example, charge types and charge distribution are canonical examples for exploring new peptide-based therapeutics. Another option to create different supramolecular assemblies is scrambling peptide sequences. Heat treatment and different incubation conditions are important factors that are known to play a role in the nucleation and growth of polymeric materials. Recently, various research groups have reported that temperature can also influence the nucleation and growth of supramolecular materials, such as peptide amphiphile and aromatic peptide amphiphile. However, few studies have examined the thermal effect on pure peptide materials, let alone on amyloid-like SAPs, which are investigated in this thesis. By changing temperature and incubation conditions, researchers can explore the full potential of a material and reduce the time needed to synthesize more materials. Systematic studies of structure-property correlations are usually labor-intensive and require much trial and error. In principle, computer simulations can accurately predict the structure and stability of amyloid-like SAPs with short amino acid sequences (less than 10 amino acids), but challenges remain for longer sequences. Additionally, the databases of assembly structures and functional properties remain limited. The ultimate challenge will be predicting not only the structure and stability but also the resulting properties of the materials.

From a biological perspective, developing an in-depth understanding of how organisms, particularly neural cells, respond to these self-assembled nanostructures is essential to advancing the development of neural therapeutics based on amyloid-like SAPs. For example, the EF-C derived peptides investigated in this thesis demonstrated encouraging neurotrophic effects on a human neuroblastoma cell line based on ATP level and cell morphology. In this thesis, the majority of biological experiments were conducted using human neuroblastoma cells, indicating that there is less concern about experimental results being ineffective across species. However, there are a wide variety of neurons, including sensory neurons, excitatory neurons, inhibitory interneurons, etc., and the neural therapeutic effect of EF-C derived peptides may not apply equally to all of them. Therefore, it is important to understand the biological mechanisms by which EF-C-derived peptides are neurotrophic before testing them with different neurons. Last but not least, handling

neural cell cultures is difficult because they proliferate slowly, and some have intermediate neuronal states. Furthermore, harvesting primary neurons for these studies usually requires sacrificing animals, which should be minimized. Developing high-throughput and accurate methods for biological readouts can definitely accelerate and advance the development of amyloid-like SAPs for new neural drugs and neural tissue engineering.

Appendix

List of peer-review publications, book chapters, and preprints

1. **Y.-L. Tsai,** Sotiria Moschopoulou-Triantafyllidou, Jiyao Yu, Sa'id Albarqawi, Tommaso Marchesi D'Alvise, Lothar Veith, Rüdiger Berger, Christopher Synatschke, Peptide photoimmobilization by thiol-ene chemistry for enhancing neural cell adhesion (under peer review in ACS Biomaterials Science & Engineering) ChemRxiv, **2025** https://doi.org/10.26434/chemrxiv-2025-3t1tl

2. **Y.-L. Tsai,** P. Cavallo, Q. Lu, C. P. Ender, J. Link, K. Amann-Winkel, K. Endres, C.V. Synatschke, T. John, Design of the Hydrophobic Core of Self-Assembling EF-C Peptide Fibrils for Enhanced Neural Regeneration, (under revision in Small Science) ChemRxiv, **2024,** http://doi.org/ 10.26434/chemrxiv-2024-mzghg

3. **Y.-L. Tsai**, J. Song, R. Shi, B.Knöll, C. V. Synatschke, A roadmap of peptide-based materials in neural regeneration, *Adv. Healthc. Mater.* **2024**, 2402939. https://doi.org/10.1002/adhm.202402939

4. **Y.-L. Tsai**, C. V. Synatschke, Functional Materials from Self-Assembling Peptide–Polymer Hybrids. *In Supramolecular Nanotechnology* **2023** *(eds O. Azzaroni and M. Conda-Sheridan)*. https://doi.org/10.1002/9783527834044.ch35

5. L. Busch, Z. a. Taleb, **Y.-L. Tsai,** V. T. T. Nguyen, Q. Lu, C. V. Synatschke, K. Endres, B. Bufe, Amyloid beta and its naturally occurring N-terminal variants are potent activators of human and mouse formyl peptide receptor 1, *J. biol. Chem.*, **2022**, 298, 12, 102642. https://doi.org/10.1016/j.jbc.2022.102642

Curriculum Vitae

Personal information

Name	Yu-Liang Tsai
Date of birth	12.12.1993
Place of the birth	Taipei, Taiwan (R.O.C)
Nationality	Taiwanese
Address	Isaac-Fulda-Allee 4, 55124, Mainz, Germany

Education and work

04.2021– present	**Doctoral Candidate**, Max Planck Institute for Polymer research, Mainz, Germany Thesis: Structural variations of amyloid-like peptides and their interaction with neural cells
09.2018– 03.2021	**Master of Science**, Polymer Science and Engineering, Institute of Polymer Science and Engineering, National Taiwan University, Taiwan Thesis: A 3D-printable, glucose-sensitive and thermoresponsive hydrogel as sacrificial materials for constructs with vascular-like channels
10.2017– 10.2018	**Substitute Military Services,** Public Administration Substitute Services in Xizhi Household Registration office, New Taipei City, Taiwan
09.2013– 08.2017	**Bachelor of Science**, Material Science and Engineering, Department of Material Science and Engineering, National Taiwan University of Science and Technology, Taiwan
02.2013– 07.2017	**Exchange Program**, Department of mechanical engineering, RheinMain University of Applied Sciences, Germany

Honors and Awards

2020.09	**Best Poster** of 2020 Taiwan Bio-Development Foundation seminar
2017.03	**Outstanding Youth Award Certificate,** National Taiwan University of Science and Technology
2017.01	**Certificate of Excellence, College of Engineering,** National Taiwan University of Science and Technology
2016.11	**Certificate of award,** Undergraduate research project, Department of Materials and Science and Engineering, National Taiwan University of Science and Technology
5 times	**Certificate of academic achievements**

Languages

Chinese	Native	
English	Fluent	GRE Q: 168/170, V: 153/170, A: 3.0/6.0
		TOEFL iBT L: 26, R: 28, W: 24, S: 23 (101/120)
German	Good	B1 Zertifikat (Telc, Deutsch-Test für Zuwander)